



**HAL**  
open science

# Characterization of the Dynamics of the Atmosphere of Venus with Doppler velocimetry

Pedro Miguel Borges Do Canto Mota Machado

► **To cite this version:**

Pedro Miguel Borges Do Canto Mota Machado. Characterization of the Dynamics of the Atmosphere of Venus with Doppler velocimetry. Astrophysics [astro-ph]. Observatoire de Paris; Université de Lisbonne, 2013. English. NNT : 2013OBSP0270 . tel-02337921

**HAL Id: tel-02337921**

**<https://hal.science/tel-02337921>**

Submitted on 4 Nov 2019

**HAL** is a multi-disciplinary open access archive for the deposit and dissemination of scientific research documents, whether they are published or not. The documents may come from teaching and research institutions in France or abroad, or from public or private research centers.

L'archive ouverte pluridisciplinaire **HAL**, est destinée au dépôt et à la diffusion de documents scientifiques de niveau recherche, publiés ou non, émanant des établissements d'enseignement et de recherche français ou étrangers, des laboratoires publics ou privés.

UNIVERSIDADE de LISBOA

FACULDADE de CIÊNCIAS da  
UNIVERSIDADE de LISBOA

Doutoramento em Astronomia e Astrofísica

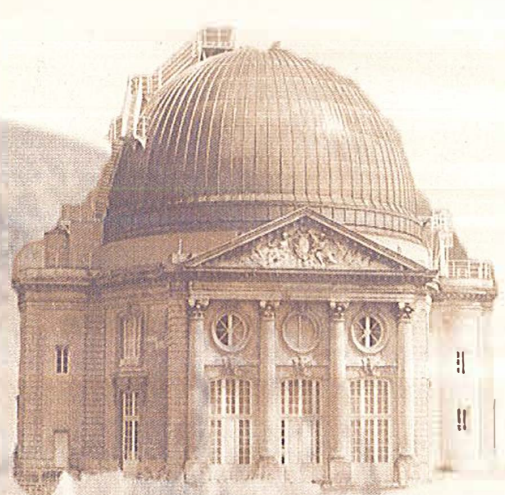
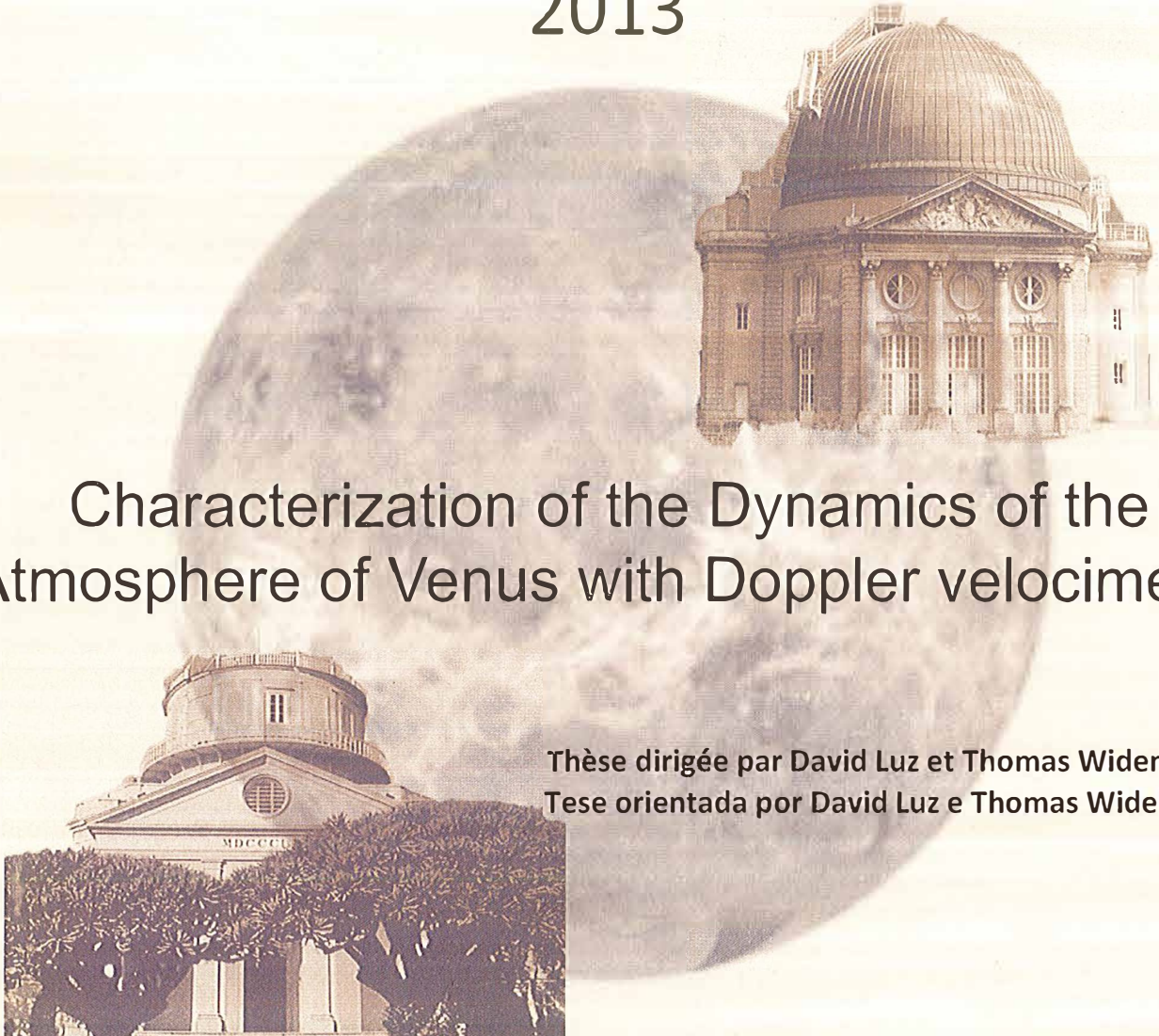
OBSERVATOIRE de PARIS

ÉCOLE DOCTORALE ASTRONOMIE ET  
ASTROPHYSIQUE D'ILE-DE-FRANCE


Doctorat en Astronomie et Astrophysique

Pedro Miguel Borges do Canto Mota MACHADO

2013



# Characterization of the Dynamics of the Atmosphere of Venus with Doppler velocimetry



Thèse dirigée par David Luz et Thomas Widemann  
Tese orientada por David Luz e Thomas Widemann

Soutenue le 2 Décembre 2013 devant un jury composé de:  
Tese defendida a 2 de Dezembro de 2013 perante o júri:

Didier Pelat (LUTH - Obs. de Paris)  
Robert Todd Clancy (Space Science Institute)  
Wojciech Markiewicz (Max-Planck-Institut für Aeronomie)  
Thérèse Encrenaz (LESIA - Obs. de Paris)  
Giuseppe Piccioni (INAF – IAPS)  
José Afonso (CAAUL/FCUL - Universidade de Lisboa)  
David Luz (CAAUL/FCUL - Universidade de Lisboa)  
Thomas Widemann (LESIA - Obs. de Paris)

Président du Jury  
Rapporteur  
Rapporteur  
Examineur  
Examineur  
Examineur  
Directeur de thèse  
Directeur de thèse

UNIVERSIDADE de LISBOA

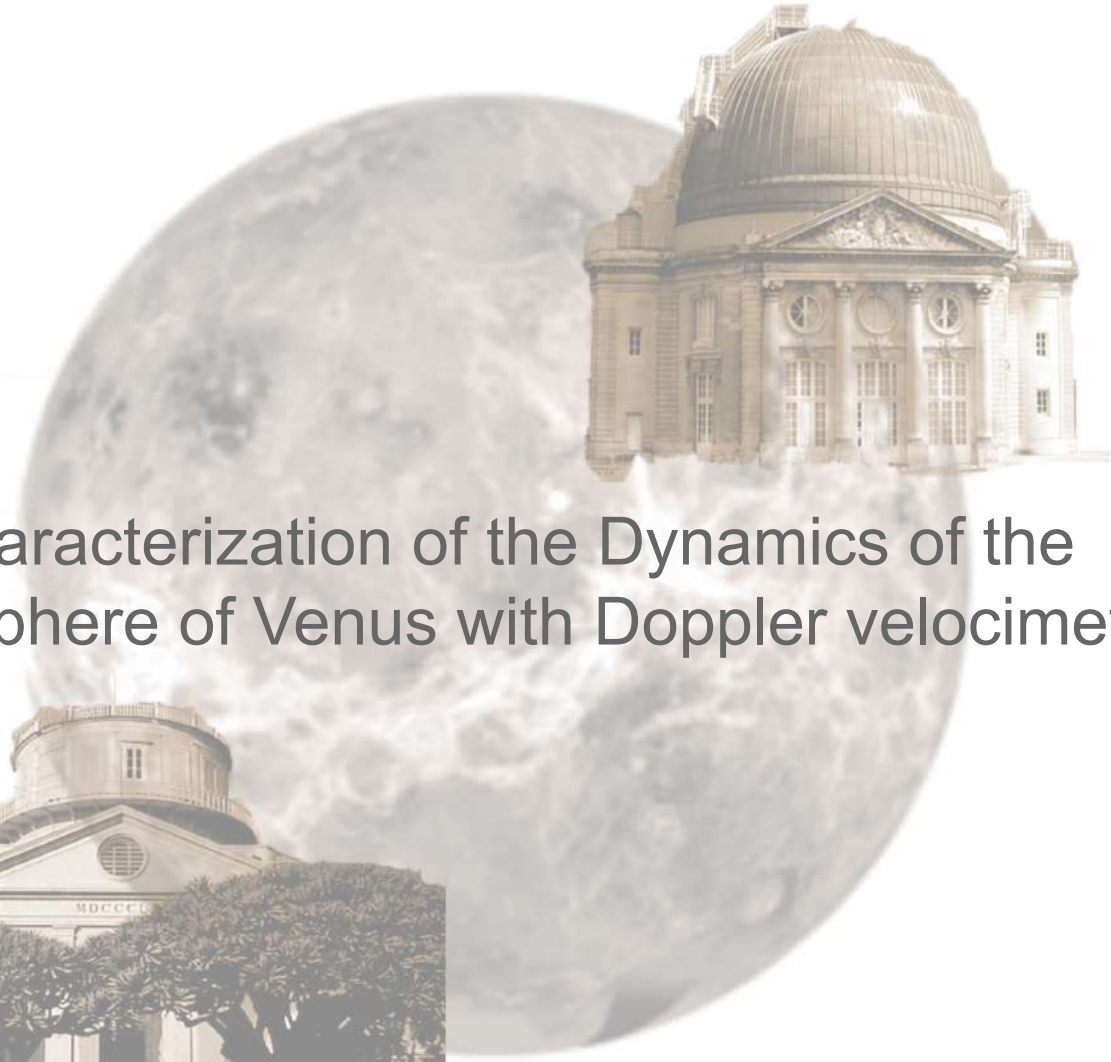
FACULDADE de CIÊNCIAS da  
UNIVERSIDADE de LISBOA  
Departamento de Física



UNIVERSIDADE  
DE LISBOA

OBSERVATOIRE de PARIS

ÉCOLE DOCTORALE ASTRONOMIE ET  
ASTROPHYSIQUE D'ILE-DE-FRANCE



# Characterization of the Dynamics of the Atmosphere of Venus with Doppler velocimetry



Pedro Miguel Borges do Canto Mota MACHADO

PhD in Astronomy and Astrophysics

2013



UNIVERSIDADE de LISBOA



FACULDADE de CIÊNCIAS da  
UNIVERSIDADE de LISBOA  
Departamento de Física



UNIVERSIDADE  
DE LISBOA

OBSERVATOIRE de PARIS

ÉCOLE DOCTORALE ASTRONOMIE ET  
ASTROPHYSIQUE D'ILE-DE-FRANCE



# Characterization of the Dynamics of the Atmosphere of Venus with Doppler velocimetry



Pedro Miguel Borges do Canto Mota MACHADO

Thesis directed by Dr. David Luz and Dr. Thomas  
Widemann, specially elaborated to obtain the degree of PhD  
in Astronomy and Astrophysics.

2013



*“Nous nous découvrons, nous aussi, emportés vers un avenir  
ignoré, à travers la pensée des vents...”*

**Antoine de Saint-Exupéry** (*Terre des hommes*)





# Aknowledgements

Along this long journey I was so fortunate that I had two beacons who helped me finding a safe way. The winds are not always peaceful. There are storms and hurricanes, tornadoes and dangerous shallows which can sink the boat. It is true that now I just feel a gentle breeze swelling my boat's sails. It is true that I smile listening the whistle of the wind...now returning to harbour after having gave name to blank territories in old maps...I return from a harsh voyage, but I kept the love for sailing...and for the wind. I am already started dreaming about the next destination. There is no such thing as an old wind...the wind is always new, always fresh...

I am grateful to my supervisors David Luz and Thomas Widemann. They were always a reference and an example of dedication and seriousness as scientists, always preserving an ethical and responsible attitude. I learned a lot with them, and I thank them for their patience and availability. We worked hard but the atmosphere was always dynamic and vibrant of joy. It was a privilege belonging to a crew which captain loves his job. Now I feel I am a much better sailor and I am eager to resume the navigation in the deep seas of science.

It was a real privilege for me to work at the *Observatoire de Paris*. It was also a pleasure to work there. To my dear colleagues, I leave here a friendly hug, and I will remember with delight the spirit of mutual help, which has always reigned amongst us. My debt of gratitude to several researchers and staff is huge and I will remember with affection all the help and sympathy that they always provided me.

The Lisbon Observatory was the place that saw my first steps on science...so, it is my home, to which I am very happy to return. The Lisbon's Center of Astronomy and Astrophysics (CAAUL) is a pleasant and wonderful place to work, always full of enthusiasm. It seems that each one that works there is a brick in the building walls.

It was an honour for me that such distinguished jury accepted to participate in this decisive stage of my life. I am very happy for that and I hope that I deserved their time and attention. I acknowledge all elements of the

jury, specially the two *rapporteurs*, for the attention dedicated to this thesis.

I will be always grateful to my wife, Patrícia, for amplifying all that I am and by valuing what I care about. She endured this true marathon with a generous and compassionate spirit. Despite my frequent absences she was always present and the restoring force towards her was enhanced by the distance, even in a direct proportion.

My dear sons, Miguel and Filipe remained my beloved friends, despite all those nights I could not tell them stories to sleep. And for not forgetting me, even if I was so often away from their cheerful company.

My journey would not have been possible without the many people who cheered me on and helped me through the grey tough days. I am deeply grateful to my dear friend Eddie, that welcomed me in his house, were I felt always a warm and friendly atmosphere. I will always remember our philosophical chats and the cultural life that we shared together. It was very funny sailing together...the wind is always a pleasant bond. I thank him for the lasting encouragement, kind hospitality, and words of motivation with which I breathed the will and dedication. He will remain in my heart as a wonderful person.

To my parents, Jacinto Machado and Julia, by having instilled on me the taste for mathematics and science in general. I am grateful to them for having developed and amplified on me a sharp curiosity for knowledge, by having helped me developing a cultural and artistic sensibility and encouraged me in choosing as a major goal, the pursuit of wisdom.

A special word to my mother in law, Josefa, to whom I owe having had the possibility of being absent so often, without harming too much the stability of my family. I thank her for her patience and dedication.

I would like dedicate a special thanks to my colleagues, researchers and friends who have supported and helped me from the very beginning of this true marathon. I highlight Javier Peralta, João Retrê, Emmanuel Lellouch, Sanjay Limaye, Bruno Siccardi, Francoise Roques, Manuela Sornig, Brad Sandor, Dimitri Titov, Agustin Sánchez-Lavega, Ricardo Hueso, Felipe Braga Ribas, Maryam El Moutamid, João Lin Yun, Rui Agostinho, Eliot Young, Lucie Maquet, Quentin Kral, J.F. Donati, Y. Matsuda and Masahiro Takagi for the helpful and useful advice, fruitful suggestions and for many valuable discussions.

I would also like to extend my gratitude to all the exceptional teachers that provided me accurate knowledge, extremely useful tools, helped to develop my scientific background, and a critical and ethical sense. They showed me how science can be fun, relevant and honest. With their help now I feel that the universe, in addition to being fascinating, can be great fun.

I acknowledge the *Fundação Luso-Americana para o Desenvolvimento*

(FLAD) for the travel grant which they attributed to me.

I also acknowledge the support of the Portuguese Foundation for Science and Technology (FCT) for providing me the opportunity and the financial support to carry out the research presented in this thesis by the funding of the PhD grant (reference: SFRH/BD/66473/2009).



# *Abstract*

Currently the study of the Venus' atmosphere grows as a theme of major interest among the astrophysics scientific community.

The most significant aspect of the general circulation of the atmosphere of Venus is its retrograde super-rotation. A complete characterization of this dynamical phenomenon is crucial for understanding its driving mechanisms.

This work participates in the international effort to characterize the atmospheric dynamics of this planet in coordination with orbiter missions, in particular with Venus Express. The objectives of this study are to investigate the nature of the processes governing the super-rotation of the atmosphere of Venus using ground-based observations, thereby complementing measurements by orbiter instruments.

This thesis analyzes observations of Venus made with two different instruments and Doppler velocimetry techniques.

The first part of the thesis presents ground-based Doppler velocimetry measurements of the zonal winds based on observations carried out with the Ultraviolet and Visual Echelle Spectrograph at ESO's Very Large Telescope. Using Doppler-shifted Fraunhofer lines from the solar spectrum, this high resolution spectrograph ( $R \sim 100,000$ ) allows to measure the velocity of Venus' upper cloud layer with a precision of about  $5 \text{ ms}^{-1}$ . Under the assumption of predominantly zonal flow, this method allows the simultaneous direct measurement of the zonal velocity across a range of latitudes and local times in the day side. The technique, based on long slit spectroscopy combined with the observations' high spatial resolution, has provided the first ground-based characterization of the latitudinal profile of zonal wind in the atmosphere of Venus, the first zonal wind field map in the visible, as well as new constraints on wind variations with local time. Mean zonal wind amplitudes were measured between  $106 \pm 21$  and  $127 \pm 14 \text{ ms}^{-1}$  at latitudes between  $18^\circ\text{N}$  and  $34^\circ\text{S}$ , with the zonal wind being approximately uniform in  $2.6^\circ$ -wide latitude bands ( $0.3''$  at disk center).

The zonal wind profile retrieved is consistent with previous spacecraft measurements based on cloud tracking, but with non-negligible variability in

local time (longitude) and in latitude. Near  $50^\circ$  the presence of moderate jets is apparent in both hemispheres, with the southern jet being stronger by  $\sim 10 \text{ ms}^{-1}$ . Small scale wind variations with local time are also present at low and mid-latitudes (Machado et al., 2012).

The second part of the thesis presents results of Venus' mesospheric winds at cloud top level, based on ground-based Doppler velocimetry of cloud-top winds and inter comparison of cloud tracking measurements from the Venus Express spacecraft.

Doppler wind velocimetry obtained with the 3.60 m Canada-France-Hawaii telescope (CFHT) and the visible spectrograph ESPaDOnS in February 2011 consisted of high-resolution spectra of Fraunhofer lines in the visible range to measure the wind velocity using the Doppler shift of solar radiation scattered by cloud top particles in the observer's direction (Widemann et al., 2007, 2008; Machado et al., 2013). The complete optical spectrum was collected at a phase angle  $\Phi = (68.7 \pm 0.3)^\circ$ , at a resolution of about 80,000. The obtained ground-based measurements on Venus are compared with simultaneous observations using the Visible and Infrared Thermal Imaging Spectrometer (VIRTIS) instrument from the VEx orbiter. CFHT observations included various points of the dayside hemisphere observed at a phase angle of  $67^\circ$  from CFHT, between  $+10^\circ\text{N}$  and  $60^\circ\text{S}$ , by steps of  $10^\circ$ , and from sub-Earth longitude  $[\phi - \phi_E] = 0^\circ$  to  $-50^\circ$  corresponding to 7:30a - 10:50a, while VIRTIS-M UV ( $0.38 \mu\text{m}$ ) cloud tracking measurements extended on the dayside south hemisphere between  $30$  and  $50^\circ\text{S}$  and 9:05a - 10:50a at simultaneous spacecraft orbit VV1786. Doppler wind retrievals using either 1- or 2-wind circulation regimes are in good agreement with measurements based on cloud tracking from Venus Express.

Were observed zonal wind field variations in the latitudinal and temporal scales within stable mean background velocities of  $\bar{v}_z = 117.35 \pm 18.0 \text{ ms}^{-1}$  on Feb. 19, and  $\bar{v}_z = 117.5 \pm 14.5 \text{ ms}^{-1}$  on Feb. 21, respectively.

It is presented the first unambiguous detection from the ground of a poleward meridional wind flow on the morning dayside hemisphere, of  $18.8 \pm 11.5 \text{ ms}^{-1}$  on Feb. 19, and  $19.0 \pm 8.3 \text{ ms}^{-1}$  on Feb. 21.

Wind temporal, local variation at the hour-scale of  $\pm 18.5 \text{ ms}^{-1}$  were detected near morning terminator at low latitude. To provide the best description of the wind field observed, the retrieved results were compared to a series of wind circulation models and their characterization at cloud top level.

The data analysis technique allowed an unambiguous characterization of the zonal wind latitudinal profile and its temporal variability, as well as an investigation of large-scale planetary waves signature and their role in the maintenance of the zonal super-rotation, and suggest that detection and

investigation of large-scale planetary waves can be carried out with this technique.

These studies complement the independent observations of the european space mission Venus Express, in particular as regards the study of atmospheric super-rotation, meridional flow and its variability.

***Keywords:*** Venus, Atmospheres, Dynamics, Observational Techniques, Zonal Winds, Spectroscopy, Super-rotation.





# Résumé

L'atmosphère de Vénus présente une combinaison peu commune d'extrêmes en ce qui concerne les atmosphères de type terrestre. L'inclinaison de l'axe de rotation de Vénus est de  $177,3^\circ$ . La rotation atmosphérique se faisant dans le même sens que la rotation planétaire, vue de la Terre l'atmosphère tourne dans le sens rétrograde. De plus, l'atmosphère est dans un état de super-rotation, dans laquelle la période de rotation du corps solide, de 243,02 jours, contraste avec une courte période de rotation atmosphérique au niveau supérieur de la couche nuageuse (4,4 jours à l'équateur). La très forte concentration en  $\text{CO}_2$  dans l'atmosphère (environ 95,6%) a entraîné un effet de serre dramatique dans l'atmosphère de Vénus au cours de son évolution. Malgré l'albédo élevé de la couche nuageuse (plus de 75% du flux de l'énergie solaire reçue), l'effet de serre porte la température moyenne de la surface à environ 735 K. Ainsi la surface de Vénus est la plus chaude de tout le système solaire, cette planète est ainsi une étude de cas extrême pour le réchauffement global et les changements climatiques qui lui sont associés.

L'aspect le plus significatif de la circulation générale de l'atmosphère de Vénus est sa super-rotation rétrograde. La caractérisation complète de ce phénomène dynamique est cruciale pour comprendre les mécanismes qui le créent et le maintiennent. L'atmosphère est caractérisée par une couche dense de nuages de gouttelettes d'acide sulfurique et d'un composé encore non identifié qui absorbe le rayonnement UV ( $\lambda < 320 \text{ nm}$ ). Les contrastes des nuages qui en résultent sont des traceurs presque parfaits du mouvement atmosphérique. Il est ainsi possible, en suivant le tracé des nuages, de calculer la vitesse des vents. La présence de gaz et d'aérosols interagissant avec le rayonnement solaire permet de plus de réaliser des mesures de la vitesse du vent basées sur l'étude des raies spectrales d'absorption et d'émission, comme dans le cas des techniques Doppler hétérodyne, ou par diffusion, dans le cas de la vélocimétrie Doppler sur la base du rayonnement solaire dispersée par la couche supérieure de nuages. C'est cette dernière méthode qui est utilisée dans ce travail de thèse. Le projet développé et présenté ici est centré sur l'effort de caractérisation de la dynamique de l'atmosphère de

Vénus en utilisant des observations à partir du sol, qui complètent ainsi les mesures obtenues par les missions spatiales.

Ce doctorat est réalisé en régime de co-tutelle entre l'Université de Lisbonne et l'Observatoire de Paris, sous la co-direction de David Luz (Faculté des Sciences de l'Université de Lisbonne) et Thomas Widemann (Observatoire de Paris).

Les travaux réalisés au cours de la première phase de ce travail se sont appuyés, dans un premier temps, sur les observations effectuées avec le Very Large Telescope (VLT) de l'ESO (Paranal, Chili), associé au spectrographe UVES. À partir des spectres de haute résolution obtenus, la technique de mesure des vents a été perfectionnée à partir des déviations Doppler sur les raies spectrales du rayonnement diffusée par la partie supérieure de la couche nuageuse (à environ 70 km d'altitude où la profondeur optique atteint la unité). Ce travail utilise un procédé de mesure directe des vents planétaires basé sur la spectroscopie de haute résolution dans la bande du visible. L'atmosphère de Vénus contient des aérosols en suspension hautement réfléchissants au niveau de la couche nuageuse qui recouvrent complètement la planète, lui imposant ainsi un albédo élevé. Ces particules sont transportées par le vent et emmènent ainsi avec elles des informations relatives à la dynamique atmosphérique.

Les observations ont été réalisées lorsque Vénus était proche de l'élongation maximum Est (angle de phase d'environ 90 degrés), permettant ainsi l'observation simultanée du limbe planétaire diurne et du terminateur. Le point sub-solaire était près du limbe alors que le méridien central était proche du terminateur du soir. Afin de couvrir une gamme représentative de latitudes et longitudes tout au long de l'hémisphère diurne, une configuration de fente longue a été utilisée (0,3 secondes d'arc de largeur et 20 secondes d'arc de longueur), permettant une résolution spatiale d'environ 107 km au centre du disque planétaire. Deux configurations principales d'observation ont été utilisées. Une avec la fente spectroscopique alignée parallèlement à l'axe de rotation planétaire. Dans l'autre situation, la fente était placée perpendiculairement de l'axe de rotation planétaire, avec la position de la fente initialement alignée avec un parallèle sur le disque de Vénus. Cette géométrie a permis de mesurer directement la magnitude des vents zonaux, vitesse instantanée, pour chaque latitude observée.

Cette méthode a permis la mesure directe et simultanée de la vitesse du vent zonal, sur une large gamme de latitudes et longitudes (heure locale) du côté diurne de Vénus. La technique, basée sur la spectroscopie de fente longue associée à une haute résolution spatiale grâce au VLT, a permis la caractérisation du profil latitudinal du vent zonal dans l'atmosphère de Vénus à partir des observations réalisées sur Terre. Elle a également permis la réalisation

d'une carte des vents sur Vénus, ainsi que l'obtention de nouvelles limites sur la variabilité du vent en heure locale. Nous avons mesuré des amplitudes de vent zonal entre  $106 \pm 21 \text{ ms}^{-1}$  et  $127 \pm 14 \text{ ms}^{-1}$  dans des bandes de latitudes entre  $18^\circ\text{N}$  et  $34^\circ\text{S}$ , le vent zonal étant approximativement uniforme sur des bandes de latitude de  $2,6^\circ$  ( $0,3$  secondes d'arc en relation au centre du disque). Le profil du vent zonal obtenu est cohérent avec des mesures antérieures des sondes spatiales (Galileo, Pioneer Venus, Venus Express) basées sur le suivi des nuages, mais fournit de nombreuses informations importantes sur la variabilité du vent en heure locale (longitude) et latitude (puisque le caractère innovateur du procédé est de fournir des mesures instantanées et simultanées tout au long d'une vaste région sondée).

Près des  $50^\circ$  de latitude a été détectée la présence de jets atmosphériques modérés dans les deux hémisphères, celui de l'hémisphère Sud étant plus intense d'environ  $10 \text{ ms}^{-1}$ . J'ai constaté que la vitesse baisse de façon significative pour les latitudes supérieures à  $50^\circ$ . Des variations temporelles de la composante zonale du vent ont été détectées pour des échelles de temps de l'ordre de 3 heures. Les résultats obtenus (Machado et al., 2012) ont donné lieu à une publication dans la revue *Icarus*. Les résultats de ces travaux ont également été présentés lors de la commémoration des 50 ans de l'Observatoire Européen Austral (ESO) à Garching en Allemagne (septembre 2012). Ce travail complète de façon indépendante les observations de la sonde spatiale Venus Express de l'ESA.

Dans la seconde partie de mon projet de recherche, des observations obtenues avec le Canada-France-Hawaï-Telescope (CFHT) à Mauna Kea à Hawaï en février 2011 ont été utilisées. Pour ces observations le spectrographe de haute résolution ESPaDOnS a été utilisé.

L'instrument ESPaDOnS a une résolution spectrale de  $R \sim 80\,000$  et couvre une gamme de longueurs d'onde de  $0,37\text{-}1,05 \mu\text{m}$  collectées dans un échellogramme de 40 ordres spectraux, son champ de vue (FOV) est de  $1,6$  secondes d'arc, équivalent à  $570\text{-}600 \text{ km}$  sur le disque planétaire pour des observations avec un angle de phase de  $109^\circ$ . La corrélation croisée des raies spectrales dans l'atmosphère de la Terre (raies telluriques) et des raies solaires du rayonnement solaire diffusé au niveau supérieur de la couche nuageuse de Vénus (environ 7000 raies solaires de Fraunhofer) à l'aide d'une double gaussienne, permet d'obtenir la vitesse Doppler du mouvement des aérosols diffuseurs. Les écarts Doppler mesurés ont une précision individuelle de  $5\text{-}10 \text{ ms}^{-1}$ .

Le choix des dates d'observation s'est fait en fonction du meilleur compromis entre la nécessité de maximiser le diamètre angulaire de Vénus (résolution spatiale sur le disque planétaire) et de minimiser l'angle de phase de l'observation. Les observations, effectuées les 19 et 21 février 2011, ont été

coordonnées avec des observations simultanées des mêmes régions de Vénus effectuées par Venus Express. Les spectres de haute résolution obtenus à partir d'observations de 2 à 5 secondes de temps d'exposition, ont été recueillis en 40 ordres spectraux avec une résolution spectrale d'environ 80.000. L'angle de phase des observations de 2011 a été de  $67^\circ$ , les bandes de latitude sondées vont de  $10^\circ\text{N}$  à  $60^\circ\text{S}$  par bandes de  $10^\circ$  de latitude. La zone sondée a couvert les longitudes de  $+70^\circ$  à  $-12^\circ$  en relation au méridien sous-terrestre par bandes de  $12^\circ$  de longitude sur le côté jour.

Les observations de 2011 ont permis d'explorer le modèle zonal, méridien et de circulation entre le point sous-solaire et le point anti-solaire, tout au long de bandes de latitude entre l'équateur et les latitudes moyennes. Les observations obtenues à partir du sol ont été comparées aux observations obtenues par le spectromètre VIRTIS, instrument à bord de Venus Express. Les observations réalisées par le CFHT ont inclus différents points de l'hémisphère diurne, observés avec l'angle de phase de  $67^\circ$  et couvrant une gamme de latitudes entre  $-10^\circ\text{N}$  et  $60^\circ\text{S}$ , par bandes de  $10^\circ$  et des longitudes sous-terrestres ( $0^\circ$  étant considéré le point sous-terrestre)  $[\phi - \phi_E] = 0^\circ$  jusqu'à  $-50^\circ$  qui correspond, en heure locale, à 7h30 - 10h50. Les observations de suivi de nuages, réalisées par VIRTIS-M dans l'UV (380 nm), ont porté sur l'hémisphère Sud diurne, entre  $30^\circ$  et  $50^\circ\text{S}$ , soit de 9h05 à 10h50 en heure locale, le long de l'orbite VV1768, coordonnée et en simultané aux observations à partir du sol. Les vents Doppler obtenus en utilisant soit le modèle de vent uniquement zonal, soit le modèle à deux composantes de vent (zonal et méridien) ont révélé un bon accord avec les vents obtenus avec la méthode de suivi des nuages (*cloud tracking*).

Les champs de vitesse mesurés, dans la région de latitudes et longitudes couvert par les observations, ont révélé une vitesse moyenne de  $\bar{v}_z = 117.35 \pm 18.0 \text{ ms}^{-1}$  le 19 février, et de  $\bar{v}_z = 117.5 \pm 14.5 \text{ ms}^{-1}$  le 21 février.

Ce travail de thèse présente aussi la première détection à partir du sol d'un vent méridien dans l'hémisphère diurne. Les valeurs obtenues sont de  $18.8 \pm 11.5 \text{ ms}^{-1}$  et  $19.0 \pm 8.3 \text{ ms}^{-1}$ , les 19 et 21 février respectivement.

Une variabilité temporelle, locale et à l'échelle horaire, de la vitesse du vent de  $\pm 18.5 \text{ ms}^{-1}$  a été détectée près du terminateur du matin aux basses latitudes. De façon à obtenir la meilleure description possible du champ de vent mesuré, les résultats obtenus ont été comparés avec différents modèles de circulation de vent et de sa caractérisation au niveau supérieur des nuages. La possibilité de détection d'ondes planétaires de large échelle par cette technique a aussi été démontrée.

Les résultats les mieux ajustés pour les vitesses obtenues ont montré des magnitudes de vent cohérentes avec les mesures antérieures obtenues par la méthode de suivi des nuages (Pioneer-Venus, Galileo/SSI, VEx/VMC et

VIRTIS) et par vélocimétrie Doppler (Widemann et al., 2007, 2008; Machado et al., 2012).

Pendant cette période de doctorat j'ai aussi participé activement à la campagne internationale d'observation du passage de Vénus de juin 2012 (Venus Twilight Experiment) menée par l'Observatoire de Paris, m'ayant été confié l'observation de ce phénomène à partir d'Udaipur en Inde. À cet effet, des coronographes spécifiques, adaptés à cette observation unique, ont été développés (Cythérographe), de façon à mesurer le rayonnement de l'auréole présentée par Vénus entre les 1er et 2e contact et entre les 3e et 4e contact du passage. La réfraction différentielle de la lumière solaire traversant les couches atmosphériques permet la construction d'un profil de températures en altitude. Cette campagne eût également pour objectif d'utiliser ces observations pour développer un outil qui pourra être utilisé pour l'étude des exoplanètes. Des résultats préliminaires de l'analyse des données obtenues par cette campagne ont été présentés lors de conférences internationales.

J'ajoute également que j'ai reçu une formation dans le domaine des occultations stellaires à l'Observatoire de Paris et j'ai participé à l'observation d'occultations stellaires par des objets trans-neptuniens (TNO) tels que Quaoar, que j'ai observé dans l'île de Santiago, au Cap-Vert (avril 2012). Dans le cadre de la préparation au passage de Vénus, j'ai également participé aux tests optiques et d'observation avec les cythérogaphes à l'Observatoire de Nice, en avril 2012; j'ai également participé à l'entraînement avec ces mêmes instruments à l'Observatoire de Paris en mai 2012.

Dans le but de mesurer le champ des vitesses du vent dans l'atmosphère de Vénus au niveau de la base de la couche de nuages (environ 48 km) et de caractériser le profil latitudinal du vent à cette altitude, ainsi que d'étudier la variabilité du vent et les ondes planétaires de large échelle présentes dans l'atmosphère, avec également pour objectif de dresser une carte de la distribution et de la structure des formations nébuleuses, nous avons réalisé des observations au *Telescopio Nazionale Galileo* (TNG) à La Palma, Îles Canaries. Les observations ont été réalisées du 24 au 27 juillet 2012 et ont été coordonnées avec des observations de même type menées par Venus Express, ainsi qu'avec un réseau d'autres observateurs à partir du sol dans une campagne internationale d'observations synchronisées. Les couches les plus basses de l'atmosphère de Vénus constituant une source intense de rayonnement thermique, nous avons obtenu des séquences d'images, sur le côté nuit, dans la fenêtre à 2,28  $\mu\text{m}$ .

La nécessité de procéder à l'intégration des mesures des vents à des altitudes différentes demeure essentielle, c'est-à-dire en utilisant le rayonnement de différentes longueurs d'onde, de façon à mieux comprendre la dynamique de l'atmosphère de Vénus et les processus qui la maintiennent en super-

xviii

*RÉSUMÉ*

rotation.

# Resumo

A atmosfera de Vénus apresenta uma combinação incomum de extremos em relação às atmosferas de tipo terrestre. A inclinação do eixo de rotação de Vénus é de  $177,3^\circ$ , sendo quase perpendicular ao plano da eclíptica e a maior de entre todos os planetas do sistema solar, a rotação atmosférica é no mesmo sentido da rotação planetária, de modo a que vista da Terra a atmosfera gira no sentido retrógrado. Além disso, a atmosfera está num estado de super-rotação, em que o período de rotação do corpo sólido, de 243,02 dias, contrasta com o curto período da rotação atmosférica ao nível do topo da camada de nuvens (4,4 dias no equador). Devido ao grande teor de  $\text{CO}_2$  na atmosfera (cerca de 96,5%) e à elevada pressão superficial (92 bar) desenvolveu-se um efeito de estufa dramático e descontrolado na atmosfera de Vénus, durante a sua evolução. Apesar da elevada reflectividade por parte da camada de nuvens (mais de 75% do fluxo de energia solar recebida), o efeito de estufa aumenta a temperatura média da superfície para cerca de 735 K. Assim, Vénus apresenta a superfície mais quente de todo o Sistema Solar, constituindo um notável caso de estudo para o aquecimento global e as subsequentes alterações climáticas.

O aspecto mais significativo da circulação geral da atmosfera de Vénus é a sua super-rotação retrógrada. A caracterização completa deste fenómeno dinâmico é crucial para compreender os mecanismos que a criam e a mantêm. A atmosfera está envolta por uma densa camada de nuvens formadas por gotículas de ácido sulfúrico e de um composto ainda não identificado que absorve a radiação ultravioleta. As nuvens, assim contrastadas, são traçadores quase ideais do movimento atmosférico, o que possibilita, através do seguimento dos seus movimentos, calcular a velocidade dos ventos. A presença de gases e aerossóis que interagem com a radiação solar permite, por sua vez, realizar medições da velocidade do vento com base no estudo das riscas espectrais de absorção e de emissão, caso das técnicas Doppler heteródino no infravermelho e velocimetria Doppler com base na radiação solar visível dispersa pela camada superior das nuvens, o qual é o método utilizado neste trabalho de tese. O projecto desenvolvido e aqui apresentado, centra-

se no esforço para caracterizar a dinâmica atmosférica de Vénus utilizando observações realizadas a partir do solo, complementando assim as medições obtidas pelas missões espaciais.

Este doutoramento foi realizado em regime de associação (co-tutela) entre a Universidade de Lisboa e o Observatoire de Paris sendo orientador o Doutor David Luz (Faculdade de Ciências da Universidade de Lisboa) e co-orientador o Doutor Thomas Widemann (Observatoire de Paris). Os trabalhos foram realizados no Centro de Astronomia e Astrofísica da Universidade de Lisboa (CAAUL) e no *Observatoire de Paris - Laboratoire d'études spatiales et d'instrumentation en astrophysique* (LESIA). Durante o período do doutoramento beneficieei de uma bolsa da Fundação para a Ciência e a Tecnologia (FCT) (referência: SFRH/BD/66473/2009) a quem reitero o meus profundo agradecimento.

Os trabalhos desenvolvidos ao longo da primeira fase do meu projecto de investigação basearam-se em observações efectuadas com o Very Large Telescope (VLT) do ESO (Paranal - Chile), associado ao espectrógrafo de alta resolução *Ultraviolet and Visual Echelle Spectrograph* (UVES). A partir dos espectros de alta resolução obtidos, foi aperfeiçoada a técnica de medição de ventos a partir dos desvios Doppler nas riscas espectrais da radiação difundida pelo topo da camada de nuvens (a cerca de 70 km de altitude onde a profundidade óptica atinge a unidade). Neste trabalho utilizou-se um processo de medição directa dos ventos planetários baseado em espectroscopia de alta resolução na banda do visível, com comprimentos de onda entre 300 e 1100 nm. A atmosfera de Vénus contém aerossóis altamente reflectores em suspensão, ao nível da camada de nuvens que recobrem por completo o planeta, impondo-lhe um elevado albedo. Essas partículas são transportadas pelo vento, carregando assim consigo a informação relativa à dinâmica atmosférica.

As observações foram feitas quando Vénus estava perto da máxima elongação leste (ângulo de fase de cerca de 90 graus), permitindo observar simultaneamente o lado diurno e nocturno e o terminador. O ponto sub-solar estava perto do limbo enquanto o meridiano central e o eixo de rotação estavam perto do terminador da tarde. A fim de cobrir uma gama representativa de latitudes e longitudes ao longo do hemisfério diurno foi utilizada uma configuração de fenda longa (0,3 segundos de arco de largura e 20 segundos de arco de comprimento). Obteve-se uma resolução espacial de aproximadamente 107 km no centro do disco planetário. Foram usadas duas configurações de observação principais. Uma com a fenda espectroscópica alinhada paralelamente ao eixo de rotação planetário. Na outra situação, a fenda foi colocada na perpendicular ao eixo de rotação planetário, com a posição da fenda inicialmente alinhada com um paralelo sobre o disco de Vénus. Para



esta geometria foi possível fazer o cálculo directo da magnitude dos ventos zonais, velocidade instantânea, para cada latitude observada.

Este método permitiu a medição directa e simultânea da velocidade do vento zonal, numa vasta gama de latitudes e longitudes (hora local) do lado diurno do planeta Vénus. A técnica, com base na espectroscopia de fenda longa combinada com a alta resolução espacial permitida pelo VLT, proporcionou, pela primeira vez, a caracterização do perfil latitudinal do vento zonal na atmosfera de Vénus a partir de observações a partir da Terra. Permitiu também a realização de um mapa de ventos em Vénus, assim como a obtenção de novas restrições sobre a variabilidade do vento em função da hora local. Foram medidas amplitudes do vento zonal entre  $106 \pm 21$  m/s e  $127 \pm 14$  m/s em bandas de latitudes entre  $18^\circ\text{N}$  e  $34^\circ\text{S}$ , com o vento zonal sendo aproximadamente uniforme em faixas de latitude de  $2,6^\circ$  ( $0,3$  segundos de arco em relação ao centro do disco). O perfil de vento zonal obtido é consistente com medições anteriores realizadas por sondas espaciais (Galileu, Pioneer Venus, Venus Express) com base no seguimento de nuvens, mas introduz muita informação relevante sobre a variabilidade do vento em hora local e latitude (dado o carácter inovador das medições serem instantâneas e simultâneas ao longo de uma vasta região sondada).

Perto dos  $50^\circ$  de latitude foi detectada a presença de jactos atmosféricos moderados em ambos os hemisférios, sendo o do hemisfério Sul, mais intenso em cerca de 10 m/s. Constatei que a velocidade baixa de forma significativa para latitudes acima dos  $50^\circ$ . Foram detectadas variações temporais da componente zonal do vento para escalas de tempo da ordem de 3 horas. Os resultados obtidos (Machado et al., 2012) deram azo a uma publicação na revista *Icarus* (revista de referência na especialidade) e inclusive foi um dos trabalhos cujos resultados foram apresentados na conferência comemorativa dos 50 anos do Observatório Europeu do Sul (ESO) em Garching na Alemanha (Setembro 2012). Este trabalho complementa de forma independente as observações da sonda espacial Venus Express, da ESA.

Na segunda fase deste projecto de investigação, foram utilizadas observações obtidas com o Canada-France-Hawaii-Telescope (CFHT) em Mauna Kea no Hawaii, em Fevereiro de 2011. Para estas observações foi utilizado o instrumento de espectroscopia de alta resolução ESPaDOnS.

O instrumento ESPaDOnS tem uma resolução espectral de  $R \sim 80000$  e cobre a gama de comprimentos de onda de  $0.37\text{-}1.05 \mu\text{m}$  registados num echelograma com 40 ordens espectrais. O seu campo (FOV) é de  $1,6$  segundos de arco, equivalente a  $570\text{-}600$  km sobre o disco planetário para observações com um ângulo de fase de  $109^\circ$ . A correlação cruzada entre as riscas espectrais na atmosfera da Terra (riscas telúricas) e as riscas solares da radiação solar difundida ao nível do topo da camada de nuvens em Vénus (cerca de 7000

riscas solares de Fraunhofer) e uma dupla Gaussiana, permite obter o desvio Doppler resultante do movimento dos aerossóis presentes na atmosfera de Vénus e responsáveis pela dispersão da radiação solar. Os desvios Doppler medidos têm uma precisão, associada a cada uma das mediações efectuadas, de  $5\text{-}10\text{ ms}^{-1}$ .

O ângulo de fase das observações de 2011 foi de  $67^\circ$ , as bandas de latitude sondadas vão desde os  $10^\circ\text{N}$  e os  $60^\circ\text{S}$  em faixas de  $10^\circ$  de latitude. A zona sondada cobriu as longitudes  $+70^\circ$  a  $-12^\circ$  em relação ao meridiano subterrestre em bandas de  $12^\circ$  de longitude ao longo do lado diurno do planeta Vénus. A escolha das datas de observação permitiu combinar a necessidade de maximizar o diâmetro angular de Vénus (resolução espacial sobre o disco planetário) e minimizar o ângulo de fase da observação.

As observações de 2011 permitiram explorar o modelo zonal, meridional e da circulação entre o ponto sub-solar e o ponto anti-solar, através de um ajuste efectuado entre as velocidades obtidas e estes modelos de circulação ao longo de bandas de latitude entre o equador e as latitudes médias. As observações obtidas a partir do solo foram comparadas com as observações obtidas pelo *Visible and Infrared Thermal Imaging Spectrometer* (VIRTIS), instrumento a bordo da sonda orbital Venus Express da agência espacial europeia (ESA). As observações de seguimento dos padrões de nuvens, efectuadas pela VIRTIS-M (no ultravioleta a  $380\text{ nm}$ ) a partir do espaço, incidiram no hemisfério Sul diurno, entre os  $30$  e os  $50^\circ\text{S}$ , ou das  $9:05\text{a.m.}$  às  $10:50\text{a.m.}$  considerando a hora local, ao longo do órbita VV1768, coordenada e simultânea às observações de solo. Os ventos Doppler obtidos usando, quer o modelo de vento zonal único, quer o modelo com duas componentes de vento (zonal e meridional) revelaram uma boa concordância com os ventos obtidos a partir do método de seguimento de nuvens (*cloud tracking*).

Os campos de velocidade medidos, no campo de latitudes e longitudes abarcado pelas observações, apresentaram uma velocidade média de  $\bar{v}_z = 117.35 \pm 18.0\text{ ms}^{-1}$  em 19 Fev., e de  $\bar{v}_z = 117.5 \pm 14.5\text{ ms}^{-1}$  em 21 Fev.

Nesta tese é ainda apresentada a primeira detecção a partir do solo de vento meridional, no hemisfério diurno, os valores obtidos são:  $18.8 \pm 11.5\text{ ms}^{-1}$  e  $19.0 \pm 8.3\text{ ms}^{-1}$ , a 19 e 21 de Fevereiro, respectivamente.

Foi detectada uma variabilidade temporal, local e à escala horária, da velocidade do vento de  $\pm 18.5\text{ ms}^{-1}$ , perto do *terminador* da manhã a baixas latitudes. De modo a obter a melhor descrição possível do campo de velocidades de vento medida, os resultados obtidos foram comparados com vários modelos de circulação de vento e da sua caracterização nível do topo das nuvens.

A técnica utilizada na análise dos dados, permitiu a caracterização do vento zonal a nível latitudinal, em termos do seu perfil em função da hora

local e da sua variabilidade temporal. Foi também investigada a presença de ondas planetárias de larga-escala e do seu papel na manutenção da super-rotação zonal.

Os resultados de melhor ajuste para as velocidades obtidas revelam magnitudes de vento consistentes com medições prévias pelo método de seguimento das nuvens (Pioneer-Venus, Galileo/SSI, VEx/VMC and VIRTIS) e por velocimetria Doppler (Widemann et al., 2007, 2008; Machado et al., 2012).

Os estudos, aqui apresentados, complementam de forma independente as observações da missão espacial Venus Express, em particular no que diz respeito ao estudo da super-rotação atmosférica, circulação meridional e à sua variabilidade.

Durante o período do doutoramento participei de forma activa na campanha internacional de observação do trânsito de Vénus de Junho 2012 (Venus Twiligh Experiment) liderada pelo Observatoire de Paris e que me confiou a observação do fenómeno a partir de Udaipur, na Índia. Para o efeito foram desenvolvidos coronógrafos específicos e adaptados a essa observação única (baptizado Citerógrafo) de modo a recolher a informação da radiação da auréola apresentada por Vénus entre o 1º e o 2º contacto e entre o 3º e 4º contacto do trânsito. A refração diferencial da luz solar ao passar pelas camadas atmosféricas de Vénus permite a produção de um perfil de temperaturas em altitude com relevância para o estudo da atmosfera venusiana. Esta campanha visou também utilizar estas observações para desenvolver uma ferramenta que poderá vir a ser utilizada no estudo dos exoplanetas. Resultados preliminares da análise dos dados obtidos nesta campanha foram apresentados em várias conferências internacionais.

Tive formação na área das ocultações estelares no Observatório de Paris, e participei na observação de ocultações estelares por objectos trans-neptunianos (TNO), caso do objecto Quaoar que fui observar na Ilha de Santiago, Cabo Verde (Abril 2012). Na sequência da preparação para o trânsito de Vénus, participei, também, nos testes ópticos e de observação com os coronógrafos adaptados no Observatório de Nice, França, Abril 2012; também participei no treino com os mesmos instrumentos no Observatório de Paris, Maio 2012.

Com o intuito de medir o campo de velocidades do vento na atmosfera de Vénus ao nível da base da camada inferior de nuvens (cerca de 48 km de altitude) e de caracterizar o perfil latitudinal do vento a essa altitude, assim como estudar a variabilidade do vento e estudar as ondas planetárias de larga escala presentes na atmosfera e a sua relação com o estado de super-rotação dessa atmosfera e ainda com o objectivo de mapear a distribuição e a estrutura das formações nebulosas, participei em observações no Telescópio Nazionale

Galileo (TNG) em La Palma (Canárias). As observações realizaram-se de 24 a 27 Julho de 2012 e foram coordenadas com observações do mesmo tipo levadas a cabo pelo orbitador da ESA, Venus Express, e com uma rede de outros observadores utilizando telescópios a partir do solo numa campanha internacional de observações sincronizadas.

As observações foram efectuadas no lado nocturno e na gama de comprimentos de onda do infra vermelho próximo. As camadas mais baixas da atmosfera de Vénus constituem uma fonte intensa de radiação térmica. O  $\text{CO}_2$  gasoso presente na atmosfera permite o escape dessa radiação a 1,74 e a 2,28  $\mu\text{m}$ . Obtivemos sequências de imagens, no lado nocturno, na janela observacional dos 2,28  $\mu\text{m}$  de modo a realizar o seguimento dos padrões de nuvens e assim obter os campos de velocidades dos ventos e a estrutura das nuvens, às altitudes e nas regiões sondadas.

Permanece essencial a necessidade de proceder à integração de medições de vento a diferentes altitudes, i.e. utilizando radiação de diferentes comprimentos de onda, de modo a compreender melhor a dinâmica da atmosfera de Vénus e os processos que a mantêm em super-rotação.

# Contents

<b>Aknowledgements</b>	<b>v</b>
<i>Abstract</i>	<b>ix</b>
<b>Résumé</b>	<b>xiii</b>
<b>Resumo</b>	<b>xix</b>
<b>Figure index</b>	<b>xxv</b>
<b>Table index</b>	<b>xxv</b>
<b>1 Thesis overview</b>	<b>1</b>
1.1 Scientific context . . . . .	1
1.2 Objectives . . . . .	2
1.3 Thesis structure . . . . .	5
<b>2 Introduction</b>	<b>7</b>
<b>3 Venus: Earth's paradoxical twin</b>	<b>17</b>
3.1 The planet Venus . . . . .	17
3.1.1 Geologic evolution . . . . .	22
3.1.2 Venusian volcanism . . . . .	26
3.2 History of Venus exploration . . . . .	29
3.2.1 20th century exploration . . . . .	29
3.2.2 Present Venus exploration . . . . .	32
3.2.3 Future scheduled missions . . . . .	40
3.3 Atmospheres of telluric planets . . . . .	42
3.3.1 Genesis of the atmospheres in telluric planets . . . . .	42
3.3.2 Brief notions of atmospheric dynamics . . . . .	43
3.4 The Venus atmosphere . . . . .	52
3.4.1 Origin of Venus' atmosphere . . . . .	52

3.4.2	The present Venus atmosphere . . . . .	54
3.4.3	Global atmospheric circulation . . . . .	74
3.4.4	Venus atmospheric evolution . . . . .	90
3.4.5	Brief comparative climatology . . . . .	92
<b>4</b>	<b>VLT/UVES observations</b>	<b>99</b>
4.1	UVES - Ultraviolet-Visual <i>Echelle</i> Spectrograph . . . . .	99
4.2	VLT and UVES description . . . . .	100
4.2.1	Telescope light path . . . . .	108
4.2.2	Opto-mechanical design . . . . .	110
4.2.3	High resolution spectroscopy with UVES . . . . .	112
4.2.4	High-precision wavelength calibration . . . . .	113
4.3	Observations with UVES . . . . .	116
4.3.1	Objectives . . . . .	116
4.3.2	Description of Observations . . . . .	117
4.3.3	Data . . . . .	122
4.3.4	Problems that affected the observations . . . . .	122
4.4	Doppler velocimetry with UVES . . . . .	124
4.4.1	Doppler shift geometric projection factor . . . . .	130
4.4.2	Young effect . . . . .	131
4.5	Sensitivity Tests . . . . .	133
4.5.1	Synthetically reconstructed spectra tests . . . . .	133
4.5.2	Fully synthetic spectra tests . . . . .	136
4.6	Results (UVES) . . . . .	138
4.6.1	Slit parallel to rotation axis . . . . .	138
4.6.2	Slit perpendicular to rotation axis . . . . .	141
4.6.3	Analysis of spatial variations . . . . .	144
4.7	Discussion (UVES results) . . . . .	149
<b>5</b>	<b>CFHT/ESPaDOnS observations</b>	<b>151</b>
5.1	The CFHT telescope and the ESPaDOnS instrument . . . . .	151
5.1.1	The Canada-France-Hawaii-Telescope (CFHT) . . . . .	151
5.1.2	ESPaDOnS - Instrument Description . . . . .	152
5.2	Observations with CFHT/ESPaDOnS . . . . .	162
5.3	Doppler velocimetry with ESPaDOnS . . . . .	168
5.3.1	Projected radial velocities . . . . .	168
5.3.2	Velocity extraction . . . . .	169
5.3.3	Young effect correction . . . . .	171
5.3.4	Monitoring the instrumental drift . . . . .	171
5.3.5	Error estimate . . . . .	175
5.3.6	Altitude of observations . . . . .	176

5.3.7	Doppler velocimetry analysis . . . . .	176
5.3.8	Observing geometry correction . . . . .	177
5.3.9	Kinematical wind models . . . . .	179
5.4	Results (ESPaDOnS) . . . . .	182
5.4.1	De-projected wind circulation . . . . .	182
5.4.2	Zonal wind variable component . . . . .	192
5.5	Cloud tracking VEx/VIRTIS-M analysis . . . . .	206
5.5.1	Instrumental description . . . . .	206
5.5.2	VEx/VIRTIS-M observations . . . . .	206
5.5.3	Cloud tracking analysis . . . . .	209
5.6	Comparing Doppler velocimetry and cloud tracking . . . . .	210
5.6.1	Simultaneous velocity measurements with CFHT/ ES- PaDOnS and VEx/VIRTIS . . . . .	211
5.6.2	Comparison with previous visible Doppler velocimetry measurements . . . . .	216
5.6.3	Comparison with previous CT measurements . . . . .	218
5.7	Discussion (ESPaDOnS results) . . . . .	222
<b>6</b>	<b>Observing missions</b>	<b>225</b>
6.1	The 2012 Venus transit . . . . .	225
6.1.1	Preparation . . . . .	226
6.1.2	Transit event . . . . .	228
6.2	<i>Observing Venus with TNG/NICS</i> . . . . .	234
<b>7</b>	<b>Conclusions and outlook</b>	<b>237</b>
7.1	Conclusions . . . . .	237
7.2	Future work . . . . .	240
7.3	Final remarks . . . . .	241
	<b>Publications</b>	<b>269</b>





# List of Figures

2.1	Large-scale motion of planetary atmospheres at Venus (right) and Earth (left). . . . .	10
2.2	Cloud, pressure and temperature structure of Venus atmosphere.	13
3.1	Venus image from the Galileo mission. . . . .	17
3.2	Venus surface temperature southern pole region. . . . .	18
3.3	Venus image synthesized from radio images of Magellan probe	20
3.4	False colour Venus' cartographic image from the Magellan probe	23
3.5	Volcanoes and lava flows upon Venus. . . . .	25
3.6	Mariner 2 . . . . .	29
3.7	Venera mission suite of landing images. . . . .	30
3.8	<i>Venus Express</i> : final payload assembling procedures. . . . .	33
3.9	High elliptical <i>Venus Express</i> polar orbit. . . . .	34
3.10	ESA's <i>Venus Express</i> space probe. . . . .	36
3.11	<i>Venus Express</i> dayside, with VMC, and nightside, with VIR-TIS images . . . . .	39
3.12	Scheme of the cyclostrophic balance, where the centrifugal force is balanced by the pressure gradient force. . . . .	48
3.13	Zonal wind and stream function results from Venus' atmosphere modelling. . . . .	50
3.14	Venus image in the ultraviolet by <i>Pioneer Venus</i> . . . . .	52
3.15	Evidence of the Venus' atmosphere during the 2004 transit. . . . .	53
3.16	Venus atmospheric structure and interactions. . . . .	55
3.17	Cloud formation distribution as a function of altitude. . . . .	56
3.18	Venus' sulphuric acid cloud deck and hazes extension in altitude.	57
3.19	South pole vortex and comparison with a terrestrial hurricane.	58
3.20	Altitude of Venus cloud tops. . . . .	59
3.21	Venus atmosphere relative composition. . . . .	61
3.22	Summary of atmospheric species spectral contribution. . . . .	62
3.23	$SO_2$ cycle and radiative interactions. . . . .	64

3.24	Measurements of Venus' atmosphere composition from Vex mission. . . . .	65
3.25	Genesis of Venus' magnetosphere. . . . .	66
3.26	Bowshock of the interaction between the plasma particles of solar wind and the induced Venus' magnetosphere . . . . .	68
3.27	Venus' runaway greenhouse effect. . . . .	69
3.28	Venus atmosphere temperature's profile. . . . .	70
3.29	Temperature versus atmospheric pressure at Venus and Earth. . . . .	72
3.30	Venus atmosphere stability. . . . .	73
3.31	Venus atmosphere's global circulation. . . . .	74
3.32	Scheme of the Venus atmosphere's different circulation regimes. . . . .	76
3.33	Cloud tracked latitudinal zonal wind profile retrieved from VIRTIS measurements with three different filters, and so probing three different altitudes. . . . .	77
3.34	Cloud tracked zonal winds based on VMC images. . . . .	78
3.35	Comparison from VMC and VIRTIS-UV zonal wind latitudinal profile. . . . .	81
3.36	Cyclostrophic wind, from VeRa, VIRTIS (thermal winds) and comparison with VMC cloud thwacked winds. . . . .	82
3.37	Three dimensional structure of the polar vortex. . . . .	83
3.38	Recent 3-D determination of winds at different altitudes on Venus with VIRTIS. . . . .	85
3.39	Ground-based equatorial wind observations summary. . . . .	87
3.40	Venus-Earth comparison of the abundance of atmospheric neutral gases. . . . .	93
3.41	Relevant comparable properties of Venus and Earth. . . . .	94
3.42	Comparison of the averaged thermal profile and condensable species. . . . .	94
3.43	General comparison of atmospheric global circulation for solar system bodies with a terrestrial-type atmosphere. . . . .	95
3.44	Earth's global atmosphere circulation diagram. . . . .	96
4.1	ESO's telescopes at Paranal, Atacama desert, Chile. . . . .	99
4.2	UVES optical path. . . . .	101
4.3	The two CCD detectors in UVES. . . . .	102
4.4	<i>Setup</i> of observed images to the CCD . . . . .	103
4.5	Continuous flow cryogenic system (CFC). . . . .	104
4.6	Study of the relation between temperature and spectral line shifts. . . . .	105
4.7	UVES' operational specifications . . . . .	106
4.8	UVES spectrograph's mount of its diverse elements. . . . .	107

4.9	Characteristics and observing capabilities of the UVES spectrograph. . . . .	109
4.10	UVES instrument optical light path. . . . .	110
4.11	Coupled instruments to the UT2/VLT telescope. . . . .	111
4.12	UVES monolithic <i>echelle</i> . . . . .	111
4.13	Spectral orders seen after the data reduction process applied to the FITS science images provided by UVES. . . . .	112
4.14	UVES efficiency . . . . .	113
4.15	Spectral resolution as a function of the slit width . . . . .	114
4.16	Telescope slit viewer's image. . . . .	116
4.17	Geometry of the observations, showing the various slit position offsets on the planetary disk. . . . .	119
4.18	<i>Echelogramme</i> with the various spectral orders. . . . .	123
4.19	Scheme of the measurement process in case of pure photon noise. . . . .	124
4.20	Algorithm for obtaining the radial velocity using only a single spectral line shift. . . . .	126
4.21	Steps for obtaining spectra from a UVES echellogramme . . . . .	127
4.22	Geometric correction Factor. . . . .	129
4.23	Efeito de Young em função da longitude, ao longo do equador. . . . .	132
4.24	Doppler shift curve for spectra shifted with a 10 m/s step relative to the central spectrum, between -300 m/s and +300 m/s. . . . .	134
4.25	Synthetic spectrum all orders, 16 for the MIT and 23 for the EEV detector. . . . .	134
4.26	Velocimetry algorithm's sensitivity to the signal-to-noise ratio. . . . .	135
4.27	Example of velocity curves produced in two stages of the data analysis. . . . .	140
4.28	Differential velocities between each pixel and the central pixel of the slit, de-projected and corrected for the Young effect, for the observations in the PL orientation . . . . .	142
4.29	Relative velocity between points symmetric relative to equator (case PL). . . . .	143
4.30	Zonal wind versus longitude for the observations made with the spectroscopic slit parallel to the equator (case PP). . . . .	145
4.31	Map projection of the zonal wind. . . . .	146
4.32	Summary of the measurements made with the slit perpendicular to the rotation axis . . . . .	148
5.1	The Canada-France-Hawaii-Telescope (CFHT) . . . . .	151
5.2	High resolution spectrograph and spectropolarimeter ESPaDOnS . . . . .	152
5.3	ESPaDOnS optical path. . . . .	153

5.4	ESPaDOnS devices, on the optical bench. . . . .	154
5.5	Wavelength calibration with a Th-Ar lamp exposure . . . . .	155
5.6	Derivation of the dispersion law, based on a Thorium-Argon reference spectra. . . . .	156
5.7	Spectral orders from a flat field image made of a ESPaDOnS exposure with a tungsten lamp. . . . .	157
5.8	Spectral orders from a flat field image made of a ESPaDOnS exposure with a tungsten lamp. . . . .	158
5.9	Inverse of the measurements variance as a function of the ADU counts from the respective measurement. . . . .	159
5.10	Example of a ESPaDOnS solar spectrum obtained in the near infrared (760 nm), there are also present strong telluric lines. . . . .	160
5.11	The 3.6-m CFHT bonnette guiding camera field on February 15, 2009 at 10:40UT. . . . .	162
5.12	Coordinated observations between ESPaDOnS and VEx/ VIR- TIS. . . . .	167
5.13	The retrieval of apparent velocity of lines uses a least-square deconvolution in the solar system barycentric rest frame. . . . .	170
5.14	Doppler winds $v_i$ and $v'_i$ on February 19 UT, 18:57-22:10 UT. . . . .	173
5.15	Doppler winds $v_i$ and $v'_i$ on February 21 UT, 18:01-22:30 UT. . . . .	174
5.16	Kinematical fit to a mean/background zonal wind fit $\bar{v}_z$ on Feb. 21 data. . . . .	183
5.17	Feb. 19, Feb. 21 2011 sequences of instantaneous horizontal velocities time-series. . . . .	185
5.18	Results for horizontal wind velocity $v_{z,i}^-$ reported at each offset position for Feb. 19, 2011. . . . .	186
5.19	Results for horizontal wind velocity $v_{z,i}^-$ reported at each offset position on Feb. 21, 2011. . . . .	187
5.20	Kinematical fit $\bar{v}_m$ to Feb. 21 differential wind field. . . . .	189
5.21	Retrieved meridional velocities $v_{m,lat}^-$ plotted as a function of S latitude. . . . .	190
5.22	Best-fit $\bar{v}_m$ of the meridional wind along the null zonal wind meridian on Feb. 21, 2011. . . . .	191
5.23	Day-to-day variations of <i>day-averaged</i> $v_{z,i}^-$ horizontal wind re- sults $v_{z,i}$ . . . . .	194
5.24	Latitude plots of variations of <i>day-averaged</i> horizontal wind velocities data. . . . .	197
5.25	Variations of <i>instantaneous</i> horizontal wind velocities $v_{z,i}$ for Feb. 19, 2011. . . . .	200
5.26	Variations of <i>instantaneous</i> horizontal wind velocities $v_{z,i}$ for Feb. 20, 2011. . . . .	202

5.27	Temporal variability of instantaneous zonal wind $v_{z,i}$ for successive surveys of same latitude bands. . . . .	204
5.28	Temporal variability of instantaneous zonal wind $v_{z,i}$ at latitude $30^\circ$ and W. . . . .	205
5.29	Morphology of the upper cloud observations by Venus Express/ VIRTIS-M images at 380-nm. . . . .	208
5.30	Wind vectors map on 21 Feb. 2011, showing simultaneous wind velocity measurements of VIRTIS-M UV and ESPaDOnS. . . . .	213
5.31	Simultaneous cloud-tracking wind velocity measurements of VIRTIS-M UV and CFHT/ESPaDOnS instantaneous Doppler winds on February 21, 2011. . . . .	215
5.32	Longitudinal (local time) variations of the zonal velocity observed simultaneously from the ground and from space using Venus-Express VIRTIS-M. . . . .	217
5.33	Comparison between zonal wind measurements made with CFHT/ESPaDOnS, VLT/UVES, VEx/VIRTIS-M, Galileo and Pioneer Venus. . . . .	220
6.1	Predicted Quaoar's shadow cone passing along the Earth. . . . .	226
6.2	Field of stars with the star that was occulted by the TNO Quaoar at 17 April, 2012. . . . .	227
6.3	Venus' transit at 5-6 June, 2012, world visibility map. . . . .	228
6.4	Scheme of the coronagraph optical design. . . . .	229
6.5	ESPobs . . . . .	231
6.6	Hinode's solar satellite image from the Venus' transit. And the glowing Venus' "aureole" short after transit's third contact. . . . .	233
6.7	Continuum-K image of Venus' nightside and visualisation method. . . . .	234
6.8	Galileo telescope and a preliminary image of the 48 km Venus' cloud layer. . . . .	235
7.1	To end with a smile . . . . .	275



# List of Tables

3.1	Summary of Venus atmosphere minor constituents abundances.	64
3.2	Compared results for Venus' atmospheric water composition and observed Deuterium/Hydrogen ratio. . . . .	67
4.1	North Pole position angle, apparent radius of Venus, latitude of sub-solar point and phase angle at the dates of the observations. . . . .	120
4.2	Summary of the geometry and circumstances of the observations. The cases PL and PP correspond to slit orientations parallel and perpendicular to the Venus rotation axis (slit position angle of $7.84^\circ$ and $100.92^\circ$ ), respectively. The offset number represents a position on the disk, N is the number of exposures taken for each offset and the times are given at the start of the first exposure. The integration time for all exposures was 1 second. Lat and Long are the coordinates of the slit's central point on the disk for each offset. The latitude and longitude values given are affected by the VLT/UVES nominal pointing and offset uncertainty, with a total uncertainty $\simeq 0.14''$ . . . . .	121
4.3	Summary of latitudes covered, and mean zonal wind velocities	144
5.1	Orbital geometry and circumstances of ground-based CFHT/ESPaDOnS observations in this work. . . . .	164
5.2	Scanning sequences on Venus' dayside hemisphere using CFHT/ESPaDOnS during the Feb. 19-21, 2011 observing run. . . . .	166
5.3	Point local characteristics and Young effect at the time of CFHT/ESPaDOnS February 19-21 data acquisition. . . . .	172
5.4	Velocity symbols used in this paper for deprojected and modeled horizontal flows in the reduction and analysis of visible Doppler velocimetry. . . . .	179
5.5	Mean/background zonal velocity $\bar{v}_z$ on Feb. 19 and Feb. 21. .	182

5.6	Mean Meridional wind velocity $\bar{v}_m$ along the zonal's Doppler null meridian. . . . .	188
5.7	Variability of 1-wind fit to $v_{z,i}$ values to a cloud-top zonal velocity. . . . .	196
5.8	Hour-time scale variation of 1-wind fit to a cloud-top zonal velocity per lat. band $v_{z,lat}$ on Feb. 19, 2011. . . . .	199
5.9	Hour-time scale variation of 1-wind fit to a cloud-top zonal velocity per lat. band $v_{z,lat}$ on Feb. 20, 2011. . . . .	203
5.10	Hour-time scale variation of 1-wind fit to a cloud-top zonal velocity per lat. band $v_{z,lat}$ on Feb. 21, 2011. . . . .	203
5.11	ESA Venus Express/VIRTIS-M observations circumstances. . . . .	207



# Chapter 1

## Thesis overview

### 1.1 Scientific context

The core atmospheric processes of Venus and Earth are similar, despite the different evolutionary paths they took since their common formation in the close vicinity of the Sun (encompassing Sun's habitable zone).

Since Venus Express spacecraft operations started in 2006, a continuous effort has been made to coordinate its operations with observations from the ground using various techniques and spectral domains. In the context of the Venus-Express mission, the zonal circulation at the cloud tops has been subject to an intense scrutiny both from the spacecraft instruments (VIRTIS, e. g. [Sánchez-Lavega et al. \(2008\)](#) ; VMC, e. g. [Moissl et al. \(2009\)](#)) and ground-based observations ([Widemann et al., 2008](#); [Gaulme et al., 2008](#); [Gabsi et al., 2008](#)).

Satellite measurements of the retrograde, zonal super-rotation of the atmosphere of Venus can be traced back to Mariner 10 data ([Belton et al., 1976](#); [Limaye and Suomi, 1981](#)), Venera 9, Pioneer Venus and Galileo SSI ([Rossow et al., 1990](#); [Belton et al., 1991](#); [Toigo et al., 1994](#)). Renewed interest in measuring the winds at clouds top from the ground has emerged in the course of the Venus Express mission as well as reanalysis of Galileo observations ([Limaye et al., 2007](#); [Peralta et al., 2007](#)).

On Venus Express, atmospheric circulation at 70 km (and as well near 50 km) has been measured from cloud tracking by both VIRTIS-M and VMC ([Markiewicz et al., 2007](#); [Sánchez-Lavega et al., 2008](#); [Luz et al., 2011](#); [Hueso et al., 2012](#); [Peralta et al., 2012](#); [Garate-Lopez et al., 2013](#)). VMC and VIRTIS measurements by cloud tracking show, however, a high dispersion of the direct measurements of wind vectors, as well as variability with local time, and suggest time-dependency of the mid-latitude jet. These measurements

show considerable day-to-day variability which needs to be carefully assessed.

Considering the context of Venusian dynamics at the time the work reported here first started, some important issues remained to be answered, such as: how can the atmosphere be accelerated to the observed high velocities on the slowly-rotating Venus planet, or what are the mechanisms that support and maintain super-rotation and the vertical wind shear. We can also note that different studies assessed different heights or planetary regions, due to the specific techniques or instruments they used. It is in this framework that my work finds its place, providing instantaneous wind measurements at cloud tops.

Therefore, the present study fills a gap and is complementary of measurements of lower cloud level winds ( $\sim 45$  km, e.g. Hueso et al. (2012)) and higher altitude measurements ( $\sim 100$  km, e.g. (Lellouch et al., 2008; Clancy et al., 2008, 2012; Rengel et al., 2008; Sornig et al., 2008, 2011, 2012)), contributing to construct a three dimensional wind velocity field. The cross-comparison of measurements from different latitudes, from the equator to the polar region (Markiewicz et al., 2007; Luz et al., 2011; Hueso et al., 2012; Peralta et al., 2012; Garate-Lopez et al., 2013) with our midlatitudes measurements is relevant as well. Comparing Doppler velocimetry winds with studies of tracers of the dynamics such as  $SO_2$ ,  $CO$ ,  $OCS$  (Sandor and Clancy, 2012; Clancy et al., 2012; Cottini et al., 2012; Encrenaz et al., 2012; Matsui et al., 2012; Marcq et al., 2005, 2006), is also of major interest for constraining the global atmospheric circulation.

Detecting the presence of planetary waves and other transient motions has also been addressed in the framework of this study, since these may be important for constraining global transport of angular momentum.

Addressing almost same height wind measurement (Moissl et al., 2009; Sánchez-Lavega et al., 2008; Hueso et al., 2012; Peralta et al., 2007; Limaye et al., 2007) can also be an important aspect of this work, since they used independent techniques and so this research can complement the surveyed regions, and contribute to cross-validate both techniques.

## 1.2 Objectives

Currently, there is a considerable effort from the planetary science community, to study and characterize the dynamics of Venus' atmosphere. To this, contributes decisively the wealth of observations provided by the ESA's Venus Express spacecraft (which is at present time in orbit and continues its successful mission). Ground-based coordinated observation campaigns also have an important role in the characterization of the winds and temperature field, for

the adequate determination of the dynamic regime that rules atmosphere's circulation, and in this way achieving a better constrain on atmosphere's dynamics. Venus is a case study of a slowly rotating planet, with an atmosphere in quasi-cyclostrophic balance, and a complete characterization of the Venusian superrotation is crucial for understanding its driving mechanisms. In the lower mesosphere (65-85 km), visible observations of Doppler shifts in solar Fraunhofer lines have provided the only Doppler wind measurements near the cloud tops in recent years (Widemann et al., 2007, 2008; Machado et al., 2012, 2013). The region is important as it constrains the global mesospheric circulation in which zonal winds generally decrease with height while thermospheric subsolar-antisolar (SS-AS) winds increase (Bougher et al., 1997; Lellouch et al., 1997).

The main purpose of this thesis is to contribute to a better understanding of the dynamics of the Venusian atmosphere, constraining its characterization at cloud top level, complementing the observations of the Venus Express spacecraft with ground-based observations. In order to achieve this objective of studying the atmospheric super-rotation, I measured the zonal wind velocity (westward circulation parallel to equator) and its spatial and temporal variability, by means of high precision spectroscopy and Doppler velocimetry. The observations were made with the high-resolution spectrograph UVES with ESO's Very Large Telescope (VLT) and with the high-resolution ES-PaDOnS spectropolarimeter at the Canada-France-Hawaii telescope (CFHT) at Mauna Kea observatory. I used a method of direct measurement of the planetary winds based on high resolution spectroscopy in the visible range. The atmosphere of Venus contains highly scattering aerosols in suspension, mostly at cloud top layer. This cloud deck covers entirely the planet, imposing an unusually high albedo. These particles are carried by the wind, carrying with them the information on atmospheric dynamics. The upper cloud layer is located about 70 km altitude. This altitude corresponds to the maximum velocity of zonal superrotation. The method used, in the case of long-slit observations obtained with VLT/UVES, allowed to characterize the spatial variations of zonal wind as a function of latitude (since the slit is thin compared to the size of the disk image of Venus).

This method allowed us to: search for jet-like structures at high latitude and its variation with time; study the variation of the wind according to local time (longitude) and search for a meridian wind component.

Because errors on absolute wind velocities on Venus are of the order of  $100 \text{ m s}^{-1}$ , this implies a  $\Delta\lambda/\lambda \sim 10^{-6}$ , if the Doppler shift of a single spectral line is used for wind measurements. In that case the spectral resolution would have to be  $R \sim 10^6$ , which is manifestly impractical with currently available instruments. This spectral resolution points to the need of a method based

on Absolute Astronomical Accelerometry (AAA) (Connes, 1985), which uses the full spectral information available in individual line shifts. As the sunlight dispersed by clouds of Venus contains several thousands Fraunhofer absorption lines in the wavelength domain covered by the spectrograph, AAA provides in this case an accuracy of the order of a few  $\text{m s}^{-1}$  for determining radial velocities of atmospheric air, at a spectral resolution of  $R \sim 100000$ .

ESO's Very Large Telescope (VLT) with the long-slit spectrometer UVES has been used. The observations were made in May and June of 2007, when Venus stood near its greatest East elongation (which enabled the observation of the planet near quadrature and therefore showing simultaneously both day and night hemispheres, with the terminator very close to the planetary rotation axis). The advantage of this instrument is threefold: (i) the availability a large band pass (the entire 480-670 nm range is covered at once), making possible the use of hundreds of Solar lines for the Doppler shift measurements (ii) the large collecting area of the telescope (iii) the small pixel size ( $\sim 0.3$  arcsec) and the 1-D instantaneous spatial dimension of the instrument. The first two aspects allow a large gain in accuracy in the wind field, while the third allows both an instantaneous comparison of wind velocities measured in different regions of the planet and an excellent, seeing-limited spatial resolution on the planet. Thus, both short-term variations and small-scale structures can be studied. In particular, the latitudinal dependence of the zonal wind at cloud level and the existence of wave patterns can be investigated and correlated with winds determined from cloud tracking in the VEx VIRTIS-M and VMC UV images.

In a second stage, the observations carried out with CFHT/ESPaDOnS on 19-21 February, 2011, were mainly focussed in southern hemisphere mid-latitudes. This strategy aimed to obtain same-region, simultaneous observations with coordinated Venus Express observations, in order to yield a comparative study upon the wind velocities retrieved.

ESPaDOnS and the sequential technique of visible Doppler velocimetry has proven, as well, a reliable way to constrain wind gradients in the lower mesosphere and global wind circulation models. The main purpose was to provide direct, and instantaneous, wind measurements in the southern hemisphere, dayside, from visible Fraunhofer lines scattered at Venus' cloud tops. This will also contribute for cross validation of the cloud tracking method used in many orbiter-based measurements (Machado et al., 2013).

The observations carried out with CFHT/ESPaDOnS, allowed a wind velocity survey along meridians and latitudinal bands, by sequentially moving the spectrograph beam along these specific trajectories. In the course of this study, it became clear that was possible to take advantage of the half phase angle meridian, where the measured Doppler due to the zonal wind is null,

in order to measure the meridional wind component. These ground-based observations benefitted from coordinated/simultaneous observations of the same regions upon Venus, from Venus Express. Our aim, was in the one hand, to study both techniques consistency in overlapping regions, and on the other hand, to clearly show the complementary aspects of both methods.

Given the results obtained by orbiter *in situ* observations, those obtained from the ground have the important task of confirming (or otherwise) the values obtained by space missions using different and independent techniques, contributing to a cross-validation of both techniques. Furthermore, another relevant question relates to the assistance that can be provided in the preparation of future space missions. Finally, another important factor is the rather smaller financial effort that these observations implies compared to the high costs of space missions. So, all the contributions that ground-based techniques can offer are a great help for the integrated planetary research.

The main goal of this research programme is therefore, to provide direct, and instantaneous, wind measurements using visible Fraunhofer lines scattered at Venus' cloud tops. This will also contribute for cross validation of both methods, the Doppler wind velocimetry and the cloud tracking method, which measure winds independently.

### 1.3 Thesis structure

This thesis is organised as follows:

Chapter 2 gives a brief and introductory description of the Venus' atmospheric dynamics state of the art, the kind of observations performed and method developed in order to achieve the proposed objectives.

Chapter 3 is dedicated to the research target of this work, the planet Venus. It is described, even if briefly, its genesis, evolution and present conditions. After, is given an overview about some relevant planetary aspects, which comprise: its geology and volcanism, composition, thermal history, chemistry and atmosphere. A particular emphasis is given in the description of the atmosphere, focusing on its dynamics and global circulation, mainly at the mesosphere and the cloud top region. A brief history of Venus' exploration is presented as well.

Chapter 4, firstly describes the UVES high-resolution spectrograph that is coupled to the 8-meter class telescope VLT, and with which the observations that are the basis for the first part of this work research programme, were carried out. The observations, the data analysis method and the corrections of the Young and geometric projection effects are described in the following. Sensitivity studies of the data analysis method were performed in

order to assure the robustness and reliability of the Doppler velocimetry used, a dedicated section is presented in this chapter as well. After, the results of wind measurements with the two types of observational geometries used are presented. The interpretation of the results, in particular their comparison with previous spacecraft observations and with Venus Express observations by the VIRTIS and VMC instruments, and with other ground based techniques are presented in this chapter's last section. The essential procedures and results presented on this chapter can be found in [Machado et al. \(2012\)](#) published in Icarus journal.

Chapter 5 is dedicated to the Doppler velocimetry research programme based on CFHT/ESPaDOnS high-resolution spectrograph observations. Besides the similarities with the previous chapter long-slit techniques, this experiment required specific development and adaptations of data analyses Doppler velocimetry method. The chapter structure is quite similar to the precedent one. The major difference relies in the splitting in two fundamental sections. One is dedicated to atmospheric dynamics studies of the zonal wind, meridional wind flow, temporal and spatial variability and their hypothetical coupling with planetary wave propagation. The other section is a comparison study of coordinated/simultaneous Venus Express observations. The results obtained on this work were also compared with previous observations, both space and ground-based ones. The comparison between different techniques was also assessed, which is the case of the cloud tracking and the Doppler velocimetry methods in order to retrieve wind velocities ([Machado et al., 2013](#)).

In chapter 6 we can find a short report about my participation in observational campaigns with relevance to this thesis, from which it is highlighted my contribution to the Venus' transit worldwide coordinated campaign in the framework of the Venus twilight experiment. It is also shown the relevance of these observations for the study of Venus climate.

Finally, chapter 7, summarizes and discusses the results of this doctoral thesis and gives an outlook on possible future work.

# Chapter 2

## Introduction

In a first approach Venus and Earth are similar planets. Both planets evolved from the same proto-solar nebula, and were formed at nearly the same time, have similar densities, size, mass and bulk chemical composition (Svedhem et al., 2007). They both have a thick atmosphere and important cloud systems (Bengtsson and Grinspoon, 2013). But a closer look, reveals the evidence of the striking present differences between them. Despite solar system's formation arguments that sustain the similarity of initial atmospheric conditions for Venus and Earth, they evolved in radically different ways (Grinspoon, 1997). The surface pressure is about 90 times Earth's and its high concentration in CO<sub>2</sub>, re-enforced by the presence of extremely reflective clouds of sulphuric acid aerosols, led to a runaway greenhouse effect. Time evolution drove this planet to an arid and torrid desert with high surface temperatures (735°K) that precludes the existence of liquid water (Bullock and Grinspoon, 2001). Also, the lack of water, that plays an essential role in plate tectonics as a lubricating substance that lowers the soil layers' viscosity, contributed to a standstill of any plate dynamics that might have existed in Venus' early history, now a single-plated planet (Bengtsson and Grinspoon, 2013). In the broader context of comparative planetology, the compelling reasons for studying the Venus climate are, mainly, twofold:

- The slow but steady increase in solar luminosity could have placed the evolution of Earth's atmosphere, in long time-scales, in the same trend of Venus. The comparative study of Venus and Earth atmospheric physics and dynamics may help us to understand the enormous differences that led planetary evolution in both planets, and also constrain the prevision of their long-term atmospheric transformations. Concerning the specific case of Venus and its runaway greenhouse effect (Tomasko et al., 1980), its study should improve our understanding of

the present climate change process taking place on Earth.

- Understanding the climate of Venus should be a prime task for planetary science as well as for the exoplanet community. Understanding, in detail, how our false twin planet evolved in such a different way, in terms of the magnetic field, volcanism (Smrekar et al., 2010), internal heat processes, plate tectonics, presence of condensable volatiles and the existence of past oceans and cloud layers, atmospheric composition and atmospheric dynamics, is of major importance to improve our understanding of planetary atmospheres and their evolution. The recent discoveries of earth-size exoplanets and the construction of even more sophisticated observational instruments, that will enhance our capabilities of extra-solar planets detection, will allow to go beyond the study of its size, gravity constant and equilibrium temperatures to a next step of a detailed study of their atmosphere's composition and dynamics, in the near future years. Comparative climatology between Venus and Earth will also contribute to constraining the concept of *Habitable Zone* (HZ) and its application to Earth-like exoplanets.

Mesosphere of Venus (65-120 km) is the site of important and unexplained variability of the flow in both long and short timescales, while measurements of the vertical profiles and horizontal distributions of trace species such as water vapour, carbon monoxide and sulphur dioxide indicate different and sometimes conflicting compositions (Crisp et al., 1991; Drossart et al., 1993; Ignatiev, 1997; de Bergh et al., 2006; Marcq et al., 2008; Bézard et al., 2009; Encrenaz et al., 2012). On the other hand, no study has established a link between the polar vortex structure, motion or local conditions of the polar atmosphere, and little is known about the causes for wind variability, wave activity or turbulent processes. If we also recall super-rotation and the meridional circulation, to date, no comprehensive model has been able to fully reproduce these phenomena.

The atmosphere of Venus is in superrotation, a state in which its averaged angular momentum is much greater than that corresponding to co-rotation with the surface. The rotation of the solid planet (with a period of 243 terrestrial days, Mueller et al. (2011)) contrasts dramatically with the much faster clouds' rotation, which circle the planet in only 4.4 d at 70 km altitude and about 6 d at 48 km. The circulation up to the cloud tops is characterized by an increasing zonal retrograde wind (in the East-West direction), determined from Pioneer Venus probe tracking. The wind starts to build up at 10 km and amplifies with altitude, reaching a maximum at cloud tops ( $\sim 70$  km). Although the clouds are almost featureless in visible light, there are prominent features in UV and infra-red wavelengths (Titov et al., 2008, 2012).



Dominant length scales are larger than 1000 km and few features are smaller than 20-30 km (Rossow et al., 1990). The cloud deck extends in altitude from 45 to 70 km, and can be divided into three main regions, centered at 48, 54 and 60 km (Esposito et al., 1997). The lowest of these is the lower cloud, where fundamental dynamical exchanges that help maintain superrotation are thought to occur (Lebonnois et al., 2010). On the superrotating zonal retrograde circulation, two main large scale, non-axisymmetric features are superimposed. The four-day planetary wave at low and mid-latitudes and a polar vortex in the polar regions. The four-day planetary wave consists of a Y-shaped feature seen in UV images which has been identified as a Kelvin wave (Gierasch, 1997). The oscillation there can reach 10% of the mean zonal wind velocity. The polar vortices are visible as IR-bright features (Taylor et al., 1979; Piccioni et al., 2007) and the southern polar vortex has been shown to be displaced from the pole and precessing about it (Luz et al., 2011).

A complete characterization of the Venusian superrotation is crucial for understanding its driving mechanisms. The so called Gierasch-Rossow-Williams (GRW) mechanism was one of the earliest explanations of Venus' superrotating atmosphere. In this mechanism the coupling between Hadley circulation and planetary waves transfers angular momentum from the surface and stores it in the atmosphere (Fig. 2.1), and part of these exchanges take place in the lower cloud. The Hadley circulation consists on average of two equator-to-pole cells, with rising air at low latitudes and subsiding air at the poles. The net upward transport of angular momentum by the Hadley cells is able to maintain an excess of angular momentum in the upper atmosphere, balanced by equator-ward transport by planetary waves (Gierasch, 1975; Rossow, 1979). However, this Hadley circulation has not been clearly characterized observationally (Sánchez-Lavega et al., 2008) and remains very much a theoretical construct in need of quantitative support.

The previous measurements by Pioneer Venus, reanalyzed in Limaye et al. (2007), showed the presence of high latitude zonal jets close to 50 degrees latitude in both hemispheres, with a slight asymmetry between the northern and southern ones. However, long temporal averages of cloud-tracked winds by the Galileo SSI instrument (Peralta et al., 2007), and by the Venus Express VMC and VIRTIS instruments (Sánchez-Lavega et al., 2008; Moissl et al., 2009) do not display any clear evidence for high latitude jets at cloud tops, although shorter time scale averages of VMC measurements in Moissl et al. (2009) indicate that jets may occur but are short-lived. Rather than being discrepant, different wind measurements have provided important insight into the variability inherent to the circulation of Venus. In this work direct measurements of instantaneous zonal winds brings additional evidence for the occasional presence of jets and, in general, for variability. The realization

that latitudinal wind profile with jets such as measured by Pioneer Venus is likely to be barotropically unstable (Limaye et al., 2009), is an argument in favour of significant variability at various spatial and temporal scales.

The circulation up to the cloud tops is characterized by an increasing zonal wind in the retrograde sense (East to West). The RZS is accompanied by a Hadley-type meridional circulation from the equator to poles and both converge to an unique polar vortex circulation (Suomi and Limaye, 1978). The polar vortices are visible as IR-bright features, and the southern polar vortex has been shown to be displaced from the pole and precessing about it (Luz et al., 2011; Garate-Lopez et al., 2013), and is accompanied by a surrounding stream of colder air (Taylor et al., 1980; Piccioni et al., 2007; Tellmann et al., 2009). This transient jet stream shows a temporal variability and vertical extension that are still a matter of debate (Markiewicz et al., 2007; Piccialli et al., 2012). Wind fields were also derived from the vertical temperature profiles using the approximation of cyclostrophic balance (Limaye, 1985; Piccialli et al., 2012; Zasova et al., 2007).

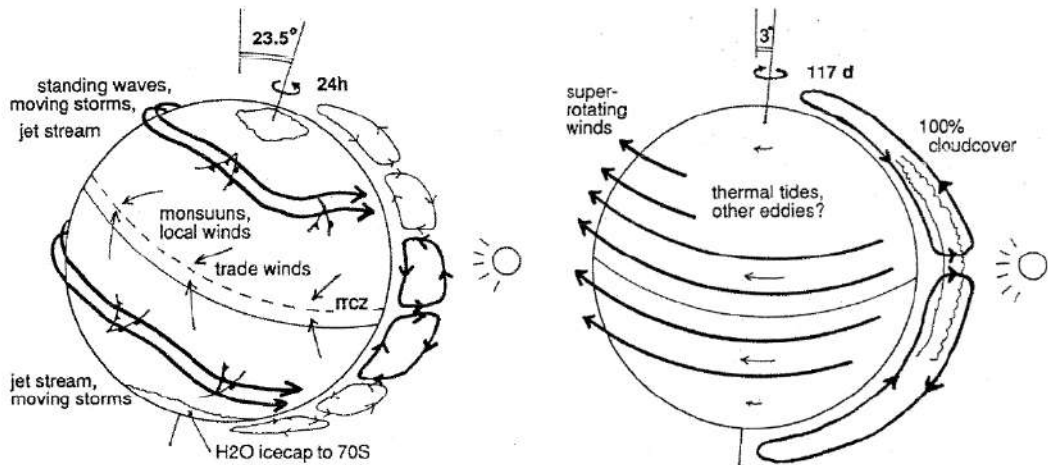


Figure 2.1: Large-scale motion of planetary atmospheres are dominated by various types of circulation patterns according to latitude, altitude and local time (left: Earth ; right: Venus).

Renewed interest in measuring the winds at clouds top from the ground has emerged in the course of the Venus Express mission (Drossart et al., 1997; Svedhem et al., 2007) as well as the above cited reanalysis of Galileo observations (Limaye et al., 2007; Peralta et al., 2007). On Venus Express, the zonal atmospheric circulation at 45 and 70 km has been measured from

cloud tracking with combined VIRTIS-M and VMC instrument's observations (Markiewicz et al., 2007; Sánchez-Lavega et al., 2008; Hueso et al., 2012). However, winds derived in this manner do not necessarily trace the true circulation. They may instead represent the phase speed of a condensation wave, as in the case of orographic clouds which remain fixed to mountain tops regardless of the wind velocity, while cloud particles are moving at the horizontal wind velocity. This fact raised the relevance of using other independent techniques, as is the case of Doppler velocimetry, seen that this method measures directly the aerosol particles motion, and the retrieved wind velocities are instantaneous measurements.

In addition, the cloud tracking method is not able to measure wind fields above cloud level, where wind inferences have to rely on indirect hypothesis such as the validity of thermal wind equation and the altitude/latitudinal extension/validity of the cyclostrophic balance approximation (Schubert et al., 2007; Gierasch et al., 1997; Read, P., 1986; Drossart et al., 2007; Piccioni et al., 2007).

In spite of comprehensive wind fields retrieved using the cloud tracking technique, in order to better constrain mesosphere's dynamics, and despite the high spatial resolution allowed by the Venus Express instruments, the wind vectors produced are time averaged ones, so this technique it is not the best research approach to study wind variability and the presence, and propagation, of planetary waves, such as gravity waves and solar lock tide waves. The main purpose of this work is, therefore, to provide instantaneous direct wind velocity measurements using visible Fraunhofer lines scattered by Venus' cloud tops. Thus, our Doppler velocimetry technique constitutes a complementary way of probing the Venus' atmosphere, and a unique approach from the ground.

The retrograde zonal superrotation wind (RZS) is foreseen to be associated with a Hadley-type meridional circulation from the equator to poles and both converge toward the unique polar vortex circulation (see figures 2.1 and 2.2). Venus' middle atmosphere (65-120 km, also known as the mesosphere) is a transition region between the zonal retrograde circulation of the lower atmosphere (up to 65km) and the subsolar to antisolar (SS-AS) flow of the upper thermosphere (above 120 km). Thermal profiles and winds in the mesosphere have revealed that these two types of circulation coexist, with winds varying by tens of metres per second over both long (yearly) and short (weekly or daily) timescales (Sánchez-Lavega et al., 2008). Although, the results presented in this work (and in Machado et al. (2013)) , mainly from ESPaDOoS' and VIRTIS' observations, could help to constrain this matter. In the lower mesosphere (65-85 km), visible observations of Doppler shifts in solar Fraunhofer lines have provided the only Doppler wind measurements

near the cloud tops in recent years (Widemann et al., 2007; Gabsi et al., 2008; Widemann et al., 2008; Machado et al., 2012, 2013). This region is important as it constrains the global mesospheric circulation in which zonal winds generally decrease with height while thermospheric SS-AS winds increase (Bougher et al., 1997; Lellouch et al., 1997; Hueso et al., 2012).

In the thermosphere, the atmosphere dynamics is characterized by the presence of thermal circulation cells from the subsolar to the antisolar point (SS-AS), that show the evidence of significant variability on its zonal component, as is shown by complementary observing techniques such as ground-based wind measurements from Doppler-shifted infrared, sub-mm and millimeter spectral lines (Goldstein et al., 1991; Lellouch et al., 1994; Clancy et al., 2008, 2012; Rengel et al., 2008; Lellouch et al., 2008; Sornig et al., 2008), as well as ground-based and Venus Express/SPICAV observations of non-LTE airglow emission variability on the night side (Ohtsuki et al., 2008; Gerard et al., 2009; Soret et al., 2010, 2011). This high-altitude variability must be integrated with the mesosphere measured variability, in order to build a three dimensional variability map that enables a deeper understanding of the atmosphere dynamics mechanisms, since will be possible to integrate the two-dimensional wind velocities and variability, at each altitude probed, with a better constrained wind altitude profile. As is the case of the presence and evolution of waves upon the planet.

Since the Venus Express spacecraft operations started in 2006, a continuous effort has been made to coordinate its operations with observations from the ground using various techniques and spectral domains (Lellouch and Witasse, 2008). Both ground-based and Venus Express measurements show considerable day-to-day variability, which needs to be carefully assessed (Sonnabend et al., 2008, 2010; Sornig et al., 2008, 2011, 2012; Widemann et al., 2008; Luz et al., 2011; Hueso et al., 2012; Machado et al., 2012, 2013).

Independent ground-based observations have been of major importance to complement space-based observations and have contributed to a more complete picture of the Venus atmospheric dynamics. The early ground-based wind measurements using the cloud tracking method (Boyer and Camichel, 1961; Dollfus et al., 1975) were based on the monitoring of large-scale ultraviolet markings, and were very sensitive to wave motions and convection features, rather than the real atmospheric particle velocity. This is a potential problem which affects all wind measurements based on cloud tracking (ground and space-based). Recently, cloud tracking in the near infrared using the observational window in the night side of the continuum K near 2.26 microns (Young et al., 2010), as well as quantification of middle and lower cloud variability and mesoscale dynamics from Venus Express/VIRTIS observations at 1.74  $\mu\text{m}$  (McGouldrick et al., 2011) allowed the monitoring of

wind conditions in the lowest layer of clouds (45 km). On the other hand, visible observations, or more specifically Doppler shift observations of solar Fraunhofer lines and of  $CO_2$  lines in the lower mesosphere have provided wind measurements near the cloud tops based on direct Doppler velocimetry (direct velocity in the observer’s line-of-sight) (Widemann et al., 2007, 2008).

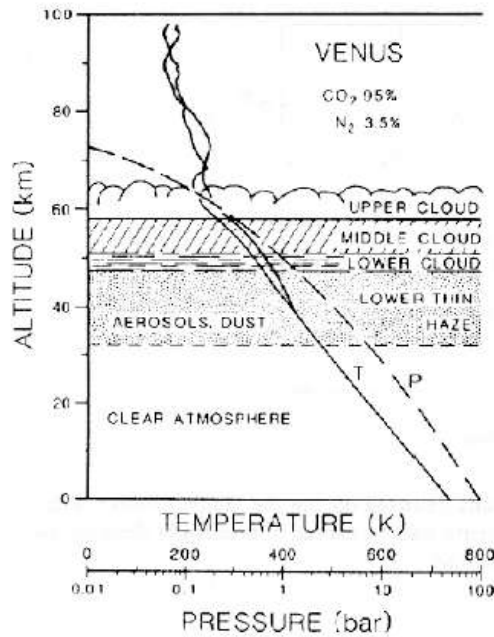


Figure 2.2: Cloud, pressure and temperature structure of Venus atmosphere.

The technique of Doppler measurements in the visible range was pioneered by Young (1975). Andrew Young first realized that this type of observations are affected by a systematic bias, due to the finite angular size of the Sun as seen from Venus and to the fast equatorial solar rotation ( $\sim 2 \text{ km s}^{-1}$ ). The early visible Doppler measurements showed a large dispersion of results (Young, 1975; Young et al., 1979; Traub and Carleton, 1979; Lellouch et al., 1997), and it is now clear that they were affected by what has been called the “Young effect”.

The methods applied in recent planetary wind measurements using high-resolution spectroscopy in the visible range (Luz et al., 2005a, 2006; Widemann et al., 2007; Gabsi et al., 2008; Widemann et al., 2008; Machado et al., 2012, 2013) all address the fundamental problem of maintaining a stable velocity reference during the acquisition process. In order to measure the global circulation at cloud top altitude, we need to address wind amplitude varia-

tions (or wind latitudinal gradients) on the order of 5-10 m/s projected on the line-of-sight (Widemann et al., 2007). Such an accuracy cannot be achieved by single line fitting, even at high spectral resolution (with the exception of very high resolution heterodyne techniques, which require dedicated instrumentation). Therefore, it becomes necessary to optimally measure relative Doppler shifts between two sets of absorption lines (Connes, 1985), while simultaneously monitoring the change in spectral calibration with time (Widemann et al., 2008).

There are two alternative ways to deal with the previous questions. First, *sequential* Doppler shift measurements (Widemann et al., 2007; Gabsi et al., 2008; Machado et al., 2013), where a continuous monitoring of the pixel versus wavelength relation, prior to velocity measurements, is performed. Differential measurements of line shifts are performed while the change of spectral calibration with time is monitored. This method has been applied in retrievals based on the Doppler shifts of CO<sub>2</sub> absorption lines (Widemann et al., 2007, 2008). The second option is to perform *simultaneous* measurements of relative Doppler shifts between two points in the disk using long-slit spectroscopy. This automatically suppresses the Doppler shift due to the relative motion between Earth and Venus, as well as any systematic drifts due to time variation of the calibration (Civeit et al., 2005; Luz et al., 2005a, 2006; Machado et al., 2012). This method has the advantage of providing an instantaneous, one-dimensional image of the wind Doppler shift, enabling a direct determination of spatial variations in the flow, and to search for wave and tidal structures if sufficient spatial resolution is possible. This method has been previously applied for determining the radial velocities of stars (Baranne et al., 1996), in asteroseismology (Martic et al., 1999), and was recently used in planetary wind measurements in the visible range for Titan, from the Doppler shifts of the backscattered solar spectrum (Luz et al., 2005a, 2006). Its applicability to the case of Venus atmospheric winds has been tested in Observatoire de Haute Provence by Martic et al. (2001).

Here we report on observations of Venus made with the Ultraviolet and Visual Echelle Spectrograph (UVES) at ESO's Very Large Telescope, with the objective of measuring the latitudinal profile of the zonal wind and searching for local disturbances at the upper cloud level. For Doppler velocimetry at visible wavelengths the optical depth reaches unity at 70 km (Ignatiev, 2009), which is also the altitude studied with cloud tracking measurements based on imaging in the UV and thermal infrared wavelengths, with both VEx/VMC and VEx/VIRTIS instruments (Moissl et al., 2009; Sánchez-Lavega et al., 2008; Peralta et al., 2012). This allows a direct comparison of magnitudes and spatial variations obtained with VLT/UVES and with Pioneer Venus, Galileo (SSI), and Venus Express. These observations were part of the first

campaign of coordinated in-orbit and ground-based observations of Venus, taking advantage of the simultaneous presence of the Venus Express orbiter and of the Messenger flyby in 2007. The objective of this campaign has been to provide unique data from measurements that were not possible with Venus Express, to improve the temporal baseline for time-varying phenomena, to allow cross-validating measurements from different techniques, and to obtain simultaneous measurements sampling a wide range of altitudes (Lellouch and Witasse, 2008).

Long-slit spectroscopy, such as that afforded by the VLT/UVES cross-dispersed *echelle* spectrometer, has the advantage of providing an instantaneous one-dimensional image of the wind Doppler shift, enabling a direct determination of the latitudinal dependence of the zonal flow and facilitating the search for wave and tidal structures.

We used ESO's Very Large Telescope (VLT) using the long-slit spectrometer UVES. The advantage of this instrument is three-fold: (i) the availability a large band pass (the entire 480-670 nm range is covered at once), making possible the use of hundreds of Solar lines for the Doppler shift measurements (ii) the large collecting area of the telescope (iii) the small pixel size ( $\sim 0.3$  arcsec) and the 1-D instantaneous spatial dimension of the instrument. The first two aspects allow a large gain in accuracy in the wind field while the third aspect allows both an instantaneous comparison of wind velocities measured in different regions of the planet and an excellent, seeing-limited spatial resolution at the planet. Thus both short-term variations and small scale structures can be studied. In particular, the latitudinal dependence of the zonal wind at cloud level and the existence of wave patterns can be investigated, and correlated with winds determined from cloud tracking in the VEx VIRTIS-M and VMC UV images.

The UVES instrument achieves both high spectral resolving power ( $R \approx 100000$ ) and high spatial resolution. The narrow long slit width combined with the large angular size of the planet allowed a direct determination of latitudinal (slit perpendicular to equator) or longitudinal (slit parallel to equator) dependence of the zonal winds in both N and S hemispheres.

We present, as well, wind results based on observations from 2011 obtained with the 3.60 m Canada-France-Hawaii telescope (CFHT) and the Visible Spectrograph ESPaDOnS. We measured the winds using Doppler shifted solar lines and compared with our measurements with VLT/UVES (Machado et al., 2012) and with previous measurements with Venus Express, and Galileo. From these 2011 observations we also present the results of the synchronized coordinated observations made by the VIRTIS instrument from the Venus Express orbiter.

With ESPaDOnS, the complete optical spectrum, from 370 to 1050 nm, is collected at a resolution of about 80,000 (Donati, 1997). The Doppler shift measured in solar scattered light on Venus dayside is the result of two instantaneous motions: (1) a motion between the Sun and Venus upper clouds particles, which scatter incoming radiation in all directions including the observers; this Doppler velocity is minimal near Venus sub-solar point; (2) a motion between the observer and Venus clouds, resulting from the topocentric velocity of Venus cloud particles in the observers frame; this effect is minimal near Venus sub-terrestrial point. The measured Doppler shift is the sum of these two terms, and it varies with planetocentric longitude and latitude. ESPaDOnS and the sequential technique of visible Doppler velocimetry have proven a reliable way to constrain wind gradients in the lower mesosphere and global wind circulation models.

In the frame of the effort made in order to coordinate the VEx operations with observations from the ground, were carried out concerted ground-based observational campaigns using various techniques and spectral domains (Lelouch and Witasse, 2008). Both ground-based and Venus Express measurements show considerable day-to-day variability which needs to be carefully assessed. This work observations of small scale perturbations in the observations with VLT/UVES in 2007 (Machado et al., 2012), and the ones from CFHT/ESPaDOnS taken in 2011 and whose results are published in Machado et al. (2013) points to small scale wave motions as the most likely processes by which the instability unfolds.



## Chapter 3

# Venus: Earth's paradoxical twin

### 3.1 The planet Venus

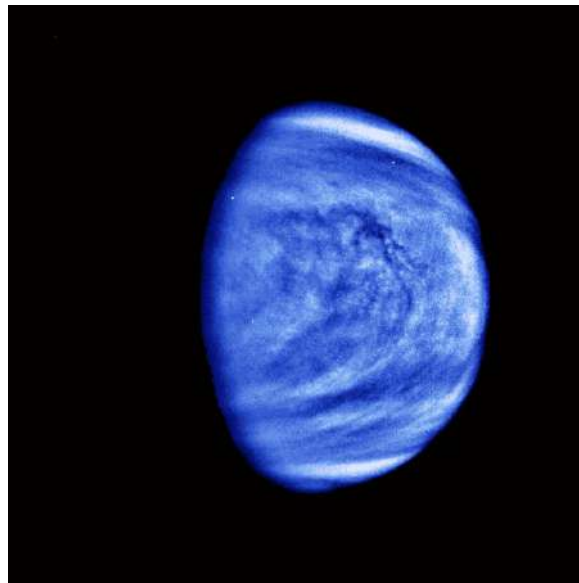


Figure 3.1: Image obtained by the Galileo mission, where are highlighted the small-scale patterns of cloud formation by the false blue colour that emphasizes the clouds. The mottled clouds of sulphuric acid in the equatorial region are evidence of intense convective activity, near the sub-solar point at Venus midday (at right in the picture and a little below the center), (Figure: *site* NASA/JPL).

Venus is usually the third brightest celestial body in the sky after the Sun and the Moon (reaching the magnitude of -4.6). Given the small an-

gular distance that separates the Sun from Venus as seen from Earth, it is seen as a "morning star" or "evening star" this by appearing in the twilight that precedes the sunrise, or after sunset. Even with a small telescope it is possible to observe its phase, depending on the fraction illuminated by the Sun function of its phase angle (Cattermole, 1994).

At the dawn of the modern age, in the year of 1610, Galileo Galilei started pointing his refractor towards Venus. He was the first man observing the phases of Venus, which became a decisive argument to support the heliocentric theory. The *coup de grâce* in the ancient Ptolemaic geocentric model came soon after with the observation of a Venus' passage behind the Sun, finally an unquestionable argument in favour of the Copernicus theory (Grinspoon, 1997).

Astronomical observations of Venus by Cassini and Schröter (respectively centuries 17th and 18th) were the first attempts to determine the planet's rotational period, both advanced with the hypothesis that it was similar to the Earth case. However, it was only in 1890 that Schiaparelli proposed a much slower rotation velocity to Venus.

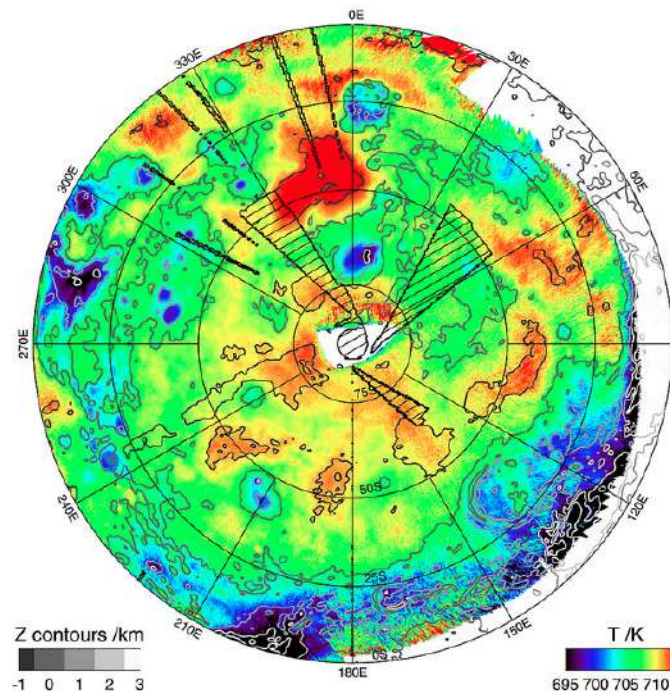


Figure 3.2: (Venus surface temperature southern pole region. Image credits: ESA/VIRTIS/INAF-IASF/Observatoire de Paris - LESIA).

In the international campaign for observing the Venus transit on May 26, 1761 (June 6, 1761 in Gregorian calendar), Lomonosov observed a glowing aureola around the planetary disk, a phenomena just observable during the ingress (and egress) of Venus upon the solar disk. This observation was interpreted as the first tangible evidence that Venus had an atmosphere. Verification that I had the deep pleasure of repeating during the last transit of Venus at 4 June, 2012, at Udaipur Solar Observatory (USO - in Rajasthan, India) as part of the observational international campaign *Venus Twilight Experiment* (see section 6).

Several singularities make this planet unique in the solar system. One, is the fact that Venus presents a retrograde rotation motion, isolated case among the solar system's telluric planets. Another, is the huge disparity between the slow rotation of the solid globe (a "slow" rotation with a period of 243.02 Earth days) and the revolution of the atmosphere which has a period of 4.4 Earth days. It is noted that the Venus solar day, i.e. the time lapse between two positions of the sun at the zenith, is the result of the rotation of Venus around the sun and its orbit, and from the combination of the two motions comes a solar day with about 117 earth days (Grinspoon, 1997).

Having originated from the same "cloud" of gas and dust, Venus and Earth formed at roughly the same time, they have endured the same statistical debris bombardment in the early solar system (as icy planetesimals, cometary-like bodies or rocky asteroids); despite all that, they followed widely divergent paths of planetary evolution. The two planets are similar in size, averaged density and bulk composition. The amount of initial radioactive elements might have been similar, as well, so both planets might have a close starting point of their thermal history (Turcotte, 1995). The initial volatile abundances and composition, should be initially equal, in particular the initial general amounts of water (Ip and Fernandez, 1988). It is yet unclear in the surface temperature has ever been low enough to allow condensation of water, even in possibly reduced solar illumination conditions in the early solar system (Chassefière et al., 2012). These facts make Venus the prime case study for comparison with Earth.

One of the striking characteristics that distinguishes Venus from Earth is the obliquity of the globe ( $177^\circ$ ). This high obliquity of the axis turns the planetary rotation almost perpendicular to the ecliptic, and makes the rotation of either the atmosphere or the solid body retrograde, when viewed from the Earth. The two hemispheres receive approximately the same amount of radiation over the year, thereby seasonal variations are negligible (Bougher et al., 1997).

Despite its proximity to Earth, Venus have long remained, obstinately, an

impenetrable mystery due to the opaque clouds, that cover it completely. The atmosphere reflects and absorbs about seventy-eight percent of the sunlight that falls on it (figure 3.1), for comparison Earth's reflects about 32% of the incoming solar radiation (albedo). Being about the same size as the Earth and with an average distance of 0.72 AU from the Sun, Venus receives about twice as much solar energy as the Earth.



Figure 3.3: Venus image synthesized by computer from the mosaic of radar images and radar altimetry obtained by the Magellan probe during its first cycle mapping the planet. (Image: *site* NASA/JPL).

With closest approach to Earth on the order of 41 million kilometers, Venus was an obvious target on the eve of planetary exploration, more by its inviting glow on the terrestrial sky and notion of proximity than by the distance to travel to get there (because, as we know, the minimum energy orbit between the two planets entails much larger than the distance between them - Hohmann's orbit). The first probes of the *Venera* project were launched in 1961, but operational problems led to that the first flyby was carried out, in fact, by *Mariner 2* in December 1962. The images sent by the probe were a disappointment because it revealed only an opaque atmosphere that shrouded entirely the planet, like a veil that hid the planet's surface.

From the mid-1960's the *Venera* probes got luckier. They plunged through the dense atmosphere towards the ground, but the hostile environment had been underestimated and the high pressures and high temperatures eventually crushed the first devices soon after their landing. Only *Venera 7* was able to achieve the desired goal of reaching the surface and send some data back to Earth. For those who expected a pleasant environment and, eventually, could support life, this was the stroke of mercy, as the readings indicated surface pressures of the order of hundred times the terrestrial atmospheric pressure ( $\approx 90$  bars) and ground temperatures around  $460^\circ\text{C}$  ( $\approx 735\text{ K}$ , see figure 3.2, Marov et al. (1973); Tomasko et al. (1980)).

The hostile surface conditions are so remarkable that the extremely high pressure that is similar to that at roughly 1 km depth at a terrestrial sea, with a visual horizon that does not extend beyond 400 meters in a yellowish desolated world (possibly due to sulphur compounds, Grinspoon and Bullock (2007), see also subsection 3.4.2). Thermodynamically speaking, the pressure and temperature at surface led the atmospheric properties to be closer to the liquid phase than the gaseous one. This is the case of its major compound,  $\text{CO}_2$ , that has its critical point at a temperature of 304 K and a pressure of 73 bars, so at the first scale height of Venus atmosphere, the carbon dioxide is a supercritical fluid (Kastings, 1988).

The surface of Venus began to be mapped from the ground, using Goldstone and Arecibo antennas, then by orbiters using radar (radio waves could pass through the opaque cloud layer in a wavelength window through the medium opacity). On the other hand, new reinforced probes in order to withstand the extreme environment surface conditions, corroborated the first readings. The images of Venus' surface showed a desolated landscape of chemically eroded basaltic rocks, separated by minor amounts of soil.

The NASA *Pioneer* mission, in the 1970's and 1980's, made an invaluable contribution for the study of this planet, mapping the planetary surface, again by radar. The detailed cartographic survey only became possible with the sophisticated *Magellan* probe, which operated between 1989 and 1994. The resolving power of this probe was such (of the order of 30 km/pixel) that in addition to be able to establish the altitude and topography, it could describe the terrain slopes, the surface roughness and texture of the soil and could even distinguish regions where the soil was composed by different minerals (Rossow et al., 1990).

Present time temperatures at Venus' atmosphere are maintained as the result of the competing effects of the greenhouse and cloud albedo. These striking high temperatures at Venus are consequence of a positive reinforcement of atmospheric warming by an efficient carbon dioxide and water greenhouse effect, along time's planetary evolution, and by the radiative properties

of its global cloud cover. The major infrared absorber is at same time the principal atmospheric constituent, carbon dioxide. If it could have reacted with the surface rocks, the greenhouse effect would diminish cooling the atmosphere in the process, provoking a rapid climate change. Nevertheless, this phenomena is not likely to happen as evidenced by the crust lack of carbonated minerals (Bullock and Grinspoon, 2001).

However, this prevailing greenhouse ( $CO_2$ ) effect and the cloud layer as well, are sensitive to the atmospheric variability in the abundance of gaseous sulphur compounds and water vapour for two reasons: (1) water vapour is mainly radiatively active at different wavelengths than  $CO_2$  (Sagan, 1972); (2) the sulphur compounds, such as  $SO_2$ , absorb preferentially in carbon dioxide-water infrared windows (Pollack et al., 1980). As we note below, although they are minor species, these atmospheric constituents have an essential role in the maintenance of the atmosphere thermal equilibrium. Both molecules are tied to the sulphuric acid cloud layer that shrouds the planet and control its albedo (Esposito et al., 1983).

The referred minor constituents, despite their trace amounts in the atmosphere, could influence the long term thermal balance, even driving climate change (Bullock and Grinspoon, 1996). For the above, it is crucial to constrain the planetary-scale processes involving these species, namely the cycles that govern, over time, the transport and sequestering of these compounds. Some escape to space, as the hydrogen from photolysed water vapour, it is mandatory to study its concentration fluctuations, as it has direct consequences in cloud formation. Others of these radiatively active species, as is the case of the sulphur dioxide, undergo chemical reactions that alter its concentration, also the sulphuric acid droplets, from clouds, dive in atmosphere and react with surface rocks. In order to maintain an atmospheric equilibrium, sources are necessary to replenish the diminishing species. Volcanism is surely one important source, at least for some volatiles like  $SO_2$ . As all these processes are temperature and concentration dependent, variability in the atmospheric composition, even for minor components, leads to atmospheric balance modifications. Due to the lack of effective replenishment of some atmospheric constituents, as is the case of water that endures an atmospheric continuum loss to space (Grinspoon and Bullock, 2007), is more likely that Venus is undergoing an evolutionary process, at least at large time-scales.

### 3.1.1 Geologic evolution

Most thermal models agree that the initial composition of Venus, was essentially chondritic material. Most of its radioactive reservoir might be accumulated in the center and, over time, the planet was gradually warming up.

The patent similarity between the mass density of Venus and Earth points to a probable similar thermal history, controlled by core differentiation.

Since Venus and Earth are approximately the same size and being formed from similar primordial materials, the internal heat production due to the approximately equal amounts of radioactive elements, might also be similar, at least at the beginning of the planetary history (about 4.5 billion years). Some of this heat escapes through molten crust rocks at *hot spots* (Phillips and Malin, 1983). Based on Magellan probe gravity data, it was found that Venusian *hot spots* were not randomly scattered but rather clustered in defined areas, believed to be mantle plumes (Smrekar et al., 2010). In the Earth's case, the plate tectonics mechanism is closely linked to the carbon dioxide cycle, literally burying large amounts of it at subduction zones, stabilizing in this way the atmospheric  $CO_2$  (Holland, 1978), a process that is not available in the one-plated Venus.

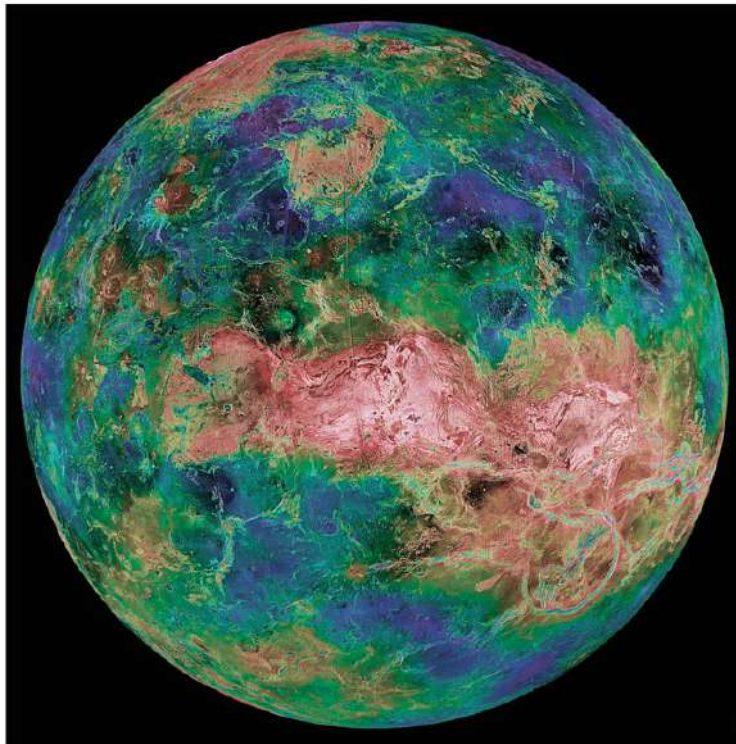


Figure 3.4: False colour Venus' cartographic image from the Magellan probe. (Image: *site* NASA/JPL).

Venus with its 12104 km in diameter is almost the size of Earth. The gravity at the surface is 0.9 times the terrestrial one, and the internal structure is very similar to the Earth's, with a thin silicate crust, a thick mantle

and a core of heavy metals (nickel and iron). One significant difference is that the core of Venus shows evidence of being solid and comparatively much colder than the Earth's one (Lewis, 2004).

Our knowledge of Venus' surface topography is due, essentially, to extensive surface mapping by the Magellan mission (figure 3.3). Radar images showed that the surface of Venus has been geologically active on a global scale. The accuracy of the radar surface geology images obtained using 12.6 cm radio waves, with a spatial resolution on the order of 200 m (Saunders et al., 1992), provided new constraints on the dating and amounts of volatile outgassing in the planet's history (Bullock et al., 1993).

An intriguing fact is the low rate of impact craters, and furthermore their almost pristine condition. Also astonishing at first sight is the fact that the impact craters appear to be randomly scattered at the planet's surface (Schaber et al., 1992). The detailed radar images show an average crater density that points to a surface age of 600-1100 million years (Schaber et al., 1992). From the more than 960 identified impact craters upon Venus' surface just one third of them present tectonic damages (essentially due to vertical motions) and just a few were partially filled by volcanic lava. This strongly suggests that an older surface was swept away and literally submerged by a large scale resurfacing process, and from there, started again a "new" impact history in the flooded areas. Stratigraphic analyses of Magellan images pointed to a major catastrophic resurfacing that occurred within 10-100 million years. A cataclysmic event of this kind would entirely disrupt the crust and as a consequence, a large amount of volatiles would be released into the atmosphere.

Most of the planet is covered by basaltic plains (nearly 80%), from which a wide variety of volcanic features emerge. There are huge shield volcanoes, ring shaped features (*Coronae*), fluvial-like landforms, channels stretching over thousands of kilometres with features resembling river deltas (Kargel et al., 1994).

The surface-atmosphere chemical equilibrium indicates the existence of calcite and anhydrite among other salts in the superficial crust composition. Since that at the surface high temperatures these salts must be molten, the hypothesis was advanced of the existence of a salty sub-superficial layer that could liquify in contact with the surface higher temperatures, thus carving the observed hydrographic-type system (Kargel et al., 1994). Also at surface, due to its high temperatures, it occurs another relevant atmosphere-surface chemical reaction, calcium silicates undergo a substitution reaction process that transforms them in calcium sulphates (Fegley and Treiman, 1992).

It is still important to point out the consequences arising for each planet from its different planetary rotation rate, both in terms of the solid globe



and their specific atmosphere dynamics. This influence can be seen regarding, for instance, the meridional wind system at each one of the terrestrial planets with atmosphere. While on Earth there is a triple cell mechanism (as explained in the next section) for the meridional wind circulation, on Venus, there is a single Hadley cell in each hemisphere extending from the equatorial region to the polar region.

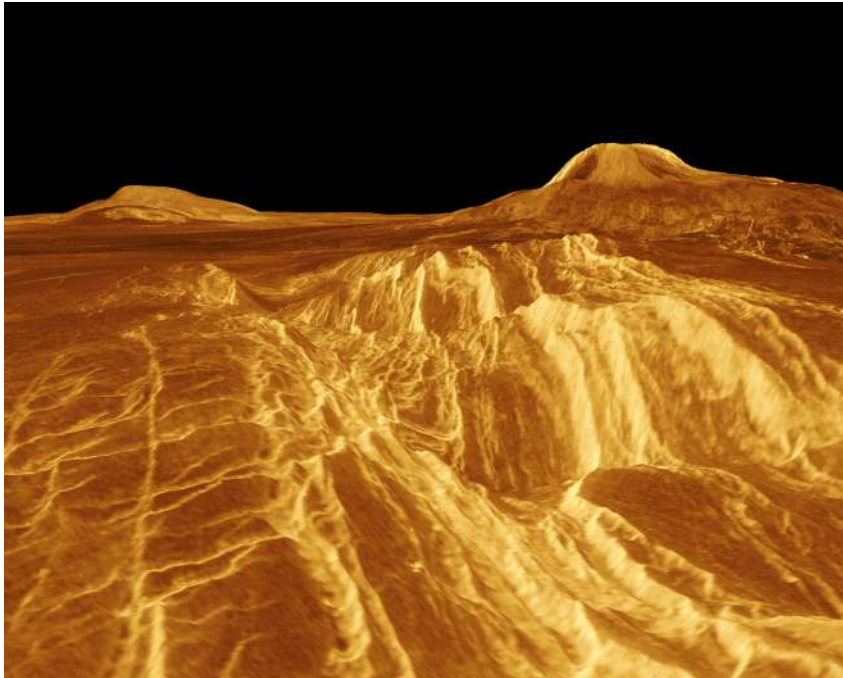


Figure 3.5: Three dimensional images of Venus' surface, synthesized from the radar images taken by the Magellan spacecraft. Sif and Gula Montes in Eistla Regio. The volcano on the left of the image is about 3 km height (Gula). In the foreground we can see lava flows through the fractured plains. (Image: *site* NASA/JPL).

Although Venus does not present active tectonic plates, there are evident "scars" of deep gorges and canyons attesting the strong possibility of there having been significant active tectonic activity in the past (see figure 3.5). This is the case of the "chasmata" canyons, that intersect at the planet's equatorial latitudes (Cattermole, 1994). The terrain on Venus shows great diversity. At the northern hemisphere extends a prominent mountain system, from the surrounding plains, this is the case of the Lakshmi plateau.

Statistical studies on the size and scattering of impact craters suggest that the current surface of Venus is no more than 400 million years old (except at higher altitude, that are much older than the proposed mean

age, named the *tessera* terrain), thus pointing to a hypothetical date for the last major volcanic disruption of the surface of Venus, and subsequent resurfacing of molten material that might covered completely the low lands, thereby obliterating the pre-existing craters (Cattermole, 1994).

So, the impact craters are few in number, especially in the lowlands, which results from having been erased by the generalised volcanic eruption process. The impact craters that can be found on the Venus' surface are generally quite large because of the high density of the atmosphere, which protects the planet from most impacts of smaller objects, incinerating them when they enter the atmosphere. On the other hand, due to the extremely high pressure at surface's level and high air viscosity, the fragments resulting from impact are not thrown at large distances from the crater (Pater et al., 2001) and a number of craters exhibit a parabolic halo of dark material, of aeolian origin.

### 3.1.2 Venusian volcanism

Despite the gentle name of the mythical goddess of love, in fact the surface of Venus has more similarities with Dante's Inferno. The planet's surface is dominated by large volcanoes and lava flows, the surface temperature is high enough to melt lead and the surface pressure is much high than on Earth.

Almost all Venusian geological structures are of volcanic origin, making Venus a "world of volcanoes". Surface reconstructions based on data from the Magellan spacecraft reinforce this description of the planet, as shown by their solidified lava plains around the hills Gula and Sif (figure 3.5).

The Venus' surface contours outlined by the Pioneer Venus, show that the planet is essentially composed of volcanic plains. The highlands cover a wide range around the equator (*Aphrodite Terra*) (figure 3.5) with other minor mountainous structures scattered upon the rest of the planet. This is the case of the Maxwell Mountain, near the North Pole (which is taller than Mount Everest) and of the *Beta Regio* shield volcanoes with the summit of his pair of volcanoes exceeding the 5000 meters. *Ishtar Terra* is a mountainous complex which recalls us to Tibet and the Himalayan region on Earth.

Most of the terrestrial volcanoes result from the friction between the tectonic plates (with sharply demarcated lines of regional volcanic activity areas consistent with the well located zones of tectonic plates' confrontation), as is the case of the Pacific ring of fire. However, Venus is covered by a single plate and there is no evidence of the tectonic plates mechanism (Schubert and Sandwell, 1995). Without an heat escape valve in continuous mode, as happens on Earth, the accumulated energy warms up over the entire surface until lava erupts through more than 100,000 volcanoes of all sizes (Bougher

et al., 1997). Although, was pinpointed over the Venus' surface the existence of hotspots most likely connected with sporadic shield volcanic activity (this is the case of Idunn Mons, recently analyzed from VEx/VIRTIS emissivity data, Smrekar et al. (2010)). Two aspects are highlighted here: one which relies on a generalization of volcanic events without preferential areas, as is the case on Earth, (however, the more dispersed nature of the Venusian volcanoes is not fully random, because about 70% of the occurrences of shield volcanoes occur in about half of the planet's surface), the other has to do with the simultaneous occurrence of eruptions on a global scale as seen in the geological studies of recent years.

The planetary lowlands show broad plains that resulted from the filling by lava flows of areas of topographic depression. The presence of extensive lava channels and the evidence of preferred directions corroborate this idea. Then the latest extrusive material might be accumulated in the low flatlands and it is also where there are less impact craters (or were submerged by the eruptive material or they were very altered and damaged by the deposition of lava). On the other hand, the highlands present the oldest geologic materials and planetary formations (Kargel et al., 1994), see figure 3.5.

The plains of Venus are fractured by volcanic activity. The resulting structure presents a spider-shaped pattern, called *arachnoid* and reaching up to 250 kilometers in diameter. Covering almost the entire planet there are solidified lava flows (Cattermole, 1994). Other odd volcanic structures present on Venus' surface are the so called *pancake* domes, extending its circular structure, derived from lava domes that rose from the ground and eventually "spill" around before lava takes time to solidify. These structures are even exceeded in size by the huge *coronae*, round structures that result from the emergence of flowing material and subsequent collapse. Part of the volcanic edifices, roughly one fifth of them, are severely damaged by tectonic reasons, possibly in the prelude of the resurfacing process (Basilevsky and Head , 1995).

The surface of Venus is dominated by large land formations that result from the rising mantle to the surface of the planet (Figure 3.5). The *Coronae* networks subtend the hypothesis that have occurred an extensive activity of mantle material emersion. The fact that there is something similar to a sequence of evolutionary *Coronae* also supports the hypothesis of a resurfacing process until today. This, because some of the small *Coronae* are radially fissured, what should represent early stages in the temporal evolution of the *Coronae*.

Periodically (on a scale of billions of years) the planet endures successive eras of intense volcanism across the surface, erasing old craters and transfiguring the planet's surface in huge resurfacing processes (Basilevsky and Head

, 1995). The massive and generalised volcanism, during this resurfacing process, led to an intense volcanic outgassing of sulphur dioxide and water ( $\sim 300$  million years ago), that led to the formation of extensive sulphuric acid and water clouds, and the increasing albedo contributed to a cooling of the surface. Then it might have happened a cloud layer differentiation, with the sinking of the heavier sulphuric acid droplets, that reacted with surface rocks and were subsequently lost in the reactionary process. The thin higher water vapour cloud layer, under the upper atmosphere intense solar radiation, and seen that the Venus solar constant is almost the double than the terrestrial one, endured severe photolysis and consequent loss of atmospheric water. This statement is reinforced by the high D/H ratio observed that is roughly 1500 times higher than the verified at Earth's atmosphere (Donahue, 1982). However, this ratio might not point directly to the primordial water abundance as it could have existed atmospheric water resupplies along recent geologic history (Donahue, 1997).

Recent near-infrared observations from VIRTIS/VEx instrument revealed high ground emissivity in the neighbourhood of the already spotted *hot spots*, this could represent the evidence of ongoing volcanic activity (Smrekar et al., 2010). The subsequent increase of crustal outgassing could impact the atmospheric balance by changing the  $CO_2$  and  $SO_2$  mixing ratios, the cloud deck structure and consequently the albedo variability (Bullock and Grinspoon, 2001).

## 3.2 History of Venus exploration

### 3.2.1 20th century exploration



Figure 3.6: *Mariner 2*, launched toward Venus in August 1962. (image: NASA website).

Since ancient times, the shining light of Venus in the night sky aroused the curiosity and imagination of multiple different civilizations. This bright “wandering star” who paced the sky was subject of myth and legends, observations and astronomical previsions, and even divinised as a God or Goddess from the pantheon of different cultures. Along the path of history, from ancient Babylonia, Assyria, Greek and Roman empire till the Maya and the Incas, all of them venerated Venus in one way or the other. For instance Mayan culture developed techniques to predict the ephemerides of the rising time of this celestial body (Grinspoon, 1997).

From early telescopic observations, beyond the already cited works by Galileo, one should mention the albedo variability (1666) detected from Cassini observations (Marov and Grinspoon, 1998), and the first evidence of the existence of a Venusian atmosphere from the illuminated aureole that surrounds Venus during a transit, in 1761, by Lomonosov, although its existence had been already proposed before by Herschel (Grinspoon, 1997; Marov and Grinspoon, 1998).

More than 30 spacecraft have been launched to date toward Venus, since the beginning of robotic space exploration. More so, Venus was the first suc-

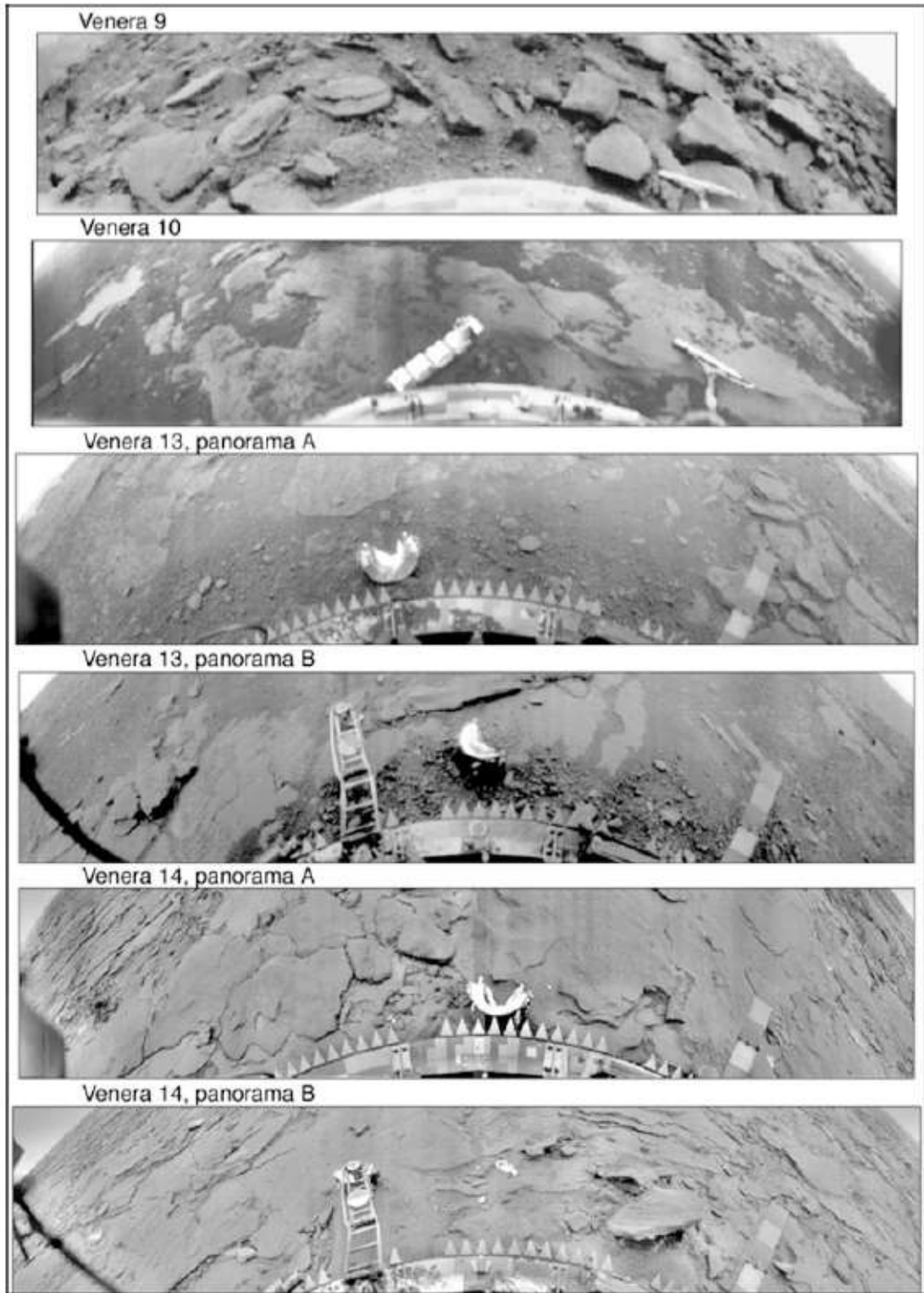


Figure 3.7: Venera mission landings - historical images from Venus' surface (image: NASA Russian Academy of sciences).

successful planetary target for human space exploration (Mariner 2). Although, the first craft ever sent to other planetary body was Venera 1, in 1961, but contact with ground control was lost soon after launch. In 1962 there was the first close contact with Earth's "twin planet" by *Mariner 2* robotic space probe. The measurements made with its magnetometer confirmed the high surface temperatures of 460° C (Sonett , 1963).

In 1974 Mariner 10 collected image data with resolutions on the order of 30 km/pixel during its closest approach to the planet.

The *Venera* program (1961-1984) achieved important mapping based in new surface data, and collected the first images from the surface and surface physical and chemical conditions. The mission began in 1961, suffering some initial failures, but quickly became quite successful with the first atmospheric data collected, in situ, and then sent back to Earth in 1967, with Venera 4. Some of these robotic probes effectively landed, surviving long enough in the surface extreme conditions, in order to transmit back to Earth data about the surface and atmosphere. The highly successful mission produced, among other scientific contributions, high-resolution radar surface mapping (Venera 15, 1983). Venera missions (4 to 7) confirmed the existence of an atmospheric super-rotation (Dollfus et al., 1975b).

The new soviet mission, Vega, was the natural continuation of the previous Venera program. It used the same basic probe and landers design, but now also with atmospheric balloons, that could survive longer than the landers and in the meanwhile measured the pressure, temperature and even the wind velocity (Blamont, 2008). The *Vega* and *Pioneer* missions were essential for the structured study of the atmospheric chemical behaviour and physical description, as will be detailed presented in the following. Their measurements showed the evidence of an extremely active atmosphere, containing corrosive gases and a thick cloud layer.

The Galileo spacecraft made a Venus fly-by gravity assisted manoeuvre on its way to Jupiter. The observations made during closest approach took advantage of its high resolution infrared camera. The images taken at that time contributed to improve the knowledge about cloud properties and their variability (Carlson et al., 1993).

Galileo Near Infrared Mapping Spectrometer (NIMS) made night-side observations of the atmosphere's infrared emission at 2.3  $\mu\text{m}$ . This instrument took advantage of the carbon dioxide and water vapour opacity wavelength window through 2.1-2.6  $\mu\text{m}$ . The region probed at this specific wavelength (2.3  $\mu\text{m}$ ) is from below the cloud deck.

In 1992, the Magellan orbiter accomplished a comprehensive radar-mapping of nearly all the planet's surface with a resolution of around 200 meters. The mission also collected high-resolution gravity data of Venus. Altimetry and

radiometry measurements were obtained, as well, in order to retrieve the surface topography and electrical characteristics. When it reached the end of its extended mission, in 1994, the probe was control-crashed into the planet with the objective of obtaining some final atmospheric data along the descent (Saunders et al., 1992).

The orbiter and multi-probe Pioneer Venus mission was launched in 1978. Its high elliptical orbit allowed a global mapping of the cloud deck, ionosphere, upper atmosphere, surface radar-mapping, among other experiments. The descent probes deployed, in turn, carried two experiments, a neutral mass spectrometer and an ion mass spectrometer to study the composition of the atmosphere. The performed measurements of cloud and atmospheric characteristics were essential in the construction of Venus atmospheric models (Colin and Hunten, 1977).

The *Pioneer* project was responsible for the first measurements of the weak magnetic field of Venus, by means of its onboard magnetometer readings, which was confirmed by later observations from ESA's *Venus Express*. This magnetic field is the result of the interaction of the solar wind with the ionosphere (not due to the planetary dynamo's model). PV also produced the first indirect measurements of mesospheric winds, estimated by observing the UV cloud tops markings. This mission was also responsible for the discovery of the vast double vortex at the northern polar region.

A remarkable extensive dataset was obtained by the Orbiter Cloud Photopolarimeter (OCP) instrument, its average spatial resolution is of the order of 30 km/pixel (Rossow et al., 1990).

Sulphur dioxide ( $SO_2$ ) is the third more abundant chemical species, after  $CO_2$  and  $N_2$ , in Venus' atmosphere. Pioneer Venus mission performed measurements of these major constituents and of the minor species, as is the case of  $O_2$ , CO,  $H_2O$  and Ar, by its gas chromatograph experiment (Oyama et al., 1980).

### 3.2.2 Present Venus exploration

#### Venus Express mission and related results

After a long pause (about a quarter of a century) in spacecraft exploration of Venus, the European Space Agency (ESA), launched on November 9, 2005 the *Venus Express* spacecraft (figure 3.8), with the task of conducting studies under the general circulation of the atmosphere, the chemistry of clouds and the atmospheric escape processes of several different volatiles, as well as the interactions between the surface and the atmosphere, with emphasis on the Venusian volcanism. Objectives also relevant were: the study of the planet's





Figure 3.8: The *Venus Express*: final payload assembling procedures. (image: ESA's *Venus Express* mission website).

energy balance and the overwhelming greenhouse effect. The *Venus Express* entered Venus' orbit on 11 April 2006 and initiated its mission nominal phase in June this year. The orbital period is of 24 hours. The orbital design is elliptical, highly eccentric, with a planetary close pericentre of 250 km and an apocentre of 66,000 km. This orbit configuration provides optimal coverage of planetary latitudes and solar local time. The highly elliptic orbit allows global large scale investigations, as high spatial resolution detailed studies of localised phenomena, at pericentric close approach.

The set of experiments onboard Venus Express aimed to cover a great deal of scientific cases and to address most of Venus' open research issues. A core mission goal was to perform a global and long term survey of the atmosphere, the surface and plasma environment, as well. The orbiter payload was designed with the special emphasis on the study of Venus atmosphere, with particular focus on atmospheric dynamics and circulation.

This orbiter can take advantage of the observation window between 1 and 3  $\mu\text{m}$  through the clouds till the planet's surface, and can probe the cloud top region as well, thus enabling a three dimensional view of the atmosphere, in contrast with the unique option of probing the top of the clouds, that the techniques of the previous missions' instruments enabled. The probe has a

magnetometer, monitoring camera (VMC), the Visible and Infrared Spectrometer (VIRTIS) instrument a radio-band Fourier spectrometer (PFS), an infrared spectrometer and ultraviolet detector, as well as a plasma and neutral particles detector.

With the orbital apocenter at Venus' south pole, it is possible to survey extensively the atmospheric circulation in this region. The repeated observation of the southern polar vortex allowed to study in detail, and for long periods of time, the vortex dynamics and morphology (Luz et al., 2011; Hueso et al., 2012; Garate-Lopez et al., 2013).

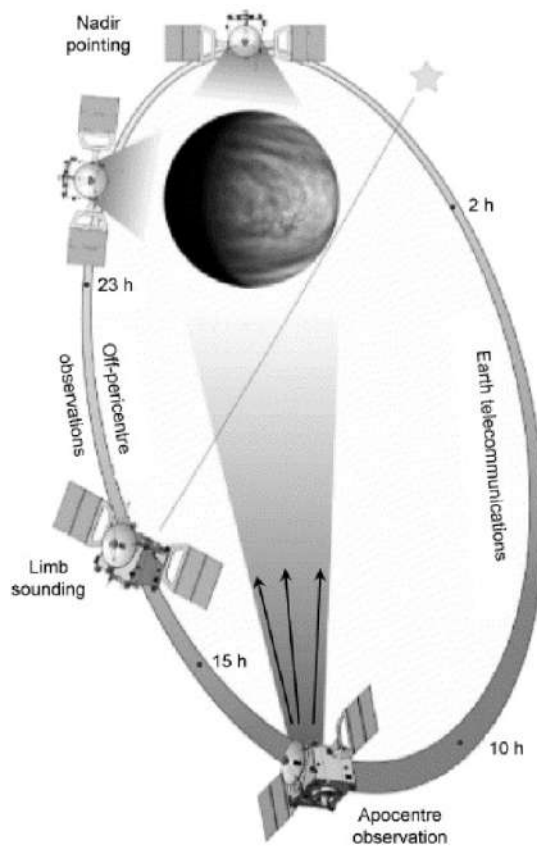


Figure 3.9: High elliptical *Venus Express* polar orbit. At pericenter the orbiter's high velocity makes this orbit's region not suitable for imagery. On the other hand, near apocenter imagery of the South pole is one of the main goals of VEx. As we can see in the orbital scheme there are specific regions to perform solar and stellar occultations (image: Venus Express website).

The possibility of studying atmospheric dynamics using the Venus Express payload is two-fold: one is using the Venus Monitoring Camera (VMC)

camera with its ultraviolet filter (Moissl et al., 2009), in order to follow the displacement of the cloud-deck UV markings ( $\approx 70$  km, Ignatiev (2009)) over time, deriving on that way the wind field at the dayside (cloud tracking method). At the nightside, it is possible to retrieve the cloud markings at infrared range with the Visible and Infrared Thermal Imaging Spectrometer (VIRTIS) (Luz et al., 2011; Hueso et al., 2012; Sánchez-Lavega et al., 2008), the probed atmospheric heights are not the same due to the different wavelength opacity of the cloud layer (48 km, 61 km and 66 km). An alternative way to calculate the wind velocities is to derive thermal winds from atmospheric thermal profiles Piccialli et al. (2008), using for this effect the thermal wind equation (see section 3.3).

In order to sound the temperature structure in the mesosphere, one can use two different onboard experiments: the Venus Radio Science Experiment (VeRa) that probes atmosphere heights between 40-90 km of altitude with a vertical spatial resolution of the order of half a kilometre, this technique exploits radio occultations at planetary limb (Häusler, 2006; Pätzold et al., 2007); the other option, but in this case for sounding altitudes ranging from 65 till 90 km, is to use exposures from the Visible and Infrared Thermal Imaging Spectrometer (VIRTIS), that sounds the southern hemisphere with spatial high-resolution, vertical resolution of 3 km and good temporal coverage, in this case is made use of spectra sounding the middle atmosphere at nightside at  $4.3\mu\text{m}$   $\text{CO}_2$  hot bands (Drossart et al., 2007b).

As we can perform coordinated observations between VIRTIS and VMC camera, is then possible to derive wind velocity fields by the cloud tracking method (UV) and compare with the coordinated thermal winds derived from VIRTIS observations Piccialli et al. (2008). The comparison between cloud tracked and thermal winds allows to verify directly the cyclostrophic hypothesis for the mesosphere Venus' global atmospheric circulation.

The Venus Express payload can be divided in three different categories from a total of seven experiments' instruments: a radio science experiment that uses a ultra-stable oscillator; a magnetometer and plasma detector in order to perform direct measurements; and the remote sensing spectrometers and spectral imagers.

A brief description is given of the seven onboard instruments that compose the payload. Figure 3.10 shows the relative position of the scientific instruments in a scheme of the Venus Express spacecraft.

- The Venus Monitoring Camera (VMC) is a four filter band CCD-based camera, UV with a 365 nm central wavelength, visible with  $\lambda_{central} = 513$  nm, and two separate near infrared filters, one around  $\lambda_{central} = 965$  nm and the other at  $\lambda_{central} = 1000$  nm (Markiewicz et al., 2007).

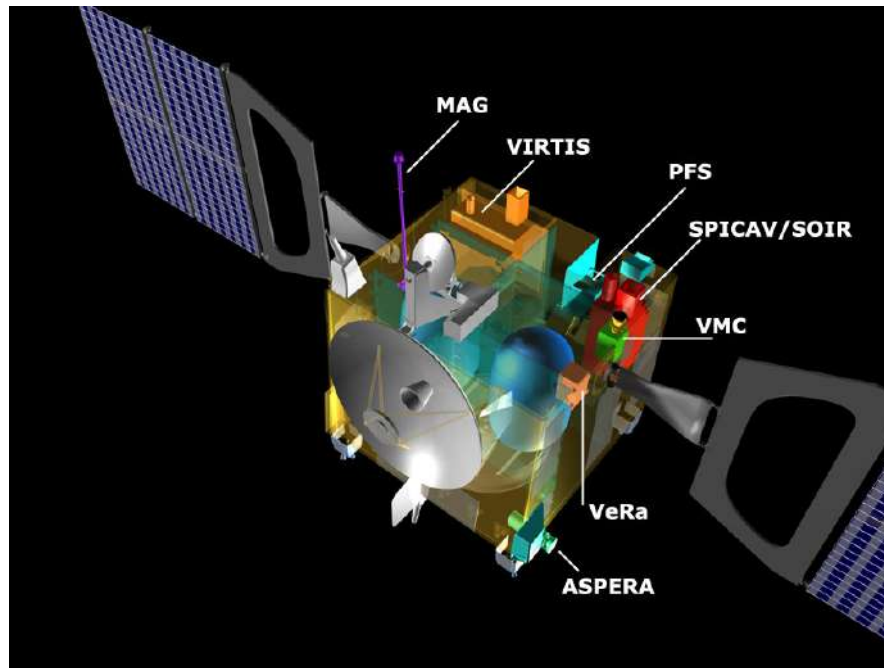


Figure 3.10: ESA's *Venus Express* space probe, scheme of the instruments onboard. (Image: *Venus Express* official site, ESA).

The nominal spatial resolution depends on the orbital position, that is a polar high eccentric ellipse, so it varies from 50 km per pixel (at apocenter), important to investigate global atmospheric observations, till a few hundred meters (near pericenter), the latest are generally used to study cloud top features and used in the frame of small-scale dynamical phenomena. The UV channel central wavelength is, on purpose, pinpointed at the spectral signature of the unknown atmospheric ultraviolet absorber. So this filter is indicated to perform the cloud tracking technique by following the motion of the UV markings at the cloud top layer. With the visible filter, the camera is sensible to the infrared emission from the planet's nightside, with most of the emission coming from a altitude ranging nearly one hundred kilometres. The 965 nm centred filter pursues the water vapour atmospheric abundance and the 1  $\mu\text{m}$  one benefits from the transparency window. Some studies have retrieved wind velocity fields from tracking of markings caused by the yet unknown UV absorber, count [Limaye and Suomi \(1981\)](#); [Limaye \(1988\)](#); [Toigo et al. \(1994\)](#); [Moissl et al. \(2009\)](#). An other method to derive wind velocities using VMC and based in clouds streak feature orientation, is represented by the work of [Smith and Gierasch \(1996\)](#).

- The Visible and Infrared Thermal Imaging Spectrometer (VIRTIS) is an extremely versatile instrument with two different channels. VIRTIS-M is an imaging spectrometer (0.25 mrad of spatial resolution) that operates in the wavelength range of 0.25 - 1  $\mu\text{m}$  and also 1 - 5  $\mu\text{m}$  with a spectral resolution  $R \approx 200$  and high spatial resolution. On the H channel, VIRTIS converts itself in a high resolution spectrometer ( $R \approx 1200$ ) covering the wavelength range of 1.84 - 4.99  $\mu\text{m}$  (Drossart et al., 2007b). The instantaneous field of view of VIRTIS-M is 0.25  $\times$  64 mrad, what consists in nearly a third of the planetary disk near apocentre, so it is necessary a mosaic of images to reconstruct all the planet disk. VIRTIS is suitable to meteorology studies in different approaches, atmospheric dynamics, composition and the retrieval of mesosphere vertical profiles of temperature. The measurement of wind velocities are possible at cloud tops, dayside and at  $\approx 70$  km (Ignatiev, 2009), and in the infrared range at nightside, sounding the height of  $\approx 50$  km. Some reference results based on VIRTIS observations: CO atmospheric composition by Irwin (2008) (VIRTIS M and H - nightside at 4.7  $\mu\text{m}$ );  $H_2O$  by Cottini et al. (2012) (VIRTIS-H at 2.55  $\mu\text{m}$ , dayside) and Bézard et al. (2009) (VIRTIS-M); CO, OCS,  $H_2O$  and  $SO_2$  by Marcq et al. (2008) (VIRTIS-H); atmospheric dynamics by Drossart et al. (2007b); Piccialli et al. (2008) (thermal winds), Luz et al. (2011); Hueso et al. (2012); Sánchez-Lavega et al. (2008); Garate-Lopez et al. (2013) (cloud tracked winds).
- The Venus Express Radio Science Experiment (VeRa) sounds the atmosphere through radio-occultation procedures. Its radio signals comprises two different bands: the 3.6 cm X-band and the 13 cm S-band. This instrument is suitable to probe the neutral atmosphere, the ionosphere and carry out gravimetric anomalies measurements as well. The same radio science package also comprises an ultra-stable oscillator (USO) in order to provide a stable frequency reference (Häusler, 2006). Mesospheric radio sounding provides vertical density profiles, and also profiles of pressure and temperature. The radio occultations observations are made near pericentre and in very specific geometries, that require precise orbital position portions for VeRa activity and orbiter attitude in relation to the planet's surface. Among the important results obtained, based in VeRa experiment observations, one can highlight the atmospheric structure and convection results (Tellmann et al., 2009), and the presence of high latitudes gravity waves (Tellmann et al., 2012)

- SPICAV/SOIR: Ultraviolet and Infrared Atmospheric Spectrometer (Bertaux et al., 2007). Based on the SPICAM/MEx from Mars Express, this imaging spectrometer retains the same ultraviolet (0.11-0.31  $\mu\text{m}$ ,  $R \approx 300$ ) and infrared channels (0.7-1.7  $\mu\text{m}$ ,  $R \approx 1300$ ), as its twin instrument. The instruments can be used in different operating modes (Nadir spacecraft attitude, star or Sun pointing and limb pointing). Some highlighted results: Bézard et al. (2011) (SPICAV/IR - water atmospheric composition), Fedorova et al. (2008); Belyaev et al. (2008, 2012) (SPICAV/IR and UV (occultation mode) -  $H_2O$ , HDO and  $SO_2$  atmospheric composition),  $SO_2$  composition by Marcq et al. (2011) with SPICAV/UV in nadir mode. All these highlighted results will be addressed in detail in the next section. A new channel tuned to observe solar occultations was added to the basic configuration. This infrared spectrometer (Solar Occultation at Infrared - SOIR) covers the wavelength range of 2.3-4.2  $\mu\text{m}$  and has a spectral resolution of  $\approx 15,000$ , analyses the solar radiation that crosses a section of Venus' atmosphere at the rising or setting of the Sun (limb pointing mode), and so carrying information about the interaction between the solar radiation and the atmosphere's layers (see subsection 3.4.3).
- PFS: Planetary Fourier Spectrometer (Formisano et al., 2006), experience that does not work due to failure in the servo motor responsible for switch the mirror between the calibration lamp and the planetary target.
- Venus Express Magnetometer (MAG) (Zhang et al., 2006).
- Analyser of Space Plasma and Energetic Atoms ( ASPERA) (Barabash et al., 2007).

The first observations of *Venus Express* mission, provided quantitative measurements of the RZ circulation of the atmosphere, as well as the presence located climate phenomena. Such the case of small-scale mottled cloud features indicating vigorous convective activity in the equatorial region, where these convective cells were identified on unprecedentedly small scales. Later observations confirmed the suspicion that Venusian clouds present electrical storms Russell et al. (2007). Another important corroboration was about the existence of atmospheric vortices in the planet's polar regions. The 4-day Kelvin wave mode, at low latitudes, was surveyed with Vex exceptional spatial resolution and benefiting from long time intervals coverage.

Due to the distance variability between the orbiter and the planet, along the orbital path, there is an hierarchy of preferences in the active instruments

at different orbital regions. Near pericenter, the priority goes to spectroscopic observations with high spatial resolution and plasma measurements, due to low orbital distance. The magnetometer would be active, as well, in the vicinity of the planet. In the apocenter, the emphasis goes to the polar vortex and atmospheric dynamics. In between, studies on atmospheric dynamics and measurements in order to study the interaction between the solar wind and the upper atmosphere (VeRa and magnetometer) are conducted.

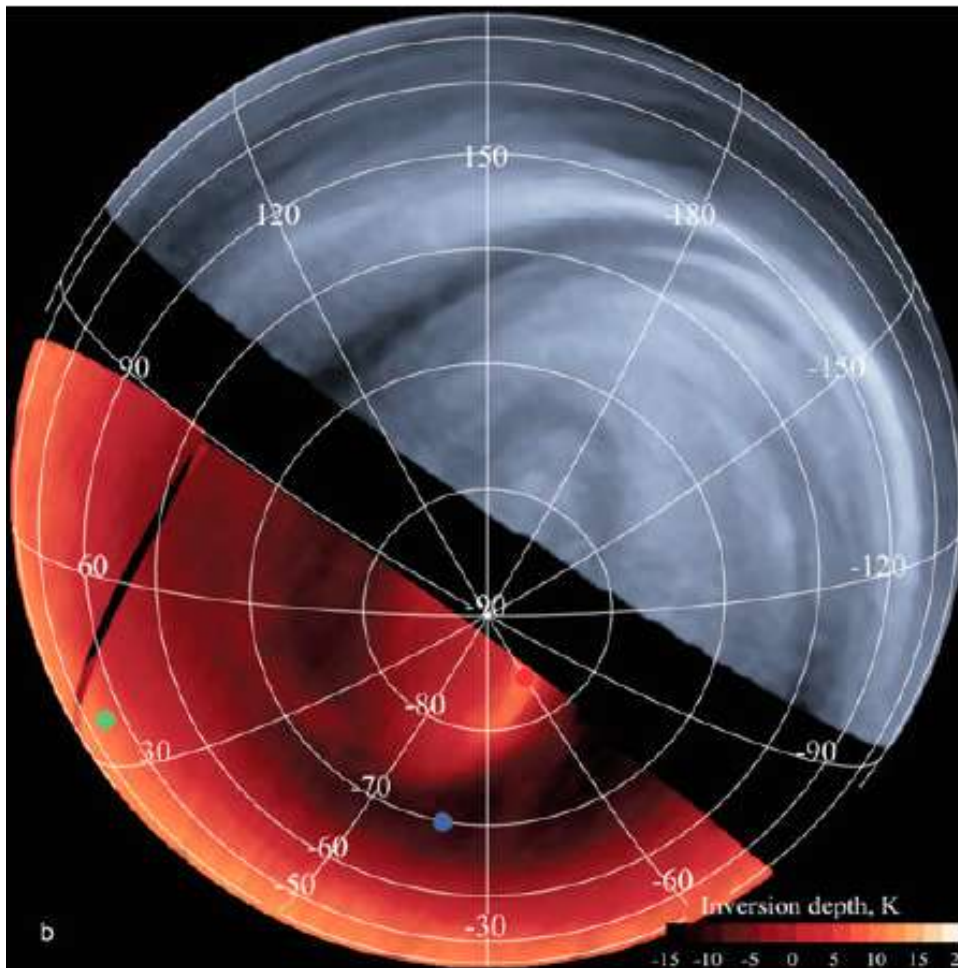


Figure 3.11: *Venus Express* dayside, with VMC, and nightside, with VIRTIS images. (image: Titov et al. (2008)).

After pericenter the priority goes to the instruments that perform radio (VeRa) and stellar/solar (SPICAV/SOIR) occultations (“limb type” observations). The detailed study of the cloud deck, its morphology and dynamics is in Markiewicz et al. (2007) and Titov et al. (2008). Regarding the atmo-

spheric dynamics field of research, a comprehensive summary is in [Drossart et al. \(2007\)](#). About surface dynamics and hypothetical present time volcanism, [Smrekar et al. \(2010\)](#) is an important reference. A description of the Venus Express' operations and science planning can be found in [Titov et al. \(2006\)](#).

Among an already long list of new discoveries based on Venus Express observations are included: the evidence of thunder storms indicated by the presence of circular polarised electromagnetic waves (*Whistler mode*), detected at Venus' nightside ionosphere by the onboard magnetometer; the observation of the atmospheric *Glory* phenomena at low angle observations ([Korablev et al., 2012](#)) by the VMC camera, this fact contributed to constrain the size and shape of the unknown UV absorber droplets, present in the atmosphere; the huge measured variability on atmospheric  $SO_2$  concentration that could indicate localised volcanic activity; the Analyzer of Space Plasmas and Energetic Atoms (Aspera) instrument measured a flux ratio of 2:1 on the escaping hydrogen than the respective flux of oxygen, pointing to a continuous loss of planetary water; lately, an ozone layer was detected (SPICAV) by occultation method, these evidence is important in order to constrain the chemistry of Venus' atmosphere ([Montmesin et al., 2011](#)), and since ozone is an astrobiological "biomarker", this discovery is important in comparative planetology and in the exoplanets research field as well.

### 3.2.3 Future scheduled missions

On the one hand, the Venus Express mission success and the general good shape of the scientific experiments payload led to several extensions of the nominal mission and VEx is still in operation today. On the other hand, the *Akatsuki* Japanese mission ([Nakamura et al., 2007](#)), launched on 20 May 2010, failed its Venus' orbit insertion for great sorrow of all the Venus' research community. However, JAXA prepared a new attempt of orbit insertion in the returning branch from the high eccentric ellipse (2015), around the Sun. This delicate manoeuvre will use only the orbiter thrusters. The *Akatsuki* planned orbit was an equatorial one, so quite complementary to the Venus Express (polar orbit). In addition, the multispectral and hyperspectral imaging experiments, are first class tools to study atmospheric minor species and small-scale cloud features.

The launch of the ESA's spacecraft *Bepi Colombo* towards Mercury is also planned for 2013, but with a Venus flyby, during the Venus close approach, in its Gravity Assisted manoeuvre, it is planned a dedicate Venus' observational programme.

After the long interval that preceded *Venus Express*, we note that there



has been a steady growth in the research interest on Venus, both, by means of space-based and ground-based observations. Among the fields with intriguing open questions, the study of atmospheric dynamics, surface and atmospheric time evolution stands out, connected with the major goals of ESA's Cosmic Vision programme, particularly with regard to the Solar System formation and evolution. Venus is a topic of high interest for the planetology in general, but with emphasis in being an Earth comparison case-study, in the context of the evolution of Earth's atmosphere and for better constraining the exoplanets' atmospheres.

## 3.3 Atmospheres of telluric planets

### 3.3.1 Genesis of the atmospheres in telluric planets

The existence of atmospheres on terrestrial planets is a consequence of their formation and evolution. The molecules that make up the atmospheric gases are present in all materials that gave rise to the solar system. The genesis of the gaseous layers around the solid globes was, most likely, a contemporary process of accretion, enduring thereafter a continuous degassing of volatiles from an intense mantle outgassing, as well, amplified by the overheating due to core differentiation processes (Bullock and Grinspoon, 2001).

It was expected that the constitution of the various terrestrial planets atmospheres were similar since they originate in the solar nebula (Cattermole, 1994). In fact, the primary atmospheres obey these criteria. But the different evolution of the various planets led to significant changes from the initial atmospheric constitutions.

The main processes by which an atmosphere gains gases are the following:

- Outgassing.
- Cometary bombardment, accretion of planetesimals and asteroidal material.
- Evaporation/sublimation of deposited materials in the planetary surface or interior.

While the five main loss processes of atmospheric gas are:

- Thermal escape.
- Condensation onto the surface or clouds.
- Chemical reactions.
- Atmospheric impacts.
- Ionized particles bombardment.

If a planet has enough mass, then it will have a "hot" inner core due both to the process of planet formation, and to the radioactive decay of unstable elements in its interior. This heating is responsible for the release of gases that may migrate from the interior to the surface, forming the planetary atmosphere (Bougher et al., 1997). However, they may not simply accumulate in the atmosphere. Given their high kinetic energy, light atoms or molecules may escape to space. It may also be that other mechanisms retain these molecules in the structure of the planet (solid or liquid phase).

### 3.3.2 Brief notions of atmospheric dynamics

A planet could maintain an atmosphere in equilibrium if its mass is high enough in order to retain the atmospheric molecular components from diverse processes that favour their escape from its gravitational pull. The main reason that leads to planetary escape is related to the temperature and the consequent kinetic energy of atmospheric atoms and molecules (Sánchez-Lavega , 2011). A planet, in order to retain a gaseous element in atomic or molecular form must:

$$\frac{GM_p}{R_p} \geq \frac{\kappa_B T}{m} \quad (3.1)$$

where  $M_p$  and  $R_p$  are, respectively, the planet's mass and radius;  $G$  is the gravitational constant,  $\kappa_B$  is the Boltzmann's constant and  $m$  is the considered atom's or molecules' mass.

On the other hand, some chemical species that have some source of atmospheric replenishment could be in an atmospheric dynamic equilibrium, even if they have a planetary high escape rate.

In the solar system, there are planetary bodies that have fully developed their atmosphere. Some of them are composed by a rocky body that, in turn, is wrapped by a gaseous layer, as is the case of Venus, Earth, Mars and Titan. Other solar system planetary corps, despite having also a fully developed atmosphere, do not have an inner rocky body. This is the case of the giant gaseous as Jupiter and Saturn or the ice giants as Uranus and Neptune. Other planetary bodies have tenuous atmospheres (exospheres), that are far from hydrostatic balance, and this group includes Mercury and Io.

The telluric planets that support a terrestrial-type atmosphere in the solar system are: Venus, Earth and Mars. Titan, the largest Saturn's satellites, also has a terrestrial type atmosphere.

In the case of a terrestrial type atmosphere, the gaseous layers are in hydrostatic balance; this state is characterized by its vertical stabilisation due to the weight of each horizontal atmospheric layer being supported by the differential pressure between its adjacent layers.

Considering that the atmospheric components are ideal gases and combining the respective equation with the one that describes hydrostatic balance, and under the assumption of an isothermal atmosphere, the pressure and the temperature would decay, as a function of altitude, exponentially. Although the real cases are not isothermal, atmospheres still present a vertical density stratification.

Under this kind of atmospheric stratification, if a parcel of air is vertically displaced, it will be positively buoyant for a downward displacement, and negatively buoyant in the opposite case. Buoyancy acts therefore as a restoring force. This restoring force in stably stratified atmospheres allows the propagation of fluid-dynamical waves, the gravity waves, where the air pressure, density, temperature and velocities fluctuate together.

Planetary atmospheres are conventionally divided into vertical layers depending on the type of temperature variation with height (see figure 3.28). At Earth, the first altitude layer where temperature decreases almost adiabatically is called the troposphere, that extends until roughly 11 km of altitude. There is a temperate inversion, due to the presence of the ozone layer that absorbs solar ultraviolet radiation, and so, along this next atmospheric layer, the stratosphere, there is a temperature increase with height. Upward from the ozone layer, the temperature resumes its falling with altitude in the mesosphere. In Earth's atmosphere, beyond the 90 km altitude the thermosphere is reached, level where the temperature raises again due to the interaction with solar high energy photons and lack of enough number of collisions between air molecules (due to low density and consequently the impossibility of treating it as a continuous fluid) in order to thermalise the high kinetic energy from particles (Andrews, 2010).

Solar photons may also be energetic enough to disrupt molecular chemical bonds. This molecular photolysis could induce photochemical reactions, dissociating atmospheric molecules, as is the case of the water's photolysis in Venus upper atmosphere.

The depart point in order to describe a gaseous layer in equilibrium with a planetary body, is the following set of "primitive" equations for a fluid on a rotating sphere (see Holton (2004) for details).

### *Primitive equations*

$$\frac{\partial \mathbf{v}}{\partial t} + (\mathbf{v} \cdot \nabla) \mathbf{v} = -\frac{1}{\rho} \nabla P + v \nabla^2 \mathbf{v} - 2\boldsymbol{\omega} \times \mathbf{v} + g, \quad \textit{momentum} \quad (3.2)$$

$$\rho C_V \frac{dT}{dt} + P \cdot \nabla \mathbf{v} = \nabla(\kappa_T \nabla T) - \nabla f_{rad} + Q, \quad \textit{energy} \quad (3.3)$$

$$\frac{d\rho}{dt} + \rho \nabla \cdot \mathbf{v} = 0, \quad \textit{continuity} \quad (3.4)$$

Where,  $\frac{d}{dt} = \frac{\delta}{\delta t} + v \cdot \nabla$ , represents the Lagrangian or material derivative (advective derivative). T is the temperature, P the pressure,  $\nabla p$  is the pressure gradient force, R is the gas constant, v is the velocity,  $\rho$  is the density,

$\omega$  is the angular rotation rate,  $C_p$  is the specific heat at constant volume,  $q$  is the heat input rate,  $g$  is the gravity constant,  $f$  is the Coriolis parameter and  $t$  is the time. With respect to equation 3.3:  $\nabla(\kappa_T \nabla T)$  represents the exchange heat by conduction,  $\nabla f_{rad}$  is the exchange heat by radiation and  $Q$  represents the heat exchange due to other internal energy sources (for details see [Sánchez-Lavega \(2011\)](#), pg. 360).

The primitive equations are complemented by the equation of state:

$$P = \rho RT, \quad \text{equation of state} \quad (3.5)$$

### Hydrostatic equilibrium and law of the gases

$$dP = -\rho g dZ, \quad \text{where,} \quad \rho = \frac{\mu P}{RT} \quad (3.6)$$

where  $R$  is the ideal gas constant and  $\mu$  is the molecular mass, and integrating we obtain the barometric law:

$$P(z) = P_0 e^{-\int \frac{dz'}{H(z)}}, \quad \text{where the scale height is:} \quad H(z) = \frac{RT(z)}{\mu g} \quad (3.7)$$

### Dynamics of planetary atmospheres

The momentum conservation for fluid motion (Newton's second law) is described by the Navier-Stokes equations. This vector equation's set takes into account three different forces applied to a fluid element: the pressure gradient force, the gravity force and frictional forces (represented by the terms on equation 3.8 right side). The following equations describe the atmospheric fluid motions due to its radiative forcing and describe the energy transport of global atmospheric dynamics.

Basic atmospheric dynamics equations:

$$\frac{d\mathbf{v}}{dt} = -\frac{1}{\rho} \nabla P + g + v \nabla^2 \mathbf{v}, \quad \text{Navier - Stokes equation in an inertial frame} \quad (3.8)$$

$$\frac{d\mathbf{v}}{dt} = -2\omega_{rot} \times \mathbf{v} - \frac{1}{\rho} \nabla P + (g + \omega_{rot}^2 r) + v \nabla^2 \mathbf{v}, \quad \text{Navier - Stokes equation(b)} \quad (3.9)$$

(b) Represents the Navier-Stokes equation that describes the motion of an air parcel in a rotating frame of reference. The term  $v \nabla^2 \mathbf{v}$  represents the

presence of frictional forces,  $-2\omega_{rot} \times \mathbf{v}$  is the Coriolis force and  $\omega_{rot}^2 r$  is the term related to the centrifugal force.

From these general dynamical equations, one can obtain simplified equations for the wind components under certain assumptions. Assuming an incompressible fluid with negligible viscosity and a centrifugal force much smaller than the Coriolis force, we obtain the following set of equation, under the geostrophic approximation in a local frame of reference:

$$\frac{du}{dt} = 2\Omega \sin \varphi \cdot v - \frac{1}{\rho} \frac{dp}{dx} \quad (3.10)$$

$$\frac{dv}{dt} = 2\Omega \sin \varphi \cdot u - \frac{1}{\rho} \frac{dp}{dy} \quad (3.11)$$

$$\frac{dp}{dz} = -\rho g \quad (3.12)$$

where  $\Omega$  is the angular velocity of the coordinate system,  $\varphi$  is the local latitude,  $z$  is the altitude,  $u$  is the zonal velocity and  $v$  the meridional velocity. See figure 3.41 for used symbols and constants consultation. Assuming that the atmosphere is in hydrostatic equilibrium and considering the overall conditions of the “shallow water” approximation (where:  $\frac{\delta P}{\delta z} \gg \frac{\delta P}{\delta x}$  or  $\frac{\delta P}{\delta y}$ ), one obtains the following simplified wind equation:

$$\frac{d\mathbf{v}}{dt} = (2\Omega \sin \varphi) \cdot \mathbf{v} \times \hat{k} - \frac{1}{\rho} \nabla P \quad (3.13)$$

where  $\hat{k}$  is an unit vector along the planetary rotation axis. The detailed derivation of the previous equations can be found in [Holton \(2004\)](#).

### Coriolis Force

The Coriolis force is the interaction resulting from planetary rotation that tends to deflect a moving air parcel to the right from its proper motion (at Earth's northern hemisphere), and to the left at Earth's southern hemisphere. The quasi-equilibrium that is established between the horizontal pressure gradient forces and the Coriolis force, leads, on Earth, to large-scale dynamical wind structures that circulate clockwise around high-pressure regions, with the wind following the isobars, and anti-clockwise around low-pressure areas, at northern hemisphere and on the opposite sense at southern hemisphere. These anti-cyclonic and cyclonic structures are prominent on planets with relatively fast rotation, fact that leads to the establishment of a planetary geostrophic balance. The Coriolis parameter is then:

$$f = 2\Omega \sin \varphi \quad (3.14)$$

### Geostrophic balance

In planetary bodies where the rotational motion is fast, as is the case of Earth and Mars, the Coriolis and the pressure gradient forces dominate in the momentum equation, and from the simplified balance between these two terms, we can derive the geostrophic wind as (see details in [Sánchez-Lavega \(2011\)](#), pg. 363):

$$\mathbf{v} = \hat{k} \times \frac{1}{\rho f} \nabla P \quad (3.15)$$

This wind blows along isobars (geostrophic approximation), so perpendicular to the pressure gradient. This kind of wind is predominant when one has low Rossby numbers ( $R_\sigma$ ) systems, much smaller than unity, meaning cases where the Coriolis effect is important.

$$R_\sigma = \frac{dv}{f v} = \frac{v}{L\Omega}, \quad \text{Rossby number} \quad (3.16)$$

where  $L$  is the horizontal scale of motion, for the detailed derivation of equation 3.21 see [Sánchez-Lavega \(2011\)](#). So if  $R_\sigma \ll 1$  one is on the framework of the geostrophic approximation. On the other hand, if  $R_\sigma \gg 1$  is valid the cyclostrophic approximation as described below.

### Cyclostrophic balance

In slowly rotating planets, the Coriolis term will be negligible in the simplified wind equation (eq. 3.13) and we obtain simplified equations for the wind components, under the same assumptions valid for equations 3.10- 3.10, but instead of neglecting the centrifugal force term, now the Coriolis term is the neglected one, then we obtain:

$$\frac{du}{dt} = \omega_{rot}^2 r - \frac{1}{\rho} \frac{dp}{dx} \quad (3.17)$$

$$\frac{dv}{dt} = \omega_{rot}^2 r - \frac{1}{\rho} \frac{dp}{dy} \quad (3.18)$$

$$\frac{dp}{dz} = -\rho g \quad (3.19)$$

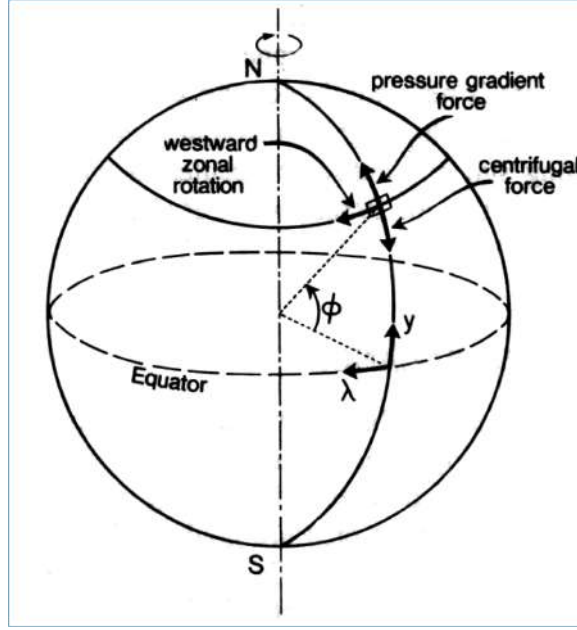


Figure 3.12: Scheme of the cyclostrophic balance, where the local horizontal component of the pressure gradient force is balanced by the horizontal component of the centrifugal force. Figure: Schubert et al. (1983).

In the case that we neglect the Coriolis term, the simplified wind equation (equivalent to eq. 3.13, but for slowly rotating planets) will assume the form:

$$\frac{d\mathbf{v}}{dt} = -\frac{1}{\rho}\nabla P, \quad \text{or :} \quad \frac{\mathbf{v}^2}{\mathbf{r}} = \frac{1}{\rho} \frac{\delta P}{\delta \mathbf{r}} \quad (3.20)$$

The detailed derivation of equations 3.20 can be found on Holton (2004). *tornadoes* and hurricanes on Earth, or in *dust devils* on Mars, the Coriolis force can be neglected as well (Piccialli et al., 2010). In all the preceding cases, the pressure gradient force will be balanced by the centrifugal force. Characteristic in slow rotating planetary bodies, the cyclostrophic balance is found at Venus and Titan. It generates a steady horizontal, and almost parallel to equator, wind flow. So, it comes for the cyclostrophic wind velocity:

$$\frac{u^2 \tan \varphi}{R_p} = -\frac{1}{\rho} \frac{\partial p}{\partial y}, \quad \text{and so :} \quad u = \pm \sqrt{-\frac{R_p}{\rho \tan \varphi} \frac{\delta P}{\delta y}} \quad (3.21)$$

where the equation on the left side is the cyclostrophic wind equation derived from the single balance between pressure gradient and the centrifugal forces, and on the right side is the zonal wind velocity expression, derived



under the assumption of cyclostrophic balance.  $R_p$  represents the planetary radius (for details see [Sánchez-Lavega \(2011\)](#) pg. 364-365).

It is possible to re-write the previous equation in order to relate the zonal wind velocity with the vertical temperature structure, under the cyclostrophic approximation as well. For that, one needs to assume the hydrostatic approximation (as seen at eq. [3.12](#)) and to introduce the geopotential definition as:  $\Phi = gz$ , where  $g$  is the gravity acceleration and  $z$  is the height.

$$\frac{\partial u^2}{\partial z} \approx -\frac{R}{\tan \varphi} \frac{\partial T}{\partial \varphi}, \quad \text{Thermal wind equation} \quad (3.22)$$

In the previous equation, is shown the approximation of the thermal wind equation for cyclostrophic balance. The detailed derivation of the previous equation can be found in [Schubert et al. \(1983\)](#).

### Radiative energy balance and radiative transfer

In order to retrieve the sub-solar effective temperature:

$$E_p(1 - A) = 4\sigma T^4 \quad (3.23)$$

where  $E_p$  is the solar constant at the considered solar system planetary body,  $T$  is the absolute effective temperature,  $A$  is the planetary albedo and  $\sigma$  is the Boltzmann constant.

To analyse the radiative transfer along a planetary atmosphere, one must consider absorption, emission and scattering processes along the radiation's path. The intensity variation for an elemental layer of thickness  $dz$  is so described by the radiative transfer's basic law:

$$dI/dz = -\alpha I + \varepsilon \quad (3.24)$$

where  $\alpha$  is the mass extinction coefficient (and result of the sum of absorption and the scattering mass coefficients) and  $\varepsilon$  is the emission at the considered atmospheric layer. Integrating  $\alpha$  vertically one obtains the optical depth for each frequency ( $\tau_\nu$ ):

$$\tau_\nu = \int_0^\infty \alpha_\nu(z)\rho(z)dz \quad (3.25)$$

Integrating equation [3.24](#) along the planetary radial direction, one derives:

$$I(z) = I_0 e^{-\int_0^z \alpha(z')dz'} + \int_0^z \varepsilon'(z') e^{-\int_{z'}^z \alpha(t)dt} dz' \quad (3.26)$$

And if we consider a purely absorbing medium, without radiation emission sources, we obtain:

$$I(z) = I_0 e^{-\int_0^z \alpha(n) dn} = I_0 e^{-\tau(z)z}, \quad \text{Beer's law} \quad (3.27)$$

Equation 3.26 reports to the radiation's intensity at a certain atmospheric parcel at the height  $z$ , general case. Equation 3.27 is an approximation that can be used in cases where local emission can be neglected. Detailed derivation of the previous equations as a deeper approach to atmospheric radiative transfer can be found in Rybicki and Lightman (2004).

### Atmosphere modelization

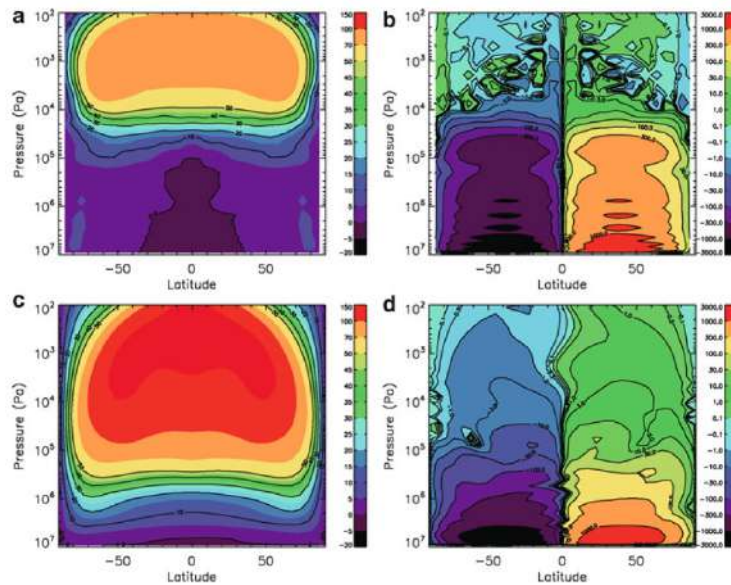


Figure 3.13: Zonal wind (left) and stream function (right) contour plots from (a,b) CCSR (Yamamoto and Takahasi, 2006) and (c,d) LMD (Lebonnois et al., 2010) Venus general circulation models. Figure: Bengtsson and Grinspoon (2013).

Due to the impossibility of carrying out large scale experiences at planetary atmospheres, this branch of planetary sciences relies deeply on atmospheric modelling. Since controlled experiences cannot be performed on planetary atmospheres, we are obliged to use atmospheric models (as the Global

Circulation models (GCM) in order to identify cause and effect phenomena, and understand coupling between processes.

The same set of basic equations to describe the telluric planets' atmospheres: conservation of the energy, continuity equation and the equations that describes the temporal evolution of momentum (Navier-Stokes equations), constitute the dynamical core of these numerical models (after applying a discretization process to the volumes of atmosphere to be modelled). Several Venus' atmosphere numerical models are based on the ones developed for Earth. To reproduce a stable super-rotating atmosphere is still an open issue and the goal of dedicated hard work.

Venus' lower atmosphere was first modelled by means of a general circulation model (GCM) developed by [Young and Pollack \(1977\)](#) and later on by [Del Genio and Zhou \(1993, 1996\)](#). The modelling attempts that conducted to [Yamamoto and Takahasi \(2007, 2009a,b\)](#) incorporated Venus nightside and a meridional circulation with one Hadley cell at each hemisphere, extending from equator to the pole, and stretching from surface till the height of 60 km.

Other studies involved the attempt of simulating the super rotation mechanism ([Gierasch, 1975](#); [Rossow, 1979](#)), atmospheric instability ([Thompson, 1970](#)) and thermal tides ([Newman and Leovy, 1992](#); [Takagi and Matsuda, 2007](#)).

Modelling research groups' recent results integrate topography constrains, and try to reproduce atmosphere-surface interactions ([Yamamoto and Takahasi, 2007](#); [Lee and Richardson, 2010](#); [Lebonnois et al., 2010](#)). The [Lebonnois et al. \(2010\)](#) model includes a thermal structure consistent with Venus' measured data, the constrains due to the diurnal cycle and atmosphere circulation coupling with topography. The super-rotation was produced primarily by the Gierasch-Rossow-Williams (GRW) mechanism, that will be discussed in the Venus atmosphere section of this thesis (section 3.4). Although, it is necessary to impose a unrealistic thermal forcing in order to produce the super-rotating zonal winds in the lower atmosphere.

## 3.4 The Venus atmosphere

### 3.4.1 Origin of Venus' atmosphere



Figure 3.14: Image of Venus obtained by the *Pioneer Venus* space probe in the ultraviolet (1979). This image shows clearly the presence of the Y-shaped pattern of clouds. (Image: NASA/JPL website).

During the formation of the solar system, planetesimals in primitive orbits swept through space, collecting dust and debris and later accreting gas. The dust were usually composed of a rocky core wrapped in ice from diverse volatiles.

During the accretion process there was a gravitational energy release, which add to the energy that comes from unstable radioactive isotopes. Due to the protoplanet rotation, which acts as a huge centrifuge, the planet suffers an internal differentiation process in layers, depending on its constituents density (Turcotte, 1995).

During the differentiation process into core, mantle and crust, volatiles sought way to the surface, remaining either in liquid form (as is the case of the oceans and superficial water on Earth), or in gaseous form (thus providing the planets' atmospheres). Another differentiation process consists of altering themselves chemically or by interaction with solar radiation, leading to the

appearance of new molecules, some of them which such low mass that easily reach escape velocity and leave the planet's gravitational sphere of influence (this is the case of water molecule in Venus atmosphere, after enduring a photolysis process and breaking up into hydrogen and oxygen (Donahue, 1997)).

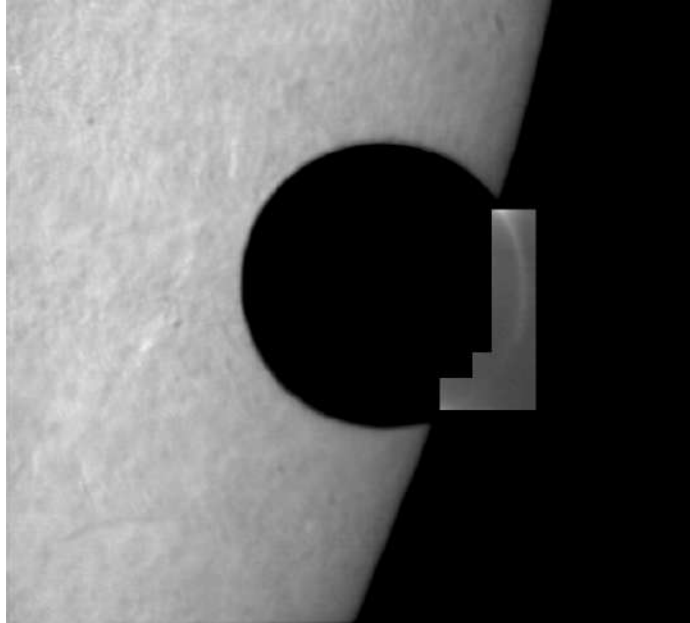


Figure 3.15: The atmosphere of Venus appears as a glowing ring (aureola) around the planetary solid disk. Image obtained during the 2004 Venus transit by the Paris Observatory, Meudon (Solar Tower). (Image: ESO *website*).

The terrestrial planets atmospheres' time evolution and equilibrium stabilising processes, depends largely in the surface-atmosphere interaction. Whether due to the ongoing chemical reactions between the lower atmosphere and surface rocks' minerals, whether due to geologic interaction processes between the mantle, the crust and the surface, with a temporal degassing variability that will have consequences in the atmospheric balance. On telluric planets, the geothermal energy is the driving force that enables the volatiles outgassing from the planet's interior to the atmosphere. So, geological processes have a direct consequence in shaping atmosphere's composition, radiative transfer's profile and the greenhouse effect (Bullock and Grinspoon, 2001).

After formation, Venus, Earth and Mars had similar atmospheres, both in primordial composition and in relative abundances of its constituents (Ip and

Fernandez, 1988). The evolutionary path that ruled each case, determined that some of them were driven to extreme situations as we know for the cases of Venus and Mars, or the Earth's case, which evolved to a state where liquid water is possible.

In the case of Venus, the fact that most of the carbon dioxide remained in the atmosphere was crucial to impose a heavy greenhouse effect (Sagan, 1972), amplified in turn by the Venus' solar constant, which is sensibly twice the terrestrial one (Kastings, 1988).

Another important factor to understand the different evolutionary path of Venus' atmosphere, from the primordial atmosphere (similar to the primordial terrestrial one), is the marked atmospheric depletion due to the solar wind and to UV solar radiation (Bougher et al., 1997).

The surface-atmosphere interactions were also a major factor for the different planetary evolution path followed by Earth and Venus. It is noteworthy the Earth's surface-atmosphere interaction of the  $CO_2$  absorption by the oceans and the Venusian profusion of volcanic sulphur into the atmosphere. Chemical reactions with the surface of Venus deposit  $SO_2$  on the ground, so to keep the dynamic atmospheric balance it is necessary to have a source of replenishment (Bullock and Grinspoon, 2001). It is here that fits the extensive volcanism evident in the Venus' surface. A closer examination of the chemical reactions that affect the Venus' atmospheric gases, shows that these constituents are in equilibrium with the rocks on the planet's surface. This means that the chemical composition of the Venus atmosphere is determined by the properties of the surface, which does not happen in Earth. The reason for this different behaviour lies in two factors: on Earth there are destabilising processes such as photosynthesis, perturbing  $CO_2$  levels, another factor relies in the very high Venus' surface temperatures that leads to fast chemical reactions between atmospheric gases and rocks, thus chemical equilibrium is reached quickly (Goody et al., 1975; Fegley et al., 1997).

### 3.4.2 The present Venus atmosphere

Venus has an atmosphere dominated by carbon dioxide. Its atmospheric dynamics are essentially driven by the solar thermal heating and its very low rotation rate, the year (224.7 Earth days) is shorter than a Venus day (243.02 Earth days) (Shapiro, 1968). As a consequence from its low rotational velocity, the Venus' atmospheric dynamics major mechanisms are quite different from Earth. Instead of a quasi-geostrophic regime that rules its global atmospheric motions, is the equilibrium from the pressure gradient force that consists in the exact equatorward component of the centripetal force (the cyclostrophic balance, that prevails at slow rotating planets) that imposes

its system of horizontal winds, parallel to equator, the *Zonal Winds*. That fact turns Venus' meteorological research even more interesting

If in the one hand Venus is a “ $CO_2$  dominated” planet, on the other hand, its atmospheric balance is fine tuned by the  $SO_2$  concentration (among other minor components) at this evolutionary stage of present atmospheric conditions (Bullock and Grinspoon, 2001).

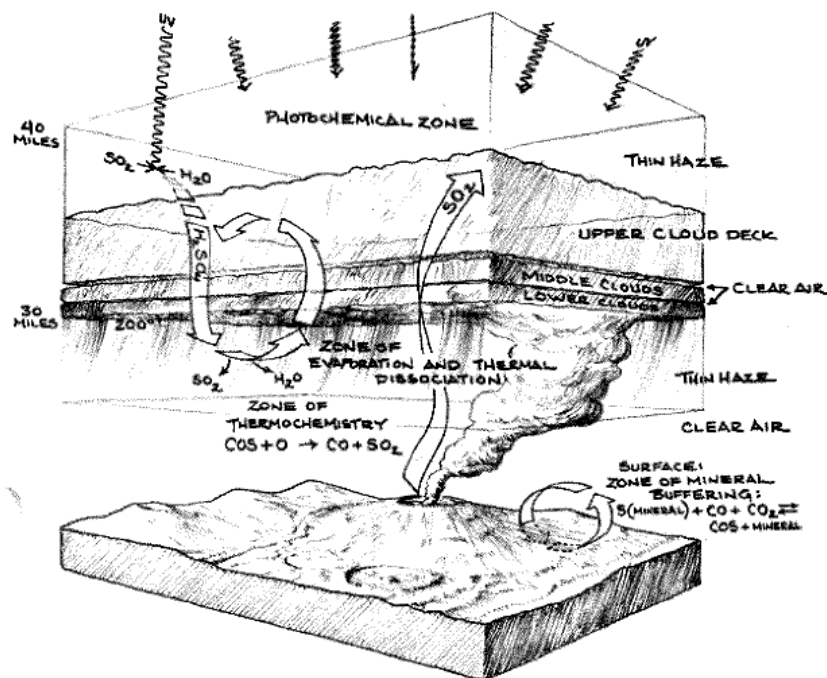


Figure 3.16: Venus atmospheric structure and interactions (Bullock, 1997). Figure credits: Carter Emmart.

The atmosphere of Venus is extremely dense (Figure 3.15) containing about 100 times more gas (92 bar) than Earth, despite the planets size similarity (Marov et al., 1973). The gas composition is predominantly carbon dioxide (0.965 molar fraction) and some nitrogen (0.035 molar fraction). Nevertheless, the minor components will have an important role in the atmospheric coupling (such as the  $SO_2$ , with only 150 ppm molar fraction). Traces of water are present (approximately 20 ppm molar fraction).

The surface pressure reaches 92 bar. The atmospheric pressure on the surface of Venus can be equated to the pressure on a body immersed in an Earth's ocean at about 1,000 meters deep. The total mass of the atmosphere

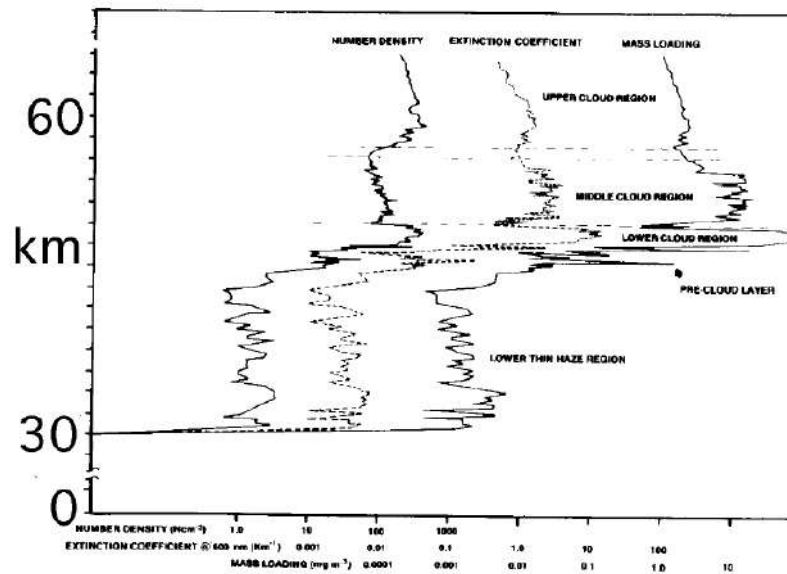


Figure 3.17: Cloud formation distribution as a function of altitude, density, number of particles and extinction coefficient, (Knollenberg and Hunten, 1980).

on Venus represents approximately 93 times the mass of Earth's atmosphere.

The surface temperature is around  $735^{\circ}K$ , far above the calculated sub-solar temperature (about 3 times), as a result of a powerful greenhouse effect, which we will study later. The surface is hidden by a thick hazy cloud cover that results from the chemical interaction between sulphur dioxide and some water vapour that generates droplets of sulphuric acid (clouds which are highly reflective).

While on Earth the total surface coverage by clouds is only, on average, forty percent, on Venus, it reaches 100%. As such the probe Pioneer Venus, that was in Venus orbit for 14 years, did not even get a glimpse of the surface, limited to a disappointing continuous observation of the cloud top layer.

The cloud layer that covers the planet consists of sulphuric acid droplets (in 85% water solution) and some other aerosols of an as yet unknown composition. The rapid retrograde motion of the cloud top cover is visible, through the time evolution of different patterns. The images obtained by the Pioneer Venus probe revealed ultraviolet dark markings in the clouds, which would be an indicator of its movement, in reality a mad rush through the skies of Venus, completing one revolution in about four Earth days (4.4 days). This super-rotation motion of the Venus' atmosphere is not yet well explained



(Bougher et al., 1997).

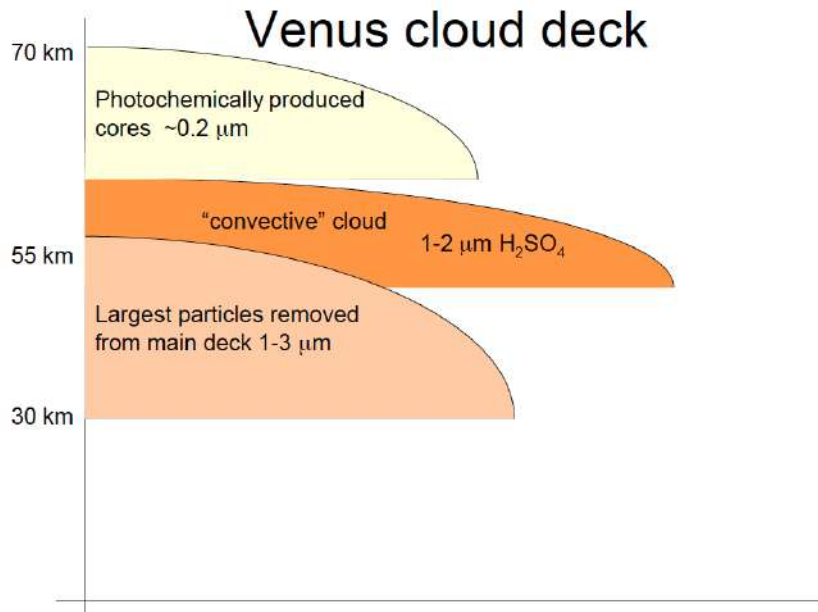
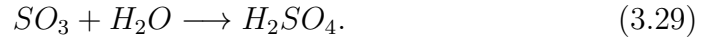
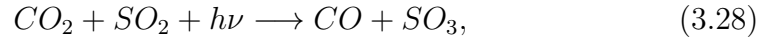


Figure 3.18: Venus' sulphuric acid cloud deck and hazes extension in altitude. Regarding the averaged aerosol particles size, the cloud deck can be divided in the three layers shown in this scheme. Figure: Titov, D., private communication.

The cloud layer extends in the atmosphere from 48 km to 70 km (about 22 km thick), with tenuous hazes above (reaching 90 km) and below the main cloud deck (from roughly 30 km) (Esposito et al., 1983). The clouds are not homogenous regarding the average size of their aerosol particles (see figure 3.18). The cloud deck (see figure 3.17), can be divided into an upper layer (57-68 km) with an averaged radius of  $0.3 \mu\text{m}$ , and a total optical depth at  $0.63 \mu\text{m}$  of 7; the middle cloud region stretches from 51 till 56 km of altitude, with a predominance of  $1-1.4 \mu\text{m}$  particle sizes, with an optical depth, at same wavelength, of about 9; finally, the lower cloud extends from the cloud base at 48 km till 50 km, optical depth of nearly 10, due essentially to  $3.65 \mu\text{m}$  size particles (Knollenberg and Hunten, 1980).

Polarimetric and spectroscopic observations point to a general composition ratio of one quarter of  $H_2O$  and three quarters of  $H_2SO_4$  in the cloud particles. The atmospheric formation of sulphuric acid, near the cloud tops, comes from a photolysis and recombination processes of  $H_2O$  and  $SO_2$  that reacts with the  $CO_2$  following the reaction chain:



Despite the cloud top deck being almost featureless in the visible range, images in the ultraviolet, revealed prominent cloud markings at atmospheric pressure levels of 40-50 mbar, where the UV optical depth reaches unity and that corresponds to altitudes of 65-70 km (Esposito et al., 1983). The UV marks are mainly produced by an unidentified UV absorber, but spectroscopic observations indicated that these dark markings were also partially due to sulphur dioxide. Cloud top morphology and dynamics, could be studied by the observation of the albedo variations due to fluctuations in the local (spatial and vertical) concentration in the UV absorbers and contrast variation due to the optical thickness cloud's variability.



Figure 3.19: South pole vortex and comparison with a terrestrial hurricane. Figure: Limaye et al. (2009).

The majority of the UV absorber is situated nearly at the top tops (Pollock et al., 1980). On the other hand, Ignatiev (2009) located the cloud top at visible range, at roughly 70 km (see figure 3.20). This coincidence will

allow us, along this work, to compare winds measured by the cloud tracking method in the UV and the Doppler winds obtained from the shift of solar Fraunhofer lines (visible).

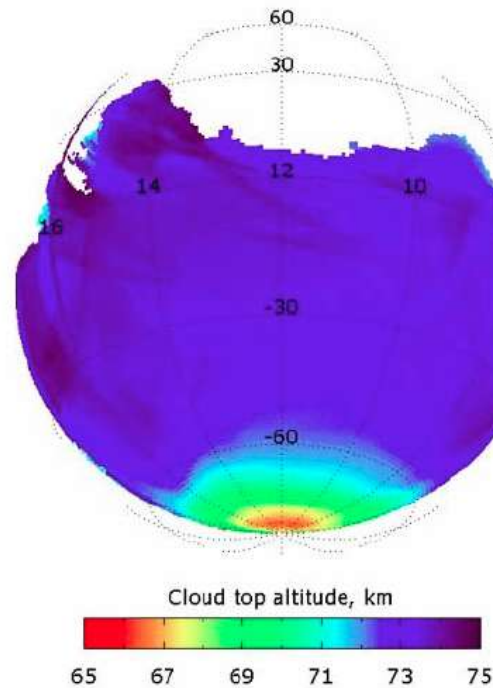


Figure 3.20: Altitude of Venus cloud tops distribution over the planet. (figure: Ignatiev (2009)).

Detailed observations of cloud structures, either at large or small scale, through the Venus Monitoring Camera (VMC) and VIRTIS instrument, onboard Venus Express, showed that the south polar region is extremely variable and can change dramatically, even at the time scale of a day. The dynamics cloud features morphology of clouds varies with latitude, moreover the nebulae formations show large temporal changes.

The cloud fuzzy systems of high latitudes exhibit some similarities with hurricanes on Earth (figure 3.19). The huge vortex at polar region surpasses in size the terrestrial major hurricanes by a factor of four. In low latitudes, near the sub solar point, the cloud pattern is mottled indicating vigorous convection and turbulence generating patterns of small cells. However, in medium latitudes ( $< 50^\circ$ ) this pattern changes into bands of nearly zonal flow (retrograde zonal wind almost constant with latitude) (Markiewicz et al.,

2007). From this transition latitude, that may be the poleward branch of the Hadley cell of the meridional circulation (Titov et al., 2008; Tsang et al., 2008), the zonal wind fades away, decreasing in velocity towards the pole. In the transition zone close to  $50^\circ$ , it is possible to observe the midlatitude jet where the wind could increase till  $20 \text{ m s}^{-1}$ , although it is highly variable, not always seen.

The variations shown by the cloud layers are due not only to the global motions of the atmosphere, but are also a consequence of wave activity in the atmospheric layers.

The process of increasing diffusion of sulphuric acid particles, and also sedimentation and mixing by eddies, have, at cloud deck altitudes, time scales of a few months, so these processes should not be very relevant to its dynamics. Moreover, the process of homogeneous nucleation can lead to the appearance of numerous particles at sub-micrometer range ( $r \approx 1 \mu\text{m}$ ) driving rapidly the system to high levels, of this size particles' concentration, supersaturation. In the case of the upper atmosphere of Venus, this implies either a fast cooling of the atmospheric layer, or a large  $\text{SO}_2$  particle injection in the respective layer (Piccialli et al., 2010).

The clouds on Venus have a determining influence on the planet's albedo, thermal structure and atmospheric energy balance. The solar radiative flux that reaches the surface, after being diffused across the dense atmosphere and thick clouds is of the order of  $17 \text{ W/m}^2$  (Tomasko et al., 1980). In spite of this low value, the massive greenhouse warming, raises the surface temperature to 735 K.

The increasing transparency of the atmosphere with altitude in the cloud upper layer is a consequence of the coagulation of the particles, which leads to lower number density and consequent increase of the layer transparency (Svedhem et al., 2007). Cloud hazes of  $\text{H}_2\text{SO}_4$  extend in the atmosphere higher than 90 km, showing high variability (Wilquet et al., 2012). Cloud chemistry, mainly of the  $\text{SO}_2$ , can be found in detail in (Zhang et al., 2010).

For a long time, the existence of lightnings in the atmosphere of Venus was controversial. It was confirmed in 2007 by the Venus Express magnetometer. Electrical discharges are relevant because they provide a huge high altitude input of energy that powers atmospheric chemistry.

An intriguing VEx discovery was the presence of an atmospheric circumpolar cold zone, the *cold collar* (Piccioni et al. 2007). It remains to establish a relationship between the superrotation of the atmosphere and this phenomena, and this question is still a major theme in current scientific research.

Venus Express' recent observations provided images of atmospheric *glories*, atmospheric phenomena that occur when the solar illumination comes from behind the observer, in a low angle. This evidence contributes to con-

strain the size and shape of the cloud particles. In the one hand, they might be spherical in order to be consistent with the occurrence of a *glory* (Korablev et al., 2012); on the other hand it also constrains the size of the particles because the type of scattering (Rayleigh or Mie) depends on particle diameters, and to be compatible with atmospheric *glories* formation (which implies Rayleigh scattering) it constrains the particles sizes with an upper limit.

An intriguing peculiarity of Venus' atmosphere is its odd nightside thermosphere temperature profile, radically distinct from Earth, where temperatures are much lower than predicted. This is still an open question in our knowledge about its atmospheric dynamics, this thermosphere region was baptised as "cryosphere".

### Venus' atmosphere present composition

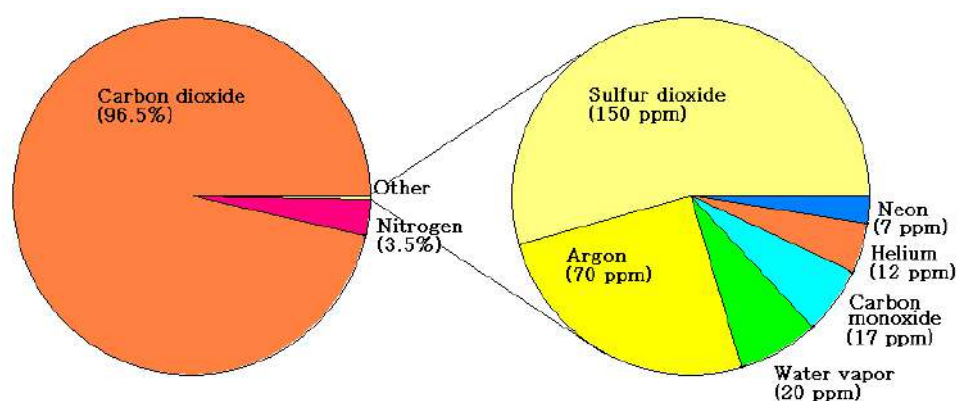


Figure 3.21: Venus atmosphere relative composition. Minor species relative abundances are given in the magnified portion of the graphic at the right side. (figure: NASA *website*).

Although initially the atmospheres of Venus and Earth had, approximately, the same amount of carbon dioxide, on Earth most of it has been buried in the crust in the form of carbonates such as limestone and other carbonated rocks, or dissolved in the oceans water. On Venus, most of the carbon dioxide is still present in the atmosphere (figure 3.21), contributing to a massive greenhouse effect, which makes it an extreme case study of the possible consequences of climate change on Earth, given the present day problems of anthropogenic excess emission of greenhouse gases.

One of the minor components of extreme importance in the atmosphere/surface coupling (as already mentioned) is the sulphur dioxide ( $SO_2$ ). It

is also worth noting the source of another minor component, the carbon monoxide (CO), in the upper atmosphere due to the photolysis of  $CO_2$ . These molecules tend to sink in the clouds toward the surface, over a timescale of weeks. It was also found evidence of the existence of  $H_2O$  in the upper atmosphere, but only at trace level (Beatty et al., 1999).

Volcanism is the dominant source in the terrestrial  $CO_2$  cycle. Due to the loss of Venus' atmospheric  $CO_2$  by photolysis in the upper atmosphere,  $H_2O$  also by photolysis and  $SO_2$  in the reactive process of sulphuric acid formation, it is necessary to have some source for these molecules. Volcanism is the elected candidate for the replenishment process and for their temporal abundance variability as well. During the episodic large-scale volcanism, the atmosphere is injected with large amounts of these molecules. However, later spectroscopic measurements (Esposito, 1984), show a substantial decrease in the atmospheric  $SO_2$  concentration, relatively to the previous, 1978, *Pioneer Venus* values. Recently, an important atmospheric input of sulphur dioxide was detected in a well localised region (Encrenaz et al., 2012), fact that is eventually connected with a recent volcanic eruption.

Another relevant process for atmospheric composition is the direct input of volatiles from the crust surface minerals into the atmosphere. This kind of heterogeneous reactions are favoured by the high surface pressure and temperature.

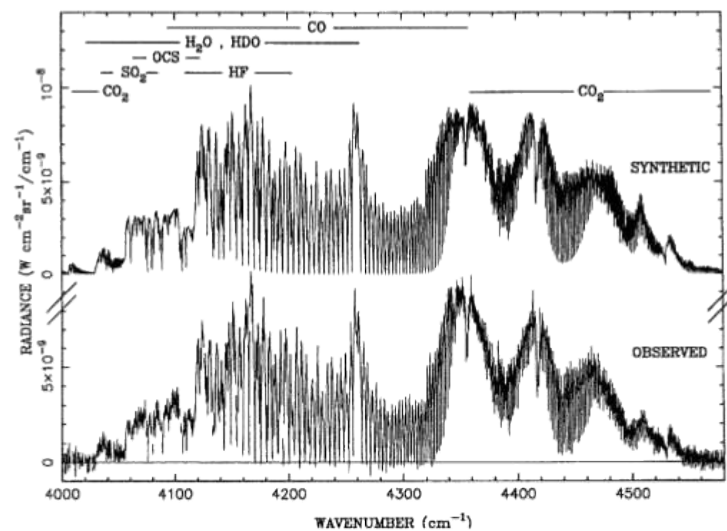


Figure 3.22: Summary of atmospheric species spectral contribution from ground-based observations. Figure: Bézard and de Bergh (2007).

The  $H_2O$  and  $SO_3$  (product of  $SO_2$  previous oxidation) reaction, pro-

duces  $H_2SO_4$  (and CO as a by-product) at 62-68 km of altitude (approximately 160 mbars). These aerosols sediment and coagulate in four major size classes of droplets, at lower atmospheric levels (Krasnopolsky and Parshev, 1983; Yung and DeMore, 1982). The aerosol particles, that at cloud level are at quasi equilibrium with  $H_2O$  and  $H_2SO_4$  vapours, undergo downward diffusion until being thermally decomposed as temperature reaches 432 K. Near surface  $SO_2$  abundance is much higher than the prediction based in the surface/atmosphere balance (Fegley and Treiman, 1992) indicating the existence of active sources of this constituent (the near surface molar mixing ratio is 180 ppm and at cloud tops is around 20 ppm (Esposito, 1984)). The results for the lower atmosphere concentration of  $SO_2$  were consistent with ground-based observations by Bézard et al. (1993); Pollack et al. (1993) and from the Vega balloons (Bertaux et al., 1996). Atmospheric abundances listed above were obtained from the Venus International Reference Atmosphere (VIRA) (Kliore et al., 1986).

Figure 3.23 shows a comprehensive scheme of the Venusian  $SO_2$  cycle. OCS is also a relevant atmospheric sulphur gas with a molar mixing ratio in the order of one third of the one from the sulphur dioxide. Hydrogen sulphide ( $H_2S$ ) is also present as a trace compound, existing at a few ppm in the atmosphere.

Ground-based observations made a remarkable contribution in identifying deep atmospheric trace species. This is the case of nightside observations in the near-infrared transparency windows. For the study of the tropospheric composition, regarding the CO,  $CO_2$ , OCS,  $H_2O$ , HDO, HCl and HF, the following studies are relevant: Bézard et al. (1990); de Bergh et al. (1991, 1995); Pollack et al. (1993), CO and OCS Marcq et al. (2005, 2006).

For mesosphere composition analyses, some highlighted results are: for HDO, OCS and  $SO_2$ : Krasnopolsky (2008, 2010); Matsui et al. (2012); HDO, CO, SO,  $SO_2$ , Sandor and Clancy (2010, 2012); Clancy et al. (2012).

Space-based (Vex) contributions for tropospheric composition research count also some notorious studies: for the CO, OCS,  $H_2O$  and  $SO_2$ , Marcq et al. (2005) (VIRTIS-H);  $H_2O$ , Bézard et al. (2009) (VIRTIS-M), Bézard et al. (2011) (SPICAV/IR) and Cottini et al. (2012).

And for mesosphere: CO atmospheric composition by Irwin (2008) (VIRTIS M and H);  $H_2O$  by Cottini et al. (2012) (VIRTIS-H);  $H_2O$ , HDO and  $SO_2$  Fedorova et al. (2008); Belyaev et al. (2008, 2012) (SPICAV/IR and UV (occultation mode));  $SO_2$  composition and variability by Marcq et al. (2013); mapping CO by Tsang et al. (2008); Irwin (2008); Encrenaz et al. (2012) (VIRTIS-M).

Abundances of some important Venus' atmospheric compounds, from the referred works, are shown in table 3.1. More recently, an ozone ( $O_3$ ) layer

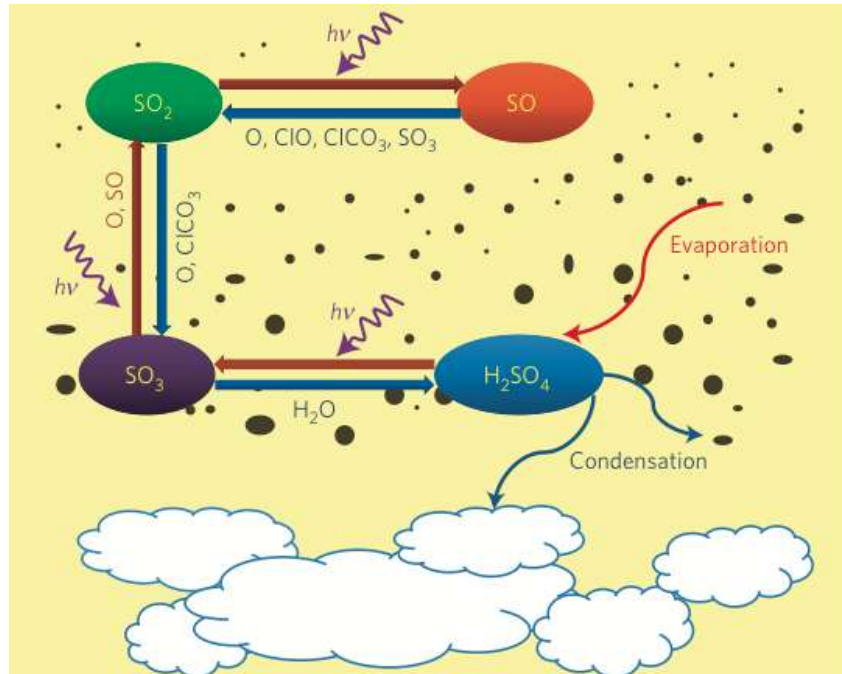


Figure 3.23:  $SO_2$  cycle and radiative interactions. Figure: Zhang et al. (2010).

	Troposphere (ppm)	Mesosphere (ppm)
$H_2O$	30	1-3
$SO_2$	150	10-1000
OCS	10	10
$H_2S$	1	1
CO	10	10

Table 3.1: Summary of Venus atmosphere minor constituents abundances. See also figure 3.24.



by Montmesin et al. (2011) was detected, based on SPICAV occultations measurements.

The study of the noble gases is highly valuable in order to constrain the planetary evolution and its outgassing history, improving thereby the constraining the volatiles origin and their possible escape to space (Zahnle, 1993).

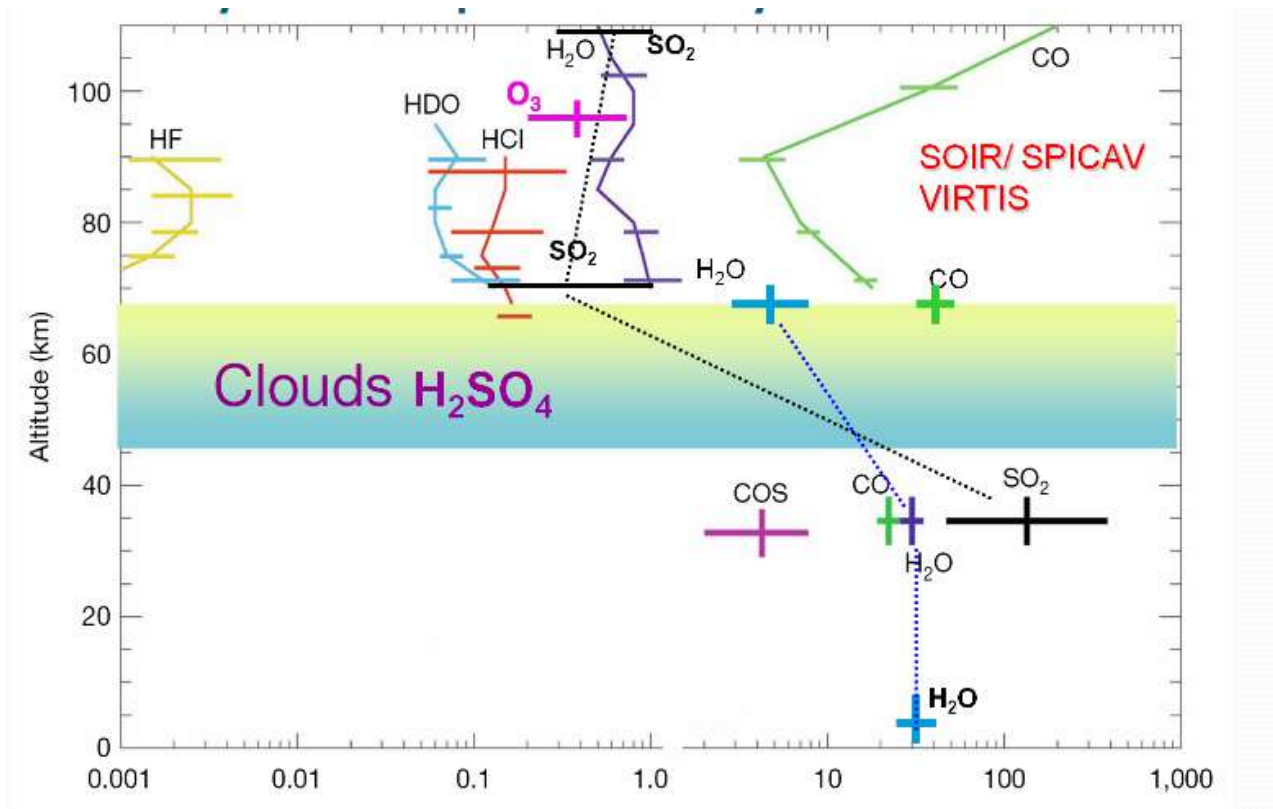


Figure 3.24: Measurements of Venus' atmosphere minor compounds composition and altitude's detection, from Venus Express mission, (image credits: ESA's Venus Express mission).

### Venus atmosphere's loss of water

The absence of an internal magnetic field and of a relevant magnetosphere, leads to a direct interaction of the solar wind with the upper atmosphere. This affects the distribution of plasma particles and atoms in the excited state, making it radically different from the Earth's.

Although, the evidence of a weak magnetic field around the planet, suggested the hypothesis of a magnetosphere generated, not by a dynamo effect,

as on Earth, but rather by the interaction of solar wind with the charged particles of the ionosphere (Goody et al., 1975). That is, an induced magnetic field. Venus' magnetosphere is weaker than Earth's and closer to the planet (figure 3.25).

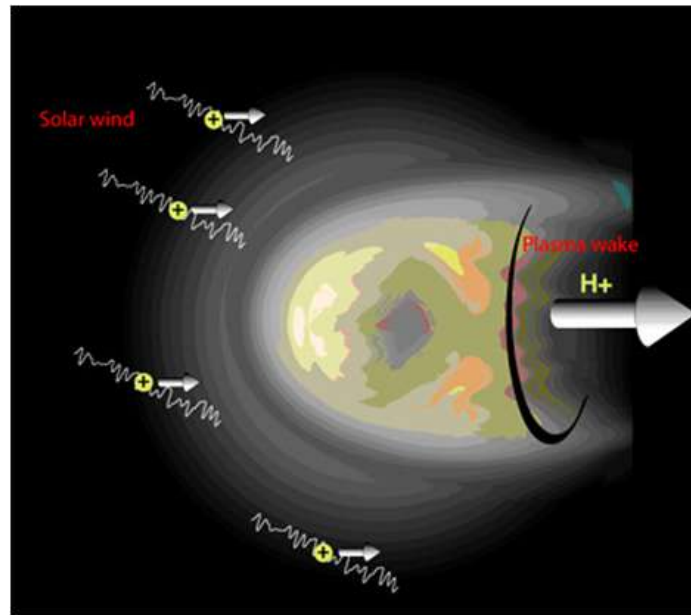


Figure 3.25: Genesis of the Venus local magnetosphere by molecule ionization in the upper atmosphere. We note the loss of  $H^+$  in the night hemisphere, i.e. in the region without magnetosphere. (Image: ESA website).

The lack of water on Venus raised quite a stir, since it is an abundant molecule in the solar system and in the universe. The probes that descended in the atmosphere of Venus only found trace amounts of water. The decline of Venus' water reservoir due to exospheric escape of hydrogen (Donahue and Hodges, 1992), suggests that Venus lost more than 99% of the water it had 800 million years ago (Bullock, 1997). However, during this lapse of time, interactions between atmosphere and surface might have exchanged large quantity of volatiles (and among them,  $H_2O$ ).

If, as suspected, Venus and Earth departed from nearly the same composition, the present Venus' water abundance is of the order of ten parts in a million relatively to the terrestrial content of water.

Previous readings indicated an isotopic ratio D/H of 0.025 (between Deuterium and atomic Hydrogen) about 150 times the one in the lower terrestrial atmosphere (de Bergh et al. (1991); Donahue (1997), see table 3.2). The Pioneer Venus neutral mass spectrometer measured, in situ, an intriguing Deu-

$H_2O$ (ppm)	$D/H_{Venus}$ ( $D/H_{Earth}$ )	Source
1.16	240	Fedorova et al. (2008)
$3 \pm 1$		Cottini et al. (2012)
1.2-2.9	200	Krasnopolsky (2010)
3.4	200	Matsui et al. (2012)

Table 3.2: Compared results for Venus’ atmospheric water composition and observed Deuterium/Hydrogen ratio.

terium to Hydrogen ratio (D/H) more than one hundred times higher than the observed on Earth (Donahue, 1982). This is consistent with a continuing loss of hydrogen (presumably largely stemming from water molecules), since the exospheric escape of the lighter isotope is predominant over the Deuterium (Donahue and Hodges, 1992; Kastings, 1988). After the  $H^+$  ion escape, from the atmosphere, comes  $O^+$  as the second more abundant escaping ion. The loss ratio between these two ions is 2 to 1, therefore sustaining the hypothesis that both ions stem from the break by photo-dissociation of the water molecule, in the upper atmosphere.

The overall abundances of carbon and nitrogen are similar to the Earth’s, which is consistent with most models that point for primordial atmospheric reservoir of the same kind of composition and relative mixing ratios. Under this assumption, water might have had about the same abundance in both planets and presumably diminished overtime due to the exospheric escape, what is subtended by the measured D/H ratio signature. However, there is some controversy about this theory since geological water sources were found, that will shuffle the predictions about primordial water abundance (Donahue, 1997). So, it is essential to calculate the water reservoirs based in the water supplying models from impact bombardments and early-planet outgassing process (Ip and Fernandez, 1988). Also, the hydrogen loss could be due to various thermal and non thermal escape mechanisms, as the Jeans escape, collisional ejection and nightside electric field driven flow (Donahue (1997), see figure 3.26).

The water abundance is deeply connected with the temperature profile, for its role in the chemistry of cloud formation and its associated albedo variation consequence and for the early water-based runaway greenhouse effect (Kastings, 1988). Another dramatic consequence of the Venus’ lack of water is that the drying process of geologic layers might have contributed for a viscosity increase of the mantle, so contributing to the observed standstill

situation with no evidence of plate tectonics (Grinspoon and Bullock, 2007). So in the end, the scarce Venus water supply could be a major responsible for the planetary surface shape.

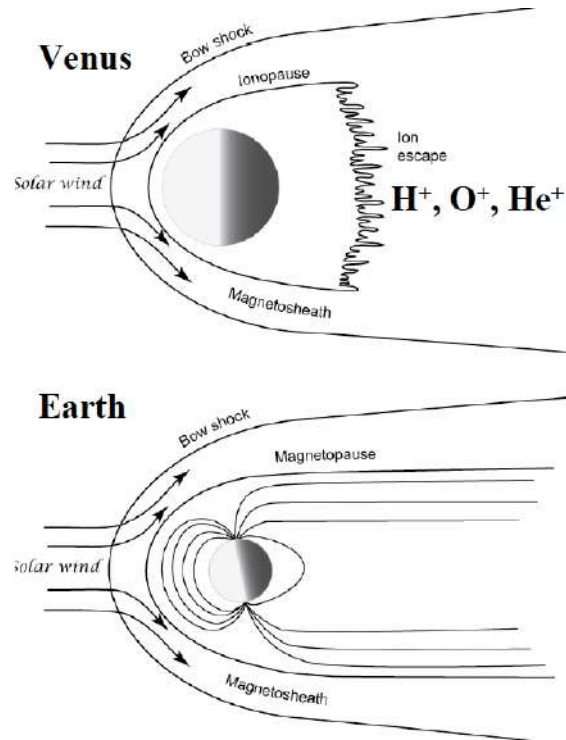


Figure 3.26: Bowshock of the interaction between the plasma particles of solar wind and the induced Venus' magnetosphere. (image: Titov, D., in "Planetary Atmospheres").

### ***Runaway greenhouse effect***

Despite the fact that the Venus solar constant is nearly the double of the terrestrial one (the effective temperature is 232 K), due to the highly reflective cloud layer which completely veil the planet, leading to an extremely high albedo of roughly 75% (2.5 times the terrestrial albedo), Venus absorbs less sunlight than the Earth (less than 10% of the incoming solar flux actually penetrate the cloud layer and the dense atmosphere till reaching the surface). Nevertheless Venus has the hottest planetary surface in the solar system, as a direct consequence of a strong greenhouse effect (Sagan, 1960; Pollack et al., 1980). The surface temperature is  $\sim 500$  K higher than the 240 K observed at cloud tops (figure 3.27).

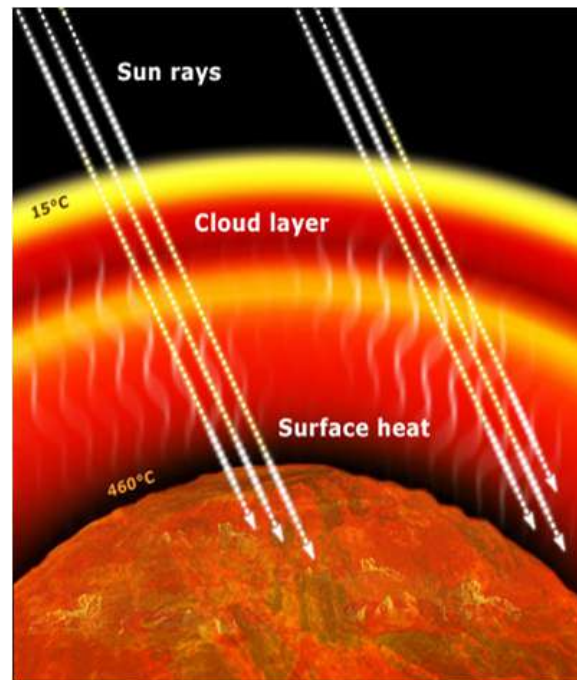


Figure 3.27: Runaway Greenhouse Effect at Venus. (Image: ESA *website*).

In a first phase of Venus' history, the atmospheric water vapour was responsible for generating an intense greenhouse effect. Then, the water molecule underwent a cleaving process at the upper atmosphere, with its oxygen being captured in the composition of sulphur compounds. The hydrogen reached escape velocity and freed up from the planet. After the massive loss of water, the greenhouse effect due to atmospheric water vapour decreased, and was supplanted by the one caused by carbon dioxide (Kastings, 1988). However, these two greenhouse gases absorb the infrared radiation at different, and complementary, wavelength ranges of the thermal spectrum (Sagan, 1960), so, if they coexisted during the planetary evolution history of Venus they could together produce a vigorous greenhouse warming that heated the Venus surface till the 735 K, observed today.

At the time of a runaway greenhouse effect led by the water vapour, the atmospheric water might have essentially existed at a tenuous stratosphere (Ingersoll, 1969), where the solar ultraviolet photons could provoke its photolysis and subsequent exospheric escape of hydrogen ions. In a positive feedback, all hypothetical surface water would have evaporated over time. Ingersoll also stated that when the solar flux surpasses a certain critical value, the condensed phase will rapidly evaporate because the equilibrium between phases will be disrupted. Thereby, an hypothetically primordial

ocean or surface water at Venus would be dried up in a short time-scale.

The average temperature of Venus (735°K), is much higher (about three times) than the actual effective temperature, because of this overwhelming phenomenon, see figure 3.27. By Wien's displacement law ( $\lambda_{max}T = 2.898 \times 10^{-3}mK$ ), the maximum of the wavelength radiation's emitted (in the approximation of blackbody radiation), is in the infrared range. Neither carbon dioxide ( $CO_2$ ) nor water molecule ( $H_2O$ ) show relevant transparency windows at this band of wavelengths.

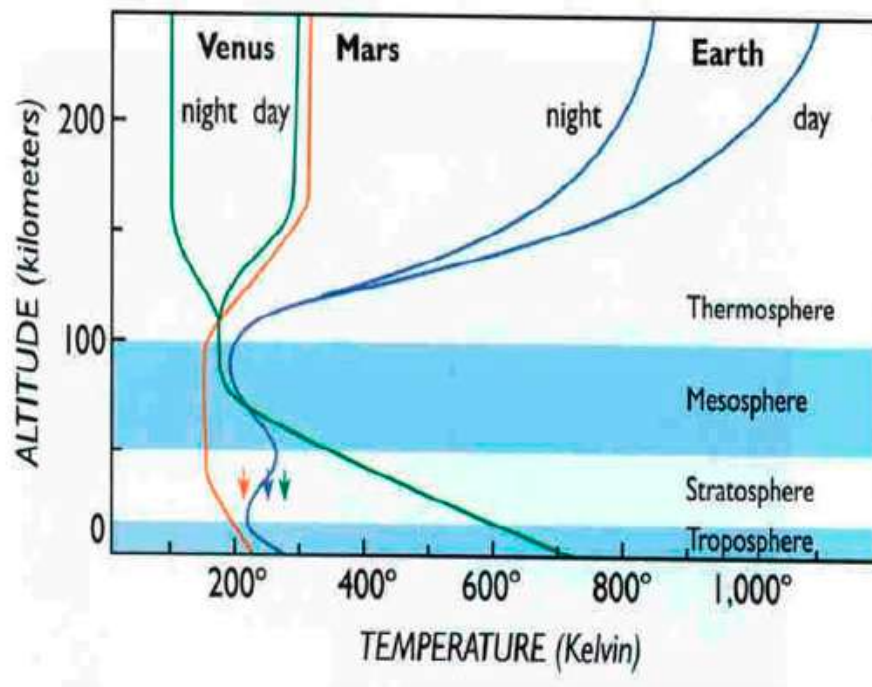


Figure 3.28: Venus atmosphere temperature profile. (image from B. Jakovsky).

An observational evidence of the existence of an overwhelming greenhouse effect, comes from the observation of night hemisphere of the planet in the infrared band. The hot surface and low atmosphere, emit strongly at 1.74 and 2.3  $\mu m$ , which shine in the nightside planetary images in areas where the sulphuric acid clouds are thinner (Piccioni et al., 2007).

### Vertical thermal structure of the atmosphere

In an atmosphere in equilibrium, the weight at each atmospheric layer will be balanced by the air pressure, which results in the *hydrostatic equilibrium* equation ( $\frac{\partial p}{\partial z} = -\rho \times g$ ). This equilibrium leads to a vertical stratification of the atmosphere, where the pressure and the density decreases exponentially with height ( $p = p_o \times e^{-z/H}$ ,  $H$  is the scale height, see table 3.41).

The variation of temperature with altitude divides Venus' atmosphere into three distinct layers: the *troposphere* (0-65 km), which extends to the top of the cloud and where the temperature decreases with altitude with the thermal gradient ratio of about  $9K \cdot km^{-1}$  (close to the adiabatic lapse rate:  $\Gamma_d = \frac{g}{C_p} = 7.39K \cdot km^{-1}$ , which shows that convection is not significant at this atmosphere region), the *mesosphere* (65-110 km) that is characterized by a less pronounced vertical thermal gradient ( $\Gamma = \frac{\partial T}{\partial z}$ ) (Ahrens, 2003), being noteworthy the relevant horizontal variability with latitude, increasing from the equator to the poles, which is consistent with the existence of a Hadley circulation cell (Taylor et al., 1980); Finally, the *thermosphere* (110-200 km) where the balance between the incident UV radiation and the thermal conductivity of the present molecules prevails. Here, there is an asymmetry between the day and night hemispheres, as the daytime temperature tends to increase with altitude between 100 and 140 km, while at night it tends to decrease along the same altitudes range, higher than 140 km the temperatures, at both hemispheres, remain stable, see figure 3.28.

Lower troposphere ( $< 30$  km) temperatures were firstly measured by the Venera and Vega descent probes (Seiff et al., 1985), providing the altitude temperature gradient already cited of  $\approx 9^\circ K \cdot km^{-1}$  and the high surface temperatures (735 K) as well. It was possible to probe the atmosphere thermal structure and composition below the cloud deck at the nightside, studying the nightside near infrared radiation. This radiation could pass through the cloud layer by the transparency windows found by Allen and Crawford (1984) in the near infrared. This new tool of analysis allowed probing the clouds at different depths and to study the variability of the clouds opacity. The mesosphere was sounded by the orbiters Venera and Pioneer Venus (Taylor et al., 1980; Zasova et al., 1999).

Most of the unidentified UV absorber abundance is at the cloud layer and it is the responsible for about half of the total absorbed energy from solar irradiation. Allied to this fact, due to the scattering, the radiation has longer paths which increase the efficiency of solar absorption. So the cloud medium, that extends from 40 mbar (cloud top) till 1bar (cloud base), see figure 3.29, absorbs roughly 92% of the incident solar flux (that it is not reflected back to space, due to the high reflective albedo ( $\sim 2.5$  the terrestrial one)) and

just the remaining 8% will reach the surface (totally different from Earth's case). By the above, it is clear that the cloud layer (and the UV absorber) is of major importance for the atmospheric energy balance.

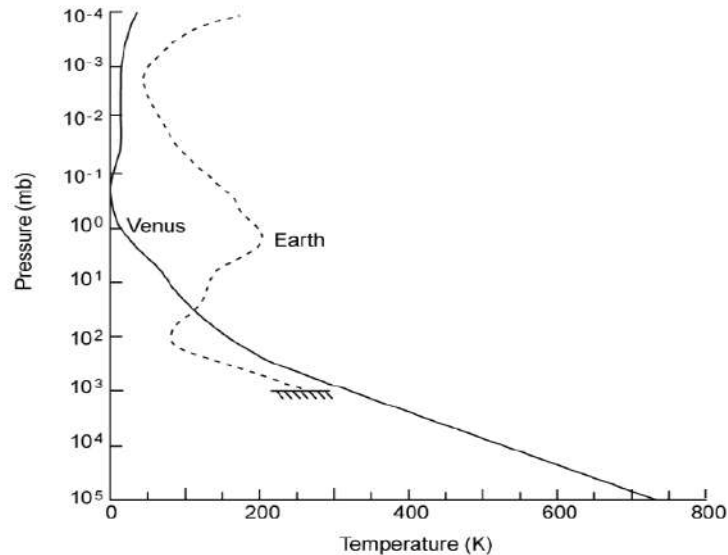


Figure 3.29: Temperature versus atmospheric pressure at Venus and Earth. Figure: (Taylor and Grinspoon, 2009)

The mesosphere shows some unexpected features, such as the latitudinal increase of temperatures from equator to poles (“warm polar” mesosphere), above 70 km of altitude. This is odd, since solar heating is higher at low latitudes than at polar region. This peculiar temperature behaviour might be due to atmospheric dynamics, and a possible cause would be a Hadley cell poleward branch that transports to high latitudes the equatorial excess of solar heating. Another curious temperature variation effect lies in the so called “cold collar”, at the heights of about 65 km, characterized by a temperature decrease from equator till approximately 65° latitude, of around 25 K (Taylor et al., 1983; Piccioni et al., 2007). characterize As a consequence of the high carbon dioxide abundance in the atmosphere which is quite efficient radiating thermal energy, in the thermosphere, above 140 km, temperature’s profile remains nearly constant ( $\sim 300$  K). From terminator, temperature sharply decreases to a low 100 K and this is why this nightside altitude region is denominated “cryosphere” (Zasova et al., 2007).

A radiative transfer model utilising data from Venera 11 and Pioneer Venus missions of cloud structure, composition, temperature measurements, was developed by Pollack et al. (1980). This model introduced, as well, the



$SO_2$ , CO and HCl as sources of infrared opacity, as well as water vapour and carbon dioxide. With these improvements, with respect to previous attempts, it was possible to accurately reproduce the observed high surface temperatures.

Regarding the stability of the atmosphere, early temperature and pressure measurements made by Venera mission and Pioneer Venus, pointed towards a highly stable atmosphere with a vertical temperature gradient of the order of 7.7 K/km, lower than the adiabatic rate (Avduevsky et al., 1970). However, more recent analyses found instability regions (at 20-30 km and 25-33 km) that might be associated with convection and turbulence (Seiff, 1983). Above the cloud deck the atmosphere stability is even higher with a  $\frac{dT}{dZ} < 3-4$  K/km (see figure 3.30), where a radiative near-equilibrium situation is expected (Seiff, 1983).

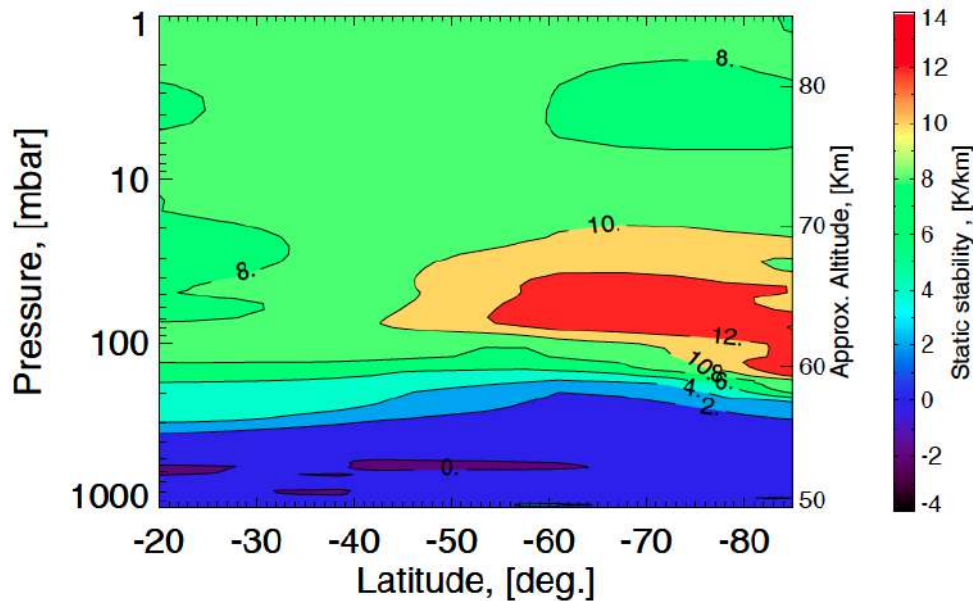


Figure 3.30: Venus atmosphere's static stability contour plot as a function of atmospheric pressure and latitude (figure: VeRa instrument's VEx website).

### 3.4.3 Global atmospheric circulation

There has been an important effort from the planetary scientific community in order to better understand the atmosphere's global circulation, with many studies based on recent data collected by *Venus Express* and ground-based observations, as well as a large modelling effort using global circulation models of Venus (GCM). Among several onboard different experiments, measurements of the zonal wind (horizontal wind, i.e. parallel to the equator moving anticlockwise, from east to west) were made by tracking cloud features in images at ultraviolet, visible and infrared wavelengths (Markiewicz et al., 2007; Sánchez-Lavega et al., 2008) and are particularly relevant to inter-comparison with the ground-based methods I developed over the course of this thesis.

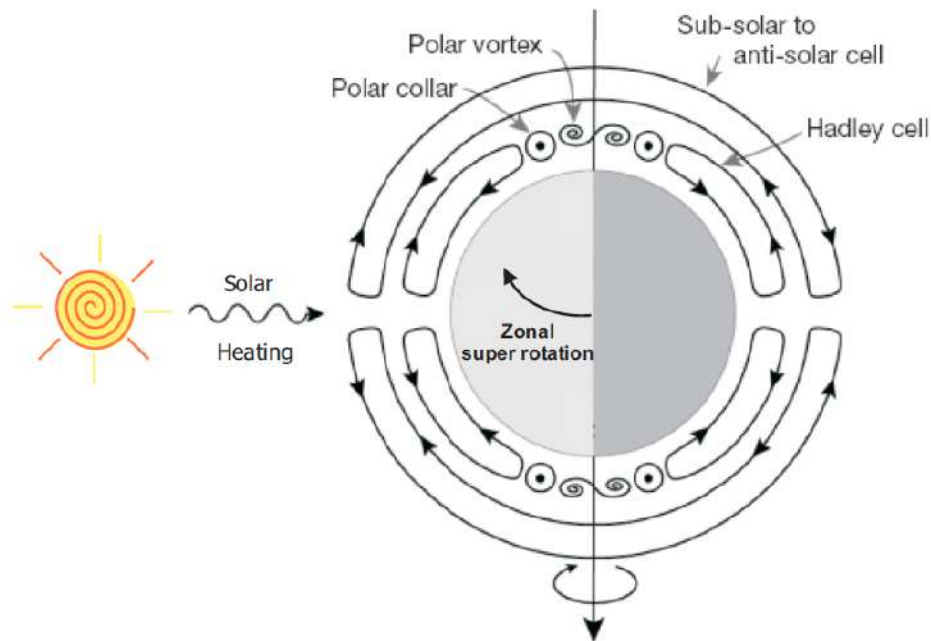


Figure 3.31: Venus atmosphere's global circulation. Figure: Taylor and Grinspoon (2009).

Venus atmospheric dynamics is essentially driven by thermal heating and by its low rotation rate. In spite of all the present efforts to better understand the atmospheric global circulation, the explanation of this phenomenon is still essentially based on the phenomenological evidence. There is currently no theory that can fully constrain the structure and the dynamics of the atmosphere.

In the atmospheric circulation at lower and middle atmosphere there is a pronounced convection mechanism at the low latitudes. Midlatitudes are characterized by the zonal wind (RZW) flowing in bands almost parallel to equator. At 50-60° a jet is sometimes detected, already found by previous missions to Venus Express but highly unstable. On the polar region close to the polar axis was found a wide binary vortex (also highly variable) structure covering several  $km^2$  and turning on itself with a period of around two and half terrestrial days (figure 3.31).

There are three major atmospheric global circulation processes that characterize the Venus atmospheric dynamics (see figure 3.31 and for more detail the figure 3.32). Mesospheric circulation (between the altitudes of 60-100 km and stretching between mid-latitudes) most relevant atmospheric motion is the super-rotational retrograde zonal wind (RZW) flowing in quasi-laminar bands parallel to equator. Super-imposed to the previous air motion stands out the sub-solar to anti-solar circulation (SS-AS) transporting the over heated air from high insolation regions towards the nightside radiation deficit area. The third dynamical macro regime is the meridional circulation, responsible for the transport of the heat excess from low latitudes, poleward to cooler high latitudes regions, see the atmospheric circulation scheme from figure 3.32. Meridional circulation is characterized by one cell in each hemisphere, with rising equatorial heated air in a highly convective region, then an upper branch of the Hadley cell drive this hot air till high latitudes where it will sink and return to low latitudes along the Hadley cell lower branch (Limaye, 1985).

As for the meridional circulation it is expected that only one Hadley cell exists in each hemisphere (North and South), transporting the air masses from the equator till the high latitudes. The Hadley circulation is due to the heat transport from the equatorial regions to the upper limit of the midlatitudes region, where the amount of solar radiation deposited is lower. This heat is transported in a cell-like motion, with air rising in the equatorial regions and moving towards higher latitudes, along high altitude atmospheric layers. The latitudinal wind profile retrieved by Doppler velocimetry (Machado et al., 2012) and from cloud tracking methods (Moissl et al., 2009; Sánchez-Lavega et al., 2008) coincide in the presence of a jet with an increased velocity of the order of  $20 \text{ ms}^{-1}$  at the latitudes of 50-60 degrees of latitude. The presence of this jet is consistent with the assumption that the Venus' atmosphere is in quasi-cyclostrophic balance, as predicted by Leovy (1973) for slow rotating planets, as is the case for Venus.

The area near the 60° latitude at each hemisphere, where we can find the jet streams (although they are highly variable), most likely marks the boundaries of the Hadley cell. Indirect evidence for this meridional circulation of

the atmosphere can be obtained by monitoring the latitudinal distribution of some minor constituents of the atmosphere, which serve as markers for the air flows in the lower atmosphere, such as carbon monoxide (CO) and the dioxide of sulphur ( $SO_2$ ).

The transition zone between regimes of the air motion is the *mesopause*, considering altitude discontinuities, situated between 100 and 120 kilometres of altitude. While below this boundary prevails the superrotation zonal winds of the lower atmosphere, above dominates the airflow of the thermosphere (SS-AS), that circulates between the planetary sub-solar point and the anti-solar one (figure 3.32).

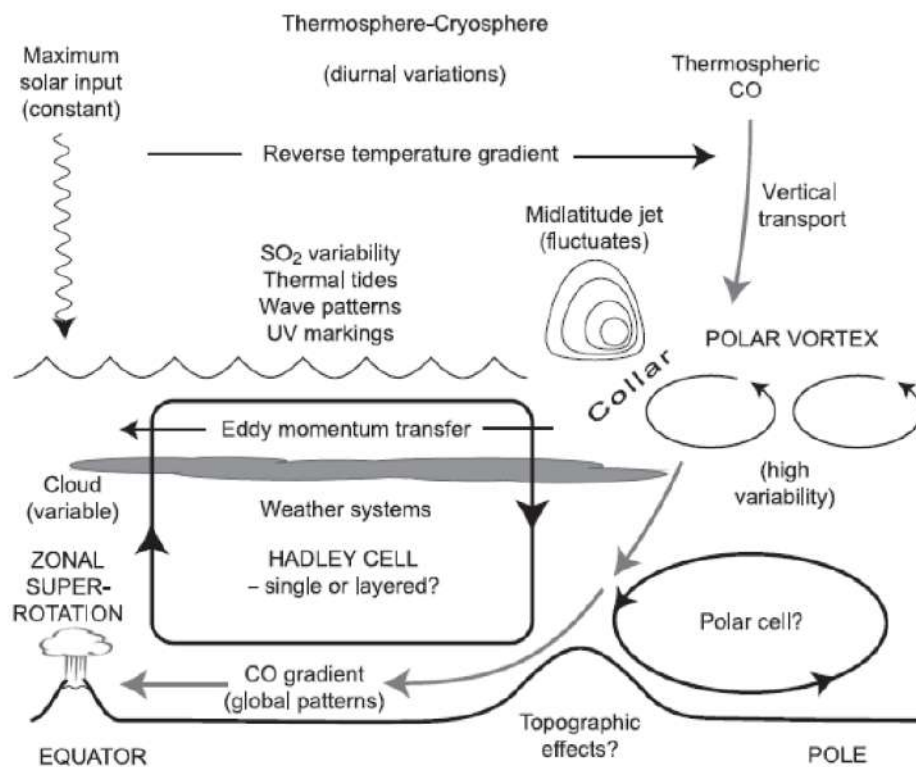


Figure 3.32: Scheme of the Venus atmosphere's different circulation regimes and summary of the atmospheric circulation main properties. Here are also marked the main open issues about Venus' atmosphere circulation. Figure: Taylor and Grinspoon (2009).

The thermosphere is characterized by a circulation between the sub-solar point and the anti-solar point. This air motion can be inferred through

the density and temperature's contrast between day and night hemispheres. These cells are superimposed on the pattern of super-rotational zonal winds. Some wind measurements of in the thermosphere reveal an intense variability of its zonal component (Bougher et al., 1997), which can not be attributed to seasonality due to the fact that seasons, as we have already seen, have a negligible effect on Venus, but it can be a consequence of altitude variations of the two dynamical regimes.

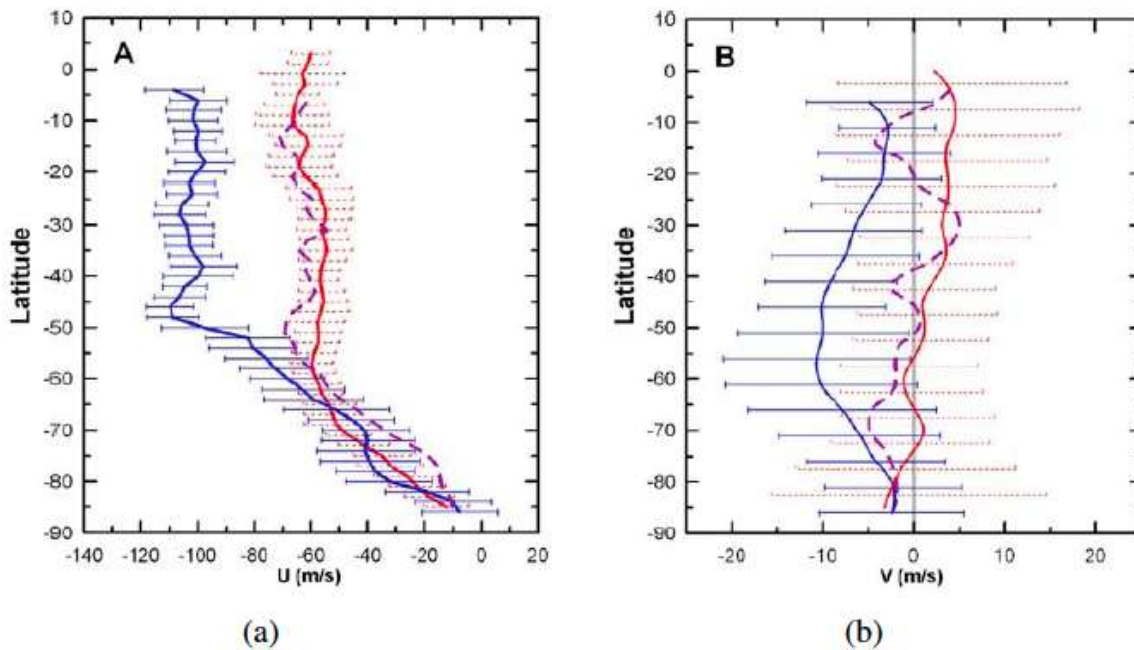


Figure 3.33: Cloud tracked latitudinal zonal wind profile (a), and meridional profile (b). The winds were retrieved from VIRTIS measurements with three different filters: ultraviolet (blue, at 380 nm,  $\sim 66$  km), near-infrared (violet, 980 nm,  $\sim 61$  km) and infrared (red,  $1.74 \mu\text{m}$ ,  $\sim 47$  km, nightside). Figure: Sánchez-Lavega et al. (2008).

There are several available different tools and techniques in order to probe the atmosphere at different altitudes. The tracking of cloud features over time, allows to retrieve winds at different wavelength ranges. The ultraviolet (UV) probes the cloud top region (70 km, Moissl et al. (2009)), while the near infrared (NIR) images sound within the cloud layer (47-61 km, (Sánchez-Lavega et al., 2008)) at the nightside hemisphere. Thermal infrared (at  $5 \mu\text{m}$ ) can be used in order to retrieve cloud tracked winds, both in the dayside and the nightside hemispheres (Luz et al., 2011). Cloud tracked winds could be

obtained, both from space-based and ground-based observations, obviously with different spatial resolution. On the one hand, VEx high spatial resolution (and wide spatial and temporal coverage) offers detailed images that enables high quality dynamic studies; on the other hand, the possibility of using high spectral resolution ground-based spectrographs, enables to perform high accuracy Doppler measurements providing, in this way, an excellent complementary tool. It is possible to measure the Doppler shifts of  $CO_2$  non-LTE thermal lines ( $10 \mu\text{m}$ , Sornig et al. (2008, 2011, 2012), probing the altitude of 110km at the transition zone between zonal and SS-AS flows), by the Doppler heterodyne technique, and at several CO millimetre lines (Rengel et al., 2008; Clancy et al., 2008, 2012; Lellouch et al., 2008), probing the altitude of about 95 till 120 km at the upper mesosphere and lower thermosphere. At dayside the high accuracy measurement of  $CO_2$  absorption lines (Widemann et al., 2007) and Fraunhofer absorption lines (Gabsi et al., 2008; Gaulme et al., 2008; Widemann et al., 2008; Machado et al., 2012, 2013) allowed to retrieve direct wind velocities at cloud tops ( $\sim 70$  km).

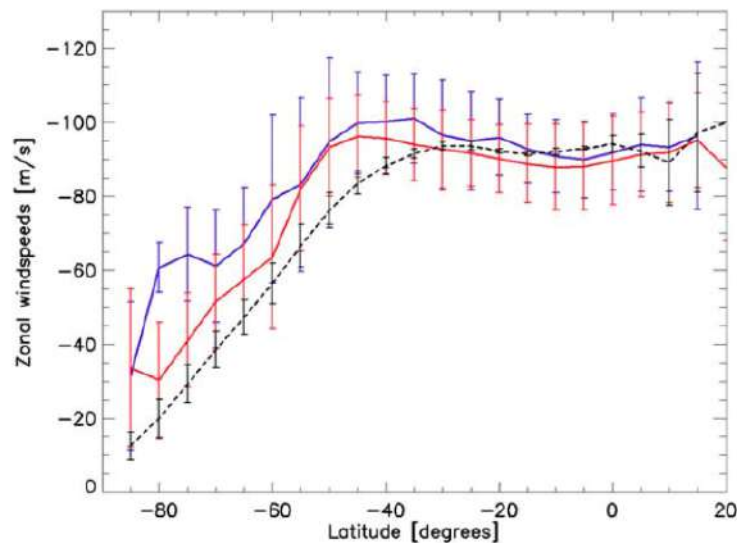


Figure 3.34: Cloud tracked zonal winds based on VMC images. In blue, the latitudinal wind profile from sequential visual tracking method. In red, the same as the previous case but for paired images. Finally in black dashed line, results from digital cloud tracking. Figure: Moissl et al. (2009).

A summary of some relevant ground-based wind determinations, from the last three decades, retrieved from different techniques and probing a wide

range of altitudes from mesosphere and lower thermosphere, is presented in the tables showed at figure 3.39.

From 60-100 km of altitude extends a transition zone, characterized by high variability and extremely complex atmospheric dynamics. Till the height of 70 km is dominated by the super-rotating retrograde zonal wind (RZW), from the troposphere till low mesosphere. In the upper mesosphere (higher than 70 km), it is observed an increasing sub-solar to anti-solar circulation.

The Doppler shift measurements of the molecular spectra from CO and CO<sub>2</sub> at infrared or millimetre wavelength band, confirmed the existence of a special wind system between 90 and 120 km altitude (Goldstein et al., 1991; Lellouch et al., 1994), and that the thermospheric circulation may sometimes intrude in the low mesosphere, although showing high variability, with wind velocities increment till 40  $ms^{-1}$  (Widemann et al., 2007).

Also using Doppler velocimetry techniques, the deep troposphere was analyzed from the Doppler effect of atmospheric descending probes and balloons (Counselman et al., 1980; Kerzhanovich and Limaye, 1985). Despite the smallness of these datasets, they provided important results, as is the case of very low wind velocities near surface,  $\geq 3$  km, with values on the order of few  $ms^{-1}$ , and from there increasing the velocity with altitude about a hundred  $ms^{-1}$  at the cloud top layer (Crisp et al., 1990). The VEGA balloons have provided a continuous survey during about two days along the balloons altitude path ( $\sim 50 - 55$  km) at equatorial region (Preston et al., 1986; Kerzhanovich and Limaye, 1985). Beyond these sparse and local measurements (15 descent probes were useful for this purpose, mostly at low latitudes), probing other altitude layers, becomes only possible by deriving wind velocities from the thermal wind equation.

In order to improve the dataset of atmospheric dynamics measurements, advantage has been taken of Mariner 10 (Limaye and Suomi, 1981) and Galileo (Crisp et al., 1991; Peralta et al., 2007) missions Venus' flybys. Later on, the Pioneer Venus dedicated orbiter, provided an extensive dataset obtained over its mission, used for retrieving cloud tracked winds (at 365 nm) by Rossow et al. (1981); Limaye et al. (2007). More recently, with Venus Express high resolution experiments, the space-based study of atmospheric dynamics gained a new breath, both in better resolution and time and space coverage, allowing the retrieval of wind velocities from UV features in VMC images (with ultraviolet filter, Moissl et al. (2009), see figures 3.33 and 3.34). VIRTIS measurements, see figures 3.33 and 3.38, (Sánchez-Lavega et al., 2008; Luz et al., 2011; Hueso et al., 2012; Garate-Lopez et al., 2013) probe the altitudes of 58-64 km (at 980 nm) or at nightside using the near-infrared windows of 1.74 or 2.3  $\mu m$  where the optical depth reaches unity at about 48

km of altitude in the lower cloud level. In spite of the previous statements about altitudes probed, it is essential to consider that there is some uncertainty in its determination, since the cloud vertical structure is not totally constrained and is variable (Rossow et al., 1990).

The cloud layer range of altitudes has been particularly studied, with emphasis at the cloud tops, since velocities at these heights could be derived from a diversity of techniques (cloud tracking, Doppler velocimetry, thermal winds). Cloud tracked winds show consistency with the measurements made by descent probes, Vega balloons and Doppler winds, with respect to the atmospheric phenomenon of super-rotation (Rossow et al., 1981; Counselman et al., 1980; Kerzhanovich and Limaye, 1985). All techniques point to a super-rotation state of the atmosphere, from near surface till cloud tops, where the zonal wind circulates the entire planet within a period of about 4.4 terrestrial days (and even faster at the polar vortex), which is roughly 60 times faster than the planetary body itself. The UV atmosphere opacity points for the UV marks coming essentially from  $\sim 70$  km of altitude (Ignatiev, 2009) and pressure levels of 40-50 mbar (Esposito et al., 1983). The cloud tracked winds from nightside retrieved from VIRTIS observations come from altitudes of 47-61 km, because opacities at the near-infrared are different from those at ultraviolet range.

Above the clouds, ground-based Doppler velocimetry coupled with thermal field studies gain an essential role since cloud tracked winds are no longer an option. With different Doppler velocimetry techniques (heterodyne technique, Doppler shifts of molecular absorption lines or solar Fraunhofer lines) it is possible to retrieve direct and instantaneous wind velocity values at selected altitudes from the upper mesosphere till the lower thermosphere. Also at the heights of about 95 km of altitude, the circulation can be inferred from the nightside oxygen airglow, both from space-based (Gerard et al., 2009) and ground-based observations (Crisp et al., 1996; Ohtsuki et al., 2008; Bailey et al., 2008).

The motion (along the line of sight) of aerosols droplets in the clouds measured by Doppler effect, as they act as scattering sources for the incident solar radiation. The motion of these particles will induce a frequency shift in the spectral absorption or emission lines (depending on the Doppler velocimetry technique). The next step is to compare the shifted lines with a reference spectra (could be a synthetic spectra as HITRAN for the infrared wavelength range or a measured spectrum chosen as a reference (that method will provide relative velocities)) and then evaluate the wavelength shift and consequently, by Doppler effect, the instantaneous velocity of the probed point. Since the shifts are usually smaller than the line widths, it is crucial to ensure a very high spectral resolution. An accurate navigation



of the points probed upon the planet is also required in order to de-project the obtained velocities along the line of sight, to “real” velocities at the planetocentric reference frame. It is also essential to discriminate the possible contributions from different dynamical motions (zonal, meridional and SS-AS circulations). All these issues will be addressed in detail in the following sections.

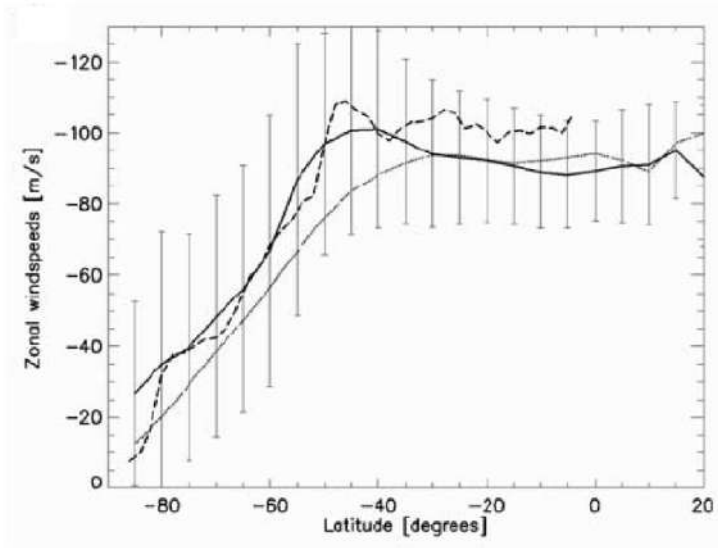


Figure 3.35: Comparison from VMC visual and digital cloud tracking, zonal wind latitudinal profile (solid line and dotted line respectively), with a latitudinal zonal wind profile retrieved from VIRTIS-UV measurements (Sánchez-Lavega et al., 2008). Figure: Moissl et al. (2009).

Using three different filters it was possible to probe the atmosphere, at nearly the same time, at three different altitudes (Sánchez-Lavega et al., 2008). At the wavelength of 980 nm (NIR) the altitudes probed are 58-64 km, while 380 nm (UV) probe the cloud tops and the nightside images, made at 1.74  $\mu\text{m}$ , sound the altitude range of 44-58 km. A detailed description of these processes and results can be found at Sánchez-Lavega et al. (2008). Recently, based on Venus Express observations, Hueso et al. (2012) produced the first 3-D wind determinations, not just at different altitudes as the previous cited work but also in wide range of latitudes and planetary local times (see figure 3.38), comparing the two referred figures it shows that the average zonal velocity increased between this two research projects.

In this work, we will present the results of coordinated observations (nearly simultaneous) from Vex/VIRTIS (space-based cloud tracked winds)

and CFHT/ESPaDOnS (ground-based Doppler velocimetry winds), following the same spirit of the previous experiment, but now using two independent techniques of retrieving wind velocities.

Another way of producing wind velocities, at the mesosphere, is to derive them from the vertical temperature structure making use of the thermal wind equation and under the assumption of cyclostrophic balance approximation (where on a slow rotating planet, the poleward component of centrifugal force is balanced by the pressure gradient force). This technique builds a wind velocity field from the measured temperature field (Piccialli et al., 2008, 2012). This method requires atmospheric temperature structure datasets. The mesospheric temperature field was probed by the Pioneer Venus mission (Taylor et al., 1983), Venera (Zasova et al., 2007) and Galileo (Roos-Serote et al., 1995).

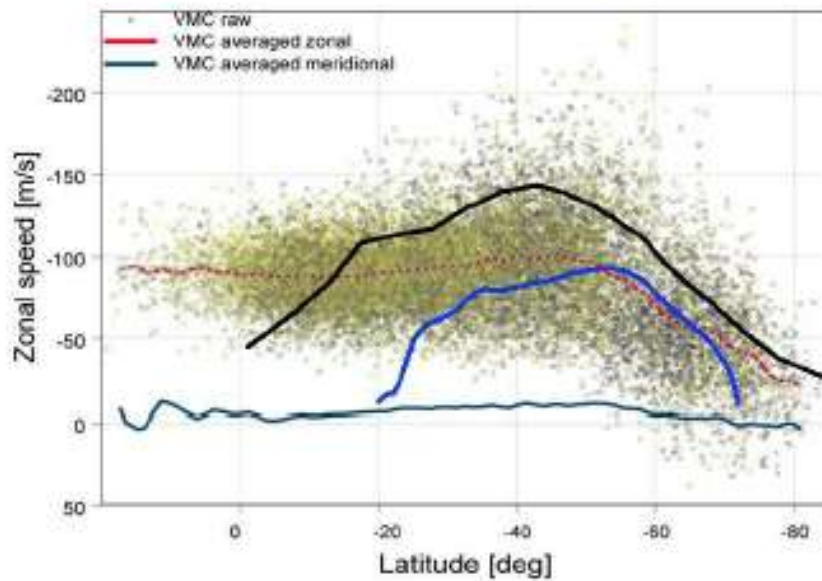


Figure 3.36: Cyclostrophic wind, from VeRa (black) and VIRTIS (blue) temperature measured fields at  $\sim 68$  km (36 mbar), and comparison with VMC cloud tracked winds (Khatuntsev, I., private communication).

From retrieved cyclostrophic winds of Venera 15 (Zasova et al., 2007) the associated latitudinal profile shows clearly a midlatitude jet with a velocity of about  $110 \text{ ms}^{-1}$  and a decrease of the wind velocity for higher latitudes. Cyclostrophic winds based on Pioneer Venus observations show a prominent midlatitude jet reaching the velocity of  $140 \text{ ms}^{-1}$  (Limaye, 1985). These

results seem consistent with VMC cloud tracked winds (see figure 3.36).

Based on VEx experiments VIRTIS and VeRa measurements, were retrieved temperatures profiles and under the cyclostrophic balance assumption, were derived the related wind velocity fields (Piccialli et al., 2008, 2012), see figure 3.36.

From the determination of atmosphere stability parameters (Richardson number inferred from temperature and thermal wind fields), it became clear that from 45 km till cloud tops the atmosphere must be dominated by convection, see figure 3.30.

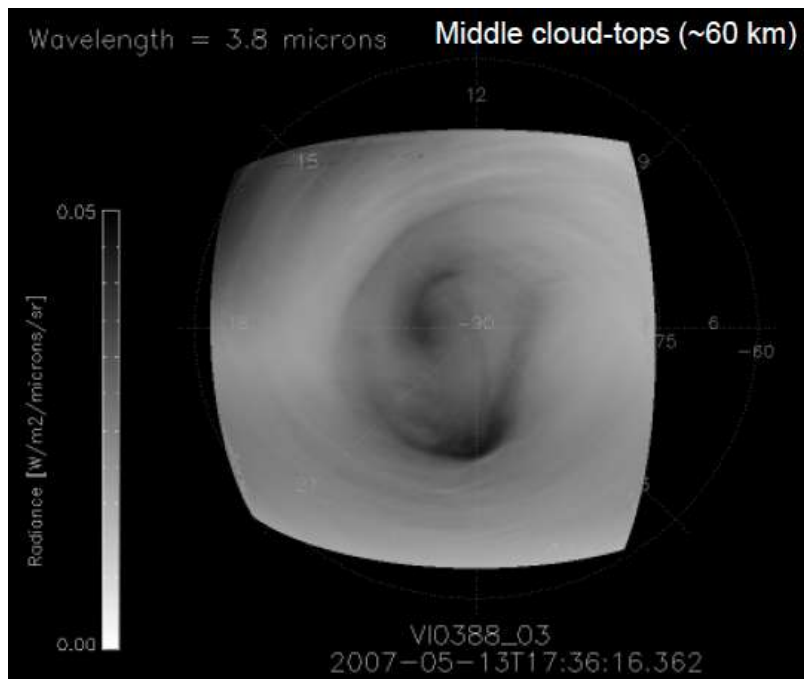


Figure 3.37: Structure of the polar vortex. A chaotic atmospheric feature (Garate-Lopez et al., 2013). Figure credits: IAPS/INAF.

The sub-solar to anti-solar circulation (SS-AS) is predominant above 110 km and is essentially driven by the temperature asymmetry between day and night hemispheres, and to the slow planetary rotating rate, the average velocities are about  $20 \text{ ms}^{-1}$  higher than the circulation at cloud tops (Bougher et al., 1997; Lellouch et al., 1997). The layer underneath these heights (mesopause) is a highly variable mixing of zonal and SS-AS circulations. The process that will maintain the super-rotating zonal winds and the transition to the SS-AS upper layer is not yet well constrained (Schubert et al., 1983; Gierasch et al., 1997).

Evidence of the SS-AS circulation at thermosphere heights is clearly seen by oxygen glow at the nightside upper atmosphere. This radiation emission that produces the observed airglow results from the recombination of oxygen atoms.

The meridional circulation is characterized by a thermally directed meridional cell flowing from equator poleward (Hadley cell). Its role is most likely to redistribute the excess of equatorial heat to higher, and cooler, latitudes (Limaye, 1985). The Hadley cell, at each hemisphere, stretches from equatorial region till about  $65^\circ$  latitude. In Earth the Hadley cell, coming from equator, breaks in three, possibly due to the faster rotating planet than in Venus case. On Earth, Coriolis force is substantially stronger than on Venus. The vertical extent of the Hadley cell is not totally constrained, but it seems that it extends from near surface till the cloud deck. Cloud tracked winds suggest that the meridional circulation does not surpass the latitude of  $65^\circ$  (Limaye et al., 2007; Peralta et al., 2007). This fact might be connected with the observed “cold collar” at nearly these latitudes (detected by entry probes), and with the upper hot branch of the Hadley cell, ensuring the necessary forcing in order to maintain this cold air belt ( $\sim 30^\circ$  lower than the surrounding air) around the planet. The Venus’ Hadley cell is characterized by equatorial ascending hot air, by convection, then transport poleward of this warm air till the referred latitude, where it will radiatively dissipate energy, cooling down and descending, while the lower branch will close the cell, transporting the cooled air back to equator. The cloud tracking measurements of meridional wind circulation were affected by the accuracy of individual measures, of the order of  $10\text{-}15\text{ ms}^{-1}$ , when the predicted meridional wind velocities were of the same magnitude.

At polar regions, North and South, spreads a huge hurricane-type structure, but much bigger than the terrestrial ones. This three dimensional feature is highly variable, and has been seen as dipole-like shape (Pioneer Venus observations) although it can change rapidly. The vortex eye rotates around the polar axis even faster than the super-rotating zonal winds of the mid latitudes range. The vortex was observed recently (Luz et al., 2011; Garate-Lopez et al., 2013) showing a period of about 2.7 terrestrial days (twice the angular velocity of the zonal wind) and an astonishing shape variability (see figure 3.37). The inner and outer part of the vortex evidenced a differential rotation rate (Luz et al., 2011). It had been seen has a dipole, triple and monopole as well (Taylor and Grinspoon, 2009; Luz et al., 2011; Garate-Lopez et al., 2013).

A world-wide coordinated campaign of observations was carried out during May and June 2007. The core idea was to compare space-based (VEx) and ground-based observations, using different techniques in order to better

constrain atmospheric dynamics at upper mesosphere, mesopause and lower thermosphere. The altitudes probed covered the heights from cloud tops ( $\sim 70$  km) till the lower thermosphere ( $\sim 110$  km).

At 110 km of altitude (Sornig et al., 2008) were measured zonal winds from equator ( $\sim 3 \pm 7 \text{ ms}^{-1}$ ) till midlatitudes ( $45^\circ$  S) with measurements of  $32 \pm 4 \text{ ms}^{-1}$  and from there decreasing steeply to higher latitudes, in good accordance with the results from other techniques. A little lower ( $103 \pm 5$  km, at 0.01 mbar, Clancy et al. (2008, 2012)) and from 85-110 km (Rengel et al., 2008), the retrieved values for zonal winds were higher than the previous case, most likely due to a combination of zonal and SS-AS circulations (Clancy et al., 2008, 2012; Rengel et al., 2008).

### Super-rotation of the atmosphere

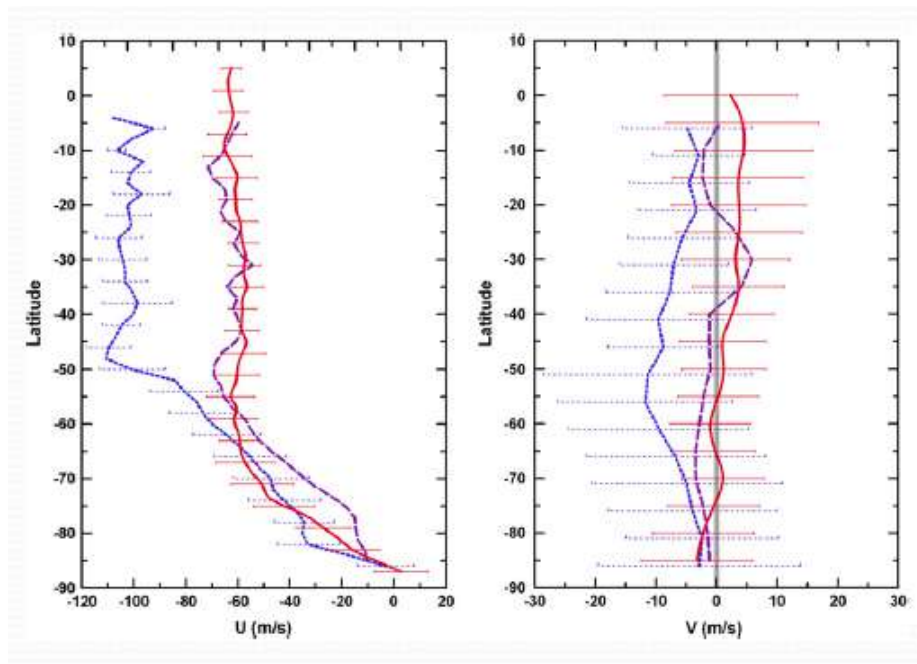


Figure 3.38: Recent 3-D determination of winds at different altitudes on Venus. Left: latitudinal profile of zonal wind component. Right: meridional profile. Winds were retrieved from VIRTIS measurements and with the same filters (same altitudes probed) as fig. 3.33. Figure: Hueso et al. (2012).

Also in the frame of this world campaign were the cloud top Doppler velocimetry observations made with UVES and the VLT telescope that retrieved a zonal wind of  $120 \pm 17 \text{ ms}^{-1}$ , this will be discussed in detail in section

4.6. Ground-based measurements, in general, pointed to the existence of high variability in the measured wind velocities.

There are still open questions concerning the understanding of Venus' atmospheric dynamics. Examples are: how the super-rotation process is driven and how is it maintained over time. What is the role of the polar vortices in the coupling of the zonal and SS-AS circulation. Why the midlatitude jets are variable. What is the deep atmosphere structure of meridional circulation Hadley cells. The atmosphere of Venus is in a state of zonal super-rotation of its upper layers.

The super-rotation state is characterized by having an averaged angular momentum much larger than the one it would have if the atmosphere were in co-rotation with the planet's surface. Till today it is not well explained, how the atmosphere could reach these high velocities, since Venus is a slow rotating body. Another intriguing issue is the process that can stabilise and maintain the super-rotation regime.

This rotation of Venus' atmosphere is not uniform, but depends on the latitude, a fact that can be seen by the relative motion of the cloud top layer, filleting the planet. The super-rotating winds spread over an altitude range from above the lowest scale height to at most about 100km. This is consistent with measurements of the nightside oxygen airglow emission (at about 97 km) that roughly indicates the absence of super-rotation. The recent VEx SPICAV and VIRTIS measurements of nightside NO airglow are quite intriguing, these observations probe an altitude of about 115 km and strongly suggest a recrudescence altitude super-rotation (Stiepen et al., 2013).

The super-rotation can be inferred from the direct observation of the cloud top layer. The fast retrograde motion (westward) of the atmosphere has firstly been found on ultraviolet images, where a large scale moving Y shape feature, circulated the planet in about four days time. From that, could be inferred that the associated wind might be on the order of  $100 \text{ m s}^{-1}$  (Boyer and Carmichel, 1961; Smith, 1967). This phenomenon was corroborated by later space-based observations by Mariner 10 (Belton et al., 1976), Pioneer Venus (Rossow, 1980) and Galileo (Toigo et al., 1994).

Another evidence for this phenomenon occurred in 1985, when the Vega probes dropped meteorologic balloons, during the Venus gravitational assist flyby on its orbit to the Halley's comet. The trajectories of these balloons denounced a rampant run of the air flow at an altitude of 54,000 meters with tangential velocities of the order of 110 m/s. The jolting trajectories also showed the presence of no negligible vertical winds.

The tracking of small scale ultraviolet markings in the clouds and the temporal evolution of these features, allowed to infer that the bulk wind velocities at midlatitudes was horizontal and parallel to equator wind system.

Alt. (km)	Date	Wind Velocity Zonal <sup>a</sup> (SS-AS) <sup>b</sup> (m s <sup>-1</sup> )	Method	Reference
66	1/03	66±5 - 91±6	Visible/solar rad.	<i>Gabsi et al. (2008)</i>
67	7/07	151±16	Visible/solar rad.	<i>Gaulme et al. (2008)</i>
68	6/07	92±14 - 155±39 <sup>d</sup>	Visible/solar rad.	<i>Widemann et al. (2008)</i>
68	8/07	104±20 <sup>d</sup>	Visible/solar rad.	<i>Widemann et al. (2008)</i>
74	2001, 2002	83±27 <sup>d</sup>	Visible/CO <sub>2</sub>	<i>Widemann et al. (2007)</i>
74	2001, 2002	67±21 <sup>e</sup>	Visible/solar rad.	<i>Widemann et al. (2007)</i>
~70 - 80	4-5/77	94±6 (-35±6 <sup>c</sup> )	10 μm heterodyne	<i>Goldstein (1989)</i>
~100	2-4/77, 1978	(Present)	CO mm.	<i>Gulkis et al. (1977); Schloerb et al. (1980)</i>
~90-105	1977 - 1982	Weak (Present)	CO mm	<i>Clancy and Muhleman (1985)</i>
~90 - 105	3/85, 588, 2/90	Weak (Present)	CO mm	<i>Clancy and Muhleman (1991)</i>
~90 - 105	12/86, 4-5/88	Strong	CO mm	<i>Gurwell et al. (1995)</i>
99±6	4-5/88	132±10 (<40)	CO mm	<i>Shah et al. (1991)</i>
94.5±6	8/91	35±15 (45±15)	CO mm	<i>Lellouch et al. (1994)</i>
102	6/07	131±13 - 147±3 <sup>f</sup> (290±44 - 322±25 <sup>f</sup> )	CO mm	<i>Lellouch et al. (2008)</i>
102	6/07	46±19 - 63±10 <sup>g</sup> (114±41 - 151±19 <sup>g</sup> )	CO mm	<i>Lellouch et al. (2008)</i>
102	8/07	-30±53 - 120±36 <sup>f</sup> (55±53 - 120±36 <sup>f</sup> )	CO mm	<i>Lellouch et al. (2008)</i>
102	8/06	40±30 - 120±90 <sup>fg</sup> (40±45 - 110±25 <sup>fg</sup> )	CO mm	<i>Lellouch et al. (2008)</i>

Alt. (km)	Date	Wind Velocity Zonal <sup>a</sup> (SS-AS) <sup>b</sup> (m s <sup>-1</sup> )	Method	Reference
103	6/07	195±70, 235±70 <sup>efgh</sup>	CO mm	<i>Clancy et al. (2008)</i>
105±9	8/91	95±10 (90±15)	CO mm	<i>Lellouch et al. (1994)</i>
~90-105	8/91	Equal Magnitude	CO mm	<i>Lellouch et al. (1994)</i>
~90-105	5-6/93	SS-AS moderately stronger	CO mm	<i>Rosenqvist et al. (1995)</i>
94.5±6	11/94	45±30 (50±35)	CO mm	<i>Rosenqvist et al. (1995)</i>
105±9	11/94	75±20 (110±20)	CO mm	<i>Rosenqvist et al. (1995)</i>
109±10	12/85, 10/86, 3/87	25±15 (120±20)	10 μm CO <sub>2</sub> heterodyne	<i>Goldstein et al. (1991)</i>
110	1990	40±3 (119±2)	10 μm CO <sub>2</sub> heterodyne	<i>Schmülling et al. (2000)</i>
110	1991	35±1 (129±1)	10 μm CO <sub>2</sub> heterodyne	<i>Schmülling et al. (2000)</i>
110	6/07	68 - 280 <sup>g</sup>	CO mm	<i>Rengel et al. (2008)</i>
110	6/07	205 - 355 <sup>f</sup>	CO mm	<i>Rengel et al. (2008)</i>
110	2007	3±7 (52±18)	10 μm CO <sub>2</sub> heterodyne	<i>Sornig et al. (2008)</i>
110	2007	18±4 - 32±4 <sup>e</sup>	10 μm CO <sub>2</sub> heterodyne	<i>Sornig et al. (2008)</i>
~95-110	7-10/91, 3-5/93	Variable	O <sub>2</sub> IR nightglow	<i>Crisp et al. (1996)</i>
~100-110	9/94	Ve <sub>q</sub> + 0.7 x V <sub>ter</sub> = 140 ± 45	CO 5 μm, winds	<i>Maillard et al. (1995)</i>
~125-145	9/94	Ve <sub>q</sub> + 0.7 x V <sub>ter</sub> = 200 ± 50	CO 5 μm, winds	<i>Maillard et al. (1995)</i>

<sup>a</sup>Zonal retrograde flow, equatorial velocity

<sup>b</sup>Subsolar-to-anti-solar flow, cross terminator velocity

<sup>c</sup>Anti-solar-to-subsolar

<sup>d</sup>Equatorial mean zonal winds

<sup>e</sup>Higher latitudes

<sup>f</sup>Nightside

<sup>g</sup>Dayside

<sup>h</sup>Combined RSZ and SS-AS

Figure 3.39: Ground-based equatorial wind observations summary and different used techniques. Table credits: Sornig et al. (2008); Lellouch et al. (1997); Brecht et al. (2011).

The derived mean value of about  $110 \text{ ms}^{-1}$  indicated that the atmosphere, at cloud deck heights, rotates about sixty times faster than the planetary solid body.

The intriguing dark Y shape feature seen at ultraviolet wavelength range, was determined to be a planetary global scale wave, flowing in the direct sense (so in the opposite sense of the RZW) with about  $20\text{-}30 \text{ ms}^{-1}$  (Del Genio and Rossow, 1990). The presence of solar-locked regimes influencing the global dynamics, was also identified. The thermal tides, induced by solar heating, have been measured in their diurnal and semi-diurnal components (Limaye, 1982; Rossow et al., 1990). The planetary wave circulating the planet in nearly four days, can be seen in the ultraviolet (UV) observations and was identified as a Kelvin wave. This component is an important element in the large-scale circulation of the atmosphere of Venus.

Superimposed on this phenomenon, there is an heating expansion on the daytime hemisphere of the Venus dense atmosphere and a contraction by a cooling of the gaseous layer beyond the night hemisphere terminator. Consequently, installing a tidal atmospheric binary between day and night hemispheres. The current planetary long period of rotation most likely comes from an equilibrium state between the gravitational tidal force of the Sun on Venus (which tends to slow its rotation) and the atmospheric described binary (Bougher et al., 1997).

Among the first attempts to understand the super-rotation mechanism, were Baker and Leovy (1987). They suggested that it is the momentum from the zonal wind (RSZ) when transported upward through the equatorial thermal tides mechanism, followed by the transport towards higher latitudes by the Hadley cell upper branch, that supports and maintains the necessary drive to stabilise the super-rotation regime. Schubert et al. (1983) proposed, as well, that the transport of angular momentum at equator through solar thermal tides is the main responsible by the maintenance of super-rotation. He also proposed an alternative process which includes the transport of momentum by atmospheric eddies.

However, despite the fact that this factor could explain the dynamic structure of the atmosphere above 50 km, it does not explain satisfactorily the movement of the air layers in the mesosphere.

The solar tide is a stationary wave relied to the sub-solar point, which then moves against the stream relative to the atmospheric fluid flow. The absorption of radiation by the cloud layer at about 60 km altitude, will excite a gravitational wave that will propagate vertically depositing momentum in the upper layers where it is absorbed. As a result of this phenomenon the air, undergoes a certain deceleration some scale heights above the cloud top layer, generating, as a direct consequence, an acceleration at the cloud deck level.



However, this is not in agreement with the simulations where the generated waves, below the cloud layer, produced a deceleration of the air flow above the clouds (Baker et al., 1999), thus reducing the super-rotation at cloud tops.

Another plausible explanation for this super-rotation phenomenon lies in the Gierasch-Rossow-Williams (GRW) mechanism, in which it is the coupling between the Hadley circulation and planetary waves that generate the atmospheric super-rotation.

The Hadley cells on Venus, are summarised to a cell in the northern hemisphere and one in the South hemisphere. The air rises in the low latitudes and dive into the circumpolar region. The rising air in the equatorial region imposes an increase of angular momentum in the upper layers of the atmosphere, and this excess of angular momentum is balanced by the momentum transport, from high to low latitudes, by planetary waves to the equatorial region (Gierash, 1975; Rossow, 1979).

The presence of planetary scale waves (gravity waves), could also contribute to explain the existence the circumpolar belts of the “cold collar”. These gravity waves might be generated by an atmospheric resonance due to atmospheric density variations and having gravity as a restoring force.

The presence of “bow-shaped” waves might be a particular consequence of a convective upwelling motion of heated equatorial air, in the vicinity of the sub-solar point, that would interact with the zonal wind as a dragging obstacle propagating downstream in the air flow, as waves (Belton et al., 1976; Rossow, 1980).

The super-rotating zonal wind, however, is generally constant in midlatitude regions, although some variability connected with solar tides was observed, ultimately depending of the local solar time (LST), this solar locked dependency manifests as averaged higher velocities toward the morning and evening terminators (Sánchez-Lavega et al., 2008; Moissl et al., 2009), and by lower velocities at local midday local time (mainly between 11-13h LST).

The temporal variability of the zonal wind is best assessed by instantaneous techniques of wind velocity measurements, as the Doppler velocimetry techniques. The study developed by Widemann et al. (2007), based upon the spectra Doppler emission line shifts of non-LTE oxygen and carbon dioxide at the nightside airglow, shows relevant temporal variability on the zonal wind profile. On the dayside cloud tops, the back scattered solar radiation also exhibits Doppler shifts due to scattering sources (aerosol cloud droplets) proper motion (Widemann et al., 2008; Machado et al., 2012, 2013). All these studies are convergent in the clear evidence of a quite relevant temporal variability (and spatial as well) in the produced wind fields of zonal velocity.

In recent years the variability of the super-rotating zonal wind (RSZ) has been demonstrated with an increase by  $\sim 30\%$  in the last six years as revealed by a large set of measurements along this period of time (Kouyama et al., 2013; Khatuntsev et al., 2013).

The measurements of the Venus' wind velocity profile show a structure approximate to the cyclostrophic equilibrium, which postulates the balance between the pressure gradient force and the centrifugal force at a certain atmospheric layer. This leads to the appearance of a wind's zonal flow, parallel to equator. In contrast to this case, we have the most well-known geostrophic balance, the one established on Earth, where the Coriolis force has an essential role in the genesis of the well known cyclonic and anticyclonic structures and their macro structures of the prevailing winds, such as the trade winds or the westerlies. In the Earth's case (and Mars), the Coriolis force overlaps the centrifugal effect due to the higher Earth's rotational velocity.

### Surface winds

The surface winds are "slow" (no more than a few  $\text{ms}^{-1}$ ), given the wide thermal uniformity as a function of the latitude. Due to the low obliquity (less than  $3^\circ$  compared to the  $23^\circ$  of the terrestrial one), the temperature latitudinal profile is essentially symmetric and seasons are non-existent (see figure 3.2).

The small obliquity of the rotational axis and the large thermal uniformity, also lead to a weak relevance of the Milankovitch cycle in large time scales for climate variations (Goody et al., 1975).

The massive and dense atmosphere implies a large thermal inertia. This leads to an almost uniform surface temperature (isothermal surface) with latitude and between dayside and nightside hemispheres (Bougher et al., 1997).

Due to topographic features, it is possible to relate the presence of waves in altitude with the drag of the extremely dense atmosphere at surface topographic relief.

Because of the scarce observations at the basis of Venus atmosphere, the study of the lower atmospheric dynamics is limited to a numerical analyses approach, in order to try to reproduce the few and local results obtained by entry probes and balloons.

### 3.4.4 Venus atmospheric evolution

Venus climate is utterly dependent on the abundances of the radiatively active gases, and their variability is directly connected with the temporal atmo-

spheric evolution. Radiative transfer studies are essential to determine these physical and chemical processes on Venus and their couplings (Bengtsson and Grinspoon, 2013).

Variations in the cloud layer opacity, cloud microphysical and optical properties, are determining factors in the overall planetary energy balance. Consequently, as radiative forcing plays a major role in the atmospheric dynamics, it is expected that these sources of variation will affect decisively the atmospheric global circulation.

Minor species, such as  $SO_2$  and  $H_2O$  have an extraordinary importance in the thickness of the cloud layer. The balance of these species could be disrupted, if the volcanic outgassing, heterogeneous reactions with surface rocks or exospheric escape (case of the hydrogen), were to endure severe alterations overtime.

If the sources of atmospheric  $SO_2$  and  $H_2O$  replenishment diminish, it is most likely that the cloud deck would become much thinner, eventually, even until total dissipation on a timescale of a few million years (Bullock and Grinspoon, 2001). The hypothesis cannot be discarded that Venus may already have had a temporal epoch of clear skies, and could experience it again in the future. The lower albedo would affect all the low atmosphere radiative transfer process and ultimately the surface temperature.

An increase in the amount of  $SO_2$  outgassing could also interfere in the ongoing crust geologic processes (Bullock and Grinspoon, 2001). As already mentioned, at present time carbon dioxide does not react with the surface, due to the high temperature that makes it a supercritical fluid. If a hypothetical increase of volcanic  $SO_2$  outgassing leads to an atmospheric abundance increase in the order of 3-10 times the present concentration, this fact will decisively contribute to cool down the surface temperature to a level where carbon dioxide could react with the soil minerals. Then, huge amounts of atmospheric  $CO_2$  will be literally buried in the form of carbonated rocks (as on Earth). In this way, a reinforced *runaway* cooling process would be triggered, at a planetary scale. The mechanism of positive feed-back would be characterized by a weaker greenhouse effect (Bullock, 1997).

With this scenario, the climate evolution could lead to a totally new planetary balance, where the surface pressure could be lowered to about half the present case, and roughly the same in terms of superficial temperature. On the other hand, if the outgassing of  $SO_2$  dramatically decreases, that fact could precipitate a global warming process. In this case, the warming mechanism will be based in the reverse chemical reactions of carbon dioxide with surface minerals, what would imply its increase in the atmosphere, by the decarbonation of soil minerals. That will provoke the broadening of  $CO_2$  absorption bands and consequent increase of infrared opacity, what will

severely affect the greenhouse effect and drive to a planetary global warming.

The largely admitted theory of a global scale resurfacing process on Venus, allied extensive planetary scale volcanism, might be closely related to atmospheric's injection with large quantities of radiatively active volatiles. The relatively fast disturbance of these species in the atmosphere could have provoked dramatic perturbations in the atmospheric equilibrium, both in the past Venus history, and the process may also occur again in the future.

The steady loss of atmospheric water by exospheric escape will influence the cloud formation rate due to the chemical role of  $H_2O$  in the hydrolyses of  $SO_2$  and formation of sulphuric acid, which then condensates in aerosol droplets forming clouds and hazes. This decreases the abundance of water vapour at the cloud top level and consequently affects the albedo, due to lower cloud formation rate, increasing surface temperature in the process. In spite of this, there is also an antagonistic effect, because water vapour is a greenhouse gas. Its decrease implies a lowering in the total greenhouse efficiency. However, this must be a minor side effect since, presently, there is a very low abundance of atmospheric water vapour, and greenhouse effect is essentially controlled by the atmospheric carbon dioxide abundance.

On Venus, the coupling between the albedo and the atmospheric radiative and convective balance is quite complex. Couplings between the cloud thickness and the  $SO_2$  and  $H_2O$  atmospheric abundances, and their influence on the radiative and convective equilibrium, play an essential role regarding the climate's stability.

### 3.4.5 Brief comparative climatology

The hypothesis of planetary evolution from similar departing situations has already been discussed. Now, the diverse reality between the solar system telluric atmospheres will be stressed, with emphasis to the Earth-Venus singularities.

The key present time differences between these two planets are: the almost double solar constant for Venus relatively to the Earth's one; the much faster Earth's rotation rate, what will privilege atmospheric geostrophic balance for the fast rotating planets (Earth and Mars) and cyclostrophic equilibrium in the slower ones (Venus and Titan), see figure 3.43; the existence of an inner magnetic field and correlated "protective" magnetosphere on Earth, whereas on Venus there is just a weak induced magnetic field due to the interaction between solar wind and the upper atmosphere; the  $23^\circ$  obliquity of Earth's axis, while Venus has the axis reversed and almost normal to the ecliptic (Shapiro, 1968); the neutral gases composition of Venus' and Earth's atmospheres (Table 3.40) ; The relative high density and superficial pressure

<b>Species</b>	<b>Venus</b>	<b>Earth</b>
Carbon dioxide	0.96	380 ppm
Nitrogen	0.035	0.770
Sulfur dioxide	150 ppm	0.2 ppb
Argon	70 ppm	9340 ppm
Carbon monoxide	30 ppm	0.1 ppm
Water vapor	20 ppm	~ .01
Helium	12 ppm	5 ppm
Neon	7 ppm	18 ppm
Atomic oxygen	trace	trace
Hydroxyl	trace	trace
Atomic hydrogen	trace	trace

Figure 3.40: Venus-Earth comparison of the abundance of atmospheric neutral gases. From: [Taylor and Grinspoon \(2009\)](#).

on Venus; the much faster winds on Venus (zonal super-rotation) than on Earth, table 3.41; The presence of water vapour and oceans on Earth, in contrast with the almost absence of water on Venus; the diverse temperature profile as seen on figure 3.42; the presence of a *runaway* greenhouse effect on Venus and a much smoother one on Earth; The condensables being on Earth essentially water vapour, while on Venus sulphuric acid (on Mars it is the carbon dioxide and water, and on Titan the ethane); The kind of terrestrial volcanism and the plate tectonics, by opposition of the single-plated Venus and its specific volcanism; Also noteworthy is the stabilising presence of a terrestrial satellite (the Moon) while there is none on Venus.

All these topics were previously addressed, now they were listed in order to stress their present consequences on the planetary equilibrium achieved in each case.

Venus is a “ $CO_2$  dominated planet” (as Mars), which decisively contributes to its huge greenhouse effect due to its large atmospheric abundance (table 3.40). The efficiency of the greenhouse effect on Venus is of the order of 450 K, while on Earth it does not surpass the 35 K (and 7 K on Mars). As a consequence, the temperature profile, seen on figure 3.28 and on figure 3.42, shows clearly the higher Venus’ superficial temperature (and pressure), the absence of an *ozonosphere* temperature inversion, as on Earth, the marked difference between day and night (cryosphere) thermosphere. Partially due

Scale	Symbol	Venus	Earth
Vertical scale	H	15.9 km $\approx 10^4$ m	$\sim 10$ km
Zonal velocity	U	$\sim 100$ m s $^{-1}$	$\sim 10$ m s $^{-1}$
Meridional velocity	V	$\sim 10$ m s $^{-1}$	$\sim 10$ m s $^{-1}$
Vertical velocity	W	$\lesssim 1$ m s $^{-1}$	$\sim 1$ cm s $^{-1}$
Radius	a	$\sim 6.0 \times 10^6$ m	$\sim 6.0 \times 10^6$ m
Rotation rate	$\Omega$	$2.99 \times 10^{-7}$ rad s $^{-1}$	$7.29 \times 10^{-5}$ rad s $^{-1}$
Acceleration of gravity	g	8.8 m s $^{-2}$	9.81 m s $^{-2}$
Timescale	T	$\sim 10^6$ s	$\sim 10^5$ s

Figure 3.41: Relevant comparable properties of Venus and Earth. Table credits: Kerzhanovich and Limaye (1985), for Venus, and Holton (2004), for Earth.

to the Venus' slow rotation rate, the thermospheric temperature on the night-side decreases with altitude (hence the name “cryosphere”), while it increases with altitude at dayside (Keating, 1979; Schubert et al., 1980).

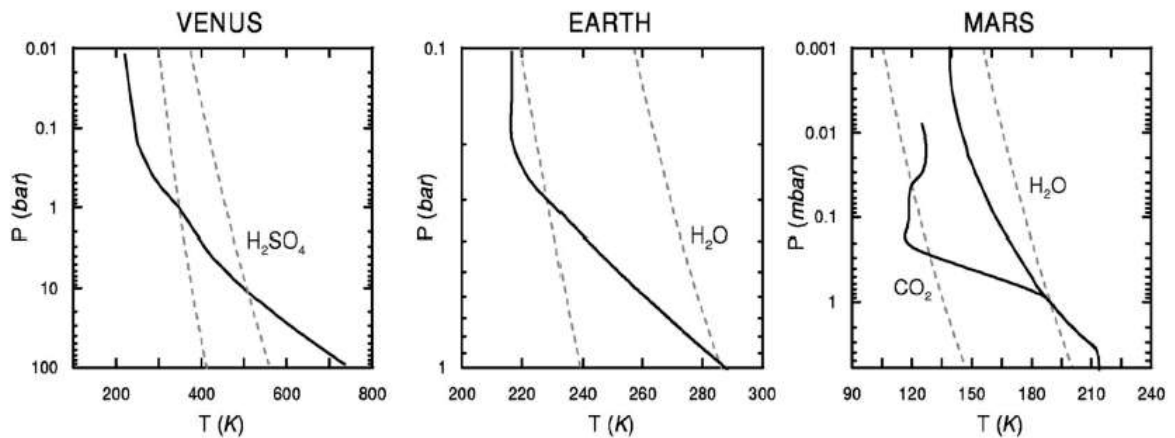


Figure 3.42: Comparison of the averaged thermal profile and condensable species. Figure: Sánchez-Lavega et al. (2004).

One of the major differences in the neutral gases composition comes from the excessive  $CO_2$  abundance on Venus. This is due to the lack of oceans' absorption, as on Earth, or to the possibility of surface deposition by surface-atmosphere chemical reactions, as a result of the supercritical state of the

Venus' atmospheric carbon dioxide at the overheated surface. Another relevant difference is the presence of abundant water vapour and oxygen on Earth, mainly due to its water liquid phase favourable surface temperature, and obviously due to the presence of life's oxygen producing photosynthesis, see table 3.40. In spite of the proportional difference in nitrogen abundance on Venus and Earth, it should be noted that the global amount is nearly the same on both planets, pointing in the direction of similar evolutionary starting points.

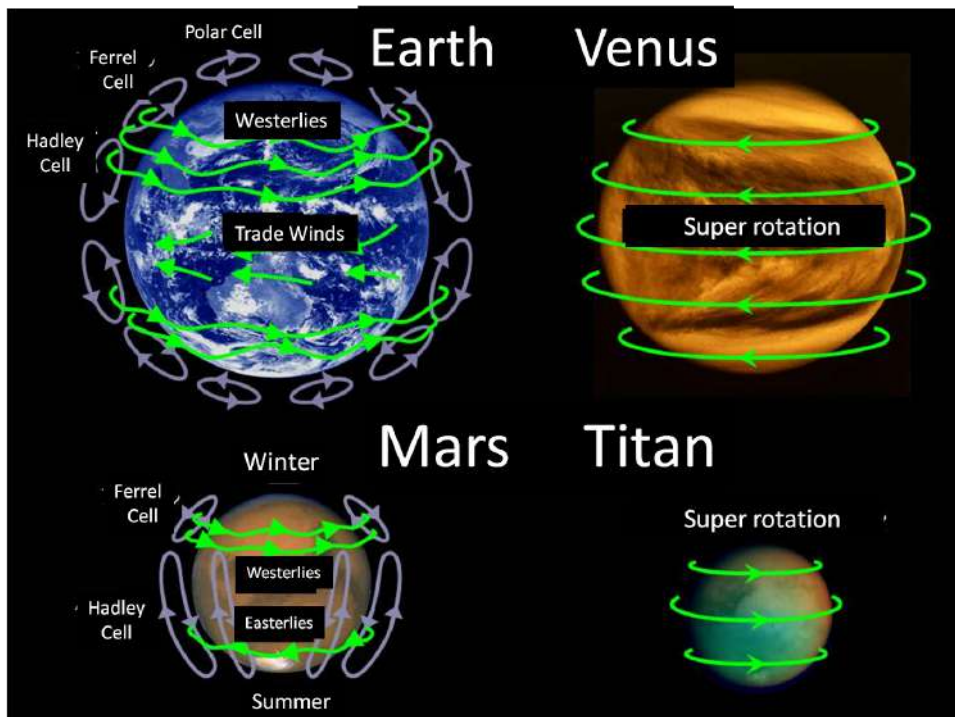


Figure 3.43: General comparison of atmospheric global circulation for solar system bodies with a terrestrial-type atmosphere. Figure credits: Takahashi, Y., private communication.

The presence of the terrestrial ozone layer ( $O_3$ ) on the stratosphere, affects, as already seen, both the radiative transfer and the altitude temperature profiles. Besides, this is an evidence of a biologic interaction (as the presence of large amounts of molecular oxygen ( $O_2$ ) in the atmosphere) once the  $CO_2$  and  $H_2O$  are globally more stable than the pure oxygen chemical compounds. Even, its presence works as a biomarker on the astrobiology research field.

Topographically, the main differences lie on the relative Venus' flatness at

lowlands, most likely a consequence of a dramatic resurfacing process (Seiff, 1983). On Earth, the most remarkable surface features are the oceans and the mountain ridges that reflect the titanic confrontation of the tectonic plates.

Venus sulphuric acid clouds, which cover the whole planet, are quite different in planetary coverage, related albedo, structure and radiatively properties, from the terrestrial water vapour clouds on Earth (Montmesin et al., 2011). The mottled aspect on the Venus' equatorial zone, the quasi-laminar cloud flow on the midlatitudes range and the polar vortices, are direct consequences of the specific global circulation dynamics. On Earth, the general aspect of cloud coverage mostly due to local and mesoscale phenomena. Many features, however, are created by the global circulation. Highlighted features are cyclonic and anticyclonic macro structures connected with easterlies, trade wind systems and cell convergence such as the ITCZ (see figure 3.44), nebulae formations due to mountain ridges and associated to the *monsoon* are also quite remarkable on Earth skies.

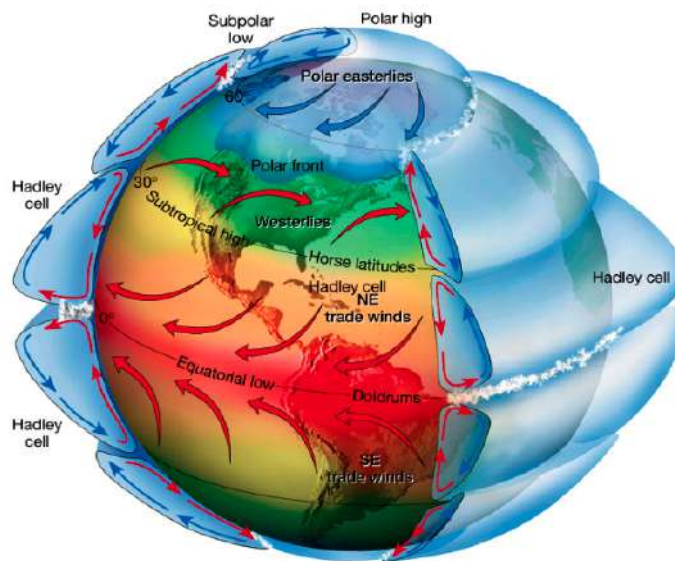


Figure 3.44: Earth's global atmosphere circulation diagram.

The outstanding Venus polar vortices are qualitatively similar to Earth's tropical cyclones (Limaye et al., 2009), dynamically and morphologically. The main differences that Venus polar vortices appear to be permanent and of a much bigger scale than the terrestrial tropical structures (lasting at most two weeks). The energetic driver for these dynamical mechanisms is of different nature. On Earth's hurricanes, the energy source is the release



of warm and humid air's latent heat. On Venus case, it is the deposition of energy from solar radiation at cloud tops and thermal emission from below the clouds. However, both cases seem to include transverse waves in the core region due to barotropic instability (Limaye et al., 2009).

In the one hand, Venus and Mars' atmospheric compositions are similar and Earth stands out by its radically different composition. On the other hand, at a dynamical approach, it is the Earth and Mars that have closer similarities, due of nearly equal rotation rate and obliquity. Venus, as an example of a slow rotating planet, is dynamically similar with Titan: on both bodies the Coriolis contribution is almost negligible and cyclostrophic balance prevails. With respect to the meridional circulation, on Venus, there is just one Hadley cell, stretching along each hemisphere. In contrast, for the relatively faster rotating Earth, the Hadley cells are restricted to subtropical latitudes and meridional circulation extends till polar region with other two cells. For a macroscopic comparative approach of the referred bodies' atmospheric global circulation see figure 3.43, and for a closer look to the Earth's atmospheric dynamics see figure 3.44.

On Mars, as we can see in figure 3.42, the surface temperature and pressure is well below the water triple point, turning the liquid phase impossible at the surface. However, recent observations point to the existence of geomorphologic evidence of fluid floods and waterways on Mars. The atmosphere is quite tenuous with an average surface pressure of about 6 mbar, although, it is quite variable since part of the atmosphere condenses at the polar caps during polar winter.

Another interesting characteristic of Mars, lies on the existence of two relevant condensables:  $H_2O$  and  $CO_2$ . On polar regions ice layers of water and carbon dioxide overlap, depending on seasonal variability. Dust storms give rise to several atmospheric phenomena, reaching a planetary scale, where storms sometimes veil the entire surface, affecting in a substantial way the albedo.

Smaller scale meteorological phenomena, as the so called "dust devils", are vortices characterized by high rotational velocity, up-lifting thin dust, low pressure vortices with warm cores and presenting relevant electrostatic fields. The energetic engine for these vortices is solar insolation, unlike the similar terrestrial "tornadoes" that are due also to the release of latent heat (Balme and Greeley, 2006). However, both "dust devils" and "tornadoes" (and hurricanes as well) are meteorological events representative of local cyclostrophic balance.

Titan has an atmosphere dominated by hydrocarbons. Methane is the leading greenhouse gas, with an efficiency that adds about 12 K to the equilibrium temperature, and methane and ethane are the major condensable

species. Titan is tidally locked to Saturn with a day of 15.9 Earth days. The superficial pressure is about one and a half the terrestrial one. Its atmosphere's dynamics resemble Venus' case, since both are slow rotating bodies where cyclostrophic balance prevails (Taylor et al., 2006), and therefore strong stratospheric zonal winds and jets at the stratosphere (Luz et al., 2006; Achterberg et al., 2008), see figure 3.43.

# Chapter 4

## VLT/UVES observations

### 4.1 UVES - Ultraviolet-Visual *Echelle* Spectrograph



Figure 4.1: ESO's telescopes at Paranal, Atacama desert, Chile. (Figure: ESO's *website*).

The UVES (Ultraviolet-Visual Echelle Spectrograph) is an *echelle* spectrograph, mounted in one of the four telescopes of the VLT (Very Large Telescope), namely the UT2 or Kueyen telescope (which means moon in ancient Mapuche language; others are Yepun (Venus), Melipal (Southern Cross) and Antu (Sun)). It is one of the facilities of the European consortium ESO,

and is located at Cerro Paranal in the desert of Atacama, Chile. The spectral resolution (nominal) designed for this unit, with an 1 arcsec slit was 40,000 (D’Odorico et al., 2000). Echelle spectrographs are tools of high priority in all projects involving large telescopes, since high-resolution spectroscopy is one of the modes of observation that most benefit from a large light collecting area. This high-resolution apparatus is mounted on the Nasmyth platform upon an optical horizontal bench, within a protective structure. UVES addresses the following scientific objectives:

- Study gas and stars’ kinematics in the galactic center.
- Kinematics and mass distribution of stellar clusters.
- Composition, kinematics and physical conditions of the interstellar medium in our galaxy and surrounding systems.
- Study of stars’ seismology and stellar oscillations.
- Substellar companions to nearby stars through studies of radial velocities with high precision and long time scales.
- Structure, physical conditions and abundances of the interstellar and intergalactic gas. Especially for gas near QSOs (quasi-stellar objects) absorption spectra with high redshift.

## 4.2 VLT and UVES description

The UVES is a two-arms cross-disperser instrument, covering wavelength bands of 300-500 nm for the “blue arm” and 420-1100 nm in the “red arm” (figure 4.2). The versatility of the tool allows the use of each arm separately or in parallel, through the use of a dichroic beamsplitter (prism that separates the incoming light into two beams of different wavelength ranges).

It uses an *echelle* of  $214 \times 840 \times 125 \text{mm}$ . The maximum spectral resolution that can be achieved by using a narrow slit, or using one image slicer, is about 110,000 in the red-arm and about 80,000 with the blue-arm. In this case the spectral resolution of the instrument is of 2 pixels (see table 4.9).

The cross dispersers produce a separation between spectral orders higher than 10 arcsec for any wavelength in the range from 300 to 1100 nm. This separation allows spectroscopy of compact and large objects, such as the planet Venus. This separation also allows a good sampling of the sky’s scattered light at red wavelengths band, also enabling an accurate estimation of the background radiation at spectral inter-orders.

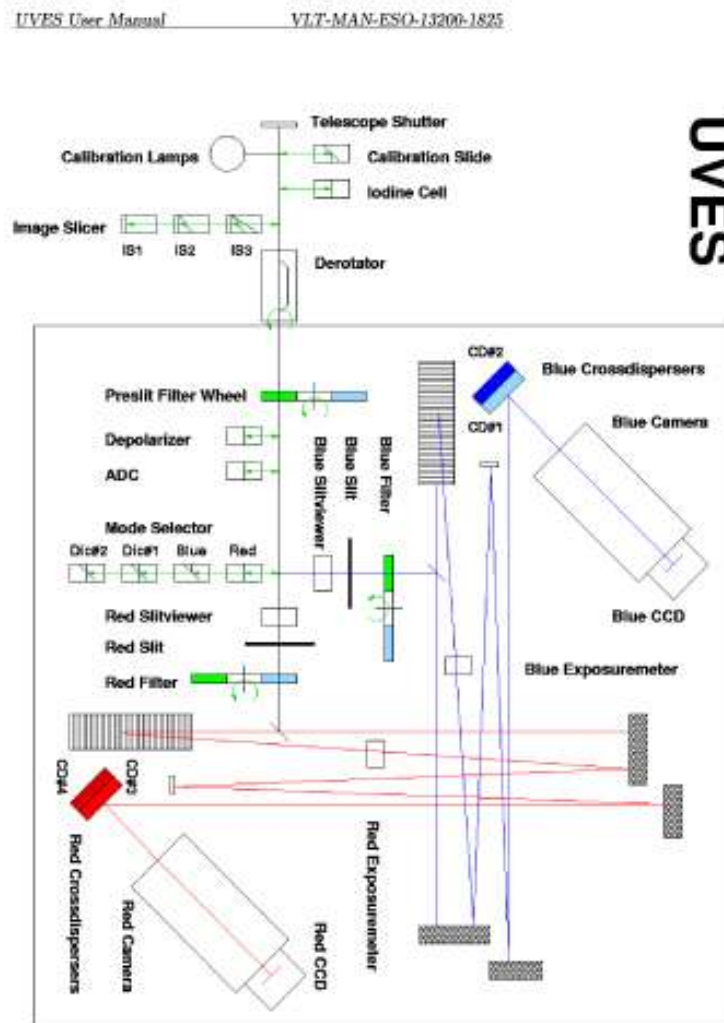


Figure 4.2: UVES optical path, from the incoming radiation entry till its acquisition by the detector's CCDs. (UVES User Manual - *Paranal Science Operations*).

The cameras are dioptrical (no central obstruction) and produce an external focal plane that facilitates the interface with the detector, other advantages are field enlarged images, good image quality and good optical transmission. The dioptrical cameras have a field with a diameter of 43.5 mm (blue) and 87 mm (red). The two crossdispersers, that are in each one of the arms, operate as first order reflectors (Dekker et al., 2000).

For radial velocities studies, the device basic resolution is about  $50 \text{ m s}^{-1}$ , however the inclusion of a iodine cell in the beam-pass increases the resolution in a decisive way, as we shall see in the next section of this chapter. The two arms of the telescope (blue and red) are equipped with large science CCD's : the red-arm shows a two chips mosaic while the blue arm has a unique chip (Dorn et al., 2000). The blue-arm CCD is equipped with a  $2\text{Kpx} \times 4\text{Kpx}$  chip, and is an EEV CCD-44 type with  $15\mu\text{m}$  per pixel. The red arm has a CCD of the same type that equips the blue arm and a second CCD of the MIT/LL type also of the  $2\text{Kpx} \times 4\text{Kpx}$  size.

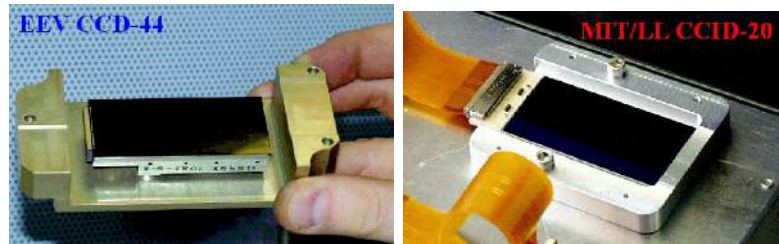


Figure 4.3: The two CCD detectors in UVES (Dorn et al., 2000).

The calibration unit contains a  $45^\circ$  mirror, lamps to perform the flat field exposures and a Thorium-Argon (Th-Ar) lamp for high-resolution wavelength calibration. This unit is mounted before the Nasmyth platform at the F/15 focal plane. As an alternative calibration process, it is also possible to mount, on the transverse mirror, a iodine lamp ( $I_2$ ), which can be coupled to the optical path, in order to insert in the spectrum a set of calibrated absorption lines for precise wavelength calibration, and thus enabling a very stable radial velocities measurement, but with the inconvenience of mixing the spectrum with an overlapping "forest" of iodine absorption lines. Also, at the focal plane F/15, can be coupled image slicers (of Bowen-Walraven type).

The UVES *echelle*, at the construction date, was the largest monolithic diffraction device developed. The importance of this technological development resided in the possibility to increase the spectrograph spectral resolution until stellar absorption lines became resolved . Some years later, in December 2002, when the high-precision HARPS spectrograph (High Accu-

racy Radial Velocity Planetary Search object) came into operation on the 3.6 meters telescope at La Silla (Chile), with the aim of finding extrasolar planets, has been chosen the same kind of UVES' *echelle* to equip it.

The readout noise is less than 2 electrons for the EEV detector and less than 3 electrons for the MIT/LL detector, that for a 50 Kpixel/s reading speed at each gate. The detector's linearity variation is under 1% peak-to-peak for a dark current level of 0,5 electrons/pixel/hour.

The EEV CCD has a capacity of 225.000 electrons, with high quantic efficiency at ultraviolet range; while the MIT CCD has a capacity of 130.000 electrons and presents high quantum efficiency at the near infrared band.

The UVES spectrograph's blue arm has an optical field of 30,7x30,7 mm, so a single CCD detector (an EEV CCD-44) with a window of 2048×3000 pixels is sufficient to cover entirely its field of view. Therefore, it is necessary to resize the active observational zone, since the first and last 551 CCD's lines are discarded, living just the 3,000 interior lines in the read out mode. Also, the first physical 50 pixels are assigned to, at each CCD output gate, pre-scan operations.

For the detector's red arm system an 61,4x61,4 mm optical field is required, which implies that most of the two CCD pixels be active in the read out mode. The MIT CCD has only a 10 pixel pre-scan, assigned at the serial register, so it is mandatory to have 40 virtual pixels in order that the images coming from each one of the CCD's have the same size, given that the two CCDs are read in parallel (Dorn et al., 2000).The UVES CCD system of optical detectors uses the FIERA controller, the ESO's *standard* protocol.

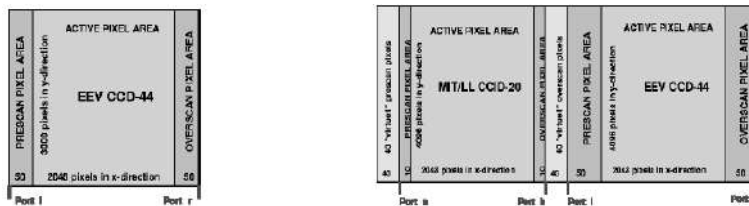


Figure 4.4: Observed images *setup* for blue arm configuration CCD (on the left), and for the two-CCD mosaic that compose the red arm's detector. (Dorn et al., 2000).

Each of the two arms is equipped with two diffraction gratings reflecting at the first spectral order; the separation of the orders has a typical value of 10 arc seconds.

The UVES can be used in conjunction with a multi-object spectrograph: Flames (*Multi Fibre Large Array Element Spectrograph*), so for this purpose it is equipped with ports for eight optical fibres with a diameter of 1 arcsec

each, six ports for observational targets and two for sky reading, all located at the red arm.

The auxiliary devices that make up the instrument include: calibration lamps, an iodine cell ( $I_2$ ) and a Thorium-Argon (Th-Ar) lamp for precision studies of radial velocities' wavelength calibration, *image slicers*, a *derotator*, a depolarizer and an ADC (atmospheric dispersion corrector).



Figure 4.5: Continuous flow cryogenic system (CFC), that keeps the detectors cooled by a continuous flow of liquid nitrogen, which surrounds the CCDs. CCDs used in astronomy must operate in the temperature range between 140 and 160 K. (Dorn et al., 2000).

The CCDs used in astronomy have to be cooled until 140-160 K in order to reduce the noise produced by the *dark current* to negligible values. Therefore, CCDs are mounted on a vacuum chamber cooled, in turn, by liquid nitrogen.

The cooling and thermal stability of CCDs is assured by a cryogenic unit which has a range of autonomy of at least two weeks. The cryostat developed by ESO, for this type of instruments, is based on a continuous flow cryostat unit (CFCs), wherein the unit of spare fluid is separated from the cooling element, which reduces significantly the dimensions of the apparatus attached directly to the sensors, see figure 4.5.



The temperature variation produces a pinstripe effect of spectral line shifts at the Thorium-Argon (Th-Ar) calibration lamp. The measurements lead to a high quality linear correlation for the obtained points and presenting a slope for the obtained linear regression equation of:  $\Delta X/\Delta T = 0.4\text{pixel}/^\circ\text{C}$ . The need of a good thermal stabilization is clear in order to achieve satisfactory results (see figure 4.6). With this kind of insulation in which the UVES' components are immersed in the cryogenic fluid, it is possible to achieve a residual thermal gradient of less than  $1^\circ\text{C}$  for a time interval of 12 hours.

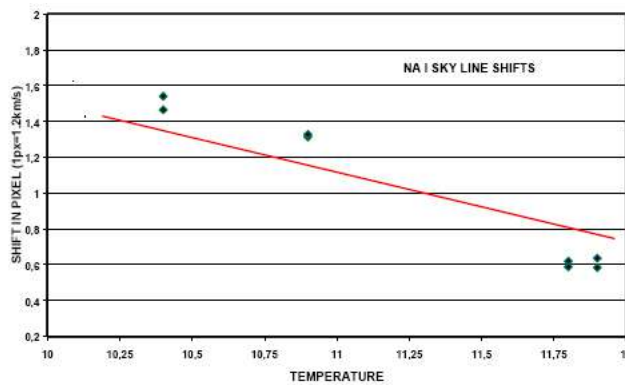


Figure 4.6: Study of the relation between temperature and spectral line shifts (in pixels), derived from the Th-Ar lamp spectrum's analyses. (D'Odorico et al., 2000).

The detection efficiency is the key parameter in evaluating the overall efficiency of an instrument, relative to its ability to collect scientific data. The parameter which succeeds in importance is the size of the spectral range covered by a single exposure. The two basic configurations of the UVES cover spectral ranges of 90 nm ( $\lambda_{center} = 346$  nm) + 200 nm ( $\lambda_{center} = 580$  nm) and of 100 nm ( $\lambda_{center} = 437$  nm) + 400 nm ( $\lambda_{center} = 860$  nm), i.e. for a single exposure, and respectively for each arm (blue+red arm). Note that the encompassed wavelengths have no intervals, except a 5-10 nm loss at the junction of the two CCDs that compose the detector's mosaic for the red arm.

On the other hand, the resolution depends on the sampling, both, at dispersion and cross-dispersion directions. For the typical values of the UVES spectral resolution with a slit width of about 0.8 arcsec (resolution of about 50,000), the spectral lines are sampled by an average of four pixels in the blue arm, and by an average of 5 pixels with the red arm. This high sampling (compared with similar instruments) is a significant advantage for the data

	Blue, EEV	Red Mosaic
Quantum efficiency	49% at 320 nm 56% at 350 nm 82% at 400 nm 88% at 500 nm	89% at 450 nm (EEV) 89% at 600 nm (EEV) 81% at 800 nm (MIT-LL) 46% at 900 nm (MIT-LL)
Number of pixels	2048 × 3000 (2048 × 4096, used in windowed readout)	4096 × 4096 (2048 × 4096 2 × 1 mosaic)
Pixel size	15 μm	15 μm
Gain (MIT-LL values in brackets)	low: 1.84 e <sup>-</sup> /ADU high: 0.54 e <sup>-</sup> /ADU	low: 1.6(1.5) e <sup>-</sup> /ADU high: 0.57(0.57) e <sup>-</sup> /ADU
Read-out noise fast read-out, low gain (slow read-out, high gain) Ultrafast readout, low gain	4.1 (2.1) e <sup>-</sup> rms	EEV 3.4 (2.0) e <sup>-</sup> rms MIT 3.8 (3.4) e <sup>-</sup> rms  EEV 4.6 e <sup>-</sup> rms MIT 4.85 e <sup>-</sup> rms
Saturation low gain (MIT-LL in brackets)	~65000 ADU	~65000 ADU (~43000 ADU)
Full frame readout (s) at 50 kpix, 2x2 bin at 225 kpix, unbinned at 625 kpix, unbinned	34 (1-port) 30 (1-port) 6.4 (2-ports)	45 (2-ports) 40 (2-ports) 10 (4-ports)
Dark current levels	0.4 e <sup>-</sup> /pix/h at -120°C	EEV 0.5, MIT 1.1 e <sup>-</sup> /pix/h at -120°C
Fringing amplitude at 850nm	-	EEV: up to 40% MIT: up to 20%
CTE	> 0.99993	> 0.99995
Read-out direction	in disp. dir.	in disp. dir.
Prescan, Overscan areas	Pix. 1-50 and 2098-2148	MIT: pix 40-50,2098-3008 EEV: pix 1-50,2098-2148
Flatness	< 15 μm peak to peak	< 60 μm peak to peak

Figure 4.7: UVES' nominal specifications, (ESO, UVE's manual).

reduction process and subsequent scientific analysis of the spectrum.

The target radiation collected by the system is partially lost through the detector's various elements, and in the case of weaker sources, the noise signal is comparable to the noise of the detector read-out and dark current noise. Since the signal-to-noise (S/N) increases with the square of the telescope's diameter, it was very important that we used a large diameter telescope class for these observations, in this case the Very Large Telescope (VLT).

In the cases when very bright objects are observed, where the photon noise is dominant, the use of a big aperture telescope is still a very relevant reason in order to achieve high S/N observations in reasonably short integration times.



Figure 4.8: UVES spectrograph's test bench mount of its diverse elements (image: ESO's *website*).

The efficiency of the spectroscope depends essentially on three factors: the spectral resolution ( $R$ ), the flux (proportional to the telescope's collecting area, and therefore, function of its diameter ( $S$ )) and the wavelength ( $\lambda$ ), coming to the overall estimated error of the radial velocity obtained (standard deviation), (D'Odorico et al., 2000):

$$1/\sigma_{R_V} \propto S^{0.5} \lambda^{0.5} R^{0.5} \quad (4.1)$$

Note that one of the ways to decrease the error in radial velocity retrievals while keeping the value of the spectral resolution ( $R$ ) and given a certain range of wavelengths, is to increase the diameter of the telescope's primary. Figure 4.14 shows the measurement of the efficiency of the telescope-detector

instrument, taken as a whole. The efficiency measurements were made from observations of two standard stars with full opening of the slits and refer to the top of each *echelle* spectral order. This confirms the choice of the VLT/UVES combination for measuring wind velocities in the atmosphere of Venus.

On the other hand, the most direct method to increase the spectral resolution ( $R$ ) would be, in turn, to use the largest possible *echelle* (monolithic scattering grating), which was secured, *a priori*, with the UVES and its top quality custom-made *echelle* (see figure 4.12).

The wavelength resolution depends on the slit width. Figure 4.15 illustrates the dependence between the spectral resolution and the spectrograph's slit width. The obtained results come from the quantitative analysis performed on the article by D'Odorico et al. (2000), in a study done to both arms of the spectrograph.

### 4.2.1 Telescope light path

The light entering the telescope is directed to one of two different gratings by a dichroic mirror (see "mode selector" in fig. 4.2). The radiation is then scattered by these two *echelle* gratings. After passing through a cross-disperser the radiation is then focused by dichroic cameras in CCD detectors described above, both the single CCD device (EEV) of the blue arm or in the mosaic device (EEV and MIT) from the red arm.

The optical beam after being diffracted by the *echelle* has a diameter of 200 mm. The parabolic collimators (who are off-axis) resend the beam towards the *echelle* of  $214 \times 840 \times 125$  mm at an angle of  $76^\circ$ .

Due to the large bandwidth wavelength covered by the spectrograph is essential to use the ADC (Atmospheric Dispersion Corrector).

The UVES uses an image *derotator*, an optical device that performs a rotation of the telescope's field of view by an given angle, called the position angle. We have used the *derotator* to align the slit with the planetary rotation axis. The position angle (PA) is measured in the plane of the sky, from North to East.

The spectroscope slit units are composed by two blades of reflecting aluminium (diamond machined), they are adjustable and provide a spectroscopic slit aperture range from 0.15 to 20 arcsec. The length of the device is 30 arcsec. The verification of the acquisition field and tracking is done using the slit viewer (a camera that "looks" at the blades of the spectral slit, thus providing an image of the target field).

	Blue Arm	Red Arm
Wavelength range	300-500 nm	420-1100 nm
Resolving power-slit product nm/pixel	41,400 0.0019 nm at 450 nm	38,700 0.0025 nm at 600 nm
Max. Resolving power (2-pixel sampling)	~80,000	~110,000
Throughput at blaze (TEL+UVES, no slit, no atm.)	12% at 400 nm	14% at 600 nm
Limiting magnitude (90m exp. time, $S/N=10$ , 0.7 arcsec slit, seeing 0.7)	18 R=58,000 at 360 nm	19.5 R=62,000 at 600 nm
CCDs	2048 × 4096 (windowed to 2048 × 3000)	two 2048 × 4096 (mosaic of different types)
Pixel (15 $\mu$ m) scale disp. dir. (varying along order) along slit (dep. on cross-disp.)	0.215" $\pm$ 20% 0.25" (CD1 and CD2)	0.155" $\pm$ 20% 0.18" (CD3), 0.17" (CD4)
Echelle (R4 mosaic)	41.59 g/mm	31.6 g/mm
Cross dispersers	CD1: 1000 g/mm	CD3: 600 g/mm
Blaze wavelength	430 nm	560 nm
Blaze wavelength	CD2: 660 g/mm 460 nm	CD4: 312 g/mm 770 nm
Typ. wavel. cov. CD1 and CD3 (CD2 and CD4 in parenthesis)	85 (126) nm in 33 (31) orders	200 (403) nm in 37 (33) orders
Min. order separation (standard setup)	10 arcsec (40 pixels)	9 arcsec (51 pixels)

Figure 4.9: Characteristics and observing capabilities of the UVES spectrograph. UVES' manual - *Paranal Science Operations*.

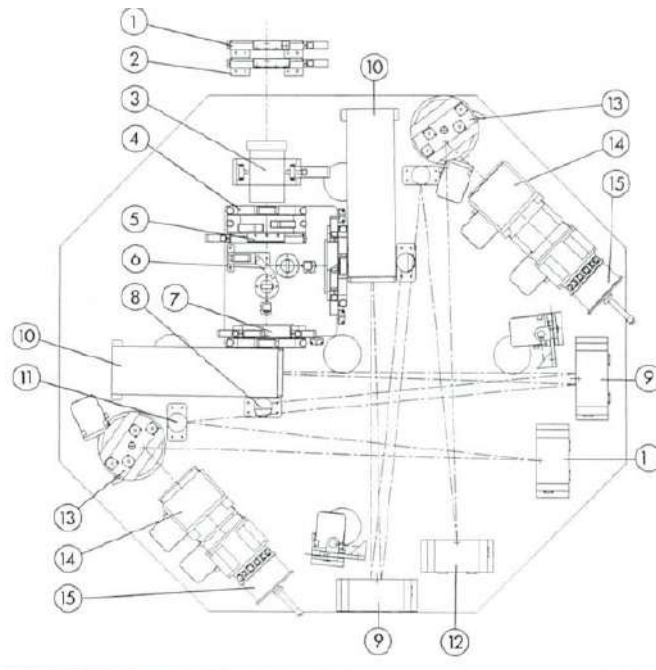


Figure 4.10: Diagram of UVES components and optical light path. See also figure 4.2. (Dekker et al., 2000).

### 4.2.2 Opto-mechanical design

The instrument consists of two main parts: the first is mounted on the rotor, which remains stationary while the telescope adapter turns to track the motion in the sky of the target field. This part includes the calibration system, a removable iodine cell, the image slicers, one optical *derotator* (permanently installed in the optical beam path). The second part consists on the spectroscopic *echelle*, the two arms cross disperser, that is mounted on one of the steel table fixed to the telescope's Nasmyth platforms.

A matter of extreme importance in the UVES' construction project was to increase the spectrograph's opto-mechanical stability in order to achieve maximum control and reduce shifts due to variations of temperature and pressure.

The perturbations imposed by the environment were seized by installing the instrument in a controlled environment *Coudé* style room, the mobile components in the optical path were minimized to the extreme, with most of the components fixed to the telescope's Nasmyth platform. Beyond the two slits of the spectrograph, the unique moving parts found in the optical path are the cross disperser and cameras.

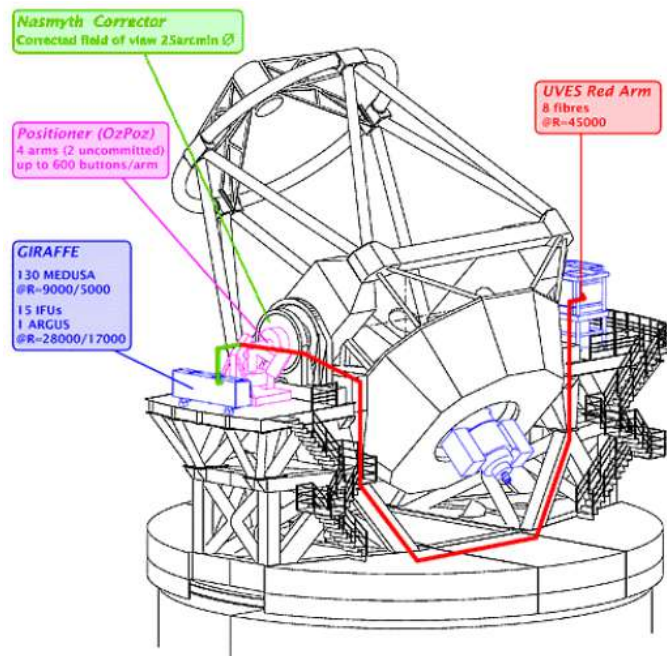


Figure 4.11: Coupled instruments to the UT2 (*Kueyen*) telescope of the Very Large Telescope (VLT) at Paranal, Chile, (scheme: ESO's website).

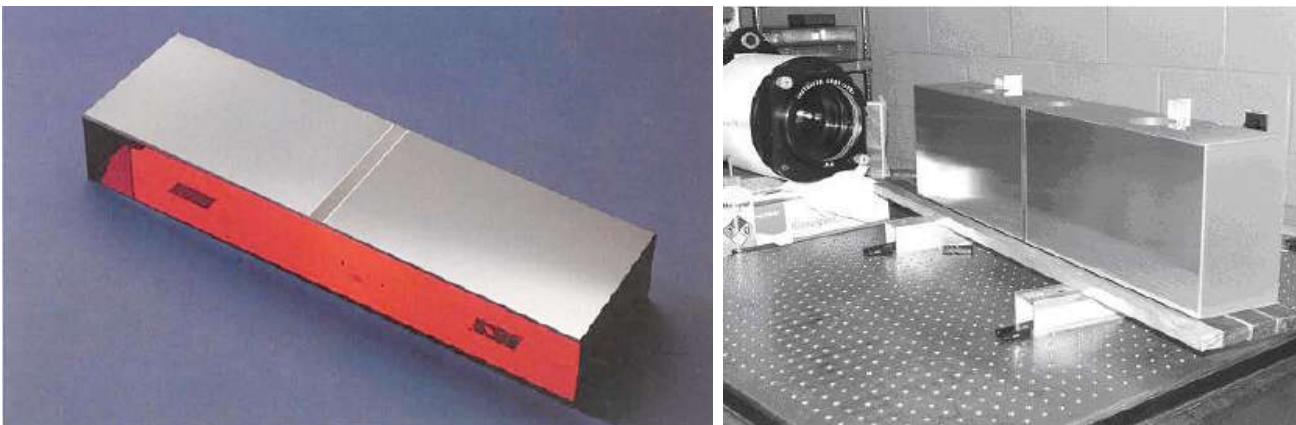


Figure 4.12: UVES monolithic *echelle* grating. This device is a piece of the highest technology in the field of high precision spectroscopy at the service of astronomy and astrophysics, (Dekker et al., 2000).

The optical table containing the instrument's elements has a length of 1.7 meters and is made of *invar* composite (since the coefficient of expansion of the *invar* is much lower than that of steel) and is placed at one of the Nasmyth platforms. Only the calibration unit, the image *derotator* and the image slicer are placed at the rotor's area. All other elements are on the optical table in order to allow access to each part of the device and to facilitate the instrument's operation as a whole.

### 4.2.3 High resolution spectroscopy with UVES

The UVES combines an optimal balance between spectral resolution and wavelength coverage. This stems from the versatility of choice options between the two arms of the spectrometer and the judicious use of the image slicers and cross-dispersers. The blue arm, which covers wavelengths between 0.3 and 0.5  $\mu\text{m}$ , has a resolution of 2 pixels, up from 90,000. The red arm, in turn, covers the range of 0.42 up to 1.1  $\mu\text{m}$  with a resolution of 2 pixels as well, up from 120,000 (Dekker et al., 2000).

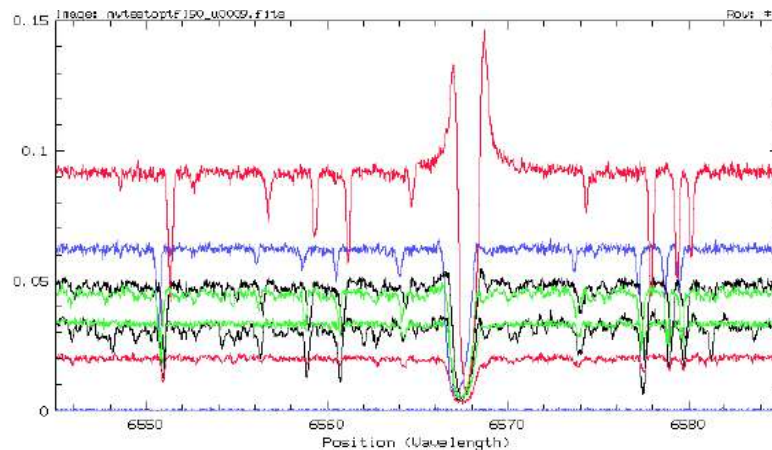


Figure 4.13: Example of the retrieved spectral orders seen after the data reduction process applied to the FITS science images provided by UVES. Image: ESO, UVES' *website*.

It is noteworthy the jump in efficiency near 860 nm, which is due to the higher efficiency in the red CCD MIT for the same area of the spectrum covered by the EEV as well. The efficiency reduction at the extreme ultraviolet direction and also at the far red wavelengths, is due primarily to decreased efficiency of CCDs.

The measured difference for two targeted stars shows the extreme precision of the instrument. With this level of efficiency and the radiation collector



power of the VLT, the UVES presents itself as a top instrument, within the high-precision spectrographs coupled to large telescopes (D’Odorico et al., 2000).

#### 4.2.4 High-precision wavelength calibration

In a first approach the wavelength calibration is made by matching the positions of spectral lines obtained from the source and the position of well known wavelength from a calibration exposure’s spectral lines. The deviations between the wavelength of the target source spectral lines and reference spectral lines, obtained at this first calibration phase, are named the long-term drifts. However, this wavelength preliminary determination is not precise enough to obtain the accuracy needed to perform the high-resolution spectroscopy required.

Then, a finer tuned wavelength calibration is performed, in order to eliminate the residual deviations of wavelengths finer drifts. With this purpose is used, preferably, the calibration technique based on the reference spectra from a Thorium-Argon (Th-Ar) lamp exposure. For observations analyzed in this work, a special request was made in order to perform specific Th-Ar calibration observations, together with each observations block.

The UVES also enables the use of another kind of wavelength calibration process, the Self Calibrating Wave Technique, which resorts to the iodine cell ( $I_2$ ). In this technique the absorption spectrum of iodine is superimposed to the spectrum of the target (e.g. the spectrum of a star under study).

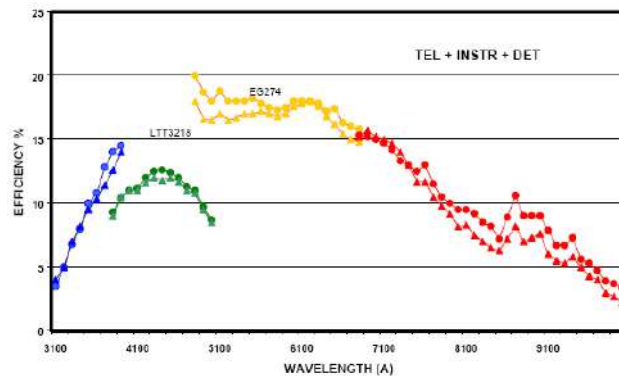


Figure 4.14: UVES efficiency, telescope included, from dichroic observations of two standard stars. The four distinct zones refer to the four baseline wavelength ranges. (D’Odorico et al., 2000).

This procedure will introduce in the spectrum under study a set of several reference lines (well known absorption lines of iodine). The limitations of

this technique lie in the fact that the iodine spectra covers only the range of wavelengths between 500 nm and 600 nm in the visible range. On the other hand, as the absorption spectrum is constructed from target radiation, this can become a serious problem when the target sources are already quite weak, since the iodine cell could absorb till 50% of the incident radiation.

The wavelength calibration technique based in exposures of a Thorium-Argon lamp, sequential reference technique, has the advantage of no longer "consuming" the target source radiation, because it performs a sequential exposure of a Th-Ar calibration lamp. Another advantage is the range of wavelengths covered, which in this case extends from 380 to 690 nm.

This technique relies on the assumption that the two spectra will follow a similar path on the detector, the one from the target and the one from the Th-Ar lamp exposure, so if there is an instrumental drift during the measurement process, both spectra are affected on the same way by the instrumental drift. This technique was already used before by the spectrograph Elodie, and is now used by various high-resolution spectroscopy instruments, such as HARPS.

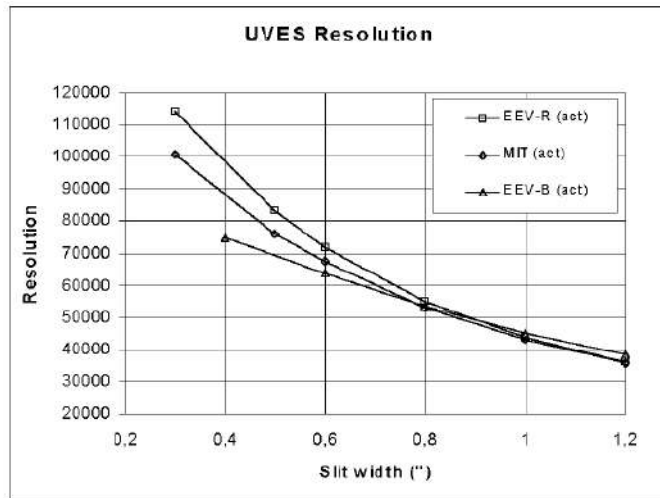


Figure 4.15: Spectral resolution as a function of the slit width, for the CCD on the detector's blue arm (EEV-B) and for the two CCDs that composes the red arm's detector mosaic (EEV-R and MIT), (D'Odorico et al., 2000).

This technique also has the advantage of high optical stability of the Th-Ar calibration source. It has a high optical efficiency, requires less exposure time, allows easy data reduction (almost in real time) and a good signal to noise ratio (S/N).

In order to be able to measure Doppler wind velocities at Venus, from the

ground, it is necessary to obtain high-precision measurements of radial velocities (RV). This required the use of a spectrograph of high accuracy (such as UVES) a very broad spectral window, very stable reference spectra (obtained by means of the already explained calibration methods), supplemented by an effective data reduction process. These techniques are also used in the demanding field of exoplanet detection where it is crucial to obtain the highest possible spectral resolution in order to obtain accurate radial velocities.

In the case of very faint stars or in the case of large target fields (such as the study of Venus atmosphere), the use of large mirrors in order to collect the radiation from the target source, become fundamental to increase the spatial resolution at extended sources (case of the Venus' atmosphere) or to improve the detection capability (case of weak sources).

On the other hand a spectroscope with the characteristics of HARPS, may be preferred in the study of individual objects (the case of exoplanets search) because of its excellence opto-mechanical stability.

In the case of HARPS, at the 3.6-meter NGT telescope at ESO's La Silla (Chile), for the detection of exoplanets, stars referenced in this kind of research programme are in general relatively close stars. The optimisation of the radial velocities accuracy makes instrument stability a preferential issue, rather than the need for a very large collecting area. It is also noted that this instrument was designed for one very specific purpose (the search for exoplanets), not having in any way the versatility that highlights UVES.

The method of radial velocity (RV) is limited to establishing the observer's line-of-sight component of the velocity, and is not sensitive to inclinations of the orbit or the transverse components of velocity relative to the direction of the observation through the telescope at the Earth's surface. For these reasons, the measurements obtained by our work, are the global Doppler velocity of Venus' atmospheric winds and must be de-projected from the line-of-sight. So, the measured Doppler velocity retrieved must be affected by a geometric factor in order to correct it from its intrinsic projection.

## 4.3 Observations with UVES

### 4.3.1 Objectives

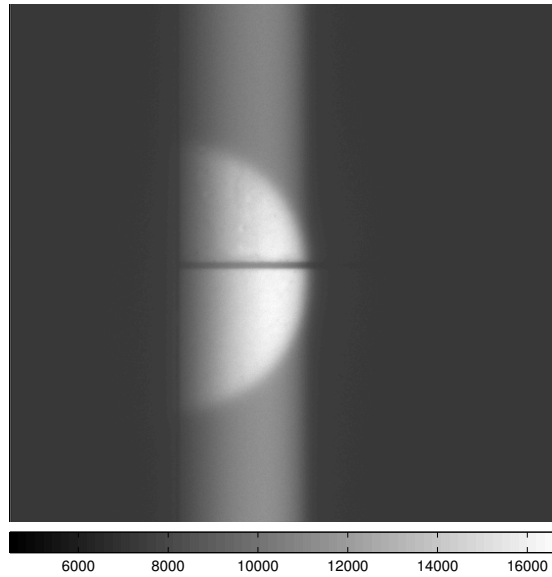


Figure 4.16: Example image from the UVES slit viewer camera, showing one of the positions of the spectroscopic slit on the disk of Venus, for one of the offsets with the slit perpendicular to the rotation axis.

Since the atmospheric motion induces into the light scattered by cloud particles, a wavelength shift proportional to the wind velocity, we applied Doppler velocimetry to the radiation back-scattered by the cloud top layer (about 70 km altitude), to study the latitudinal wind velocity profile, local time distribution of the winds, as well as its variability, in this atmospheric region of the planet's dayside.

The technique is based on the method of absolute accelerometry proposed by [Connes \(1985\)](#), described in detail in the next chapter. This method has been successfully validated by its application to Io ([Civeit et al., 2005](#)), and was first applied to measure the winds on Titan ([Luz et al., 2005a, 2006](#)).

The estimation of the exposure time and signal to noise ratio were made

using the instrument exposure time calculator (UVES ETC). A calibration special request was made, in order to obtain additional Th-Ar lamp calibration exposures given the specific need of high-accuracy in the wavelength calibration to determine high-precision radial velocities. The magnitude of Venus during this period was  $1.52 \text{ arcsec}^{-2}$ .

Exposure times were of 1 second for science observations with the red arm of the spectrograph (0.5 seconds for observations with the blue arm in dichroic mode). Were also obtained calibration exposures of 15 seconds.

The proposal was made by: David Luz (CAAUL), Emmanuel Lellouch (Observatoire de Paris), Thomas Widemann (Observatoire de Paris), Olivier Vitasse (ESA) and Jean-Loup Bertaux (Service d'Aéronomie).

The observations were carried out at the Very Large Telescope (VLT) at Eso's Chilean facility in Cerro Paranal, in two nights in May and June 2007. Since there was no critical time window, they were performed in service mode. Other observations were scheduled but were never executed due to seeing and weather constrains.

The advantage of this instrument is three-fold: (i) the availability of a large band pass (the entire 300-1100 nm wavelength range can be covered with the appropriate combinations of dichroics and cross-dispersers); (ii) the large collecting area of the telescope; (iii) the small pixel size ( $15\mu\text{m}$ , which represents approximately 0.2 arcsec in our observations) and the mapping capability of the instrument. The first two aspects allow a large gain in rms accuracy in retrieving the wind field, while the third allows both a simultaneous comparison of wind velocities measured in different points of the disk and seeing-limited spatial resolution. Therefore, small scale spatial variability with latitude and local solar time can be studied.

The observations with the UVES red arm were performed at a central wavelength of 580 nm. Additional observations were made in dichroic mode at central wavelengths 437 and 860 nm (using both the blue and red arms of UVES), but were severely underexposed and were discarded from further analysis. With the CD3 cross disperser used in these observations, the EEV detector covers the wavelength range between 480 and 570 nm in 23 spectral orders, while the MIT detector covers the region between 590 and 670 nm in 16 spectral orders.

### 4.3.2 Description of Observations

In order to cover a representative range of latitudes and longitudes on Venus' dayside hemisphere (figure 4.16) a long slit configuration was used (0.3 arcsec-wide and 20 arcsec-long for the entire slit length). The narrow slit width compared to the large angular size of the planet allows a direct determination

of latitudinal (figure 4.17a) or longitudinal (figure 4.17b) variation of the zonal winds in both the northern and southern hemispheres.

The observations were made when Venus was near greatest Eastern elongation (phase angle  $82.9^\circ$  and  $87.7^\circ$ , see Table 5.1), allowing observation of both the planetary limb and terminator simultaneously. As the sub-solar point was near the limb, the central meridian (and Venus' rotation axis) was close to the evening terminator. The seeing conditions were good on the night of 05/27 (between 0.54 and 0.58 arcsec), but considerably poorer on the night of 06/04 (between 1.23 and 1.54 arcsec) and sky transparency in the latter was also affected by passing clouds.

The fact that Venus was in its greatest elongation made possible to obtain images of the planet with large apparent angular size ( $\sim 10$  arcsec). On the other hand, the high phase angle maintained the target away from the Sun, which was essential for the safe operation of a telescope as large as the VLT (8,2 m).

In the dates when the observations were taken, Venus was near its maximum elongation (phase angle near  $90^\circ$ ). One of the reasons behind this choice was the possibility to be able to observe simultaneously the day and the night hemispheres.

Two major observational configurations were set up by using the derotator (a prism enabling field rotation by any given position angle relative to the celestial North-South direction). In the first configuration (hereafter called PL) the slit was oriented parallel to the Venus rotation axis, whereas in the second configuration (hereafter called PP) it was aligned perpendicularly to the axis. In addition, the slit was offset in the East-West or the North-South direction in order to cover different regions of the disk (see figure 4.17).

The latest is the only configuration (PP) in which we can calculate the absolute velocity of the zonal wind. To do this, we must admit that along the parallel where the slit is, the zonal wind component is uniform.

In the PL configuration, three offsets were applied: two with the slit placed over the central meridian and centered at 7 arcsec below and above the equator, referred to as positions 1 and 2, and a third offset by 8 arcsec to the West with the slit centered at the equator (position 3). Three exposures were obtained for each offset in this configuration (see table 4.2).

In the PP configuration, the first offset placed the slit center 10 arcsec south of the equator and 7 arcsec west of the rotation axis, and in the following offsets the slit was sequentially moved north by 2 arcsec ( $\sim 10^\circ$  latitude at low latitudes) relative to its previous position. Two exposures were obtained for each offset in this configuration. Only a subset of these offsets were used for analysis (see table 4.2 and fig. 4.17).

The target acquisition and guiding were done automatically, based on

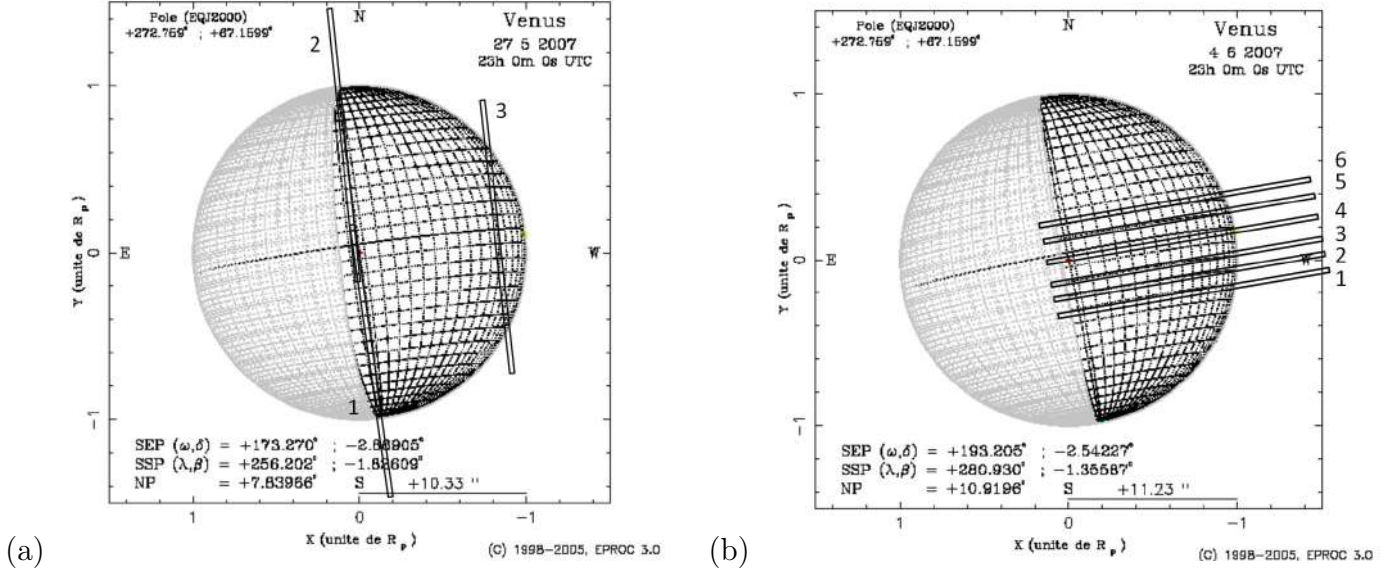


Figure 4.17: Geometry of the observations, showing the various slit position offsets on the planetary disk. (a) Case PL: slit parallel to the planetary rotation axis. (b) Case PP: slit perpendicular to the rotation axis. Slit positions are numbered (see also table 4.2).

ephemeris data provided in advance to the telescope operator. After acquisition, the position of the slit was also visually confirmed in an image of the slit viewer camera, and maintained via pointing corrections performed by the secondary guiding system. Since the Venus brightness implies very short exposure times (1 s in this work, using the neutral ND3 pre-slit filter and the SHP700 filter), target drifts are negligible. VLT pointing and UVES offset uncertainties are both equal to  $0.1''$  (nominal value), and we take as the global positioning error of the slit  $\sigma_{tot} = \sqrt{\sigma_{pointing}^2 + \sigma_{offset}^2}$ , or  $0.14''$ . The detector pixel dimension is  $15 \mu\text{m}$  and the measured pixel scale in our observations presented an average of  $0.183 \text{ arcsec/pixel}$ . The slit's active sounding window correspond of 61 detector's pixels that provided an astonishing ground-based spatial resolution, where each pixel had an average equivalent dimension of  $107 \text{ km}$  on the planetary surface (at disk centre). The  $0.3\text{-arcsec}$  slit width thus corresponds to an angle of  $2.6 \pm 1.2^\circ$  in latitude at disk center.

Since Venus is an extended target and the derotator was used in order to orient the slit in each specific configuration, the atmospheric dispersion corrector (ADC) was employed. The ADC partly compensates for differential refraction in the terrestrial atmosphere, which is highest in the elevation

Date	Position Angle	Apparent Radius	Sub-solar Latitude	Phase Angle
27 May 2007	+7.84°	10.23''	-1.83°	82.9°
4 June 2007	+100.92°	11.23''	-1.36°	87.7°

Table 4.1: North Pole position angle, apparent radius of Venus, latitude of sub-solar point and phase angle at the dates of the observations.

direction and at the blue end of the visible range.

In order to achieve accurate wavelength calibration, to check for instrument stability and to correct for optical slit curvature, exposures of the built-in Thorium-Argon (Th-Ar) lamp were taken after the science exposures for each offset in case PP, and before and after each observing block in case PL. These calibration exposures were important in correcting for the slit image curvature effect.

A derotator has been used to achieve a perfect slit's alignment with the planetary rotation axis (in order to align the 0.3-arcsec aperture between the planetary axis and the telescope field). This instrument consists in a prism that bends the telescope beam in order to adjust the target field with the plane of the sky. Was also used an atmospheric dispersion corrector (ADC) that has the task of compensating the atmospheric refraction. Another ADC relevant effect is to ensure the spatial consistency of the images in different wavelengths.

In the case of our observations, Venus was so bright that implied short exposition times, turning the guiding a relatively low importance matter. In fact were made exposures of 1 second. Nevertheless, most of the slit viewer images were overexposed. The instrumental assembly with which the observations were made (red arm), were characterized by using the ND3 pre slit neutral density filter, the red filter SHP700 and the cross-disperser unit 3.

The slit dimensions were set for a fixed width of 0.3 arcsec and the length of 20 arcsec, with this long slit configuration and the geometry of the observations performed was possible to cover a representative range of latitudes and longitudes on Venus dayside hemisphere (figure-4.17). In order to achieve very accurate wavelength calibration was made a calibrating exposure to the UVES Thorium-Argon (Th-Ar) lamp immediately after the science exposures for each offset.



Slit	Offset	Date (dd-mm-yy)	Time UT (hh:mm)	N	Lat	Long	Airmass	Seeing ( $''$ )
PL	1	27-05-2007	22:50	3	46.2 S	0	2.36	0.54
PL	2	27-05-2007	22:54	3	40.2 N	0	2.41	0.58
PL	3	27-05-2007	23:03	3	1.9 S	51.5 W	2.56	0.58
PP	1	04-06-2007	23:02	2	34.3 S	48.9 W	2.38	1.25
PP	2	04-06-2007	23:03	2	23.1 S	42.7 W	2.40	1.23
PP	3	04-06-2007	23:05	2	12.6 S	39.7 W	2.43	1.38
PP	4	04-06-2007	23:07	2	2.3 S	38.6 W	2.46	1.54
PP	5	04-06-2007	23:09	2	7.9 N	39.0 W	2.49	1.35
PP	6	04-06-2007	23:11	2	18.6 N	41.1 W	2.52	1.38

Table 4.2: Summary of the geometry and circumstances of the observations. The cases PL and PP correspond to slit orientations parallel and perpendicular to the Venus rotation axis (slit position angle of  $7.84^\circ$  and  $100.92^\circ$ ), respectively. The offset number represents a position on the disk, N is the number of exposures taken for each offset and the times are given at the start of the first exposure. The integration time for all exposures was 1 second. Lat and Long are the coordinates of the slit's central point on the disk for each offset. The latitude and longitude values given are affected by the VLT/UVES nominal pointing and offset uncertainty, with a total uncertainty  $\simeq 0.14''$ .

### 4.3.3 Data

The seeing at the beginning of the observations was 1.2 and the transparency of the sky was described as clear sky. The airmass was 3.00 and the fraction of Moon's illumination was 1.00. The Moon was located at an angular distance from the target of  $30^\circ$ . The airmass measures the optical path that the radiation from a celestial target has to traverse through the Earth's atmosphere. The radiation from the target is attenuated by the scattering and atmospheric absorption until reaching the telescope at the ground. This effect is proportional to the thickness of the atmosphere to be traversed by the radiation and therefore is more significant when the target is low on the horizon.

The source target was selected as extended type. For each position in longitude of the slit on the disk were selected two positions, one further north, and another further south, for each offset were made three exposures. After, the slit was moved to the new position and so on. To this block of observation the slit was placed in a total of 5 different positions, obtaining a total of 15 science observations (see figure 4.17).

All files were produced in FITS format. Calibration files consist of *Flat Field* and *Bias* files, as well as wavelength calibration (Th-Ar) files and spectral orders definition files (*Order definition frame*). All these files will be used in the data reduction process described in detail below.

Each pixel has a size of  $15 \mu\text{m}$ , which corresponds to  $0.215 \text{ arcsec}$  ( $\pm 20\%$ ), or  $0.25$  ( $\pm 20\%$ ) if cross disperser CD # 2 is used for blue arm and  $0.155 \text{ arcsec}$  ( $\pm 20\%$ ) for red arm, or in the case of using the cross disperser CD # 3:  $0.18 \text{ arcsec}$  ( $\pm 20\%$ ).

The separation between the spectral orders' centers is of 10 arc seconds in the blue arm and about 9 arc seconds at red arm. Figure 4.18 shows an example of an *echelogramme* obtained with the blue arm.

### 4.3.4 Problems that affected the observations

The observations made on 04/06/2007 were disturbed by the appearance of clouds that negatively affected many of the PP slit's configuration exposures. These observations could not be repeated.

Another issue was that the elongation of Venus is always very small as seen from Earth, meaning that the target is always very low and close to the horizon in the sky. Therefore, observability periods were short and there was little time for each observation at reasonable conditions (about 1 hour), and some of the exposures were made with Venus already very low in the sky and at high airmass. That was the case that happened to the block of



Figure 4.18: Example *echelogramme* showing the various spectral orders. Many Fraunhofer absorption lines are visible along the spectral orders.

observations made at 24/05/2007, which had to be repeated at 26/05/2007.

From the total observational time requested, to ESO, only a fraction was executed, which was reflected in the no-realization of most scheduled observations with spectroscopic slit perpendicular to the planetary rotation axis. This fact limited some of the proposed research lines in our programme.

## 4.4 Doppler velocimetry with UVES

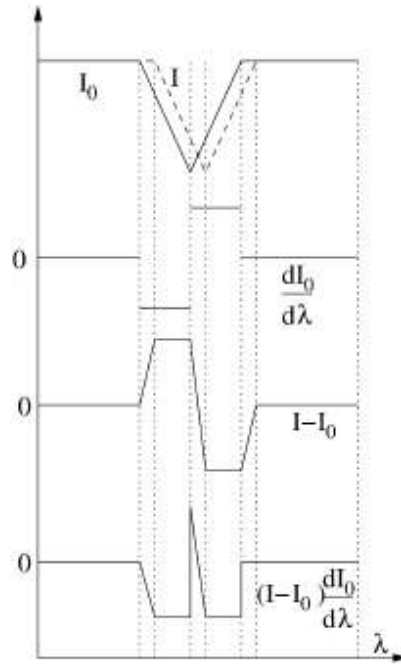


Figure 4.19: Scheme of the measurement process in case of pure photon noise. (Luz et al., 2005a)

The methods developed in recent planetary wind measurements in the visible range using high-resolution spectroscopy (Civeit et al., 2005; Luz et al., 2005, 2006; Widemann et al., 2007, 2008) address the fundamental problem of maintaining a stable velocity reference. There are systematic errors involved in trying to measure absolute wavelengths or Doppler shifts with grating spectrographs. The reason is that for simple line shifts the dispersion law and instrumental uncertainties cannot achieve an absolute accuracy better than about 100 m/s, while in measuring the global wind circulation at cloud tops, we are addressing wind amplitude variations or wind latitudinal gradients on Venus of the order of 5-10 m/s projected on the line-of-sight. One possible solution is therefore to measure relative Doppler shifts between two sets of absorption lines. The Doppler velocimetry method used is an adaptation of the Absolute Astronomical Accelerometry (AAA) developed by Connes (1985).

The Doppler measurement is based on an optimal weighting of the Doppler shifts of all the lines present in the spectrum, with relation to a reference

spectrum. In this work the measured and reference spectra are taken *simultaneously*, with the latter being taken at the center of the slit. The algorithm generates line of sight Doppler shifts as a function of pixel number along the slit length, which is converted as a function of latitude (in the PL case) or longitude (PP case), for each exposure. We then computed the average of the set of two or three velocity profiles associated with each slit position offset.

For the data analyzes procedures I adapted a software package previously developed and validated in [Civeit et al. \(2005\)](#) and subsequently used for retrieving Titan's winds ([Luz et al., 2005a, 2006](#)). The scripts are in Matlab programming language. I adapted the method to long-slit measurements of a large target body and to perform several corrections, in particular: a) by introducing a geo-referencing correspondence between pixel location and geographic coordinates; b) to change the size of the active sounding window of the slit; c) to correct for slit image curvature; d) to correct for the systematic shift known as the Young effect (Y); e) to correct for the specific geometry of the observations; f) to remove telluric lines from the spectra (though this correction proved negligible in comparison to other effects); and g) I also changed the way of correcting the slit curvature image, fact that proved to be crucial to improve the data reduction process. A batch of new tests were also performed. All this items will be discussed in detail in the following.

The data were first de-biased and flat-fielded based on sets of five bias and five flat-field images obtained on each night of observation. Master bias and master flats were constructed by computing the median of each set. Then that median was subtracted from the science images.

Wavelength calibration observations were made with a built-in Thorium-Argon lamp. This allowed producing a dispersion relation function through an interpolating process, yielding a high resolution correspondence between each pixel in the *echellogramme* and its respective wavelength.

Due to a gap of 10 nm between the two CCD chips in the red arm detector, the spectra recorded in the EEV and MIT chips need to be extracted and treated separately. Spectra of different spectral orders were also extracted and analyzed separately (see figure 4.21). The extraction has been performed by a spline interpolation along the central order. In order to avoid overlaps of spectral orders, the active sounding window of the slit was restricted to a size of 61 pixels on the detector (which corresponds to a section of approximately 11 arcsec of the total 20 arcsec slit length), with a spatial resolution of  $\sim 108$  km/pixel at disk center. Since the average pixel scale for the UVES red arm is 0.183 arcsec/pixel, the spatial extension on the planetary disk corresponds, in fact, to a rectangle with dimensions  $0.183'' \times 0.3''$ . At the extraction stage, bad pixels in the detector (pixels with an abnormal response or pixels hit by cosmic rays) were discarded by using a pre-prepared mask.

In a grating echelle spectrometer, the monochromatic image of a long slit will appear curved. This slit image curvature, on the order of a fraction of a pixel, induces non-negligible errors in the wavelength calibration and velocity retrieval. This effect has been corrected using the Th-Ar spectrum. Both shifts were measured using the velocimetry algorithm described in Connes (1985). On this way, the spectral lines deviations were corrected from the spurious shifts due to the *echelle* image's curvature.

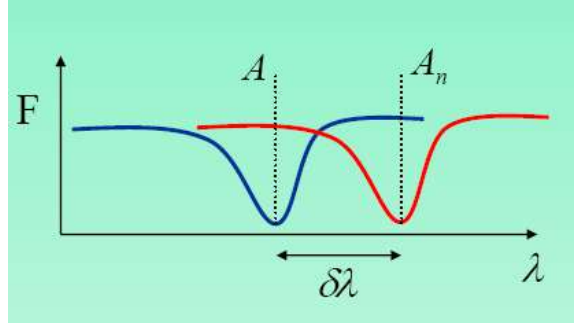


Figure 4.20: Algorithm for obtaining the radial velocity using only a single spectral line shift. (Luz et al. 2009).

This section presents a short description of the algorithm, which is at the basis of the process adapted by me for the wind velocity retrievals in this work.

Let us start assuming that wind velocities were retrieved based in the shift of just one line's Doppler deviation, with the basic Doppler shift equations:

$$\frac{\delta V_n}{c} = \frac{\delta \lambda}{\lambda} \quad (4.2)$$

Here, Taylor's first order approximation can be used for the deviation of the spectral lines, since the shifts are much smaller than the line widths.

$$I_n - I \approx \frac{\partial I}{\partial \lambda} \delta \lambda \quad (4.3)$$

Where  $I_n$  is the location of the shifted line and  $I$  the position of the same line in the reference spectrum. Combining the two previous equations yields the relative velocity between the reference spectrum and the shifted spectrum.

$$\frac{\delta V_n}{c} = \frac{I_n - I}{\lambda \frac{\partial I}{\partial \lambda}} \quad (4.4)$$

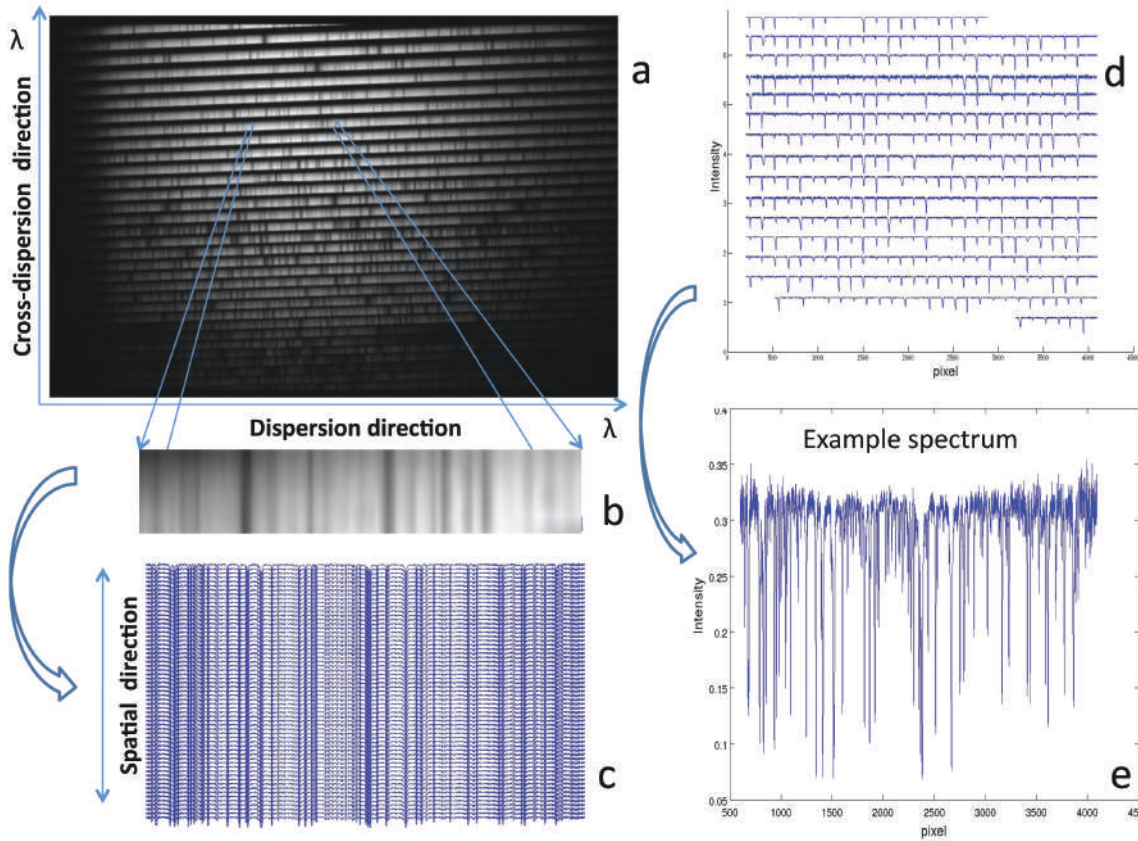


Figure 4.21: Steps for obtaining spectra from a UVES echellogramme (example). (a) Raw echellogramme showing the spectral orders for one of the detectors. (b) Magnification of part of one order, where absorption lines (dark vertical bands) are visible. From each order, a stack of 61 spectra are extracted (the active window of the slit). (c) Set of 61 spectra, with each one corresponding to one pixel in the slit's active window. (d) Each spectrum is divided into 16 orders in the MIT detector and 23 orders in the EEV detector. The plot shows an example of the 16 components of an MIT spectrum, each coming from one spectral order. (e) Example spectrum from one order and one location in the Venus disk.

Or, considering the same result at the location of the pixel “i”, which it is more convenient to the data analyses:

$$\delta v_i = \frac{c}{\lambda(i)} \delta \lambda_i = \frac{I(i) - I_o(i)}{\frac{\lambda(i)}{c} \left( \frac{\partial I_o}{\partial \lambda} \right)_{\lambda=\lambda(i)}} \quad (4.5)$$

The index “i” refers to each pixel along the slit and the index “o” refers to the reference pixel (along this work the reference is the slit’s central pixel).

However, the Doppler shifts associated with single-line wind velocities to be measured (on the order of a few  $ms^{-1}$ ) imply a spectral resolution (R) of about  $10^6$ . Which is impossible with current instruments.

By analyzing the whole spectral range rather than line by line, namely using the Absolute Astronomical Accelerometry (AAA) technique, allows to achieve a theoretical precision of a few m/s. This is done by performing a weighted average of the single-line Doppler shifts, using the inverse of the variance as a weighting factor:

$$\delta v = \frac{\sum \delta v_i \omega_i}{\sum \omega_i} \quad \text{where} \quad \omega_i = \frac{1}{\sigma^2[\delta v_i]} \quad (4.6)$$

The shift of solar Fraunhofer lines scattered by clouds tops is measured simultaneously on the full high-resolution spectrum between 480-570 nm (blue region, EEV CCD) and 590-670 nm (red region, MIT CCD). The visible solar spectrum contains around 4400 solar lines.

The weights ( $\omega_i$ ) are the inverse of each individual line velocity contribution variance. For that we must rely on the assumption that the representative noise is only of photonic origin. The relevance of this assumption relates to the fact that, doing so it is possible to obtain the radiation intensity’s variance directly ( $\sigma^2[I] = I$ ) and thus derive the equation for calculating each line relative velocity’s variance contribution ( $\sigma^2[\delta v_i]$ ).

The overall uncertainty in the differential velocity determination comes:

$$\sigma[\delta v] = \frac{1}{\sqrt{\sum \omega_i}} \quad (4.7)$$

For each exposure, the velocity profile has been measured as a weighted average of the shifts for the various spectral orders. The dispersion of the measurements obtained from the different orders is the main source of uncertainty for Doppler shifts. As for pointing, the combined pointing and offset error of the VLT/UVES is around 0.14". The PFS error due to the seeing, around 0.6" in the PL case and 1.3" in the PP case, is dominant.

The profiles of Doppler shift are impacted by two observational biases affecting the measurement of the zonal winds: the geometric projection factor



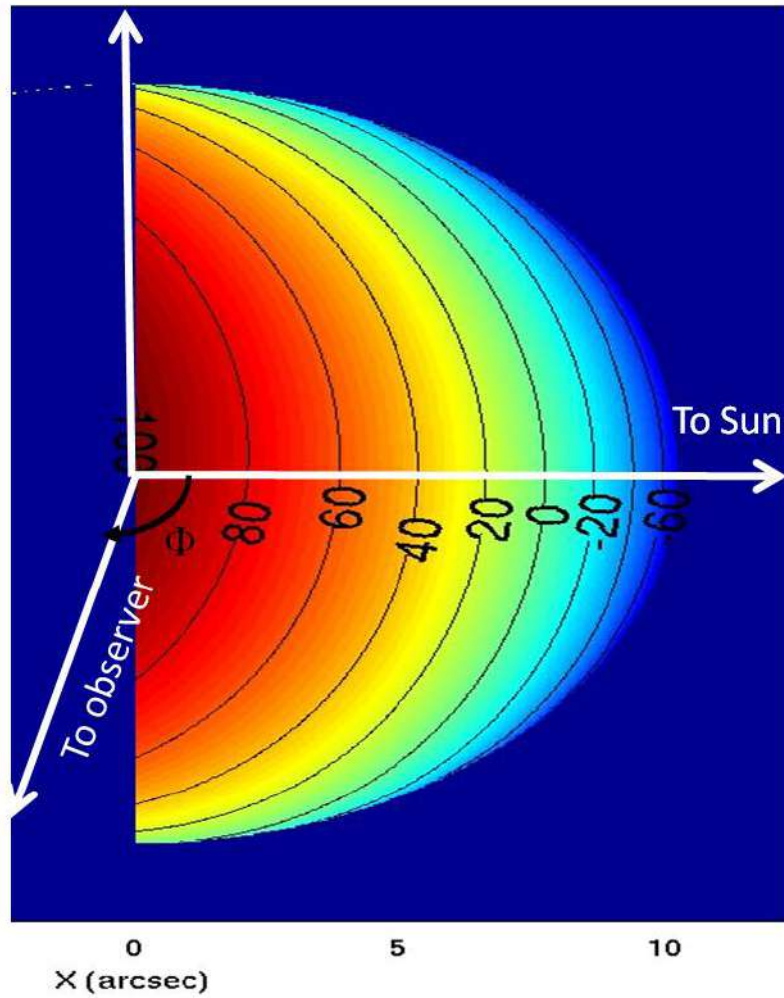


Figure 4.22: Isolines of geometric projection factor. The Doppler shift has been computed assuming a solid body rotation of the atmosphere with an equatorial velocity of 100 m/s. Note the existence of a local time meridian where the projection factor is null due to the compensation between the redshift induced by absorption and the blueshift induced by emission towards the observer. For the June 4 observations, the bisector is at  $-43.85^\circ$  longitude.

(F) and the Young effect (Y), which result from the observational geometry and the finite solar diameter as seen from Venus. Furthermore, the line-of-sight Doppler shift at each pixel on the planetary disk results from the combination of the relative Earth-Venus orbital motion ( $\sim -14\text{km/s}$ ), the retrograde planetary rotation (1.81 m/s at the equator, which is negligible in comparison to wind velocities at low latitudes) and the cloud particles' motion relative to the ground. Orbital velocities were retrieved from the NASA Horizons ephemerides website. Overall, the absolute Doppler shift measured along the line of sight at any given point in the slit is:

$$\Delta V = F \cdot V + Y + OS. \quad (4.8)$$

The orbital shift ( $OS$ ) induced by the relative Earth-Venus orbital motion is the same for every point of the slit and cancels when relative Doppler shifts are computed between two spectra acquired simultaneously at different points, at the sounding point and at a reference point at the center of the slit. The remaining effects are described below.

#### 4.4.1 Doppler shift geometric projection factor

The goal of this work is to measure the Doppler shift due to the motion of cloud particles in the direction of the line of sight, in order to subsequently determine the wind velocity. The problem can be reduced to an understanding of the interaction between solar radiation and cloud particles embedded (in the rotating atmosphere) during the scattering process.

We use the single-scattering approximation and in this framework consider the scattering process as a sequence of absorption and re-emission of the solar radiation by cloud particles in the upper cloud deck. This simplification allows computing a correction factor as a function of longitude. Assuming, for the sake of simplicity, pure zonal motion in the retrograde sense and a  $90^\circ$  phase angle (since Venus was near quadrature), two extreme cases can be considered (see figure 4.23). One, at the sub-solar point, where there is no Doppler shift in the absorption (null incidence angle) but there is a blueshift in re-emission towards Earth (radiation is emitted in a direction which is tangent to the surface). The other, at the sub-terrestrial point, is the converse situation where there is a redshift at absorption ( $90^\circ$  incidence angle), but no shift in the emission towards the Earth (direction normal to the surface).

The exact geometric projection factor (F) affecting the Doppler shift can be calculated using the bisector theorem (equation 5.4, see Gabsi et al. (2008) for a detailed explanation). It is a function of the specific observing geometry

and of the longitude. The line of sight Doppler shift is proportional to the projection of wind velocity on the bisector phase angle.

$$\Delta V = F \cdot V = V \cdot 2\cos(\Phi/2)\sin(\varphi - \Phi/2)\cos\beta \quad (4.9)$$

where  $\Phi$  is the phase angle at which the observation was made,  $\beta$  is the latitude of the sub-terrestrial point and  $\varphi$  is the longitude of the point being measured (note that the convention applied to planetary longitude is that it increases in the direction of the rotation; since the Venus rotation is retrograde, the eastern and western hemispheres are symmetric to the terrestrial case). The  $F$  quantity will be designated throughout this work as the geometric projection factor. Given the geometry of the observations, the projection factor vanishes at a longitude close to  $-40^\circ$ , where the redshift produced in the absorption of incoming solar radiation and the blueshift in the emission towards Earth cancel each other (see figure 4.23 (b)).

#### 4.4.2 Young effect

Young (1975) discussed a systematic Doppler shift affecting scattered solar radiation, which is caused by the finite angular size of the Sun as seen from Venus ( $\sim 1^\circ$ ), leading to points near the terminator of Venus being unequally illuminated by the approaching and receding limbs of the rapidly rotating Sun. The solar rotation induces a Doppler shift in the solar radiation: a blueshift in the West limb of the Sun, and a redshift in the East limb.

Since the solar zenith angle varies with longitude, points of the Venus disk at different longitudes are illuminated asymmetrically by the rim of the Sun that is blueshifted and by the opposite rim of the sun that is redshifted. As a consequence, average solar radiation is apparently shifted due to missing radiation.

The sunlight reaching Venus is already affected by this Doppler shift, which will be added to the scattering-induced shift due to the motion of the cloud particles. Its sign is negative at western elongation near local morning terminator (and positive at eastern elongation near local evening terminator).

It can be shown that this effect is of the order of the Sun's equatorial velocity ( $2 \text{ km s}^{-1}$ ), multiplied by the ratio of its apparent radius as seen from Venus, to the angular distance from the target point to the terminator, and can be empirically approximated by:

$$Y \sim \frac{V_\odot D_\odot}{\sin \theta} \quad (4.10)$$

where  $V_\odot$  is the solar equatorial velocity ( $2 \text{ km s}^{-1}$ ),  $D_\odot$  is the solar angular diameter and  $\theta$  the angular distance between the point being observed

and the terminator.

Equation 4.10 (Gabsi et al., 2008) is equivalent to the empirical relation proposed by Young (1975):

$$Y = 3.2 \tan(SZA) \quad (4.11)$$

where  $SZA$  is the solar zenith angle (Young, 1975). The Young effect becomes significant near the terminator (which was near the central meridian in our observations), where it increases substantially (see figure 4.23 (a)). In principle, equation 4.11 would lead to  $Y = \infty$  at the terminator. In reality, divergence does not occur because at the same time the illumination tends to zero. Assuming to first approximation that the solar intensity varies as  $\cos(SZA)$ , we calculated the Young effect by weight-averaging equation 4.11 over the effective pixel size (i.e. the actual pixel size convolved by the seeing), and finally corrected our Doppler shift results for this effect.

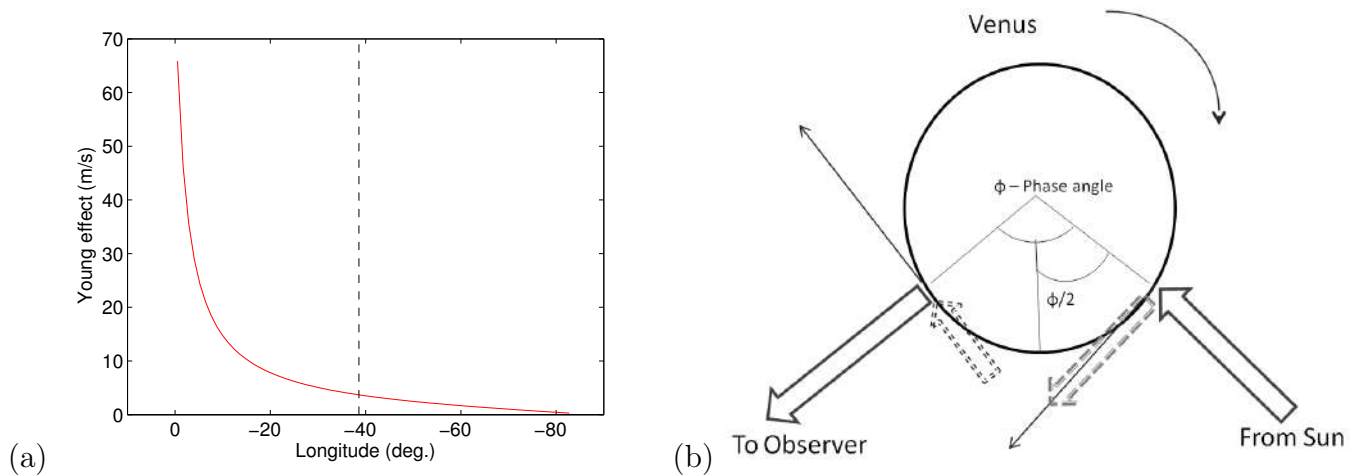


Figure 4.23: (a) Young effect as a function of longitude from the central meridian, along the equator. The dashed line marks the position of the central pixel position of the slit. (b) Schematics of the Doppler effect in the single scattering approximation. The dotted arrow at the sub terrestrial point indicates a redshift in the absorption of solar radiation by the atmospheric aerosols in this region, due to the atmosphere's retrograde rotation. The dashed arrow at the sub solar point indicates a blueshift in the solar radiation scattered towards the observer. Thin arrows indicate the direction of the zonal wind. Adapted from Gabsi et al. (2008).

## 4.5 Sensitivity Tests

In order to test the robustness, reliability and sensitivity of the Doppler velocimetry algorithm used I performed several additional sensitivity tests.

The factors studied were: the noise level, the line's density, the line's depth, the line's asymmetry level, the accuracy in the retrieved velocities as a function of the size of the deviations imposed and the algorithm wavelength sensibility response.

In addition I carried out in the removal of the telluric lines from the obtained spectra, fact that showed to be not significant in the velocity curves obtained before and after performing this alteration.

With the aim of improving the quality and increase the confidence in the results obtained we built synthetic spectra to which we imposed artificial shifts corresponding to known velocities. Than we ran the algorithm to produce the respective velocity curves and compared the velocities retrieved and the imposed ones.

The tests included the modelling of fully synthetic spectra as well as modified actual observational data to which artificial Doppler shifts were imposed (from now on denominated: synthetically reconstructed spectra).

### 4.5.1 Synthetically reconstructed spectra tests

With the goal of testing the behaviour of the data reduction algorithm we produced reconstructed spectra from spectra derived from actual observations. We then obtained the velocity curves for these changed spectra.

First of all we obtained the dispersion relation which gave us the correspondence of each pixel in the echellograme and its wavelength. After that an observation (with high signal to noise ratio) has been used and the matrices with the data from this observation echellograme were changed. For each order of the echellograme, all spectra were replaced with the reference (central pixel) spectrum (to confirm that the algorithm produces the zero relative velocity in relation of the central pixel), thereby reconstructing the spatial structure along the slit in order to remove the relative shift that was originally present in the data. We then used these reconstructed data as input to the retrieval algorithm.

In the first test the first step consisted of replacing all the 61 spectra by the central spectrum, to ensure a relative null velocity between each of the spectra and the reference spectrum. The algorithm retrieved null Doppler shifts, as expected. In the second test all the spectra except the reference one were shifted by a prescribed shift. The spectra were shifted with 10 m/s

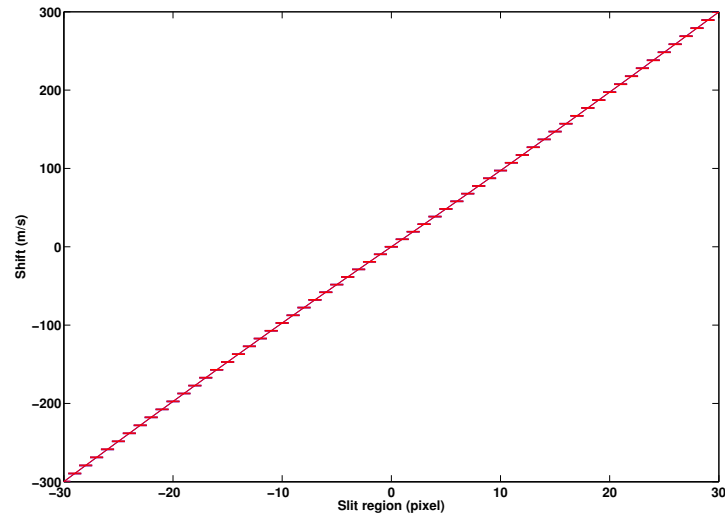


Figure 4.24: Doppler shift curve for spectra shifted with a 10 m/s step relative to the central spectrum, between -300 m/s and +300 m/s. This curve has been retrieved from a synthetic spectrum.

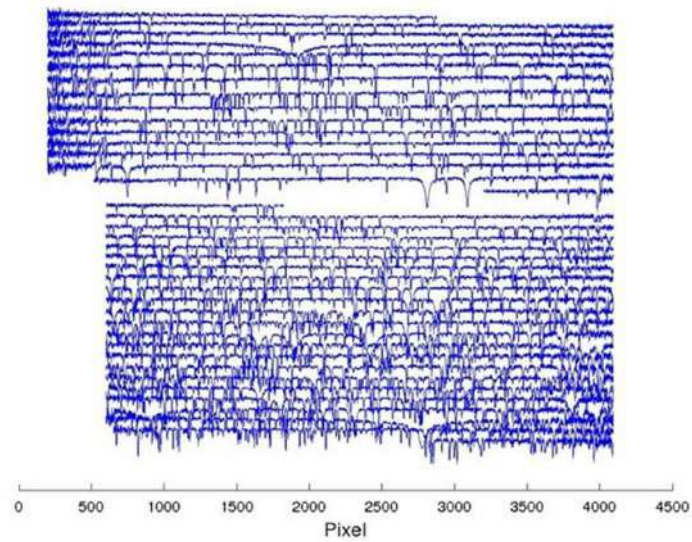


Figure 4.25: Synthetic spectrum all orders, 16 for the MIT and 23 for the EEV detector, central spectrum (spectrum relative of the pixel number 31).

increments, between  $-300$  m/s and  $300$  m/s from top to bottom of the slit. We then produced the velocity curves for these changed spectra.

This test confirmed that the velocity curves for the reconstructed spectra were consistent with the imposed deviations (figure 4.24). On the other hand, reconstructing the orders from a spectrum with a lower signal to noise ratio led to retrieved velocities lower than the prescribed ones (figure 4.26). The error bars were also higher for tests with spectra from the MIT detector, due to the higher noise of the observations at longer wavelengths in this observational offset (figure 4.26b). Additional tests with lower SNR spectra, from observations of June 4, confirmed the sensitivity of the velocity curves to noise.

To test the algorithm's response to wavelength range, reconstructed spectra were also produced in which only one of the spectral orders was reconstructed as previously described, while all other orders were replaced by an average of the continuum level. Since there was no significant discrepancy between velocity curves obtained from different spectral orders, we conclude that our method is robust with respect to the wavelength range of the data. This is not surprising since the density of spectral lines has little variation between spectral orders.

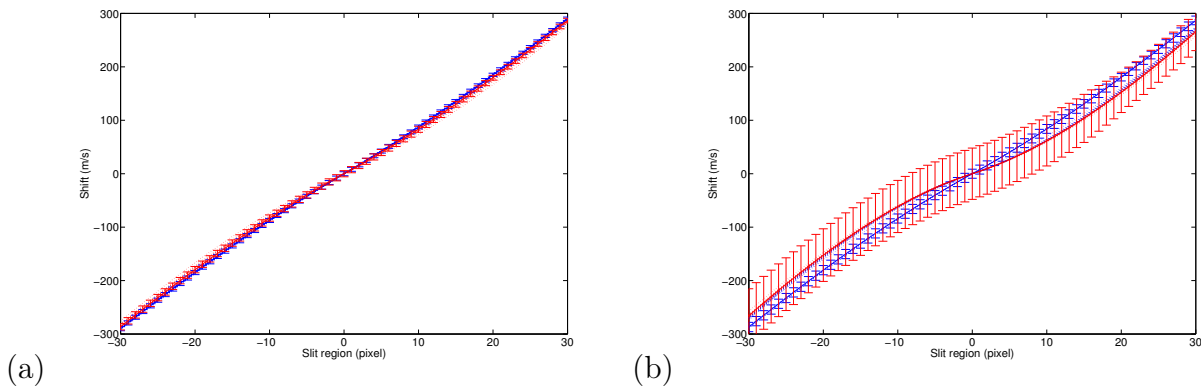


Figure 4.26: Sensitivity to the signal-to-noise ratio. The plots show the velocity curves relative to the central spectrum, with prescribed shifts between  $-300$  m/s and  $+300$  m/s. The red and blue curves are from the MIT and EEV detector, respectively. (a) Order reconstructed from a spectrum from the order center,  $\text{SNR} = 54$ ; (b) Spectrum with  $\text{SNR} = 12$ . Both spectra are from one of the exposures from offset 1, case PL.

## 4.5.2 Fully synthetic spectra tests

These tests were based on fully synthetic spectra constructed from gaussian line shapes. The reference spectrum was constructed by defining the line width, depth and density (i.e. the average number of spectral lines per nanometer) so as to match those of the data, and adding random noise at appropriate level, in order to generate the same signal to noise in the observations. The remaining spectra within each order were defined by replicating this reference spectrum. The tests were performed by numerically shifting each spectrum by a prescribed shift relative to the reference one.

As in the case of the spectra reconstructed from real data, three types of fully synthetic spectra were generated: one with a null relative shift, one with a 100 m/s shift between all the spectra in each order and the central spectrum, and a third one with a relative shift of 10 m/s between consecutive spectra, ranging from -300 m/s to 300 m/s.

The velocity curve for the zero shift fully synthetic spectra was in accordance with the basic null relative velocity imposed in the synthetic spectra. The same for the case of a imposed shift associated with a relative velocity of 100 m/s. The Doppler shift curve for the 10 m/s step shifted spectra in relation of the central spectrum (between -300 m/s and +300 among the complete set of 61 spectra) also showed high coherence between the imposed shifts and the velocity curve generated by the data reduction algorithm (see figure-4.24).

In the baseline case, in which the synthetic spectra were similar to “real” observed data, the velocity curves were consistent with the imposed shift (see figure 4.24). The impact of test variables such as the noise level, the line density and the symmetry of the spectral lines was studied by varying each of these factors independently. Decreasing the signal to noise ratio or decreasing the line density both led to velocity curves lower than the prescribed shift, with a higher discrepancy, in velocity, for spectra farther from the reference one. Increasing the noise level by a factor of four leads to a 20 percent reduction in the retrieved Doppler shift, pixel by pixel, in the velocity profiles obtained from the synthetic spectra relative to the baseline case.

Changing the line symmetry, by widening each line in its red side (by increasing the full width at half maximum of the gaussian in its high wavelength side from the line center) led to higher velocities, whereas wider lines in the blue side led to velocities lower than the imposed Doppler shift. Line symmetry is an important factor in the visible wavelength range, since it can be affected by differential atmospheric refraction if not totally compensated



by the ADC prism.

## 4.6 Results (UVES)

In this section I present the velocity measurements retrieved for each of the two observing geometries, with the position angle of the slit parallel (PL) and perpendicular (PP) to the axis of rotation. The results presented in this section come essentially from [Machado et al. \(2012\)](#), a paper published last year in *Icarus* journal.

### 4.6.1 Slit parallel to rotation axis

In the case of the PL configuration, with the spectroscopic slit parallel to the planetary rotation axis, three offsets were used, with three exposures for each one. In this case, due to the latitudinally varying zonal wind along the slit, the method yields the relative Doppler shift and zonal velocity between each pixel along the slit and the central pixel, but not the absolute zonal velocity.

For the third position offset (measurements near the limb), we can take advantage from the fact that, due to the low obliquity, pixels which are symmetric relative to the slit center fall on the same meridian. Therefore they are subject to the same projection factor, allowing to measure the latitudinal asymmetry of the zonal wind. On the other hand, for positions 1 and 2, the observational scans do not cover North and South latitudes simultaneously due to the slit length limitation.

The observations obtained on May 27 had a signal-to-noise ratio between 40 and 80 (PL geometry), much higher than the spectra from June 4 (SNR between 2 to 6, PP geometry). The reason was sky transparency variations and passing clouds affecting the signal. The better conditions allowed retrieving Doppler shifts with error bars of just a few m/s in the former date, since the noise level can have a considerable impact in the accuracy of this technique (see the section dedicated to the sensitivity tests, for a study of the impact of noise level on the results).

In positions 1 (latitude range:  $\sim 79 - 12^\circ S$ ) and 2 ( $\sim 8 - 78^\circ N$ ), all the points sounded on the disk are along the central meridian, hence affected by the same projection factor (see equation 4.8). Since the Doppler shift is computed with respect to slit's central point, and the algorithm calculates the relative velocity between each observed point on the slit and the central point, therefore, after subtracting the Young effect, and assuming a purely zonal wind, we can obtain the differential velocity between each point along the slit and the central point.

$$\Delta V_i - \Delta V_o = F_i \cdot V_i + Y_i - (F_o \cdot V_o + Y_o) \quad (4.12)$$

where the index “i” refers to each considered pixel along the slit, and the index “o” refers to the pixel at slit’s central point. And, since on the particular cases of positions 1 and 2 (with the slit parallel to the rotational axis and along a meridian):  $F_i = F_o = F$  and  $Y_i = Y_o = Y$ , then:

$$V_i - V_o = (\Delta V_i - \Delta V_o)/F \quad (4.13)$$

Figure 4.27 presents Doppler shift curves for one of the exposures for offset 1. Figure 4.27a shows the differential Doppler shifts between the spectrum coming from each pixel along the slit and the reference spectrum. The vertical dotted line represents the apparent planetary limb near the South Pole. The curves from the two parts of the detector are consistent, even in some of the small scale features, except for pixels falling outside the disk, where they diverge. Pixels to the right of the plot are in fact sounding the sky and produce spurious Doppler shifts without any physical meaning. In figure 4.27b we performed the Doppler shifts’ weighted average from the three exposures taken at this offset, the pixel positions have been converted to latitude and spectra from the portion of the slit falling outside the planetary disk were discarded.

Due to the high spatial resolution of the observations (pixel scale is on the order of 108 km at disk center) small scale features can be seen in the velocity curves that indicate higher relative velocities on the range  $\sim 10\text{--}30$  m/s over spatial scales of approximately 216 km (two pixels, such as at  $60^\circ\text{S}$ ). These have been measured in spectra recorded simultaneously on both detectors and are unlikely to be instrumentally generated.

The fact that the pixels near the limb are affected differently for the two CCDs, as we can see in figure 4.27 close to the limb between  $75^\circ\text{S}$  and  $85^\circ\text{S}$ , may be caused by the difficulty to correct for the Young effect near the terminator (which for high latitudes is also near the limb) in the presence of multiple scattering. We have adopted a purely geometric correction of the Young effect (equation 4.11), weighted by the illumination. If multiple scattering occurs, the scattered intensity is not proportional to the illumination, so it is likely that our description of the correcting factor fails near the northern and southern limbs. Furthermore, differences in the altitudes sounded for the two wavelength ranges covered by each CCD detector, leading to different wind retrievals due to a possible vertical wind shear, may be another possible reason for these differences. It is clear that the technique may be improved to extend measurements closer to the limb if a more realistic approach to the nature of the scattering process, allowing to accurately compute the contribution function for the wavelength range of each detector,

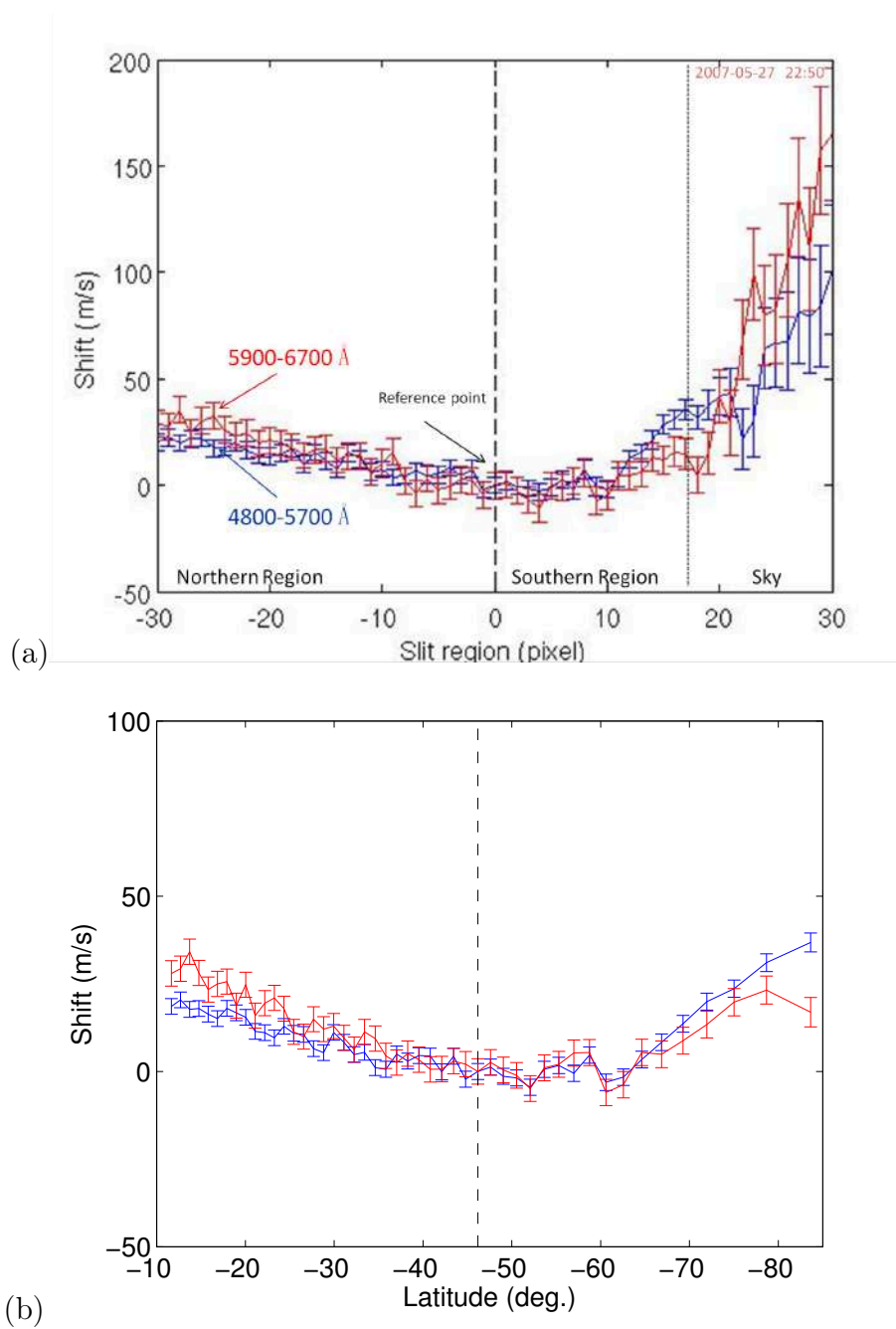


Figure 4.27: Example of velocity curves produced in two stages of the data analysis, from one of the exposures in slit position 1 (case PL, night of May 27). (a) Doppler shift as a function of the pixel. The dashed line marks the position of the slit's center point used as the reference spectrum. The dotted line marks the position of the southern limb. Doppler shifts retrieved from the MIT CCD are shown in red, and from the EEV CCD are shown in blue. (b) Velocity curves mapped to planetocentric latitude. The latitudinal coverage of the effective pixel increases toward higher latitudes due to the planetary curvature.

is introduced.

Figure 4.28 shows the final relative velocity curves from all measurements in case PL. In addition to figure 4.27b, deprojection and subtraction of the Young effect Doppler shift was made, and a weighted average was computed of the results from the three exposures in each offset and for both detectors. These curves represent relative zonal velocity (measured relative to the reference point defined as the center of the active window), and therefore require an absolute baseline value to be interpreted, which is provided by measurements made with the PP geometry. This will be done in the discussion of figure 4.32.

In slit position 3 (latitude range:  $33^{\circ}S - 31^{\circ}N$ ), any two points with symmetric latitudes are also on the same meridian and solar zenith angle. Therefore, their projected velocities can be corrected for the same projection factor and Young effect, which allows deriving the differential velocity between symmetric points in the northern and southern portions of the slit. In this case it is possible to compare the wind in low northern and southern latitudes (Figure 4.29). The maximum asymmetry in the equatorial region is  $6 \pm 5$  m/s. On average, southern zonal winds are faster than northern ones by less than 5 m/s, and within error bars the asymmetry is negligible.

$$V_2 - V_1 = (\Delta V_2 - \Delta V_1)/F \quad (4.14)$$

where, the positions 1 and 2 are not any two points on the slit, but two points with almost symmetrical latitudes.

### 4.6.2 Slit perpendicular to rotation axis

Observations made with the slit orientation perpendicular to the planetary rotation axis allow measuring the absolute magnitude of the wind velocity. In this case pixels along the slit fall on the same latitude circle, and assuming that the zonal wind depends only on latitude one can obtain the zonal wind directly from the longitudinal profile of the relative velocity (see equations 4.8 and 5.4). This requires, however, a correction for geometric projection and Young effects, since the measured spectrum and the reference spectrum (spectrum from the slit's center) are not at the same SZA. Since the geometric projection factor falls to zero and changes sign close to the center of the slit, the uncertainty of the measurement increases significantly for points in this region, because the correction is made by dividing the relative shift measured by the geometric projection factor.

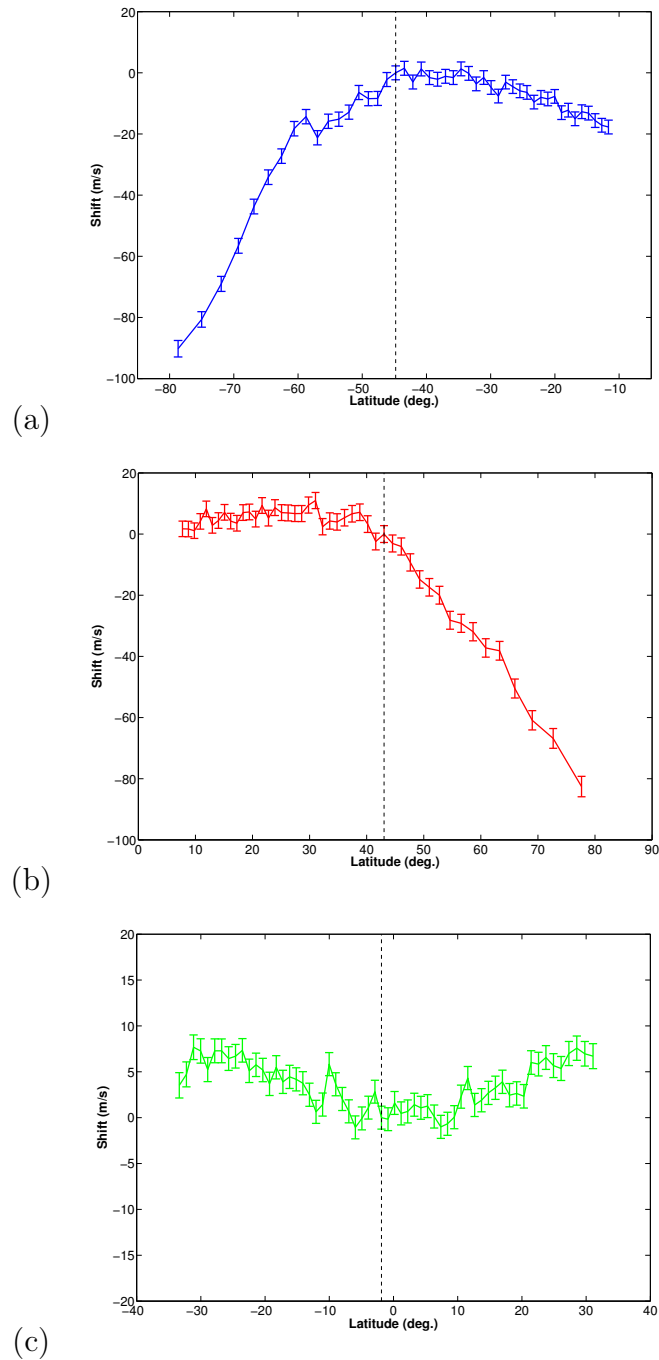


Figure 4.28: Differential velocities between each pixel and the central pixel of the slit, deprojected and corrected for the Young effect, for the observations in the PL orientation (night of May 27). The plots show the weighed average of the curves obtained with the MIT and EEV CCDs. (a) Slit position 1, covering latitudes from  $79^{\circ}S$  to  $12^{\circ}S$ ; (b) Position 2,  $8^{\circ}N$  to  $78^{\circ}N$ ; (c) Position 3,  $33^{\circ}S$  to  $31^{\circ}N$ . The dashed line indicates the reference point at the center of the slit. Note different scales.

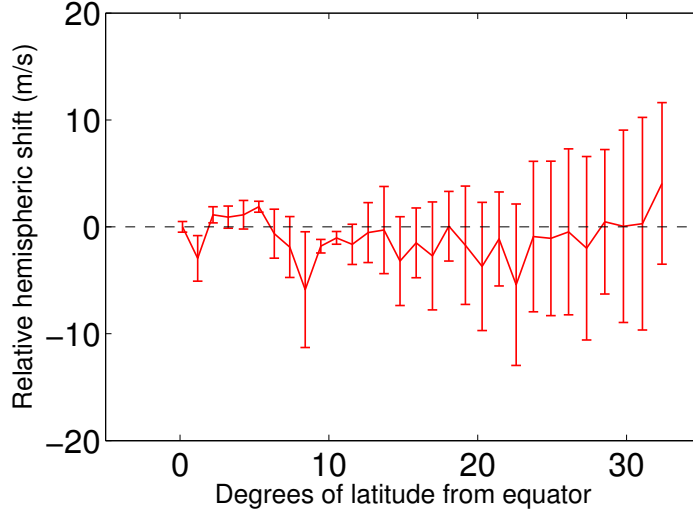


Figure 4.29: Relative velocity between points symmetric relative to equator (case PL, night of May 27). A weighted average has been computed of the results from the MIT and EEV detectors and from the three exposures in this offset.

$$\Delta V_i - \Delta V_o = F_i \cdot V + Y_i - (F_o \cdot V + Y_o) \quad (4.15)$$

Under the assumption of zonal wind depending only on latitude,  $V_i = V_o = V$  along the slit, we obtain:

$$V = \frac{\Delta V_i - \Delta V_o - Y_i + Y_o}{F_i - F_o} \quad (4.16)$$

where the index “i” refers to each considered pixel along the slit, and the index “o” refers to the pixel at slit’s central point.

Figure 4.30 and table 4.3 present the zonal wind magnitudes obtained in this case for the six slit offsets, between 18°N and 34°S. Each panel in Figure 4.30 shows the weighted average of the velocity curves obtained from the MIT and EEV CCDs and from the two exposures taken for each slit offset. These results are also displayed in a map projection in figure 4.31. The mean velocities range from 106 to 127 m/s, with an uncertainty that is directly correlated with the SNR of the observation, but which also has a contribution from local variations. In general, the zonal wind is approximately uniform at each latitude offset (validating our initial assumption to first order), with stronger winds close to the equator than at higher latitudes. However, at

Latitude	Zonal velocity (m/s)	Std. dev. (m/s)
18° North	116	53
8° North	106	21
2° South	127	14
13° South	126	11
23° South	122	14
33.5° South	116	29

Table 4.3: Summary of latitudes covered, and mean zonal wind velocities measured with the PP geometry on June 4 (figure 4.30). The zonal velocities are the weighted means of the measurements made at each offset. The weighting coefficients were the inverse of the variance obtained for each pixel. Std. dev. is the standard deviation of the weighted mean. Latitudes are given for the slit center with an uncertainty of 1.2°; the 0.3''-slit covers a latitude band 2.4° at disk center.

longitudes between  $-25^\circ$  and  $-35^\circ$ , non-negligible medium to large scale oscillations, spanning approximately two pixels, or  $\sim 216$  km, are apparent for slit positions between 8N and 23S (figure 4.30 panels b–e). The magnitude of these (second order) oscillations cannot be quantified directly, however, since our retrievals are based on the working hypothesis that the zonal wind does not depend on longitude.

Although we also made observations at latitudes higher than displayed in table 4.3, they have been discarded because of the low signal to noise ratio, which made it impossible to obtain the Doppler shifts. The same problem of high noise affected pixels at longitudes near the limb, as can be seen in the size of the error bars. Thus the pixels east of the slit center were not considered further.

### 4.6.3 Analysis of spatial variations

As explained above, the observing geometry with the slit oriented parallel to the axis of rotation (case PL) yields relative wind measurements, whereas a perpendicular slit (case PP) provides absolute wind measurements. Therefore, it is possible to use the mean values of the winds measured for each offset of the PP observations to calibrate the baseline of the PL observations, i.e., the wind at the reference point. Figure 4.32 summarizes the results after doing this. The first step of the procedure has been to calibrate the relative velocities from offset PL3, which covers the equatorial region in both



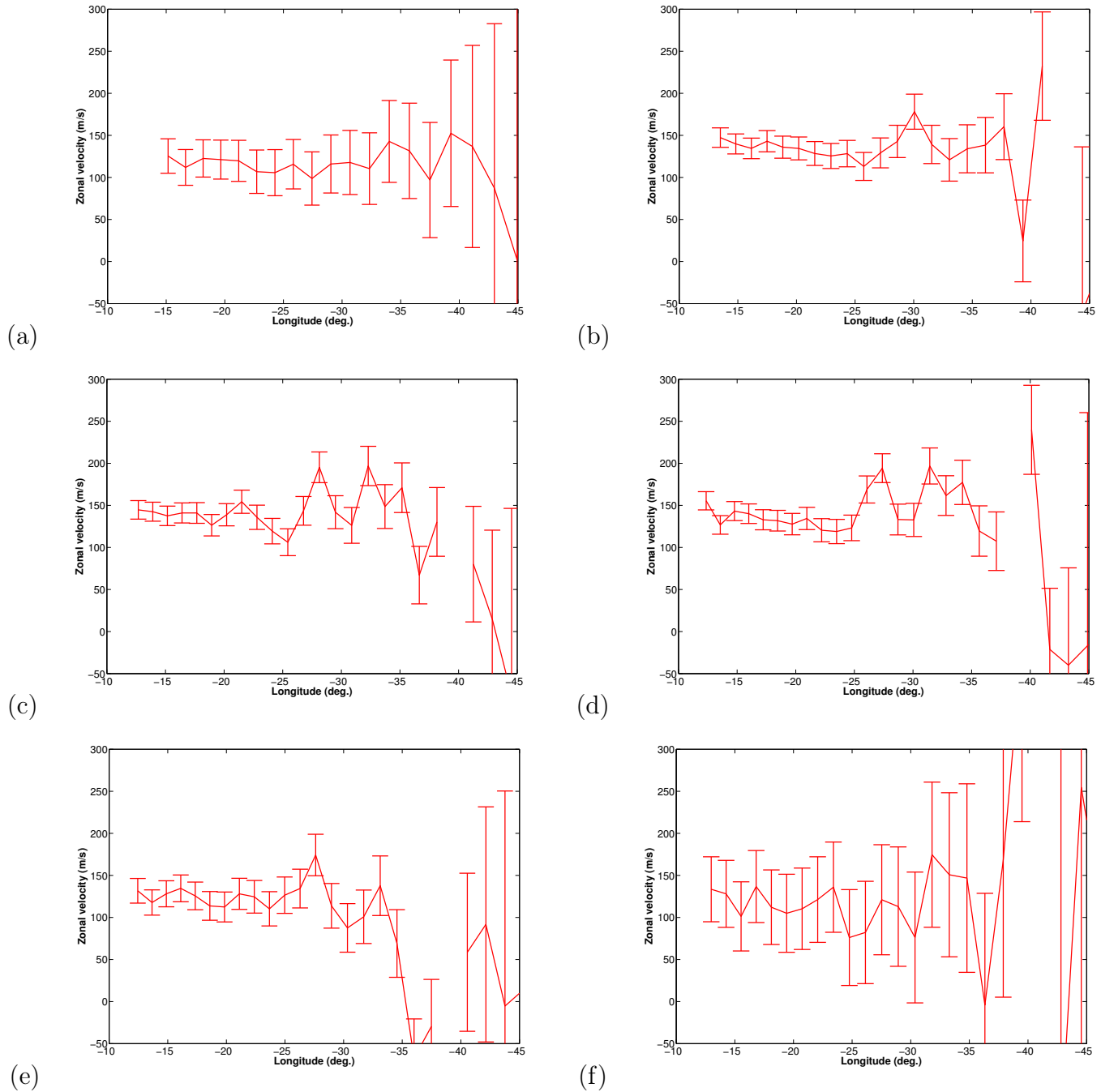


Figure 4.30: Zonal wind versus longitude for the observations made at June 4 with the spectroscopic slit parallel to the equator (case PP). Each point is the weighted mean of the retrievals from two exposures and from the EEV and MIT detectors. The latitudes are: (a) 33.5S; (b) 23S; (c) 13S; (d) 2S; (e) 8N; (f) 18N;

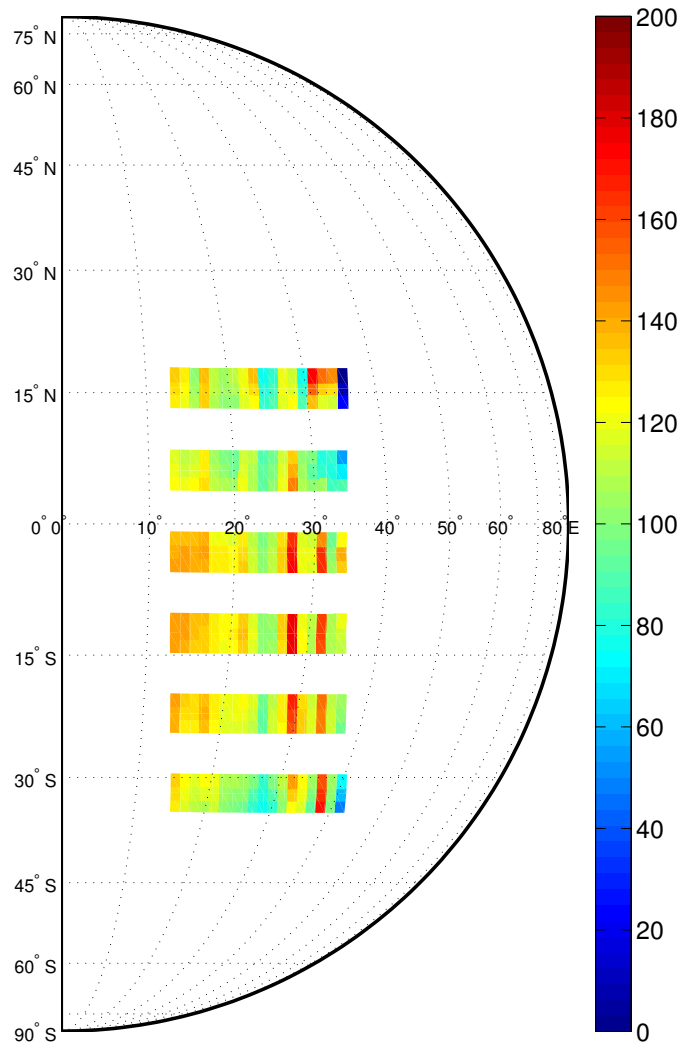


Figure 4.31: Map projection of the zonal wind for the observations of June 4. The latitudinal extent of the slit pixels has been exaggerated for clarity. Estimated pixel dimensions are approximately 108 km in longitude at disk center. See table 4.3 and figure 4.30 for the latitudes and longitudes covered.

hemispheres, using the average along the slit for the six offsets from the PP geometry (marked in the figure as black squares). The second step has been to fit the relative velocity curves from offsets PL1 and PL2 to the curve from offset PL3 in their common (overlapping) ranges of latitude. This allows obtaining a simultaneous latitudinal profile extending from high northern to high southern latitudes.

The zonal wind is stronger in mid-latitudes than in the equatorial region by 10-20 m/s. These are moderate jets, with the southern one being stronger than its northern counterpart by  $\sim 10$  m/s. The latitudinal wind shear is not very pronounced ( $\sim 0.35$  m/s per degree at low latitudes), and stronger shear ( $\sim 3$  m/s per degree) is limited to narrow regions at  $60^\circ S$ ,  $10^\circ S$ ,  $30^\circ N$  and  $40^\circ N$ .

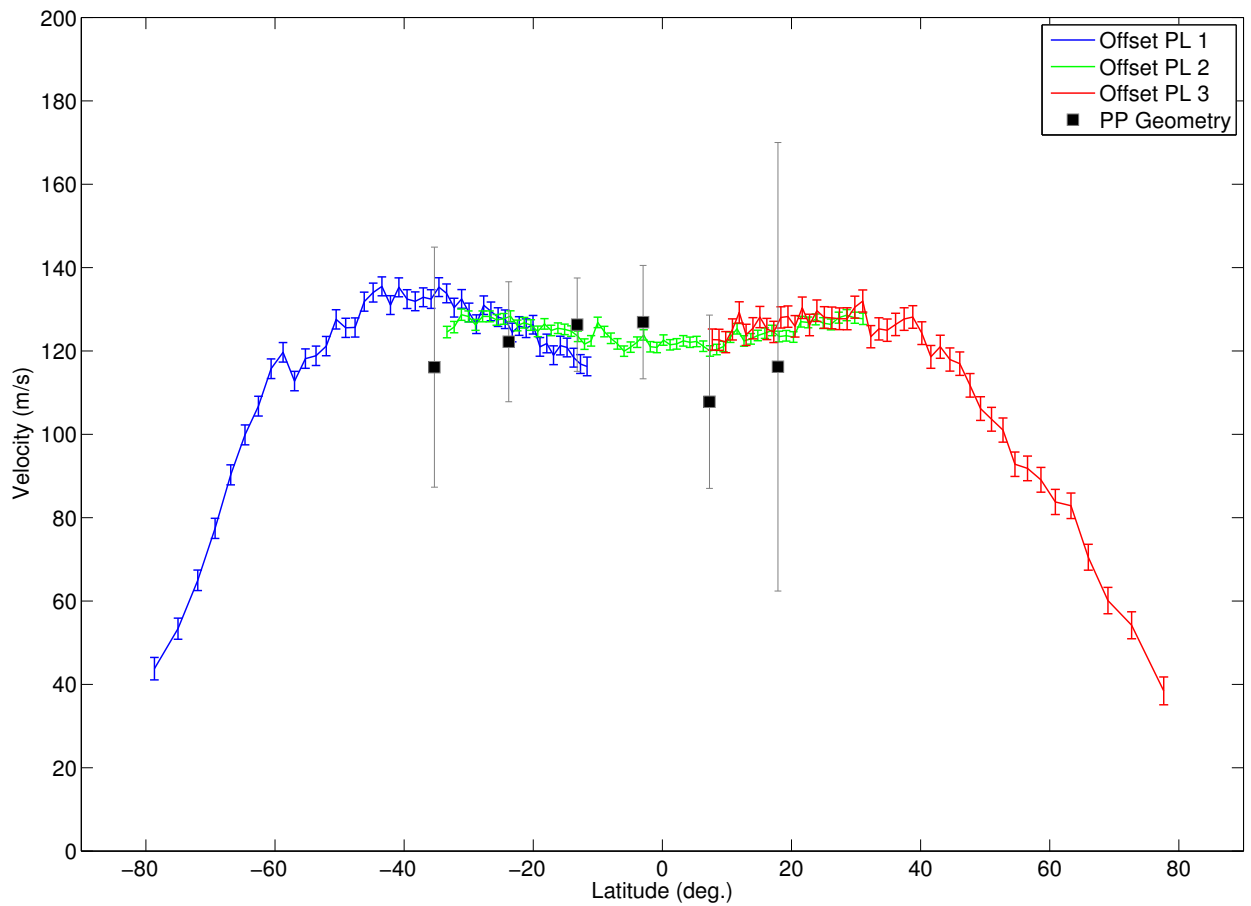


Figure 4.32: Summary of the measurements made with the slit perpendicular to the rotation axis (zonal wind velocity, squares) and parallel (relative zonal wind measurements, lines). Curve PL3 (green) has been offset vertically in order to best-fit the absolute zonal wind measurements closest to the equator. Curves PL1 (blue) and PL2 (red) were offset in order to align them with curve PL3 in their regions of overlap.

## 4.7 Discussion (UVES results)

These Doppler retrievals (figure 4.32 and table 4.3) are in general good agreement with previous measurements based on cloud tracking (Del Genio and Rossow, 1990; Limaye et al., 2007; Peralta et al., 2007; Sánchez-Lavega et al., 2008; Moissl et al., 2009). We retrieve the same order of magnitude and a similar latitudinal variation to Pioneer Venus, Galileo and VEx/VIRTIS measurements, which cross-validates both techniques and provides reasonable confirmation that cloud tracking and Doppler methods both retrieve the velocities of air masses to first order. Wind magnitudes at low latitudes (perpendicular slit configuration case), however, are about 20-30 m/s higher than these previous cloud tracking measurements. The cause for this (second order) discrepancy is twofold, and stems from the differences between the two methods. On the one hand, latitudinal wind profiles based on cloud tracking are constructed by zonally averaging sets of many measurements of the velocities of individual cloud features, made over a wide range of longitudes. On the other hand, with our Doppler technique we directly measure the instantaneous velocity of cloud particles within a particular range of local solar time (between 15h and 17h) close to the evening terminator. Since our measurements only cover this limited range of local times, it is impossible to produce a zonal mean to directly compare with cloud tracking results. It is likely that this local character of Doppler measurements accounts for the discrepancy, due to the presence of thermal tides. Del Genio and Rossow (1990) and Rossow et al. (1990) detected a solar-locked component with a 10 m/s amplitude at low latitudes which peaked close to the evening terminator, and Sánchez-Lavega et al. (2008) measured winds stronger at 15 h than at noon by  $\sim 10$  m/s, close to 40S. This thermal tide contribution would be averaged out if data were available over a complete longitude circle, but local measurements such as ours are sensitive to solar-locked extrema.

The latitudinal profiles measured with the parallel slit geometry are also local and instantaneous, and therefore the same considerations apply. Nonetheless, there is a good agreement with the VEx/VMC (Moissl et al. (2009), figure 4), Galileo (Peralta et al. (2007), figure 3) and Pioneer Venus (Del Genio and Rossow (1990), figure 12 and Rossow et al. (1990), figure 11) cloud tracking measurements, whereas the VEx/VIRTIS profile (Sánchez-Lavega et al. (2008), figure 2) has somewhat lower winds at high latitudes. This may be due to an incomplete correction of the Young effect, which is quite strong near the terminator where these velocities were retrieved, and in particular at high latitudes.

Previous measurements by Pioneer Venus, reanalyzed in Limaye et al. (2007), indicated the presence of high latitude zonal jets close to 50 degrees

latitude in both hemispheres, with a slight asymmetry between the northern and southern ones. However, longer temporal averages of cloud-tracked winds by the Galileo SSI instrument (Peralta et al., 2007), and by the Venus Express VMC and VIRTIS instruments (Sánchez-Lavega et al., 2008; Moissl et al., 2009) do not display any clear evidence for high latitude jets at cloud tops, although shorter time scale averages of VMC measurements in Moissl et al. (2009) indicate that jets may occur but are short lived. We believe that, rather than being discrepant, different wind measurements provide important insight into the variability inherent to the atmospheric circulation of Venus. Our direct measurements of instantaneous zonal winds provide additional evidence for the occasional presence of jets and for variability in general. The realization that a latitudinal wind profile with jets such as measured by Pioneer Venus is likely to be barotropically unstable (Limaye et al., 2009) is an argument in favor of variability, since such a profile generates wave motions that carry zonal momentum from the jets and into slow-moving latitudes, thus reducing the instability. Our observations of small scale perturbations (figures 4.30 and 4.31) seem to point to small scale wave motions as the most likely processes by which the instability unfolds. Further investigations regarding wave motions and their latitudinal fluxes of angular momentum should privilege the midlatitudes as the focus of this activity. The more general question remains concerning the role of the mean meridional circulation on the buildup of these jets, and their link to long-lived structures such as the polar vortex, its surrounding cold collar and the extended clouds at high latitudes.

These VLT/UVES long-slit results are complementary to the results obtained from the observations carried out with CFHT/ESPaDOnS, that are presented in the next chapter. The UVES long-slit measurements allowed to yield instantaneous wind latitudinal profiles while ESPaDOnS's measurement allowed to make sequential observations along planetary meridians and parallels, which revealed pertinent to this Doppler velocimetry studies as I will show in the next chapter.

# Chapter 5

## CFHT/ESPaDOnS observations

### 5.1 The CFHT telescope and the ESPaDOnS instrument

#### 5.1.1 The Canada-France-Hawaii-Telescope (CFHT)



Figure 5.1: The Canada-France-Hawaii-Telescope (CFHT) at Mauna Kea, Hawaii. (Image from CFHT official website).

The Canada-France-Hawaii Telescope is a 3.6 meter optical/infrared telescope and is located near the summit of Mauna Kea volcano mountain, at

Hawaii. The observatory is at an altitude of 4,204 meters and is one of the facilities that comprises the Mauna Kea Observatory.

### 5.1.2 ESPaDOnS - Instrument Description

ESPaDOnS is a visible spectro-polarimeter operating across the complete optical spectrum, from 370 to 1050 nm, collected over 40 spectral orders in a single exposure at a resolution of about 80,000 (Donati, 1997). This instrument is a high-resolution *echelle* spectrograph and spectropolarimeter, as well, the signal feeding is through a fibre connection from a *Cassegrain* module. The peak throughput is of 15 – 20% (telescope and detector included) due to its large dioptric optics with low reflectance and absorption, the high efficiency optical fibres and image slicers also contribute to its high performance.



Figure 5.2: High resolution spectrograph and spectropolarimeter ESPaDOnS. (Image from CFHT official website)

The ESPaDOnS instrument consists of two distinct units: one is the *Cassegrain* unit and is mounted at the telescope's focus, the calibration module, the guiding system and the polarimeter unit, are also part of this ESPaDOnS' compound; the spectroscopic unit is installed in a *Coudé* room (a thermally stable facility), at the core of the CFHT telescope's building, see figure 5.2. The two units are connected by a fibre link and an image slicer unit (Donati, 1997).



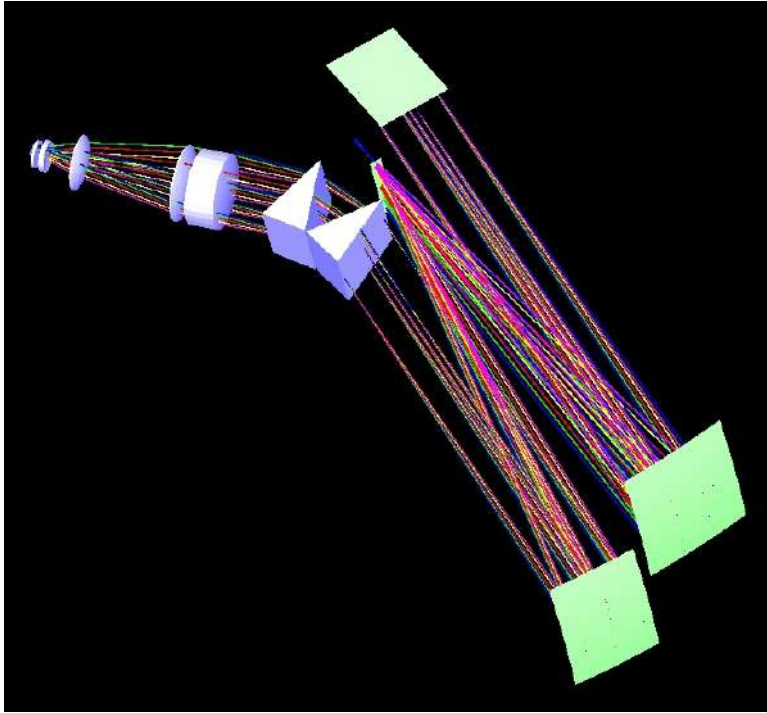


Figure 5.3: ESPaDOnS optical path. (Image from ESPaDOnS website).

In order to compensate for the atmospheric refraction the calibration/guiding module includes an atmospheric dispersion corrector (ADC) composed by two prisms that rotate independently, which allow cancelling, in real time, the atmospheric refraction. This unit also includes a compact CCD ( $1k \times 1k$ ) camera (with a wide field of view of  $100''$ ) aimed through the instrument's aperture, and so it can be used as an auto-guide system aiming the target or a reference star. The calibration unit consists in a wheel that can select various sorts of calibration light. Options are: a tungsten lamp for flat field exposure purposes, a Thorium-Argon (Th-Ar) lamp in order to perform accurate wavelength calibration, and exposures of fully polarised light to impose known vibration directions as a polarising reference.

The spectrograph apparatus consists of a dual pupil configuration with 190 mm, a double set of high-reflectance collimators, a monolithic grating *echelle* (R2 type) as the diffraction device, with a size of  $200 \times 400$  mm and 79 g/mm, a fully dioptric f/2 camera with 388 mm focal length; also in the instrument optical path there is a high dispersion prism cross-disperser and the detector's CCD ( $2k \times 4.5k$ ) with a pixel size of 0.0135 mm, inside a cryogenic cooling recipient (dewar cooling system). The optical path is the following: the beam bounces from the main collimator to a flat mirror, and

then to a transfer collimator, to the double prism cross-disperser, through the fully dioptric camera and, finally, entering the CCD dewar camera, as seen in the diagram of figure 5.3 and 5.4.

The full spectral coverage of the optical domain extends from order number 61, centred at the wavelength of 372 nm, till order 22, centred at 1029 nm, with a spectral resolution of the order of 80,000 (object only mode). The total peak efficiency is about 15% to 20%.

The instrument has three different configurations choices: a spectropolarimetric mode; an *object+sky* spectroscopic mode, where the target and the surrounding sky are recorded simultaneously, in intercalated spectral orders and with a spectral resolution of about 68,000; and the *object only* spectroscopic mode, the one used in this work, for targets much brighter than the background (as is the case of Venus in our observations), with the spectral resolution reaching 81,000.

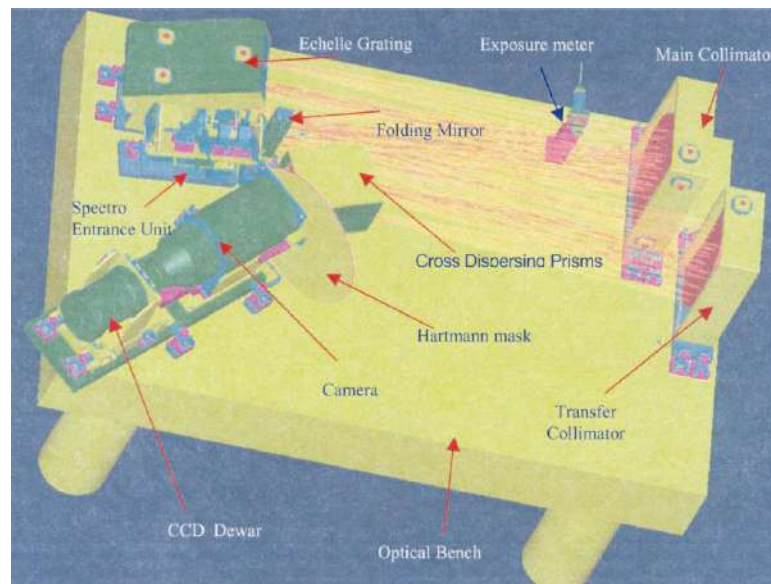


Figure 5.4: ESPaDOnS devices, on the optical bench, that interact with the entering beam along the optical path. (Image from ESPaDOnS website).

### ESPaDOnS wavelength calibration and spectral resolution

Is used an exposure from a Thorium-Argon (Th-Ar) lamp, which spectrum is well known, in order to perform the wavelength calibration. Figure 5.4 shows the *echellogramme* obtained from a Th-Ar lamp calibration exposure, as is notorious we can take advantage of the presence of a large number of

## 5.1. THE CFHT TELESCOPE AND THE ESPADONS INSTRUMENT 155

lines at each spectral order and along the wavelength dispersion's direction (spectral orders).

As there is an average of about 50 Th-Ar spectral lines per order (about 2,000 in total), which are identified by the reduction routine, using reference lists of Thorium and Argon line wavelengths, this will allow to perform an accurate correspondence between the pixel number along, and across, each spectral order and its respective wavelength. From these “anchor points” are produced interpolation polynomials covering the full spectral range. The typical accuracy of this wavelength calibration process is found to be of the order of 0.06 pixels at each given wavelength (Donati, 1997).

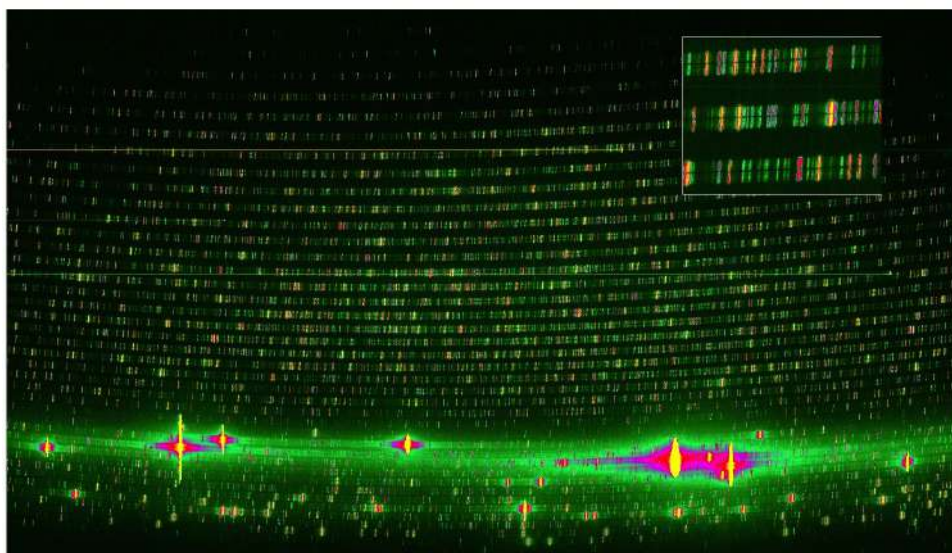


Figure 5.5: ESPaDOnS wavelength calibration with a Thorium Argon (Th-Ar) lamp exposure. In the figure we can see the respective *echellogramme*. (Image from ESPaDOnS website).

The performed wavelength calibration procedures produce a dispersion law function that is limited by the instrument's spectral resolution. The spectral resolution achieved is derived from the width of the spectral lines obtained at the *echellogramme*. A close up of the individual thorium lines is presented at the figure 5.5 insert (top right), the instrumental average width of individual spectral lines is slightly lower than 2 pixels.

The full width at half maximum (FWHM) of individual lines, from the wavelength calibration spectra, is essentially due to a broadening reflecting instrumental causes. From these measurements one can determine the ESPaDOnS spectral resolution (in each mode of operation).

Figure 5.6 shows an example of a wavelength calibrated line in two different instrument's configurations, polarimetric mode as a full line and as a dashed line for target only mode. The FWHM of this line (550.75385 nm) is on the used instrument's configuration (target only) has the width of 6.9 picometers, in good accordance with the nominal spectral resolution of  $R = 81,000$  for this operational mode.

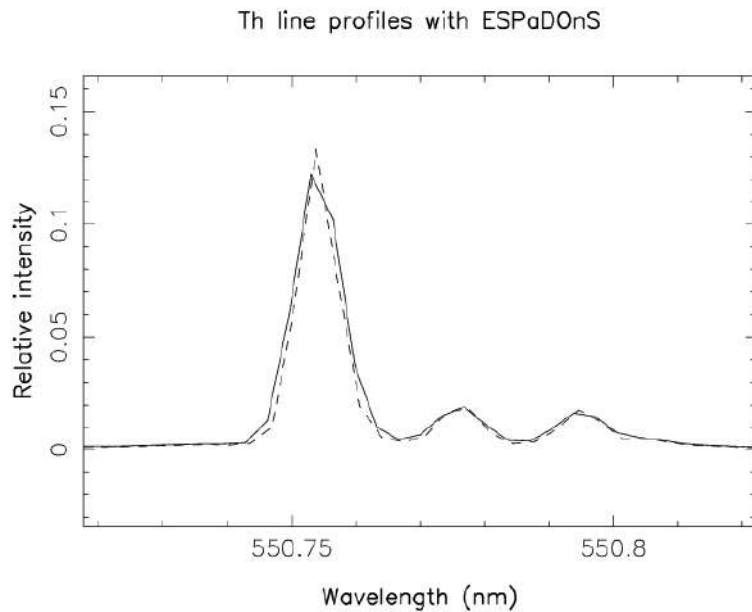


Figure 5.6: Derivation of the wavelength dispersion law, based on known spectral lines from a Thorium-Argon reference spectra. The figure shows an example of a wavelength calibrated line in two different instrument configurations, polarimetric mode as a full line and as a dashed line for target only mode. (Image from ESPaDOnS website).

As we can see on figure 5.7, that presents an ESPaDOnS flat field image taken with a tungsten lamp, the spectral orders are slightly curved and twisted (bright stripes). With this kind of illumination all the spectral orders are well visible, running from the left to the right side of the CCD. It is also clear from the image that the order separation's length is not constant along the dispersion direction, this fact is due to the different wavelength diffraction at the prism cross-disperser. The unique deficiencies that we can find along the *echellogramme* in terms of wavelength coverage, are some few tiny gaps in the three "reddest" order (bottom side of the CCD chip). In the data reducing process the location and shape of all spectral orders across the *echellogramme* are tracked with a rms accuracy better than 0.1 pixel (Donati,

1997).

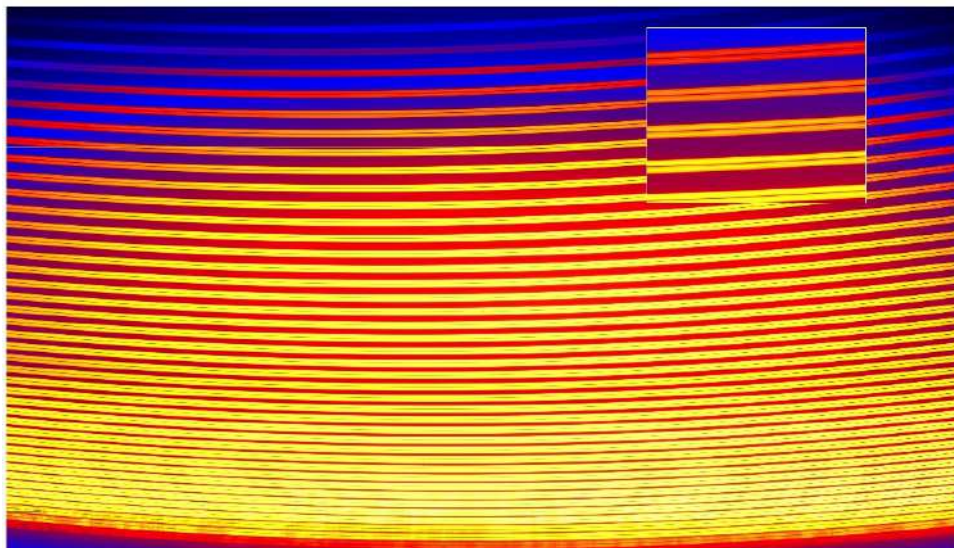


Figure 5.7: Spectral orders from a flat field image made of a ESPaDOnS exposure with a tungsten lamp. (Image from ESPaDOnS website).

The total instrument's estimated throughput is about 19% near 500 nm, dropping till merely 2% at the wavelength range limits (370 and 1000 nm). The combined efficiency of the telescope, fiber link, image slicer, spectrograph and CCD detector is roughly 40% on average, but drops down at both ends of spectral domain. At the instrument's aperture (of 1.6 arc seconds) there is a light loss of about 10%, at median seeing conditions. Also the path along the atmosphere brings down around 10% of the incoming light (considering an average airmass of 1.5). From the ensemble of this constrains, the peak total efficiency in average observing conditions is nearly 15%.

Nevertheless the estimated efficiency, the global efficiency obtained from real measurements is a bit lower, reaching an instrument's peak efficiency of around 12%. The modelled instrument response was confronted with the measured signal to noise ratio from observations, as a function of the wavelength, this comparison is presented in figure 5.8.

The instrument's temperature control lies on a double-layer thermal insulation. An inner thermally-passive enclosure that envelopes the optical bench, the spectrograph, including the optical and mechanical components; and an outer thermally-active enclosure where the temperature is regulated with an accuracy of about 0.1 degrees. The final rms level of the spectrograph's temperature stability is of the order of a 0.01°. Regarding the possible pressure gradients and pressure drifts inside the *Coudé* room, was

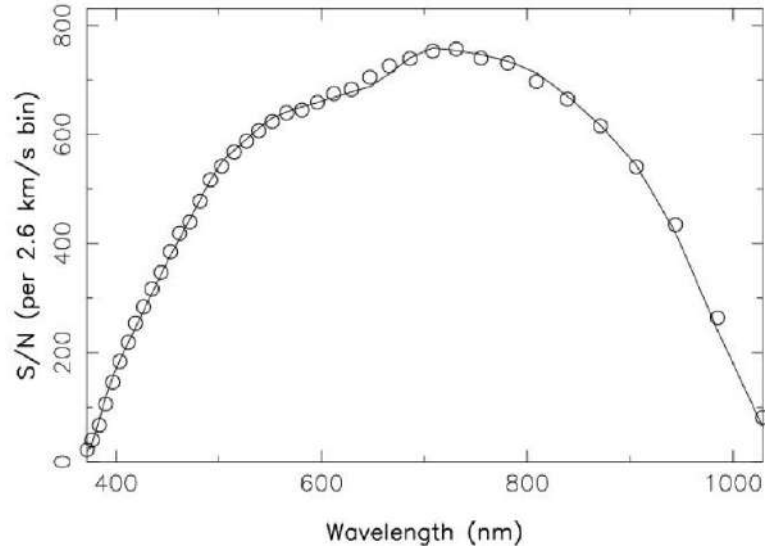


Figure 5.8: Modelled instrument response, as a full line, compared with to the measured signal to noise ratio (S/N) showed as open dots, as a function of the wavelength. (Image from ESPaDOnS website).

implemented there a digital barometer, at the inner enclosure, in order to monitor pressure fluctuations at an accuracy of better than a 0.01 mbar. The CCD detector is the only apparatus that is installed in a thermally insulated and evacuated tube. The present thermal insulation avoids short term temperature variations, however, long term variations still affect the spectrograph (on a time scale of several days), in this context can be observed till  $0.1 - 0.3^\circ K/day$  temperature fluctuations, inside the *Coudé* room.

The spectral stability was assessed by taking repeated calibration frames along a night of observations. After correlating all the image set with the first one taken on the series, it was possible to measure the spectral drifts due to temperature and pressure fluctuations. These results are very handy in order to estimate spurious radial velocities contributions induced from these thermal and mechanical relaxation causes. The average influences in the retrieved radial velocities, from temperature and pressure variability, are respectively:  $-3.5 km s^{-1}/^\circ K$  and  $0.3 km s^{-1}/mbar$ . The estimated relative stability of the instrument is better than  $10 m s^{-1}$  rms (Donati, 1997).

Regarding the CCD's detector, is used an EEV-type chip, with  $2k \times 4.5k$  of 00135 mm square pixels. In order to cover diverse cases of astrophysical applications, were implemented several readout speeds. For bright sources as is the case of the glowing Venus , where the photonic noise dominates,

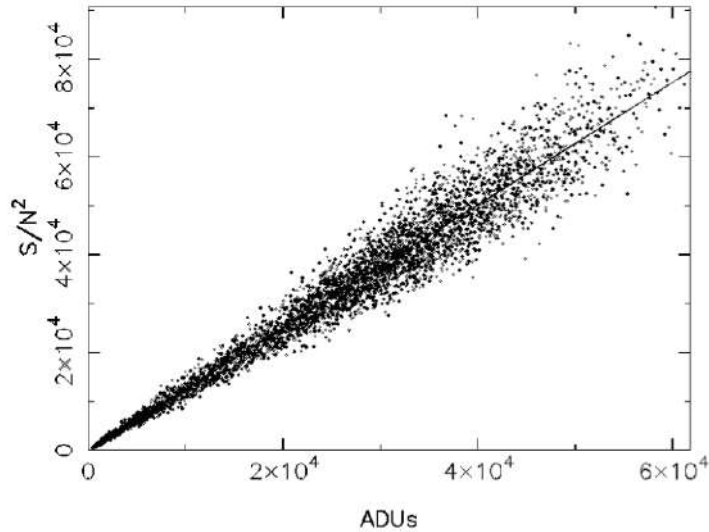


Figure 5.9: Inverse of the measurements variance (that equals the square value of the signal to noise ratio) as a function of the ADU counts from the respective measurement. (Image from ESPaDOnS website).

short readout times are crucial to avoid saturating the chip, to allow a high frequency temporal monitoring and to improve the flexibility of the observing sessions. The CCD readout is done as a background task, performed during the process of aiming the telescope to new offsets or changing the instrument configuration or even the parameters of the next exposure.

The readout velocity modes range from a 25 s time interval of full chip reading, with a readout noise of  $7.5 e^-$  (saturation at 58,000 ADU and gain of  $1.85 e^-/\text{ADU}$ ), till the extra-slow readout speed of 90 s for the entire chip readout, with a related noise of  $2.5 e^-$  (saturation level higher than 65,500 ADU and gain of  $0.84 e^-/\text{ADU}$ ). Good linearity between ADUs counts from the target and the inverse of the measurements variance (i.e. the squared signal to noise ratio) was observed till saturation level (Donati, 1997) as can be seen in figure 5.9.

The ESPaDOnS' aperture has two pinholes, the central one has a diameter of  $1.6''$  and is aimed to the observing target. The second pinhole is used to collect the sky background light, in the configuration mode object+sky, although this is not the case on the present work. There is a control agent that enables a real time display of the target, providing on that way, control upon the observations during the time lapse when they are carried out. There is also a neutral density wheel, in order to adapt the source brightness to the camera sensitivity.

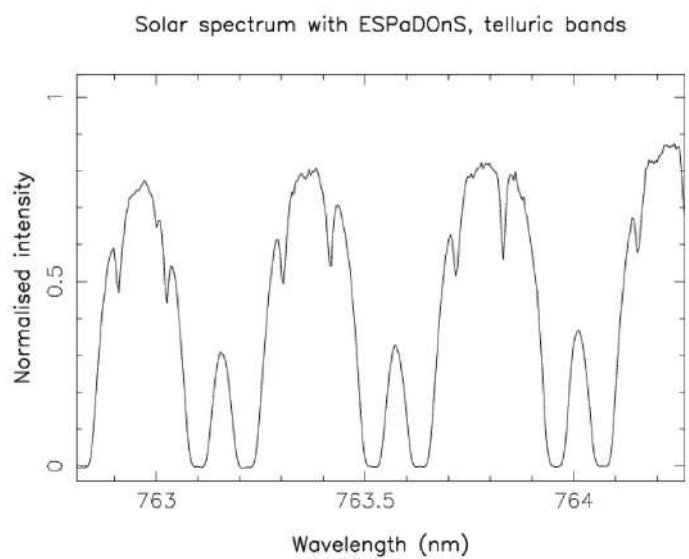


Figure 5.10: Example of a ESPaDOnS solar spectrum obtained in the near infrared (760 nm), there are also present strong telluric lines. (Image from ESPaDOnS website).

The guiding facility is a tool, developed for ESPaDOnS, that uses the target residual light from the edges of the target image in order to evaluate any possible drift from the field of view centre. If there is a de-centring, the system interacts with the telescope in order to improve the aiming. The guiding algorithm proved to be robust and it relies on a 2D gaussian fitting and a Chi square minimisation (Levenberg Marquard technique). As a by product of the guiding algorithm we can obtain the average seeing and target magnitude, in real time. A time exposure meter is also available, what can be very useful to evaluate the observing conditions along the observing session.

ESPaDOnS has a dedicated data reduction package (ESpRIT), specifically developed for reducing *echelle* polarimetric data by Donati (1997). On a first step, is performed a geometrical analyses from the calibration exposures in order to obtain the position and shape of the spectral orders on the *echellogramme*, these task is carried on based in a mean flat field image. On the other hand, the dispersion relation that assigns to each pixel, along and across the spectral orders, its respective wavelength, is computed from a Thorium-Argon wavelength calibration frame. In a second step, it is performed the optimal spectrum extraction, see an example on figure 5.10 of a near infrared (760 nm) portion of the solar spectrum, obtained with ESPaDOnS and the ESpRIT pipeline, where are notorious the intrusion of



5.1. *THE CFHT TELESCOPE AND THE ESPADONS INSTRUMENT*161

strong telluric lines.

## 5.2 Observations with CFHT/ESPaDOnS

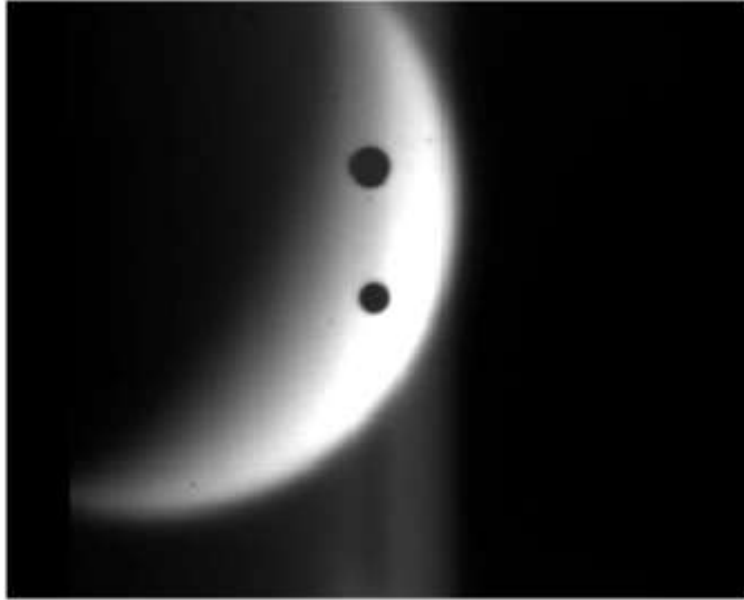


Figure 5.11: Example of the 3.6-m CFHT bonnette guiding camera field, taken on February 15, 2009 at 10:40UT. The Instrument is ESPaDOnS spectropolarimeter, operating 370-1050 nm to acquire the complete optical spectrum through single exposures at  $R = 80,000$  (Donati, 1997). The smaller aperture on Venus, pointed at Equator,  $[\phi - \phi_E] = -45^\circ$ , west of sub-Earth meridian on the sunlit hemisphere, is the 600- $\mu\text{m}$  entrance hole of the optical path. Its diameter projected on the sky plane is 1.6 arcsec. The larger spot appearing half way to CCD edge in the +Y direction is used in the case of stellar [point-source] objects for sky background subtraction and not used in this configuration. In February 2011, Venus phase angle was  $68^\circ$ , for an angular diameter of 16.8 arcsec, resulting in a projected point size on Venus of 577 km (see Table 5.1). To estimate the individual error on each velocity measurement it was repeated three times the short-time (3 s) exposures at each target point (see text).

Venus was observed at a phase angle  $\Phi = (68.7 \pm 0.3)^\circ$  using a semi-automated QSO mode during a three-day run on February 19-21 2011 at Canada-France-Hawaii Telescope (CFHT) on Mauna Kea. The run was initially approved to coincide with a coordinated campaign of ESA's Venus Express (VEx orbit 1766) and JAXA's VCO/Akatsuki orbiter missions on Feb 25-March 15 2011, the two spacecraft having both their ascending branches

on the Venus' day side during the period, with VEx/VIRTIS visible cloud tracking from apocenter corresponding to continuous cloud tracking by Akatsuki's payload instruments for up to 70 hours. Unfortunately, VCO Venus orbit insertion (VOI) scheduled for Dec 7, 2010 had failed due to a malfunction of the propulsion system (Nakamura et al., 2011). This period was also very favourable for Doppler velocimetry of the Venus' dayside cloud tops from the Earth shortly after maximum western elongation of Jan. 8, 2011. The research programme based on this CFHT/ESPADONS observations can be seen in Machado et al. (2013).

ESPADONS is a visible spectro-polarimeter covering the wavelengths range across the complete optical spectrum, from 370 to 1050 nm, collected over 40 spectral orders in a single exposure at a resolution of about 80,000 (Donati, 1997). The prime objective is to obtain a sequence of Doppler shift measurements across the disk of Venus. In addition to coordination with Venus Express and Akatsuki, our choice of observing dates offered the best compromise between the need to (i) maximize the angular diameter of Venus and spatial resolution on the disk, and (ii) minimize Venus phase angle and illuminated fraction as we only observe the day side. The observing strategy consists in displacing the entrance hole of the spectrograph along points on the dayside hemisphere while VEx/VIRTIS simultaneously acquired cloud tracking measurements on the same region (see section 5.5). Exposure times were adjusted at  $t = 3$  sec to obtain a roughly constant S/N of 400-600 on the continuum and avoid saturation, although this resulted in a significant underexposure in some regions of the disk near limb facing east sky and at high SZA on Venus, see section 5.3.8.

The relative stability of ESPADONS is 5-10 m/s rms, once corrected from temperature and pressure variation effects using apparent drift of the Earth's atmosphere molecular absorption superimposed to Venus' spectrum (section 5.3.1).

On February 19, 2011 Venus was observed between 18:57 and 22:10 UT (8:57 to 12:10 HST/UT-10) at a start Venus elevation of  $48.0^\circ$  (airmass 1.34) and end elevation of  $36.0^\circ$  (airmass 1.70). Observation was scheduled in full daylight (Sun's elevation ranged from  $28^\circ$  to  $58^\circ$ ) and required additional staff to check for solar illumination inside the dome. Seeing was 0.9 arcsec, and some thin clouds as well as early afternoon summit convection did not significantly affect the local photometric conditions. The diameter of Venus was 16.9 arcsec and its illumination factor was 68.3% (phase angle  $68.5^\circ$ ). The topocentric velocity between observer and Venus center of mass ranged between 12.3 and 12.7  $\text{km s}^{-1}$  and were later corrected in order to allow accurate Doppler velocimetry of solar lines, scattered by the cloud tops (see section 5.3.1). Scanning sequences over the South, dayside hemisphere were done in

Date	UT	Phase angle $\Phi$ ( $^{\circ}$ )	Ill. fraction (%)	Ang. diam. ( $''$ )	Ob-lon/lat ( $^{\circ}$ )	Airmass	seeing ( $''$ )	Pt size (km)
19 Feb	18:57-22:10	68.6-68.5	68.3	16.89-16.87	210.3/-1.24	1.34-1.70	0.9-0.8	574
20 Feb	19:18-23:23	68.2-68.1	68.6	16.77-16.75	213.0/-1.20	1.32-2.60	1.0	577
21 Feb	18:01-22:30	67.7-67.6	69.0	16.65-16.63	215.6/-1.16	1.48-1.78	1.1-0.6	582

Table 5.1: Orbital geometry and circumstances of ground-based CFHT/ESPADONS observations in this work : (1-2) UT date/time; (3-5) disk aspect : phase angle ( $^{\circ}$ ), illuminated fraction (%), apparent angular diameter (arcsec) ; (6) sub-observer longitude and latitude in Venus planetocentric coordinates ; (7-9) observing conditions and geometry : airmass ; seeing conditions at beginning/end (arcsec) ; 1.6" diameter size at Venus. (Machado et al., 2013).

repeated survey sequences of equal latitude at  $30^{\circ}$  S and  $40^{\circ}$  S between sub-Earth meridian near morning terminator ( $\phi_E = 0^{\circ}$ ) to  $[\phi - \phi_E] = -50^{\circ}$  with a reference point exposure, taken between each sequences at the intersection of Equator and the null zonal Doppler meridian (see section 5.3.4).

The sequences acquired on February 20, 2011 ranged between 19:18 and 23:23 UT (9:18 to 13:23 HST/UT-10) at a start Venus elevation of  $49.0^{\circ}$  (airmass 1.32) and end elevation of  $22.5^{\circ}$  (airmass 2.60). From night logs, tracking and pointing were excellent. Compared to Feb. 19 seeing was a bit degraded up to 1.2 and intermittent high altitude clouds combined with increased temperature produced occasional bad seeing during the final sequences, therefore some individual acquisitions had to be repeated. For that day the scanning sequence on the dayside hemisphere was devoted to a single latitudinal band at  $30^{\circ}$  S between sub-Earth meridian near morning terminator ( $\phi_E = 0^{\circ}$ ) to  $[\phi - \phi_E] = -50^{\circ}$ , in search for rapid variations over a timescale of several hours with the purpose of establishing a fine temporal grid for comparison with simultaneous cloud-tracking image analysis of the Venus Express/VIRTIS dataset at orbits 1766 to 1768 (see section 5.5).

On February 21, 2011 Venus was observed between 18:01 and 22:30 UT (8:01 to 12:30 HST/UT-10) at a start Venus elevation of  $42.5^{\circ}$  (airmass 1.48) and end elevation of  $33.3^{\circ}$  (airmass 1.78). Seeing was 1.0 arcsec, and some thin clouds and early afternoon summit convection did not significantly affect the locally photometric conditions. Seeing conditions improved toward the end of acquisition down to 0.6". On February 21 Venus' diameter was down 0.3 arcsec at 16.6 arcsec and its illumination factor was 69.0% (phase angle  $67.7^{\circ}$ ). Topocentric velocity between observer and Venus mass center ranged between 12.2 and 12.6 km  $s^{-1}$ . Doppler velocimetry scanning of the Venus disk on the dayside was done in raster sequences at latitudes  $30^{\circ}$  S and  $40^{\circ}$  S

between sub-Earth meridian near morning terminator ( $\phi_E = 0^\circ$ ) to  $[\phi - \phi_E] = -50^\circ$ , again with a reference zero-zonal Doppler velocity point taken on the Equator (see section 5.3.4 and Fig. 5.18).

The coincidence of ground-based observations and space-based ones involved the VIRTIS instrument and the VMC camera from VEx and the high-resolution spectrograph ESPaDOnS coupled to the Canada-France-Hawaii telescope (CFHT). Were made simultaneous observations at same planetary regions as shown on figure 5.12, at orbit 1768.

	(1) Seq. nb	(2) Loc.	(3) Time span (UT)	(4) Points order
<hr/>				
Feb. 19, 2011				
	[1]	S lat 30°	19:05-19:37	10-34-33-[13]-10
	[2]	S lat 30°	19:38-20:18	10-34-33-32-32-31-30-(29)-10
	[3]	S lat 40°	20:19-20:54	10-41-40-39-38-37-(36)-10
	[4]	S lat 30°	20:55-21:23	10-34-33-32-31-30-(29)-10
	[5]	S lat 40°	21:24-21:48	10-41-40-39-38-37-(36)-10
	[6]	S lat 30°	21:49-22:10	10-34-33-32-31-30-(29)-10
<hr/>				
Feb. 20, 2011				
	[7]	S lat 30°	19:22-19:44	10-34-33-32-31-30-(29)-10
	[8]	S lat 30°	19:45-20:14	10-34-33-32-31-30-(29)-10
	[9]	S lat 30°	20:15-20:53	10-34-33-32-31-30-(29)-10
	[10]	S lat 30°	20:54-21:33	10-34-33-32-31-30-30-(29)-10
	[11]	S lat 30°	21:34-22:05	10-34-33-32-31-30-(29)-10
	[12]	S lat 30°	22:06-22:33	10-34-33-32-31-30-(29)-10
	[13]	S lat 30°	22:34-23:14	10-[34-33-32-31-10]
<hr/>				
Feb. 21, 2011				
	[14]	S lat 10-20°	18:09-19:00	10-20-19-18-17-16-(15)-27-26-25-24-23-(22)-10
	[15]	S lat 30°	19:01-19:26	10-34-33-32-31-30-(29)-10
	[16]	S lat 40°	19:27-19:47	10-41-40-39-38-(36)-37-10
	[17]	S lat 50°	19:48-20:07	10-(48)-47-46-45-44-10
	[18]	S lat 50°	20:08-20:29	10-(48)-47-46-45-44-(43)-10
	[19]	S lat 40°	20:30-21:10	10-41-40-40-39-38-37-[43 × 4]-10
	[20]	$[\phi - \phi_E] = 0^\circ$	21:11-21:49	10-13-20-27-34-41-(48)-10
	[21]	$[\phi - \phi_E] = 12^\circ\text{E}$	21:50-22:28	10-(14-21-28-35-42-49-49-54-49-42-42-28-21)

Table 5.2: Scanning sequences on Venus' dayside hemisphere using CFHT/ESPaDONs during the Feb. 19-21, 2011 observing run : (1) acquisition sequence number; (2) location on disk, with long. to sub-terrestrial meridian; note that all Feb. 20, 2011 acquisitions are at the same S lat 30° latitude band (see sub-section 5.3.1); (3) UT date and time span; (4) points acquisition order; points 15, 22, 29, 36, 43, 48 in parenthesis, have been observed but not included in the kinematical fit for their lower S/N and/or limb or high SZA geometry (see section 5.3.8); (5) exposure repetition: each point is acquired 3 times to check for internal consistency (see sub-section 5.3.4). Points in brackets has been discarded from analysis for severe drift, seeing or tracking issues during observations. See Machado et al. (2013).

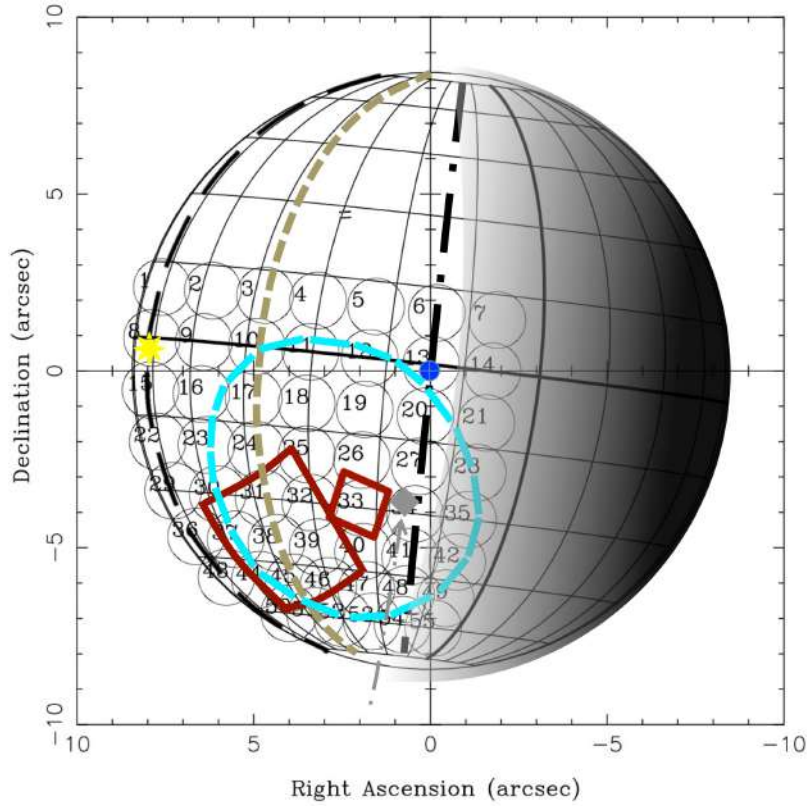


Figure 5.12: Venus seen for an observer on Earth in a celestial frame  $(\alpha, \delta)$  on Feb. 20, 2011 21h UTC. Celestial North is up. Dashed-dotted thick line is the instantaneous sub-terrestrial meridian (with sub-Earth point as a blue circle). Dashed thick line is the sub-solar meridian (with the Sun symbol at sub-solar point). Morning terminator is east of central meridian, toward negative RA. Planetocentric latitude of sub-Earth and sub-solar points are  $-1.25^\circ$  and  $-0.84^\circ$ , respectively. The brown dashed-line corresponds to the null zonal Doppler meridian at  $[\phi - \phi_E] = \Phi/2 = 34.3^\circ$  to sub-Earth longitude  $\phi_E = 0^\circ$  (see section 4.1.1). CFHT/ESPaDONs observations were scheduled Feb 19, 8:00-12:00 HST (18:00-22:00 UTC), Feb. 20, 8:00-15:00 HST (Feb. 20, 18:00 - Feb. 21 1:00 UTC) and Feb. 21, 8:00-14:00 HST (Feb. 21, 18:00 - Feb. 22 0:00 UTC) while VEx orbit predictions indicated VIRTIS and VMC instruments on during (1) orbit 1766 at : Feb. 19, 18:00 UTC - Feb. 20 4:00 UTC ; (2) orbit 1767 : Feb. 20, 18:00 UTC - Feb. 21 5:00 UTC ; (3) orbit 1768 : Feb. 21, 13:30- 20:00 UTC. Eventually, only orbit 1768 could be used for synchronized VIRTIS-M UV cloud tracking measurements at cloud tops with ground-based Doppler winds. The figure illustrates our observing strategy to match CFHT/ESPaDONs operations (thin black circles) and ESA/Venus Express VIRTIS-M instrument near 365 nm (red squares) and VMC camera (dashed light-blue circle) during orbit 1766. The ascending branch of VEx started out near the morning terminator close to sub-Earth meridian at the time the observations were scheduled at CFHT. The figure shows the footprint of VEx spacecraft position on Feb. 20, 2011 at 2:15 UTC as a grey diamond. [Machado et al. \(2013\)](#).

## 5.3 Doppler velocimetry with ESPaDONs

### 5.3.1 Projected radial velocities

The main purpose of this study is to provide direct wind velocity measurements using visible Fraunhofer lines scattered by Venus' cloud tops. The solar Fraunhofer spectrum results from absorption of continuum radiation emitted from warmer, deeper layers by atoms and molecules of the solar atmosphere (such as H, S, Si, Fe, Ba, Mg, CN) (Widemann et al., 2008). The Doppler shift measured in solar scattered light on Venus' dayside is the result of two instantaneous motions: (1) an instantaneous motion between the Sun and Venus' upper cloud particles ; this Doppler velocity is minimal near Venus sub-solar point ; (2) a motion between the observer and Venus clouds, resulting from the topocentric velocity of Venus cloud particles in the observer's frame ; this effect is minimal near Venus' sub-terrestrial point (Widemann et al., 2008; Machado et al., 2013). These combined instantaneous motions add-up and the combined Doppler shift vary spatially as a function of the planetocentric longitude and latitude at Venus.

The spectral calibration with ESPaDONs data reduction pipeline (ESPpRIT) provides Fraunhofer lines velocities in the solar system barycentric frame (B). In order to derive the wind radial velocity  $w_i$  at each point (along the line-of-sight) in the planetocentric frame (P), the spectral calibration and radial velocity measurement is performed in four steps: (i) Th-Ar spectrum, at the beginning and end of acquisition session; (ii) spectral drift, monitored during the acquisition by cross-correlation on telluric lines present on the line-of-sight; (iii) correction from Earth's spin and orbital motion (berv); (iv) least-square deconvolution is then applied to the pattern of Fraunhofer lines (G2 star mask) to provide radial velocity  $h$  in the barycentric reference frame (Widemann et al., 2008; Machado et al., 2013).

(i) The spectral wavelength calibration is performed at beginning and end of the acquisition session by means of a Th-Ar (Thorium - Argon) lamp exposure on the detector, in order to monitor the dispersion law of each of ESPaDONs' instrument spectral orders. Their spectral lines, which wavelengths are well known, are fit to a 2-D polynomial dispersion law in the spectral dimension for each order ;

(ii) Earth's atmosphere absorption lines superimposed to Venus' spectra are used as on-sky velocity calibration (in the observer's rest referential) in order to correct any spectral drift due to instrumental effects, as is the case of mechanical flexure, temperature or pressure variations in the spectrograph chamber or along the coudé optical path ;

(iii) The instantaneous velocity of Venus' center of mass  $v_{topo}$  is deter-



mined with *Horizons* ephemeris provided by the Jet Propulsion Laboratory (NASA-JPL) (Giorgini et al., 1996). It is function of both orbital and spin motions of the Earth, the geographic coordinates of the observatory site (Mauna Kea - Hawaii) and the UT time of observations. This velocity varies by the order of several m/s per minute.

(iv) the instrument's pipeline (ESpRIT) automatically extracts wavelength-calibrated intensity with associated error bars at each wavelength pixel, relative to the barycentric rest frame (Widemann et al., 2008). A least-squares deconvolution is applied to the pattern of Fraunhofer lines, using a G2 type star mask. This mask is based on the model of stellar abundances by Kurucz et al. (1993), this deconvolution provides the radial velocity (along the line-of-sight) in the solar system barycentric reference frame (B) (Widemann et al., 2008). Since solar Fraunhofer lines are also present in the spectrum of solar radiation scattered at Earth's atmosphere, the pipeline identifies two peaks (from the Venus solar radiation scattered spectra and the one from Earth) of relative shift ( $v_{topo}$ ). At the time of observations, 19-21 February 2011, the phase angle was  $\phi = 68^\circ$  and the Venus-Earth relative velocity was about  $12.75 \text{ km s}^{-1}$ , allowing a clear separation between the solar lines scattered off Venus and terrestrial ones (Fig. 5.13). The cloud top velocity along the line-of-sight is then retrieved by applying a double Gaussian fit to the correlation function between corresponding Fraunhofer lines at Venus and telluric ones.

### 5.3.2 Velocity extraction

We derive the instantaneous Doppler shift for the motion of the cloud top aerosol particles in the planetocentric frame:

$$w_i = h - (berv + v_{topo}) \quad (5.1)$$

Where  $w_i$  is the radial component of the instantaneous velocity of Venus' cloud top aerosols that scattered the solar radiation in the observer's direction.

Additional astronomical corrections are needed: (1) the influence of an unbalanced illumination from the two limbs of the rotating Sun (combination of a receding and an approaching solar limb, described as the Young effect, see sub-section 4.4.2 and 5.3.3); (2) an on-target monitoring of the instrumental drift using relative Doppler shift to a specific location on Venus' disk (see sub-section 5.3.5). Eventually, the radial velocity is de-projected in order to derive the instantaneous horizontal wind velocities in Venus planetocentric

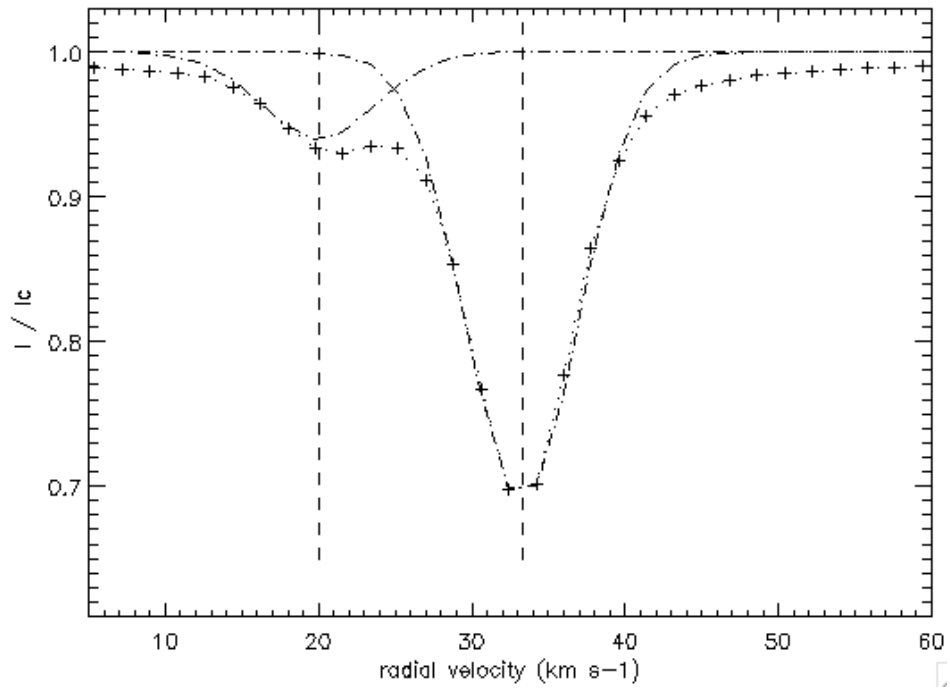


Figure 5.13: The retrieval of apparent velocity of lines uses a least-square deconvolution in the solar system barycentric rest frame observed with CFHT/ESPADONS on Feb. 19, 2011 at 22:01 UT on a point at latitude  $\lambda = 30^\circ$  S (point 31), with a 2-second exposure. The deeper line shows the Gaussian best-fit velocity shift for scattered Fraunhofer lines by Venus' atmosphere. The shallower line corresponds to solar Fraunhofer lines scattered in the Earth's atmosphere, at rest in the topocentric (observer's) frame. The two correlation peaks are separated by the Venus' topocentric velocity to observer  $v_{topo}$ . See text for details.

reference frame (section 5.3.8).

### 5.3.3 Young effect correction

Due to the large,  $1^\circ$  angular size of the Sun and its fast rotation, a differential elevation of the finite solar disk near terminator will result in unbalance between the contribution of the approaching solar limb (blue shifted radiation) and the receding solar limb (red shifted radiation) ; in such geometry, the excess of one or the other will affect the apparent line Doppler shifts measured along the Venus atmosphere (Widemann et al., 2007).

This systematic effect that affect the Fraunhofer lines was corrected on the same way as on section 4.4, more precisely in the Young effect correction's dedicated subsection 4.4.2, relative to the data analyses from the observations carried out with VLT/UVES.

The Doppler shift due to the Young effect is considered as an additional correction to apparent line-of-sight velocities. Its sign is negative at western elongation near local morning terminator (and positive at eastern elongation near local evening terminator). The calculated corrections on the measured Doppler shift, due to the Young effect, for each one of the observations carried out, are listed on table 5.14 (column 5).

To correct the measured Doppler shift from the Young effect, we proceed as follows:

$$w_{i,c} = w_i + Y(\phi, \psi) \quad (5.2)$$

where  $w_{i,c}$  is the projected wind velocity along the line-of-sight,  $w_i$  is the measured Doppler shift (Equ. 5.3.2, section 5.3.2),  $Y$  is the corrective term due to the Young effect, function of  $\phi$  and  $\psi$ , the planetocentric latitude and longitude of the observed point upon the disk.

### 5.3.4 Monitoring the instrumental drift

After the instantaneous velocity of Venus center of mass  $v_{topo}$  has been subtracted, spectral wavelength calibration is performed at beginning and end of the acquisition session by means of a Th-Ar (Thorium - Argon) lamp exposure on the detector, and atmospheric telluric absorption lines superimposed to Venus' spectra are used as additional on-sky velocity calibration, a *relative* velocity  $v_{i,ref}$  is obtained by subtracting the absolute velocity measured at each point with a reference velocity on Venus at point 10,  $[\phi - \phi_E] \simeq 34^\circ$ , lat. =  $0^\circ$ .

(1) Point	(2) $\phi - \phi_E$ ( $^\circ$ )	(3) $\lambda$ ( $^\circ$ )	(4) Local time (h:m)	(5) Young geometry corr ( $\text{km s}^{-1}$ )
8	-70 $^\circ$	0 $^\circ$	12:00p	-0.1
9	-50 $^\circ$	0 $^\circ$	10:50a	-1.1
10	-36 $^\circ$	0 $^\circ$	9:50a	-2.0
11	-24 $^\circ$	0 $^\circ$	9:05a	-3.1
12	-12 $^\circ$	0 $^\circ$	8:10a	-4.8
13	0 $^\circ$	0 $^\circ$	7:30a	-8.1
14	+12 $^\circ$	0 $^\circ$	6:40a	-19.2
15	-70 $^\circ$	10 $^\circ$ S	12:00p	-0.5
16	-50 $^\circ$	10 $^\circ$ S	10:50a	-1.2
17	-36 $^\circ$	10 $^\circ$ S	9:50a	-2.1
18	-24 $^\circ$	10 $^\circ$ S	9:05a	-3.2
19	-12 $^\circ$	10 $^\circ$ S	8:10a	-4.9
20	0 $^\circ$	10 $^\circ$ S	7:30a	-8.3
21	+12 $^\circ$	10 $^\circ$ S	6:40a	-19.4
22	-70 $^\circ$	20 $^\circ$ S	12:00p	-1.1
23	-50 $^\circ$	20 $^\circ$ S	10:50a	-1.6
24	-36 $^\circ$	20 $^\circ$ S	9:50a	-2.4
25	-24 $^\circ$	20 $^\circ$ S	9:05a	-3.5
26	-12 $^\circ$	20 $^\circ$ S	8:10a	-5.2
27	0 $^\circ$	20 $^\circ$ S	7:30a	-8.7
28	+12 $^\circ$	20 $^\circ$ S	6:40a	-20.2
29	-70 $^\circ$	30 $^\circ$ S	12:00p	-1.8
30	-50 $^\circ$	30 $^\circ$ S	10:50a	-2.2
31	-36 $^\circ$	30 $^\circ$ S	9:50a	-3.0
32	-24 $^\circ$	30 $^\circ$ S	9:05a	-4.0
33	-12 $^\circ$	30 $^\circ$ S	8:10a	-5.8
34	0 $^\circ$	30 $^\circ$ S	7:30a	-9.5
35	+12 $^\circ$	30 $^\circ$ S	6:40a	-21.7
36	-70 $^\circ$	40 $^\circ$ S	12:00p	-2.6
37	-50 $^\circ$	40 $^\circ$ S	10:50a	-3.0
38	-36 $^\circ$	40 $^\circ$ S	9:50a	-3.7
39	-24 $^\circ$	40 $^\circ$ S	9:05a	-4.9
40	-12 $^\circ$	40 $^\circ$ S	8:10a	-6.8
41	0 $^\circ$	40 $^\circ$ S	7:30a	-10.8
42	+12 $^\circ$	40 $^\circ$ S	6:40a	-24.3
43	-70 $^\circ$	50 $^\circ$ S	12:00p	-3.8
44	-50 $^\circ$	50 $^\circ$ S	10:50a	-4.1
45	-36 $^\circ$	50 $^\circ$ S	9:50a	-4.9
46	-24 $^\circ$	50 $^\circ$ S	9:05a	-6.1
47	-12 $^\circ$	50 $^\circ$ S	8:10a	-8.3
48	0 $^\circ$	50 $^\circ$ S	7:30a	-12.9
49	+12 $^\circ$	50 $^\circ$ S	6:40a	-28.7

Table 5.3: Local characteristics and pointing geometry at the time of CFHT/ESPaDOnS February 19-21 acquisition: (1) Point number (see Fig. 5.12); (2) planetocentric longitude [ $\phi - \phi_E$ ] and (3) latitude  $\lambda$  at point center ( $\phi_E$  is planetocentric longitude of sub-terrestrial meridian) ; (4) local solar time on Venus (LST) in h:m at point center; (5) Young correction at point center in  $\text{km s}^{-1}$  (see text, section 4.4.2, 5.3.3 and Machado et al. (2013)).

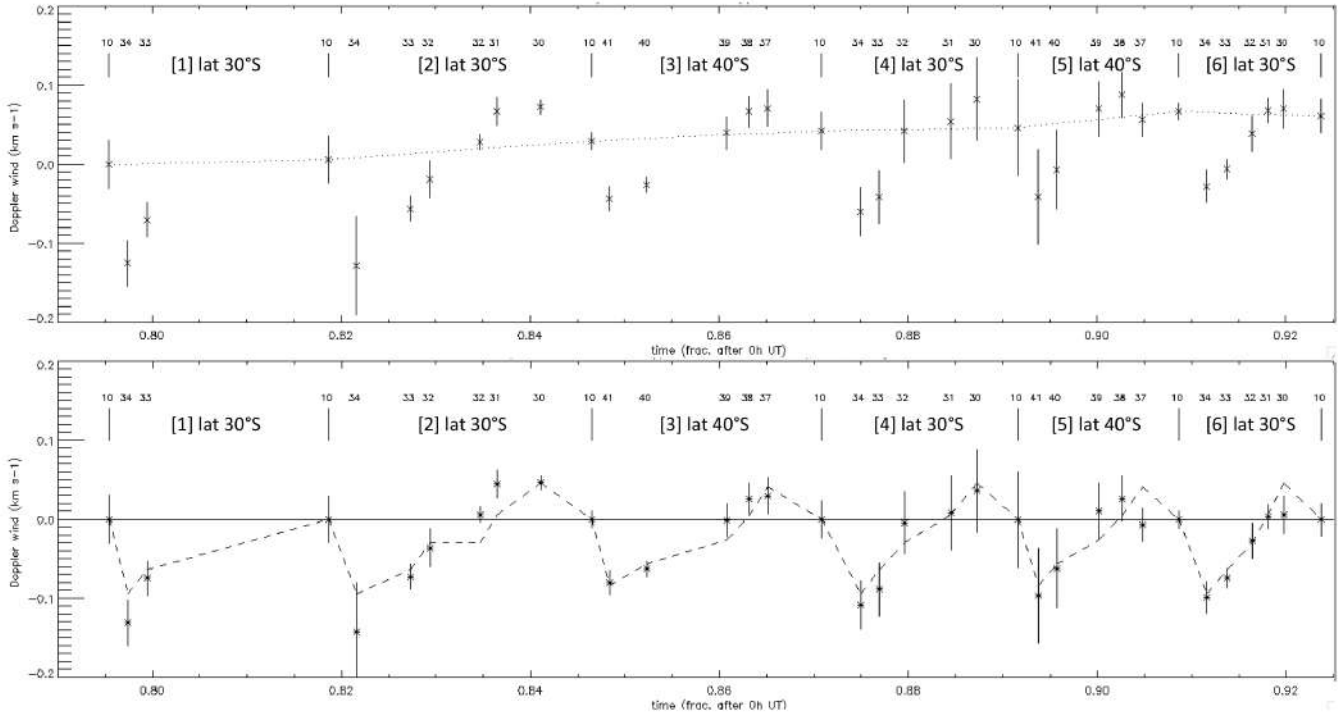


Figure 5.14: Doppler winds  $v_i$  and  $v'_i$  on February 19 UT, 18:57-22:10 UT. Numbers in brackets correspond to scanning sequences during acquisition with CFHT/ESPaDOnS with their latitude on Venus, see Table 5.2 and Fig. 5.13. X-axis is fraction of day after 0h UT (0.01 day = 14.4 minutes). (a) top: relative Doppler velocity  $v_i = w_{i,c} - w_{i,c,ref}$  of Equ. 5.3.4, where  $w_{i,c}$  is the projected wind velocity along the line-of-sight, corrected from the Young effect (sub-section 5.3.3), and the Doppler velocity at first point  $w_{i,c,ref}$ . The dotted line corresponds to  $v_{trend}(t)$  calculated on point-10 exposures (see Section 5.3.5); (b) bottom: kinematical fit to Feb. 19 differential wind field  $v'_i = v_i - v_{i,trend}$  to a pure zonal circulation with  $v = (117.5 \pm 14.5) \text{ m s}^{-1}$  (dashed line, see text, Table 5.4 and Machado et al. (2013)).

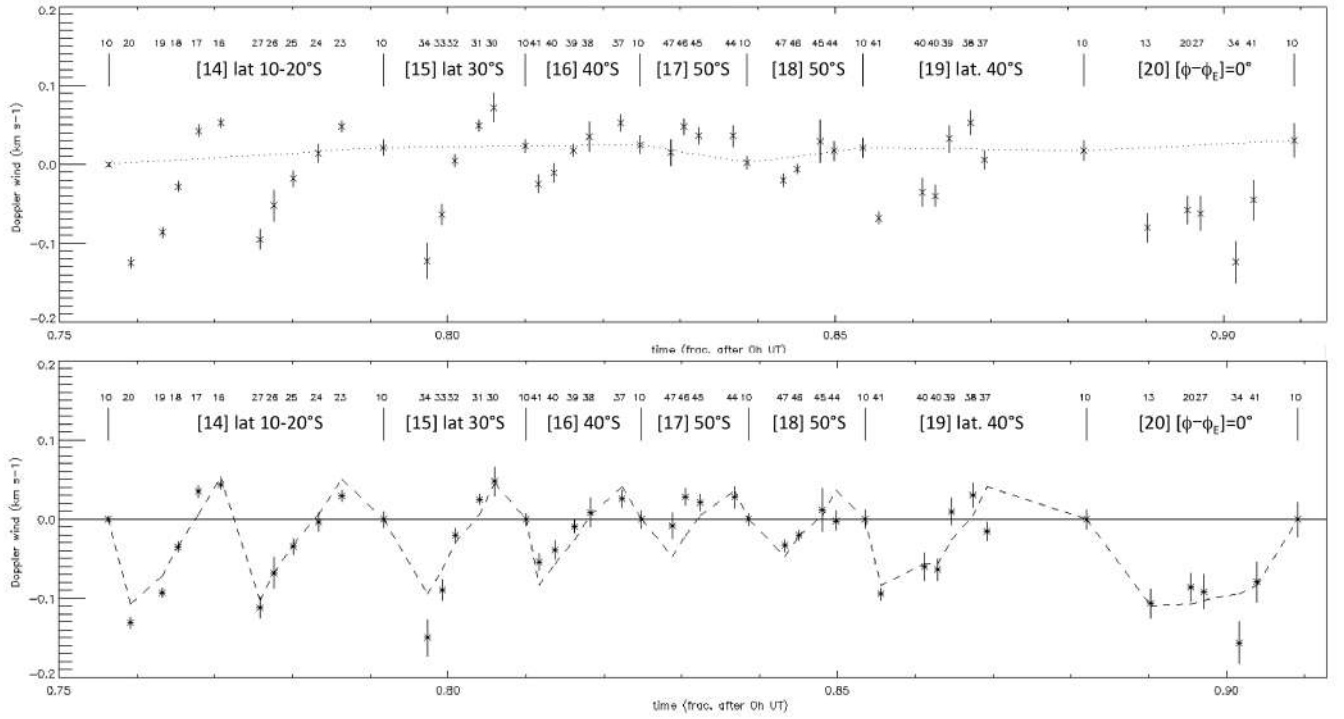


Figure 5.15: Doppler winds  $v_i$  and  $v'_i$  on February 21 UT, 18:01-22:30 UT. Point acquisition numbers are indicated in reference to Table 5.2 and Fig. 5.13. X-axis is fraction of day after 0h UT. (a) top: relative velocity  $v_i = w_{i,c} - w_{i,c,ref}$ . Dotted line:  $v_{trend}(t)$ ; (b) bottom: kinematical fit to Feb. 21 differential wind field  $v'_i = v_i - v_{i,trend}$  corrected for Young effect, to a pure zonal circulation with  $v = (117.4 \pm 18) \text{ m s}^{-1}$  (dashed line, see text and Table 5.5).

Because CFHT/ESPaDOnS acquisition on Venus disk is sequential, a relative velocity  $v_i$  is obtained by subtracting the absolute velocity measured at each point on Venus to  $w_{i,c,ref}$ :

$$v_i = w_{i,c} - w_{i,c,ref} \quad (5.3)$$

where  $w_{i,c,ref}$  is the initial measurement at point number 10,  $w_{i,c}$  is the absolute velocity of each point determined in section 5.3.3, and  $v_{i,cal}$  is the resulting relative velocity.

In their upper panels, Figs. 5.17 a) and b) show relative velocities  $v_i$  with their error bars  $\sigma_i$ . They are plotted as a function of time, with the target point numbers superimposed. Immediately apparent is a slow drift of the point 10 velocities by about  $30 \text{ m s}^{-1}$  end-to-end. This drift, presumably due to still imperfectly corrected instrumental effects and measurement of solar absorption lines with respect to telluric lines (Young et al., 1979; Widemann et al., 2007) can be fit to a series of linear segments,  $v_{trend}(t)$  plotted as a dotted line on Fig. 5.14a and 5.15a, so that

$$v'_i = v_i - v_{i,trend} \quad (5.4)$$

### 5.3.5 Error estimate

Absolute error on a given absolute velocity measurement  $w_{i,c}$  results from the combination of a number of uncertainties: (i) the Th-Ar dispersion law uncertainty, (ii) the telluric lines correlation method uncertainty, with possible fluctuations of the reference scale due to intrinsic variability; (iii) the least-square deconvolution differential rms precision; (iv) the velocity error resulting from pointing and guiding errors. This error affects all measurements including the reference polynomial  $v_{i,trend}$  therefore causing an increase of the error on relative measurements  $v'_i$  (Widemann et al., 2008). This is similar to methods in which a reference spectrum is used in the velocity fitting algorithm. Rather than trying to calculate an upper limit to the combination of the various error terms (i)-(iv), we take advantage of repetition of short-time exposures at each point, to qualitatively test the internal consistency of the retrieved radial velocity  $v$ , obtained by the least-square deconvolution of ESPrIT. To estimate the individual error on each velocity measurement we repeated three times the short-time (3 s) exposures at each target point and calculated the respective standard deviation ( $\sigma_i$ ). The variability from successive exposures at each observational point indicates a high consistency, with an upper limit of 5 to  $6 \text{ m s}^{-1}$  between the mid latitudes range, but

growing to twice this value at low SNR and/or higher latitudes or high SZA near terminator (see next section). Individual target point's velocities were obtained by weight-averaging the retrieved values from the consecutive exposures taken at each Venus target pointing instrument's offset.

Considering that  $\sigma_i$  is the error on the point 10 velocity relative to the measurement  $v_i$ , therefore the statistical combined error at each point is given by  $\sigma'_i = \sqrt{\sigma_{trend,i}^2 + \sigma_i^2}$ . To determine  $\sigma_{trend,i}^2$  on the trend fitting function  $v_{trend}(t)$  at each point  $i$ , we interpolate the errors  $\sigma_i^2$  on points 10, which have been determined by taking advantage of repetition of short-time exposures, and consider arbitrarily a linear spread of the error bar along the segment between two point-10 exposures.

### 5.3.6 Altitude of observations

The visible light is reflected and scattered off Venus' cloud tops. The determination of this altitude level originates from early polarization and photometry studies undertaken by [Henson and Hovenier \(1974\)](#). On the other hand, cloud tops 365 nm UV markings were estimated by [Kawabata et al. \(1980\)](#) to probe the same altitude level ([Gierasch et al., 1997](#); [Widemann et al., 2007, 2008](#)).

As discussed by [Widemann et al. \(2007\)](#), the [Kawabata et al. \(1980\)](#) model consists of a main cloud, with particle size of  $1.05 \mu\text{m}$ , underlain by and partly mixed with a haze with  $\simeq 0.2 \mu\text{m}$  particle size. The optical depth of the haze is about 0.6 at 40 mbar, and varies roughly as  $\lambda^{-1.7}$ , meaning a  $\tau = 1$  level is reached within one scale height of the clouds top at 70 km of altitude ([Ignatiev, 2009](#)), see figure 3.20. This is also the altitude of the UV cloud markers that enables the cloud tracking wind's measurements technique ([Moissl et al., 2009](#); [Sánchez-Lavega et al., 2008](#)). This coincidence permits to compare magnitudes and variability between ESPaDOOnS/CFHT, UVES/VLT ([Machado et al., 2012](#)) results and the ones from tracking of UV markings methods as is the case for VEx/VIRTIS-M, Pioneer Venus-OCPP and Galileo (SSI).

### 5.3.7 Doppler velocimetry analysis

In this section we present the velocity measurements retrieved with the *sequential* Doppler velocimetry technique. First, all the observations were used to produce the zonal wind velocity  $\chi^2$  best-fit for the ensemble of the instantaneous wind velocities results. This was done with the observations data from 19 and 21 Feb 2013, and under the assumption of a pure zonal



wind system. The second step consisted in performing a two-dimensional  $\chi^2$  best-fit zonal and meridional velocity fit, based in the entire set of wind velocities obtained. This procedure was then repeated for the zonal and sub-solar to anti-solar (SS-AS) two wind's system, now with the SS-AS and zonal projection coefficients, instead of the meridional and the zonal ones.

The observations at the dayside limb facing east-sky (pointing positions at longitude  $[\phi - \phi_E] = -70^\circ$  : position 15 at S lat  $10^\circ$ , 22 at S lat  $20^\circ$ , 29 at S lat  $= 30^\circ$ , 36 at S lat  $40^\circ$ , 43 at S lat  $50^\circ$  - Table 5.3 and Fig. 5.12) had to be discarded due to the inconsistent velocity values retrieved and the high error bars associated to these measurements. Our interpretation is that low signal to noise ratio (SNR), partly due to the instrument's aperture partially scanning the background sky, has a direct impact on the double-Gaussian fit on the retrieved velocities of the Fraunhofer lines. A similar effect was described in Doppler velocimetry measurements with the high-resolution spectrograph UVES at European Southern Observatory's Very Large Telescope in 2007 observations (Machado et al., 2012). Note that any incoming scattered light is blocked by the interference filter. Another line of interpretation is the anisotropy of cloud scattering (Young and Kattawar, 1977) also discussed as an interpretation to limb scan of Venus haze by the OCPP photopolarimeter on board Pioneer-Venus (Lane and Opstbaum, 1983). Multiple scattering of overlying haze above cloud tops may account to up to 80% of UV intensity near 365-nm compared to 20% contribution by singly scattered sunlight at a phase angle of  $60-70^\circ$ , see their Fig. 4. This relative contribution will vary as a function of scattering properties of upper haze particles across the entire visible range of  $0.37-1.05 \mu\text{m}$  covered by ESPaDONs and will affect the output of our Doppler analysis. Points sounding the terminator or at high S lat and/or  $\text{SZA} > \Phi = 68^\circ$  (position numbers 14, 21, 28, 35, 42, 48, 49) at  $[\phi - \phi_E] = 0^\circ$  and  $12^\circ$  east of central meridian were also discarded for they low S/N at 3-sec exposure.

### 5.3.8 Observing geometry correction

#### Null zonal Doppler meridian

The intensity of solar scattered light viewed by an observer outside the atmosphere is normally obtained by summing the contributions from many optically thin scattering elements located on Venus' dayside along the line of sight in general, plane parallel models (Lane and Opstbaum, 1983). Albedo models consists of a main cloud underlain by and partly mixed with a haze with  $\sim 0.2\mu\text{m}$  particle size (see discussion in section section and 5.6.1). The cloud tops are assumed to scatter radiation isotropically and have been simu-

lated by the isotropic field of a Lambert surface (Young and Kattawar, 1977; Lane and Opstbaum, 1983). Assuming a pure horizontal motion of the cloud top particles, two extreme cases can be considered (see Machado et al. (2012), Fig.4b). Near Venus sub-solar point, cloud particles have most of their horizontal motion in the observer's direction, while near Venus sub-terrestrial point, singly scattering particles have their maximum velocity in the Sun's direction. For this assumption we only consider the local albedo of the reflecting clouds considered a Lambert surface, and neglect the contribution to albedo of multiple scattering by haze particles. See a discussion of this approximation in properties in Lane and Opstbaum (1983).

In the global retrograde zonal circulation of Venus cloud tops, the particles motion causes the light viewed by an observer outside the atmosphere to be Doppler-shifted in one point and shifted by the opposing amount at the other point. The measured Doppler shift is the sum of those two terms. It varies with planetocentric longitude and latitude. Given the geometry of the observations on February 2011, at phase angle  $\Phi = (68.7 \pm 0.3)^\circ$ , the sub-solar meridian is close to regions of maximum apparent redshift, while maximum blueshift is near sub-Earth meridian close to morning terminator on Venus (Fig. 2). At a planetocentric longitude  $[\phi - \phi_E]$  halfway between sub-solar and sub-Earth longitude (represented by a dashed line in Fig. 5.12), i.e. half of phase angle  $\Phi$  so that  $[\phi - \phi_E] = \Phi/2 \simeq 34.3^\circ$ , the two effects cancel out in the case of a super-rotating wind field, as the particles velocities toward the radiation source and toward the observer cancel each other out, resulting in an apparent null-Doppler meridian in the case of a pure zonal wind field.

In mine CFHT/ESPaDOnS datasets, the meridian for which the Doppler shift induced by the zonal component of the wind is zero - which is henceforth designated by null-zonal Doppler meridian, for the zonal wind-field occurs at pointing positions 10, 17, 24, 31, 38, and 45, from Equator to South lat  $50^\circ$  by steps of  $10^\circ$ . Telescope offset positions to disk center were calculated and guided to point at these locations for a planetocentric longitude of  $[\phi - \phi_E] = 36.0^\circ$  using the telescope control system (TCS). For  $\Phi = 68.6^\circ$  and an apparent Venus diameter of 16.8 arcsec, the difference between true null-Doppler at  $34.3^\circ$  and calculated pointing location at west longitude  $36^\circ$  cannot exceed 0.2 arcsec, well within the ESPaDOnS FOV projected diameter of 1.6 arcsec on Venus.

### De-projection coefficients

The Doppler velocities retrieved from Eqs. 6.2, 5.2 are radial velocities, i.e., projected along the line-of-sight. To perform the de-projection of these radial velocities in order to obtain the amplitude of wind velocities, at each probed

Step	Symbol	Wind velocity data / model fit (f)	Equ.	Table	Figure
1	$w_i = h - (berv + v_{topo})$	Line-of-sight wind at pos. i	1	-	-
2	$v_i = w_{i,c} - w_{i,c,ref}$	Line-of-sight wind, Young / ref. corr.	2,5	-	4a,5a
3	$v'_i = v_i - v_{i,trend}$	Line-of-sight wind, detrended w/pt-10	6	-	4b,5b,10
4	$\bar{v}_{z,i}$	Day-av. horizontal wind at pos. i	7	-	8, 9, 13a-c, 14
5	$v_{z,i}$	Inst. horizontal wind at pos. i	-	-	7,15,16,17
6	$\bar{v}_z = v_{eq}$	Day-av. zonal wind, full disk (f)	9	5	6ab
7	$\bar{v}_m = v_{45^\circ}$	Day-av. merid. wind at 45°S (f)	11	6	6b,12
8	$\bar{v}_{z,lat}$	Day-av. zonal wind per lat. band (f)	-	7	14
9	$v_{z,lat}$	Sequence-av. zonal wind per lat. band (f)	-	8,9,10	-
10	$\bar{v}_{m,lat}$	Day-av. merid. wind per lat. band (f)	-	-	11
11	$v_{z,i} - \bar{v}_z$	Inst. zonal variable component	-	-	7
12	$v_{z,CT}$	Cloud tracking zonal wind velocity	-	-	20a, 21
13	$v_{m,CT}$	Cloud tracking merid. wind velocity	-	-	20b

Table 5.4: Velocity symbols used in this paper for deprojected and modeled horizontal flows in the reduction and analysis of visible Doppler velocimetry based on CFHT/ESPaDONs data. All data and fit units are  $\text{m s}^{-1}$  in Figures and Tables unless specified otherwise.

point in the planetocentric frame of reference we need to calculate the local "de-projection factor" (F). The de-projection factor is illustrated in Equation 5.4 presented at subsection 4.4.1 (Gabsi et al., 2008). As already discussed in subsection 4.4.1, this factor is a function of both the observing geometry and the planetary longitude as seen from Earth. In the case of a zonal circulation, the line of sight Doppler shift is proportional to the projection of wind velocity on the bisector phase angle (Machado et al., 2012).

All the coefficients have been computed for all the local points on Venus and used to convert the retrieved Doppler shifts to instantaneous velocities of cloud particles.

It is noteworthy to recall that the convention applied to planetary longitude is that it increases at sub-terrestrial meridian as the planet spins around its rotation axis; since the Venus rotation is retrograde, longitude on Venus increases in numerical value toward the east (west-sky direction).

### 5.3.9 Kinematical wind models

Projection factors for heliocentric and geocentric line-of-sight were calculated for zonal wind circulation, as well as sub-solar to anti-solar (SSAS) and a meridional wind component, with the help of a geometrical model (Lellouch et al., 1994). Explicit expressions for these projections factors are found in Goldstein (1989) and were also described in Widemann et al. (2007). Because the instrumental aperture covers a significant fraction of Venus' disk, the

projection coefficients for each particular wind regime are calculated over a fine grid of points and then averaged over the aperture on Venus (0.6 arcsec). In order to first interpret the main global wind field at cloud top level we tested two different models : (1) a uniform velocity model between  $-60^\circ$  and  $+60^\circ$  latitude range, where  $v_z(\lambda) = -v_{eq}$  ; (2) a solid body model, where  $v_z(\lambda) = -v_{eq} \times \cos \lambda$  where  $\lambda$  is the planetocentric latitude. Then the  $\chi^2$  best-fit has been performed between the measured velocities and the two described models. The parameter  $v_{eq}$  (the zonal wind equatorial velocity), minimizes the  $\chi^2$  best fit so that :

$$\chi_{vel}^2 = \frac{1}{N_{df}} \sum_i \frac{(v'_i - v'_{mod,i})^2}{\sigma_i'^2} \quad (5.5)$$

Where  $N_{df}$  is the number of degrees of freedom. The fit quality is determined using the reduced  $\chi^2$ , or  $S_{min} = \sqrt{\chi_{vel}^2}$ .

*1-wind, pure zonal* - From the weighted average of all the velocity measurements (where the ponderation coefficients used were the inverse of each point variance), obtained on each observations night, we obtain the mean zonal velocity  $\bar{v}_z$  in the planetocentric frame:

$$\bar{v}_z = \frac{\sum [c_{z,i} \cdot v'_{k,i}] / [\sigma_{k,i}^2]}{\sum [c_{z,i}^2 / \sigma_{k,i}^2]} \quad (5.6)$$

where  $c_{z,i}$  is the projection coefficient for point  $i$ ,  $v'_{k,i}$  is the measure  $k$  of velocity on the line of sight at point  $i$  and  $\sigma_{k,i}$  its associated standard deviation. Both uniform velocity and a solid body zonal wind models, yielded similar results in terms of  $v_{eq}$ , i.e. we could not distinguish the latitude dependence of the zonal flow between  $-50^\circ$  and  $+50^\circ$ .

At each individual point, a residue function  $v'_i - v'_{mod,i}$  is retrieved. Along the zonal Doppler null meridian (see section 5.3.4) at points 10, 17, 24, 31, 38, and 45 at  $\phi - \phi_E = 36^\circ\text{S}$  (see Table 5.2, and Fig. 5.13) we assumed that the residue cannot be attributed to a zonal component because geometrically, the particles zonal motion in the Sun's and the observer's direction cancel out each other. Therefore, contribution from other wind regimes such as a meridional flow could be investigated in our analysis (see sub-section 5.4.1).

*2-winds, zonal + meridional, zonal + SS-AS.* We applied a 2-dimensional  $\chi^2$  best-fit to the ensemble of the measured Doppler shifts, with input test velocities to minimize the overall statistical value and so retrieve the best fit velocity, with the addition of a meridional flow assumed to vary sinusoidally with latitude, having zero velocity at equator and the poles, and a maximum value  $v_m$  (positive for poleward motion) at lat  $45^\circ$ . Once the best fit is obtained using the zonal coefficients ( $c_z$ ) and the meridional coefficients ( $c_m$ )

we define the acceptable domain in  $v_{eq}$ , or in  $(v_{eq}, v_m)$  at  $2\text{-}\sigma$  confidence level from the condition  $S \leq S_{min} \times \sqrt{1 + 4/N_{df}}$  where  $N_{df} = N_{obs} - 2$ . The same method was applied for a best-fit to a zonal and sub-solar to anti-solar circulation coefficients  $c_s$ .

*1-wind, meridional component only at Null zonal meridian* - Since the zonal wind proved to have notorious spatial variability (see next section), this affected the 2-dimensional best-fit for the combined wind systems of zonal and meridional winds, leading to relatively high error bars and a poor reduced  $\chi^2$  quality ( $S_{min} = \sqrt{\chi_{vel}^2}$ ). On the null-Doppler zonal meridian, the residue to a 1-wind, pure zonal fit cannot be attributed to a zonal component because geometrically, the particles zonal motion projected on the Sun's and the observer's direction are equal. Therefore, after selecting only the observations on the referred meridian, we applied a best-fit method to pure meridional wind coefficients ( $c_m$ ).

Date	$\bar{v}_z$ , day averaged mean zonal wind (m s <sup>-1</sup> )	reduced $\chi^2$	$2\sigma$ m s <sup>-1</sup>	$3\sigma$ m s <sup>-1</sup>
19 Feb. 2011	117.35	1.16	$\pm 18.0$	$\pm 27.0$
21 Feb. 2011	117.50	2.12	$\pm 14.5$	$\pm 21.5$

Table 5.5: Mean/background zonal velocity  $\bar{v}_z$  on Feb. 19 and Feb. 21, 2011 CFHT/ESPaDONs data. The 1-wind regime fit is applied to all planet-wide  $v_{z,i}$  data points at latitudes 30° and 40° S (Feb. 19) and between latitudes 10° and 50° S (Feb. 21). Statistical quality of the obtained best-fit (reduced  $\chi^2$ ) is indicated at  $2\sigma$  and  $3\sigma$  confidence (see also Fig. 5.16a). Feb. 20, 2011 was dedicated to the temporal variability at latitude band 30° S (see text and Table 5.8). Machado et al. (2013).

## 5.4 Results (ESPaDONs)

The essential results presented in this section come from the paper Machado et al. (2013).

### 5.4.1 De-projected wind circulation

#### De-projected zonal wind flow

*Background zonal wind circulation* - We present in Table 5.5 the retrieved mean zonal wind velocities, under the assumption of a pure zonal one-wind system to data points acquired during sequences [1-6] (Feb. 19, 2011) and sequences [14-20] (Feb. 21, 2011), with the exception of points at the dayside limb facing east-sky and points with  $\text{SZA} > \Phi = 68^\circ$  as explained above. The obtained best-fit results for the two days of observations are self-consistent with near identical mean zonal wind  $\bar{v}_z = (117.35 \pm 18.0) \text{ ms}^{-1}$  on Feb. 19, and  $\bar{v}_z = (117.5 \pm 14.5) \text{ ms}^{-1}$  on Feb. 21, respectively. The associated error bars, at  $2\sigma$  and  $3\sigma$ , are shown in Table 5.5. Also noteworthy is the high quality level of the statistical best-fit obtained, as showed by the reduced  $\chi^2$   $S_{min} = 1.16$  (Feb. 19) and  $S_{min} = 2.12$  (Feb. 21), see Fig. 5.16a and Table 5.5.

*Variable zonal component* - The instantaneous velocities obtained at each individual points for the days 19 and 21 February 2011, are plotted on Figures 5.17a,b. As can be seen for both nights, the wind variability to the mean zonal background velocity  $\bar{v}_z$  of  $117.35 \text{ m s}^{-1}$  (Feb. 19) and  $117.50 \text{ m s}^{-1}$  (Feb. 21) is generally within  $\pm 10\text{-}15 \text{ m s}^{-1}$  of the mean zonal circulation with a few significant outliers. There is also some coherence between the

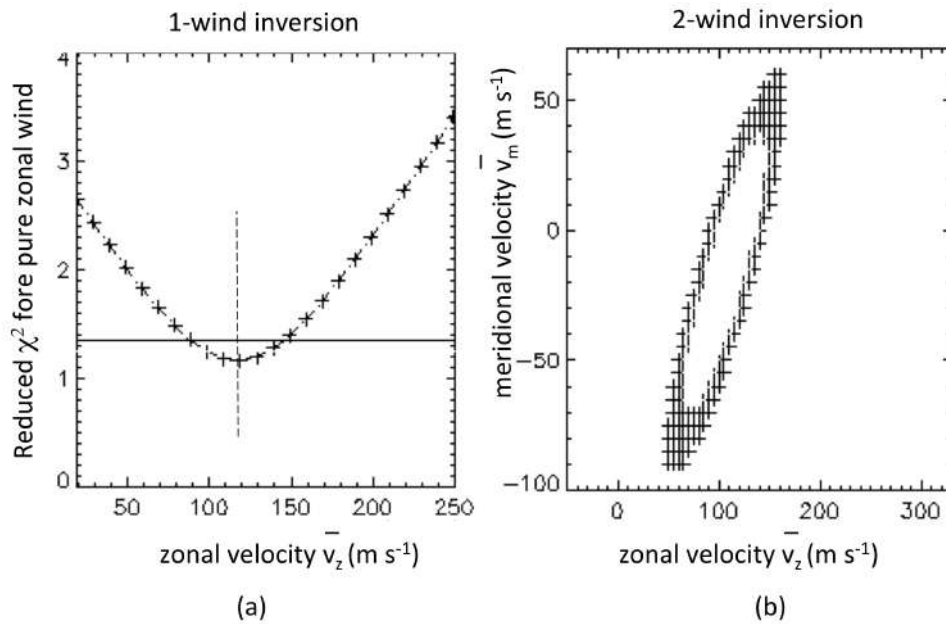


Figure 5.16: Kinematical fit to a mean/background zonal wind fit  $\bar{v}_z$  on Feb. 21 data, day averaged. Reduced  $\chi^2$  plots illustrate the quality of one- or two-wind components fit to the mean Doppler velocities field obtained on (a) One wind system - Pure zonal circulation  $\bar{v}_z$ . (b) Two winds systems - Zonal and meridional wind system  $\bar{v}_z$ ,  $\bar{v}_m$ . Data of Feb. 21, 2011 (sequences [14-20]). The inner ellipse shows the zonal and meridional results at  $2\sigma$ , the outer ellipse presents the corresponding  $3\sigma$  result. Best-fit suggests a background zonal wind  $\bar{v}_z$  of  $\sim 117 \text{ m s}^{-1}$  and a meridional component  $\bar{v}_m$  with a typical velocity of  $\sim 20 \text{ m s}^{-1}$  near  $45^\circ\text{S}$ . See Tables 5.5, 5.6 for results and sub-section 5.4.1.

same data points observed during different sequences, including over the two groups of sequences during the two days. Sequences [4-5] on Feb. 19 have been acquired through passing upper haze in the Earth's atmosphere, resulting from a degraded statistical error although the mean value remains within the same variability range, clearly reflected in the size of error bars in Fig. 5.17a at sequences [4-5]. The spatial and temporal variability will be assessed in sub-sections 5.4.2 and 5.4.2.

Figures 5.18 and 5.19 present results for a pure zonal wind on Feb. 19, Feb. 21 observing sequences. The ESPaDOnS spectrograph field-of-view (FOV) is represented to scale over the apparent Venus disk, and its projected size at disk center as indicated in Table 5.1. Zonal velocities showed at each offset position are the result of a weighed mean of individual exposures at this position over sequences [1-6] 18:57-22:10 UT, acquired Feb. 19 between and sequences [14-21] 18:01-22:30 UT on Feb. 21 with weight coefficients the inverse  $[1/\sigma^2]$  of each point variance.

### De-projected meridional wind flow

Under the approximation of a two-wind circulation system, with the additional contribution of a meridional flow, we obtain a two dimensional  $\chi^2$  best-fit presented in figure 5.16b. Best-fit suggests a background zonal wind of  $\sim 100 \text{ m s}^{-1}$  and a meridional wind circulation of the order of  $\sim 20 \text{ m s}^{-1}$  near  $45^\circ\text{S}$ . Both values are in general agreement with cloud top estimates for both circulation regimes (Peralta et al., 2007; Widemann et al., 2008; Sánchez-Lavega et al., 2008; Moissl et al., 2009; Machado et al., 2012, 2013; Hueso et al., 2012).

To search unambiguously and accurately the meridional wind circulation, a method was developed specifically for the analysis of this wind flow between the equator and the high latitudes. A two wind system  $\chi^2$  fit has been applied to the set of measurements carried out along the zonal Doppler null meridian, selecting for this case the corresponding zonal and meridional de-projection coefficients  $c_{z,i}, c_{m,i}$  so that velocity at point  $i$  can be written

$$v'_i = v_i - v_{i,trend} = c_{z,i} \cdot v_{z,i} + c_{m,i} \cdot v_{m,i} \quad (5.7)$$

The results obtained for the meridional wind flow component  $\bar{v}_m$  are presented in Table 5.6. These values and their best-fit estimate at  $2\sigma$  and  $3\sigma$ , are obtained along a selection of data points on the zonal Doppler null meridian : points 17 at S lat  $10^\circ$ , 24 at S lat  $20^\circ$ , 31 at S lat  $30^\circ$ , 38 at S lat  $40^\circ$ , 45 at S lat  $50^\circ$ , all at  $[\phi - \phi_E] = -36^\circ$  of the completed dataset of Feb. 21, 2011



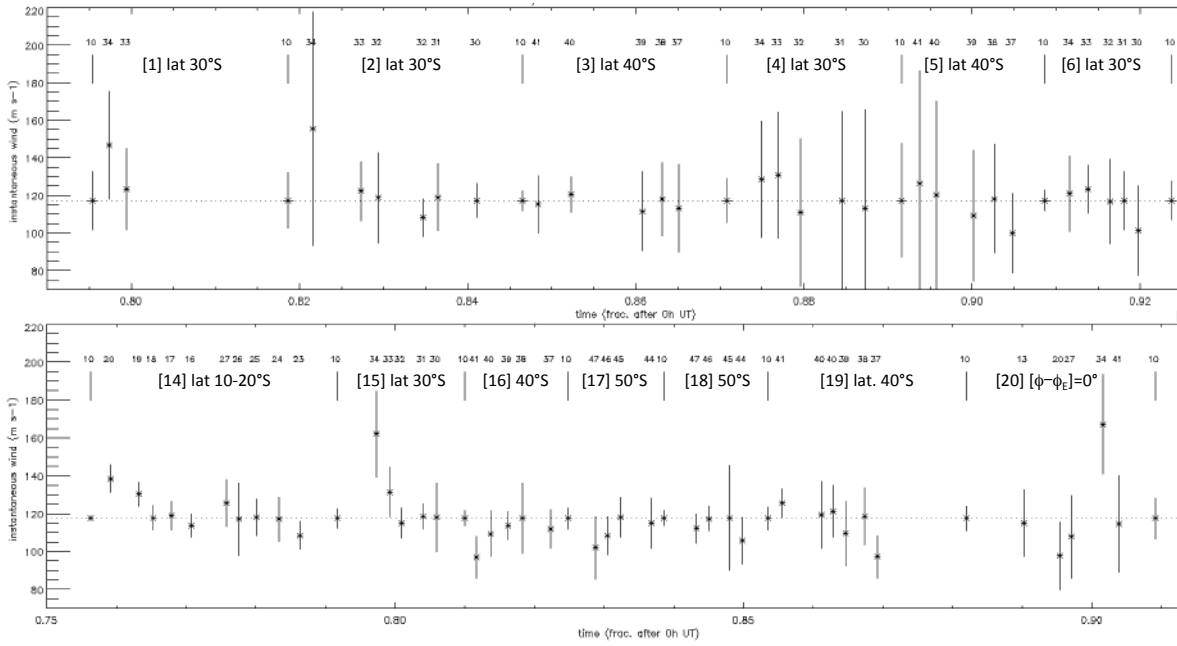


Figure 5.17: Feb. 19, Feb. 21 2011 sequences of instantaneous horizontal velocities  $v_{z,i}$ , de-projected from line-of-sight velocities  $v'_i$ , corrected for the Young effect and the trend polynomial  $v_{trend}(t)$  (see sub-sections 5.3.3 and 5.3.4). Sequences numbering is from Table 2. Top : instantaneous horizontal velocities on 19 Feb. 2011, plotted vs. acquisition time (fraction of the day). Calculated weighted mean zonal background velocity  $\bar{v}_z$  of 117.35 m/s (Feb. 19) and 117.50 (Feb. 21) is indicated as a horizontal dotted line, so that  $v_{z,i} - \bar{v}_z$  represent the variable component of the zonal wind at each point. X-axis is the fraction of day after 0h UT (0.01 day = 14.4 minutes). Bottom : instantaneous horizontal velocities obtained at sequences [14-20] on Feb. 21, 2011.

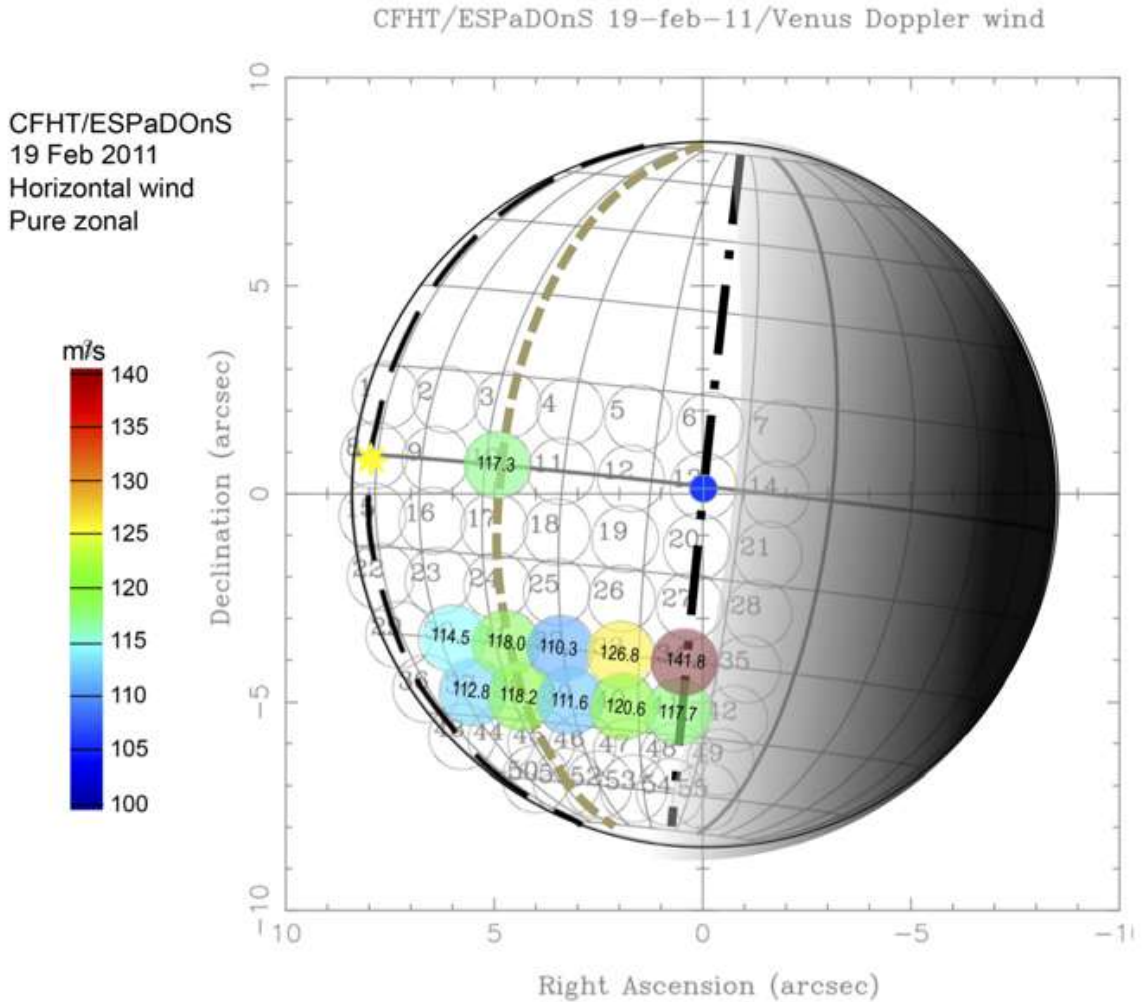


Figure 5.18: Results for horizontal wind velocity  $v_{z,i}$  reported at each off-set position for Feb. 19, 2011 observations. CFHT/ESPADONS's 1.6 arcsec field-of-view (FOV) is projected to scale over the Earth-based Venus disk, corresponding to a 574 km-diameter at Venus (Table 5.1). See caption of Fig.2 for symbol explanation. Zonal component at each position is calculated as a weighed mean of individual exposures  $v_{z,i}$  over Feb. 19 observing sequences [1-6] (Table 5.2).

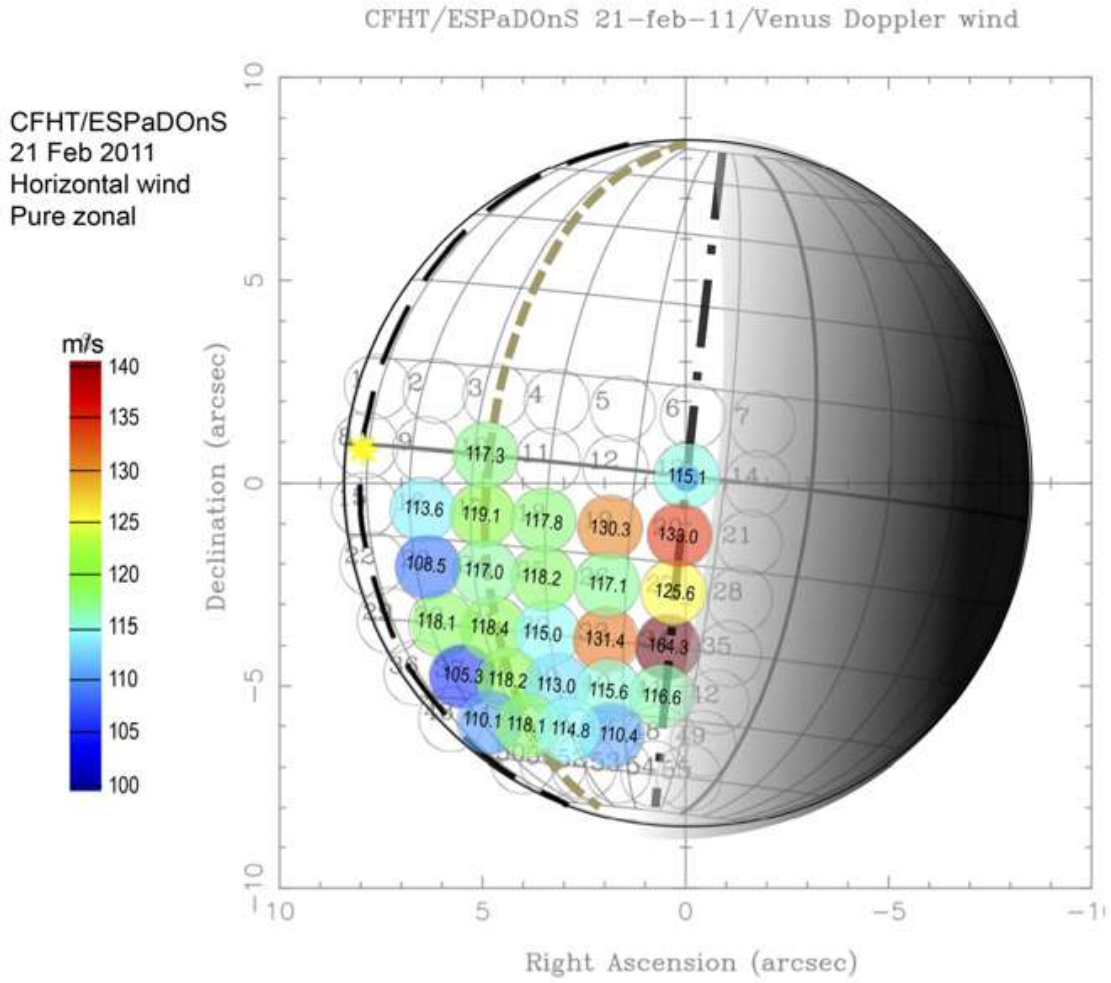


Figure 5.19: Results for horizontal wind velocity  $v_{z,i}^-$  reported at each offset position on Feb. 21, 2011. Instrument's FOV is 582 km at Venus (Table 5.1). Same as Fig.5.18 for Feb. 21 observations over sequences [14-21] (Table 5.2).

Date	Meridional velocity $\bar{v}_m$ m s <sup>-1</sup>	reduced $\chi^2$	$2\sigma$ m s <sup>-1</sup>	$3\sigma$ m s <sup>-1</sup>
19 February 2011	18.8	1.14	$\pm 11.5$	$\pm 15.5$
21 February 2011	19.0	1.36	$\pm 8.3$	$\pm 20$

Table 5.6: Mean Meridional wind velocity  $\bar{v}_m$  along the zonal's Doppler null meridian ( $[\phi - \phi_E] = \Phi/2 \simeq -36^\circ$  of longitude as seen from Earth), at  $2\sigma$  and  $3\sigma$ . Machado et al. (2013).

(Fig. 5.12, Table 5.2). As we can see (table 5.6 and figure 5.22b) the quality of the statistical adjust is remarkable (reduced  $\chi^2$ ).

Due to convection at equatorial region, hot air rises and flows poleward (upper branch), reaching high latitudes (latitudes of  $50^\circ - 60^\circ$ ), where this meridional flow dives and return to equator below cloud level (lower branch) in a Hadley cell atmospheric circulation. This overturning of the troposphere, coupled with planetary waves, produces a net transport of angular momentum from high to low latitudes that is essential in order to maintain the state of atmospheric superrotation, according to the Gierasch-Rossow-Williams mechanism. However there are still major open questions, as is the case of the connexion between the meridional circulation and the buildup of the transient mid-latitudes jet streams, its binding with the cold collars present at same latitude range, and in turn the connection with the whirl structures of the polar vortex. So, it is crucial to constrain the meridional wind circulation at cloud top level. This knowledge is also essential to Venus' Global Circulation Models (GCM).

In a third experiment, a one-wind  $\chi^2$  best-fit was applied to the Doppler velocities retrieved from the measured points along the zonal Doppler null meridian, using the meridional projection coefficients  $c_{m,i}$ , so that

$$\bar{v}_m = \frac{\sum [c_{m,i} \cdot v'_{k,i}] / [\sigma_{k,i}^2]}{\sum [c_{m,i}^2 / \sigma_{k,i}^2]} \quad (5.8)$$

The consistency from the mean meridional velocity between days is remarkable, as is the quality of the statistical adjust (reduced  $\chi^2$ ), see table 5.6 and figure 5.20.

Figure 5.20 shows the measured Doppler velocities projected along the line-of-sight, for the points along the zonal Doppler null meridian. Kinematical fit to Feb. 21 differential wind field  $v'_i = v_i - v_{i,trend}$  corrected for Young effect, to a pure meridional flow with  $\bar{v}_m = (19.0 \pm 8.3)$  m s<sup>-1</sup> (Table

5.5) is shown as a dashed line. Data points are a subset of acquisition sequences [14-19] presented in Fig. 5.15b. The differential wind field has been corrected from the trend polynomial  $v_{i,trend}$  calculated at point 10 ( $[\phi - \phi_E] = -36^\circ$ ,  $\text{lat} = 0^\circ$ ). The figure shows the largest projected velocity are at mid-latitudes (points 31, 38 and 45), as evidenced more clearly on Fig. 5.21, where meridional velocities  $v_{m,lat}$  are the result of a weighed average between all exposures taken at at the same latitude during sequences [14-19] (the weighting coefficients were the inverse of each retrieved velocity variance).

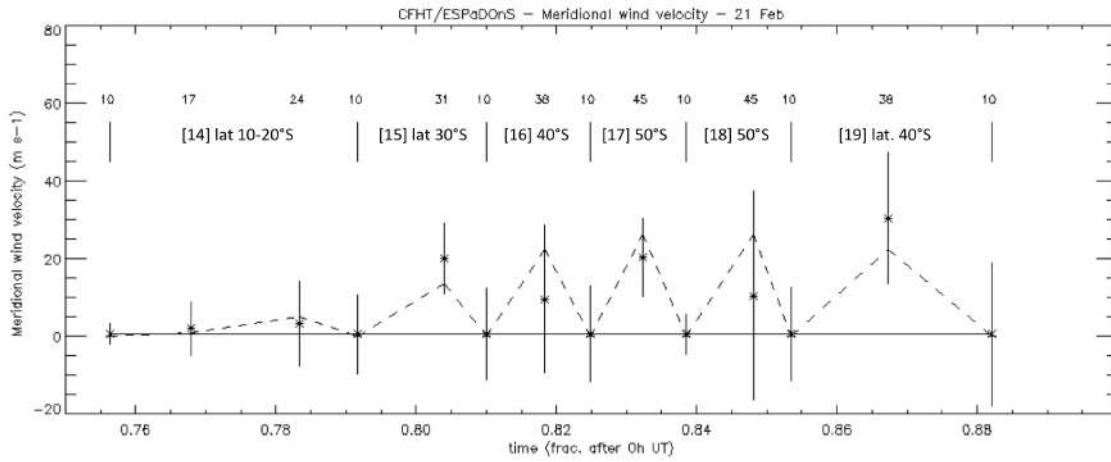


Figure 5.20: Kinematical fit  $\bar{v}_m$  to Feb. 21 differential wind field  $v'_i = v_i - v_{i,trend}$  corrected for Young effect, to a pure meridional flow with  $\bar{v}_m = (19.0 \pm 8.3) \text{ m s}^{-1}$  (dashed line, see text and Table 5.5).  $v_{z,i}$  data points are a subset of acquisition sequences [14-20] of Fig. 5.15b, centered along the null zonal Doppler meridian near  $[\phi - \phi_E] = \Phi/2 = 34.3^\circ$  for lat  $10^\circ\text{S}$  (pt  $i = 17$ ),  $20^\circ\text{S}$  (pt  $i = 24$ ),  $30^\circ\text{S}$  (pt  $i = 31$ ),  $40^\circ\text{S}$  (pt  $i = 38$ ),  $50^\circ\text{S}$  (point  $i = 45$ ).

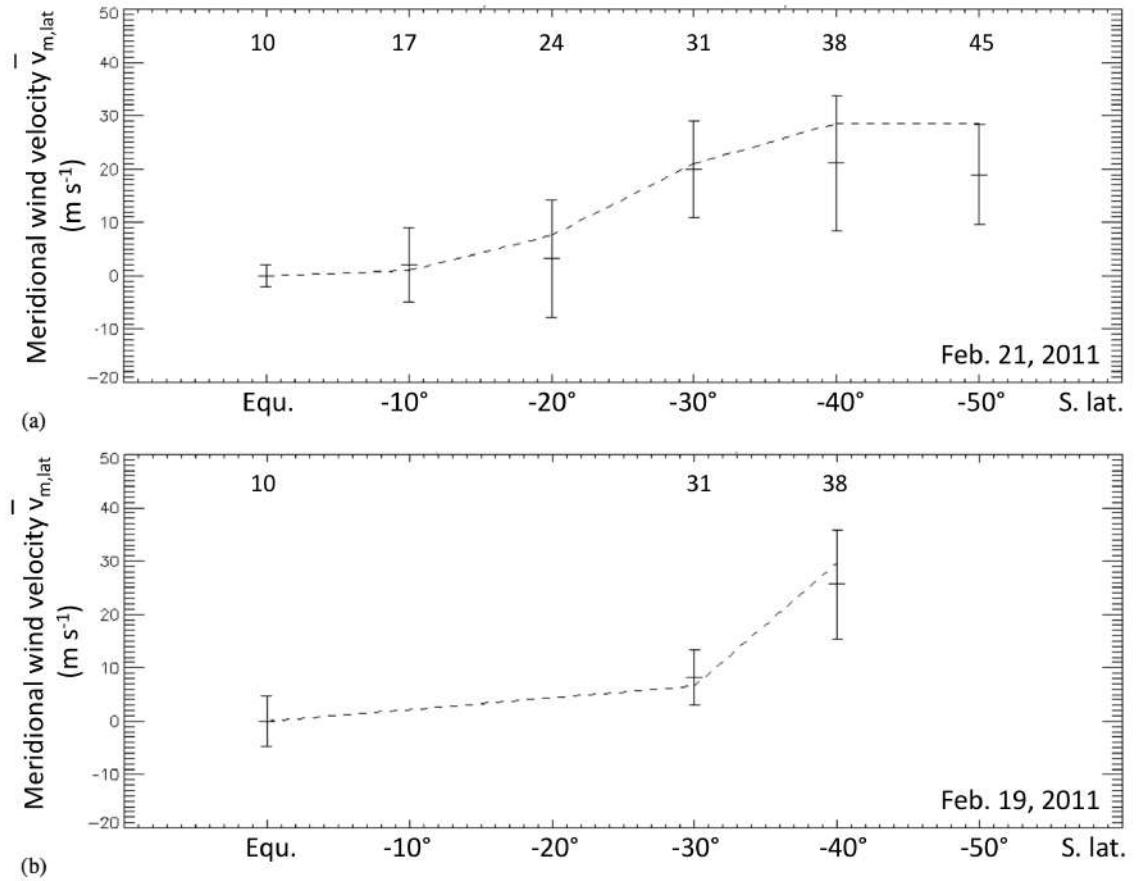


Figure 5.21: Retrieved meridional velocities  $v_{m,lat}$  plotted as a function of S latitude. (a) The dashed line fits to a pure meridional flow with  $v = (19.0 \pm 8.3) \text{ m s}^{-1}$  (Table 5.5). The values presented are the result of a weighed average between all the measurements at same points along the null zonal Doppler wind meridian of sequences [14-20] (pts  $i = 17, 24, 31, 38, 45$ ) on 21 Feb. 2011. (b) Fit to a pure meridional flow of  $v = (18.8 \pm 11.5) \text{ m s}^{-1}$  along null-zonal wind meridian for sequences [2-6] (pts  $i = 31, 38$ ) on 19 Feb. 2011 (see Table 5.6).

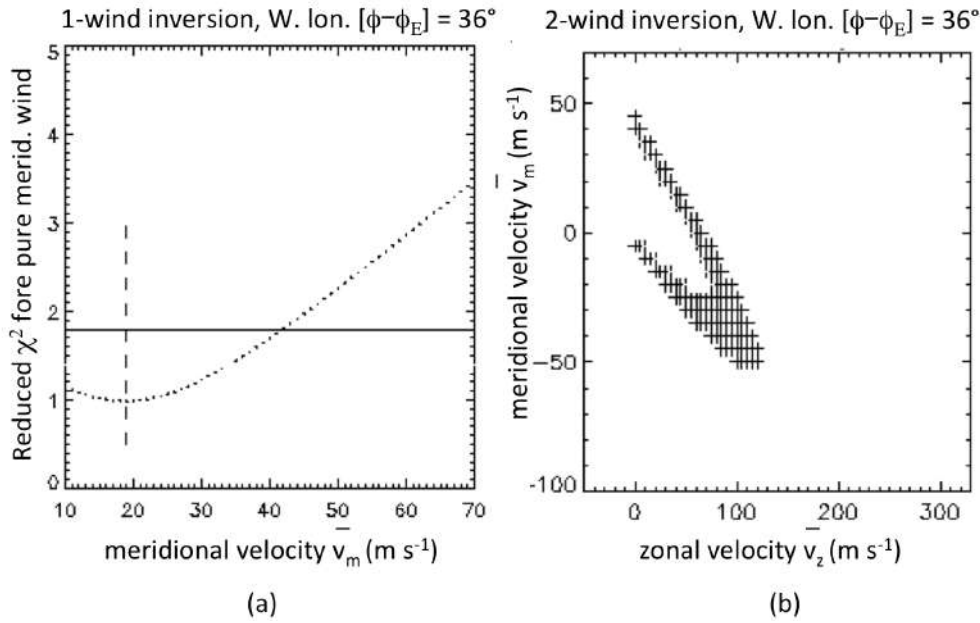


Figure 5.22: Best-fit  $\bar{v}_m$  of the meridional wind along the null zonal wind meridian at  $[\phi - \phi_E] = -36^\circ$  on Feb. 21, 2011. (a) One wind component - A pure meridional wind flow gives a best-fit value of  $(19.0 \pm 8.3) \text{ m s}^{-1}$ . (b) Two wind circulation fit along the null zonal wind meridian at  $[\phi - \phi_E] = -36^\circ$  using zonal and meridional wind de-projection coefficients  $c_{z,i}$ ,  $c_{m,i}$  (Equ. 5.4.1). Center of the  $2\sigma$  and  $3\sigma$  best-fit ellipses is coherent with a null zonal component and about  $19 \text{ m s}^{-1}$  for the meridional wind flow velocity (see text).

### De-projected SS-AS wind flow

It was also performed a two dimensional best-fit to a combined zonal wind and sub-solar to anti-solar (SS-AS) flow. The results were inconclusive, with a poor statistical fit (reduced  $\chi^2$  between 6.8 and 7.3, respectively for the observations of 19 and 21 February), due to SS-AS de-projection coefficients  $c_s$  hard to discriminate from zonal component  $c_z$  in a single Venus Earth-based phase angle  $\Phi$  observing run, an better evidenced by combining observations at opposite elongations to the Sun (Widemann et al., 2007; Sornig et al., 2012).

### 5.4.2 Zonal wind variable component

With repeated observing sequences each lasting about 1-hour at same positions / cycles of latitude bands at each day of observation (see Table 2), it is possible to (1) determine the longitudinal profile of a mean zonal wind at a given latitude, and its variation with time (sub-section 5.4.2, Fig. 5.23, 5.24) ; (2) to compare the velocities  $v_{z,i} - \bar{v}_z$  over various time scales : (i) day-to-day variability, using averaged, weighted results at each point (sub-section 5.4.2 and Figures 5.25, 5.26 and 5.27; (ii) intra-day variability by comparing repeated sequences over the same latitude bands (iii) latitudinal and local time variation of instantaneous wind  $v_{z,i}$  at each point. Those various constraints are summarized and discussed in this sub-section.

#### Longitudinal profile of zonal wind $v_{z,i}$

Figure 5.23 show day-to-day variations of  $\bar{v}_{z,i}$  horizontal wind results  $v_{z,i}$ , ordered by latitude bands. Results are the weighted average of all the measurements  $v_{z,i}$  taken at same positions at each day of observations. As all ESPADONS measurements are detrended from the on-sky instantaneous Doppler variations  $v'_i = v_i - v_{i,trend}$  monitored at point number 10, located at the equator and the null-zonal Doppler meridian, what we measure are relative velocities to a 1-wind zonal velocity fit to all the data recorded on that day  $\bar{v}_z = v_{eq}$  of Table 5.5, a value affected to point 10 on Figures 5.18 and 5.19. The reason why measurements at W lon.  $[\phi - \phi_E] = 36^\circ$  on Fig. 5.23 have similar relative velocities is because acquisition near longitude  $[\phi - \phi_E] = \Phi / 2 \simeq 34.3^\circ$  cannot detect the zonal motion of cloud top particles as they have equal and opposite heliocentric and geocentric motion (i.e. with respect to the incoming sunlight and toward the observer). At those data particular data points, a kinematical fit to Feb. 19 and Feb. 21 differential wind field  $v'_i = v_i - v_{i,trend}$  has been adjusted to a pure meridional flow with  $v = (19.0$



$\pm 8.3$ )  $\text{m s}^{-1}$  (see sub-section 5.4.1, Fig. 5.20, 5.21 and Table 5.6).

One observes that all velocity measurements  $v_{z,i}^-$  are comprised between 100 and 120  $\text{m s}^{-1}$  although some significant patterns emerge. Firstly, a relative inferior wind velocity is detected at W lon.  $[\phi - \phi_E] = 12^\circ$  and  $24^\circ$ , corresponding to local time 8:10a and 9:05a (Table 5.3). Secondly, we note in the case of the band at  $30^\circ$  S, a significant day-to-day variability close to sub-terrestrial meridian near terminator at  $[\phi - \phi_E] = 0^\circ$  (local time 7:30a), where horizontal velocity reaches 140  $\text{m s}^{-1}$  on Feb. 19 (Fig. 5.23a) and even 160  $\text{m s}^{-1}$  on Feb. 21 (Fig. 5.23c). While Fig. 5.23 gives a global picture of the wind velocity longitudinal profile at the day-scale, Figures 5.24- 5.27 examine in more details the variability per latitude band, between day-averaged data (Fig. 5.24) or at shorter time-scale of the order of one to several hours defined by the repetition of scanning sequences, as more rapid cloud top wind velocity changes are observed between CFHT/ESPaDOnS observing sequences during the same day (Fig. 5.25-5.27). We examine more closely how the longitudinal profile for the zonal velocity varies on the day-scale (subsection 5.4.2) and on the hour-scale (subsection 5.4.2) in the following text.

#### Variability on a day time-scale of mean zonal wind $v_{z,lat}^-$ at $10^\circ - 50^\circ$ S lat.

Figure 5.24 show day-to-day longitudinal variations of  $v_{z,i}^-$  horizontal wind results  $v_{z,i}$ , ordered by latitude bands at the same days. Results are the weighted average of all the measurements  $v_{z,i}$  taken at same positions at each day of observations. The Figure compares Feb. 19, 20 and 21  $v_{z,i}^-$  ordered by latitudinal band, when applicable. Figure 5.24 a illustrates the day time-scale variability of  $v_{z,i}^-$  at  $30^\circ$  S latitude band on Feb 19 (dotted line), Feb 20 (dashed line) and Feb 21 (dash-dotted line). Figure 5.24 b plots  $v_{z,i}^-$  at  $40^\circ$  S latitude band on Feb 19 (dashed line) and Feb 21 (dash-dotted line). All results of Fig. 5.24 combine observing sequences that were observed the same day at the same latitude, averaging out the hourly variations which are examined in the new sub-section 5.4.2.

In the case of the  $30^\circ$  S latitude band (Fig. 5.24a), observed during sequences [2], [6] on Feb. 19, [7] to [12] on Feb. 20, and sequence [15] on Feb. 21 (see Table 5.2 for corresponding UT start-end) the zonal velocities at local time closer to noon vary within 10  $\text{m s}^{-1}$ . Results at the zero longitude meridian (local time 7:30a) show significant day-scale variability, with an amplitude of variation reaching 30  $\text{m s}^{-1}$  between day 1 and day 3, while at  $[\phi - \phi_E] = 12^\circ$  (local time 8:10a)  $12^\circ$  longitude we can also note a day-scale variability of nearly 20  $\text{m s}^{-1}$ . On day 1,  $v_{z,i}^-$  values are 141.8  $\text{m s}^{-1}$  at W lon.

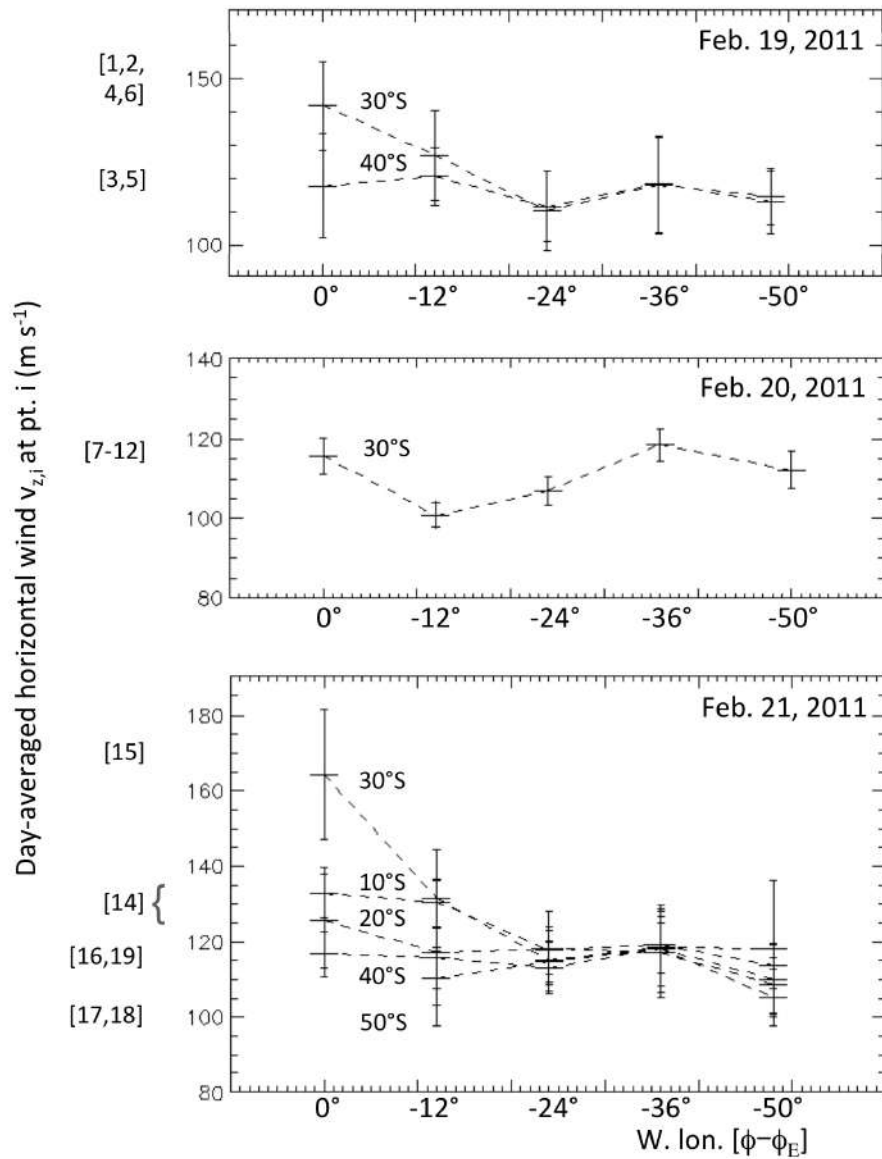


Figure 5.23: Day-to-day variations of *day-averaged*  $v_{z,i}^-$  horizontal wind results  $v_{z,i}$  : (a) 19 Feb. 2011 - Latitude bands of  $30^\circ\text{S}$  (dashed line) and  $40^\circ\text{S}$  (dashed dotted line). (b) 20 Feb. 2011 -  $30^\circ\text{S}$  latitude band. (c) 21 Feb. 2011 - Latitudes bands from  $10^\circ$  to  $50^\circ\text{S}$  lat. by steps of  $10^\circ$ . Y-axis  $v_{z,i}^-$  results are also appearing on Fig. 8, 9 map of day-averaged wind velocities at each observing point in Feb. 19 and Feb. 21 datasets. Observing sequences order by latitude band, used to determine the weighed day-average  $v_{z,i}^-$  at each point are indicated in the left margin. This plot gives a full representation of the day-to-day variations of zonal wind velocities over the dayside hemisphere of Venus. While Fig. gives a global picture of the wind velocity longitudinal profile at the day-scale, Figures 5.24- 5.27 examine in more details the variability per latitude band, on day-averaged data (Fig. 5.24) or at shorter time-scale of the order of one to several hours defined by the repetition of scanning sequences, as more rapid cloud top wind velocity changes are observed between CFHT/ESPaDONs observing sequences during the same day (Fig. 5.25-5.27).

0° (local time 7:30a), 126.8 m s<sup>-1</sup> at W lon. 12° (local time 8:40a), 110.3 m s<sup>-1</sup> at W lon. 24° (local time 9:05a), 118 m s<sup>-1</sup> at W lon. 36° (local time 9:50a), 114.5 m s<sup>-1</sup> at W lon. 50° (local time 10:50a). At this latitude, we find the instantaneous zonal wind decreases in the upper cloud at a rate of 23 m s<sup>-1</sup> per local time hour between  $[\phi - \phi_E] = 0^\circ$  and 12°, then 17 m s<sup>-1</sup> per local time hour between  $[\phi - \phi_E] = 12^\circ$  and 24°. It then increases by 10 m s<sup>-1</sup> per local time hour toward  $[\phi - \phi_E] = 36^\circ$  and decreases again towards local noon, at a marginal rate of 3.5 m s<sup>-1</sup> per local time hour between  $[\phi - \phi_E] = 36^\circ$  (local time 9:50a) and 50° (local time 10:50a).

On day 3 (Feb. 21),  $v_{z,i}^-$  values are 164.3 m s<sup>-1</sup> at W lon. 0° (local time 7:30a), 131.4 m s<sup>-1</sup> at W lon. 12° (local time 8:40a), 115.0 m s<sup>-1</sup> at W lon. 24° (local time 9:05a), 118.4 m s<sup>-1</sup> at W lon. 36° (local time 9:50a), 118.1 m s<sup>-1</sup> at W lon. 50° (local time 10:50a). On that day at this latitude, we find the instantaneous zonal wind decreases in the upper cloud at a very high rate of 50 m s<sup>-1</sup> per local time hour between  $[\phi - \phi_E] = 0^\circ$  and 12°. Later in the morning, it decreases by 17 m s<sup>-1</sup> per local time hour between  $[\phi - \phi_E] = 12^\circ$  and 24°, the same value as on day 1. It then increases by about 5 m s<sup>-1</sup> per local time hour toward  $[\phi - \phi_E] = 36^\circ$  and remains again almost constant towards local noon, at a rate of 0.3 m s<sup>-1</sup> per local time hour between  $[\phi - \phi_E] = 36^\circ$  (local time 9:50a) and 50° (local time 10:50a).

In the case of the 40° S latitude band (Fig. 5.24b), observed during sequences [3], [5] on Feb. 19, [16], [19] on Feb. 21, we can note that besides a day-scale variability of mean horizontal velocities  $v_{z,i}^-$  contained within error bars, the zonal wind flow is nearly constant at this latitude range between the three days of observations, in significant contrast with the 30° S latitude band.

This daily variability affects differently the longitudes probed by ESPaDOnS observations on Feb. 19-21 as shown in Fig. 5.24a, b. In VIRTIS-M UV dayside data (Hueso et al., 2012), the presence of a thermal solar tide is apparent in the latitude range 50°-75°S of the spatial distribution of the magnitude of the zonal wind, confirming previous findings of Sánchez-Lavega et al. (2008). In their data, the zonal wind increases in the upper cloud at these latitudes at a rate of about  $2.5 \pm 0.5$  m s<sup>-1</sup> per local time hour from the morning (9 h local time) to the afternoon (15 h). At other latitudes, VIRTIS-M do not provide evidence of the phenomenon, although Hueso et al. (2012) discuss the possible lack of enough data in mid- and low-latitude ranges near the local noon. Conversely, ESPaDOnS data cover extensively both the mid- to low latitude region at 30°- 40° S and the longitude range extending from local morning terminator close to local noon (7:30a-10:50a, see Table 5.3).

Results on Table 5.7 present the day variability of weighed velocity average along each latitude band that were considered here. To obtain those

Lat. band	Dates		
	Feb. 19, 2011	Feb. 20, 2011	Feb. 21, 2011
	$v_{z,\bar{lat}}$ (m s <sup>-1</sup> )	$v_{z,\bar{lat}}$ (m s <sup>-1</sup> )	$v_{z,\bar{lat}}$ (m s <sup>-1</sup> )
10°S	-	-	122.6 ± 2.9
20°S	-	-	114.9 ± 4.7
30°S	120.2 ± 5.2	109.3 ± 1.8	121.9 ± 4.4
40°S	116.1 ± 4.9	-	113.5 ± 3.4
50°S	-	-	113.4 ± 3.6

Table 5.7: Variability of 1-wind fit to  $v_{z,i}$  values to a cloud-top zonal velocity  $v_{z,\bar{lat}}$  for reported latitudinal bands, longitude range  $[\phi - \phi_E] = -50^\circ$  to  $0^\circ$  (local time 7:30a - 10:50a). Fit to all  $v_{z,i}$  values are calculated for each day. Machado et al. (2013).

values, a longitudinal fit to a 1-wind cloud top zonal velocity  $v_{z,\bar{lat}}$  was applied to  $v_{z,i}$  values on the morning dayside hemisphere at longitude range  $[\phi - \phi_E] = -50^\circ$  to  $0^\circ$  (local time 7:30a - 10:50a). The weighing coefficients were the inverse of each retrieved velocity's variance. The results are broadly consistent with the general results from VEx/VMC data Moissl et al. (2009), where significant zonal wind variations can be found when comparing different days of observations. CFHT/ESPaDONs Feb. 19 and Feb. 20 observations were limited to latitude bands at  $30^\circ$  and  $40^\circ$ . Feb. 19 indicated a obtain a latitudinal variation of the mean zonal wind within the error. On Feb. 21, we acquired a complete set of measurements to compare the mean zonal wind on the morning dayside at latitudes  $10^\circ$ - $50^\circ$ S. At  $10^\circ$  and  $30^\circ$  the best fit  $v_{z,\bar{lat}}$  is  $122.6 \pm 2.9$  m s<sup>-1</sup> and  $121.9 \pm 4.4$ , respectively, while values lower by about  $10$  m s<sup>-1</sup> are calculated for latitudes  $20^\circ$ ,  $40^\circ$  and  $50^\circ$  at  $114.9 \pm 4.7$  m s<sup>-1</sup>,  $113.5 \pm 3.4$  s<sup>-1</sup>, and  $113.4 \pm 3.6$  m s<sup>-1</sup>, respectively. On Figure 5.31 the latitudinal variation of the mean zonal wind field is compared to VIRTIS-M simultaneous cloud tracking measurements, and to previous observations of Machado et al. (2012) on Fig. 5.33.

### Variability on an hour time-scale of mean zonal wind $v_{z,\bar{lat}}$ at $10^\circ$ - $50^\circ$ S lat.

One now examines more closely the longitudinal profile of the cloud top zonal velocity on the hour-scale. The mean zonal wind  $v_{z,\bar{lat}}$  is now calculated through repeated sequence-to-sequence offset acquisition at identical latitude

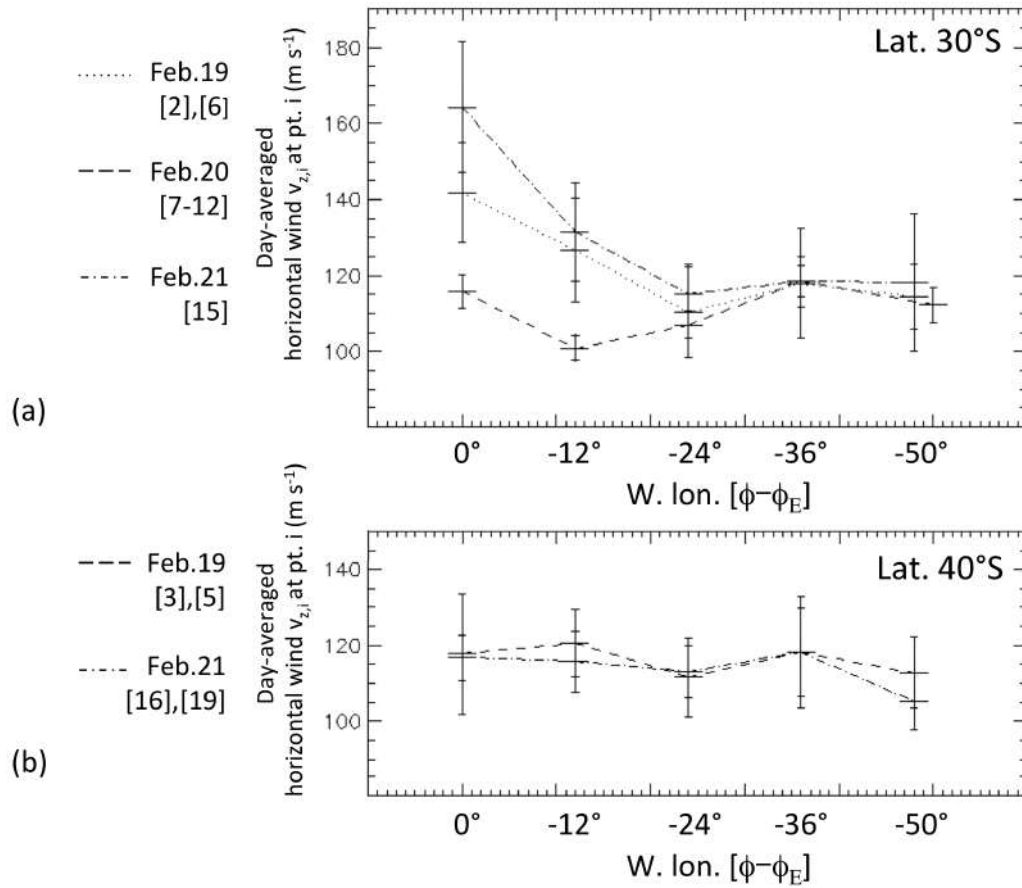


Figure 5.24: Latitude plots of variations of *day-averaged* horizontal wind velocities data  $v_{z,i}^-$  at points  $i$  of the three days of observation with CFHT/ESPaDONs. The Figures compare Feb. 19, 20 and 21  $v_{z,i}^-$  ordered by latitudinal band, when applicable. (a) Top :  $v_{z,i}^-$  at  $30^\circ$  S latitude band on Feb 19 (dotted line), Feb 20 (dashed line) and Feb 21 (dash-dotted line). (b) Bottom :  $v_{z,i}^-$  at  $40^\circ$  S latitude band on Feb 19 (dashed line) and Feb 21 (dash-dotted line).

bands. When studying the variability of cloud top circulation through cloud top velocimetry, it is important to point out that all velocity measurements  $v_{z,i}$  are relative measurements to the mean zonal velocity  $\bar{v}_z$  calculated on the ensemble of data points at each day of observation (Feb. 19 :  $(117.35 \pm 18.0) \text{ m s}^{-1}$  ; Feb. 21 :  $(117.50 \pm 114.5) \text{ m s}^{-1}$ , see Table 5.5). Again, the mean background value  $\bar{v}_z$  is then attributed to the equatorial point 10 at mid-morning longitude, located on the null-Doppler zonal meridian at  $[\phi - \phi_E] = \Phi/2 \simeq 34.3^\circ$  and used as the velocimetry reference  $v_{trend}(t)$ , an on-sky correction to spectral calibration. This method allows to inter calibrate the sequences and compensate for any uncorrected drift to radial velocity retrieval of instrumental or telluric lines origin (see sub-section 5.3.4).

Figure 5.25 a shows the results for day 1,  $30^\circ$  S latitude band, repeated observations of sequences [1], [2], [4], [6] of Feb. 19 observations, with time intervals of the order of one hour. Figure 5.25 b displays the instantaneous variability for the same day at  $40^\circ$  S latitude band during sequences [3], [5], while Figure 5.26 shows the temporal variability during day 2, on February 20. During that day only multiple scans of the  $30^\circ$  S latitude band were performed at sequences [7-12] (see also Table 5.2 for a list and UT-start/end of scanning sequences on the dayside of Venus' cloud tops). Figure 5.27 shows rapid cloud top circulation variations on day 21, comparing sequences [16], [19] at lat.  $40^\circ$  S (Fig. 5.27a) and sequences [17], [18] at lat  $50^\circ$  S (Fig. 5.27b).

*Feb. 19, 2011* - Results are presented in Fig. 5.25 and Table 5.8. At  $[\phi - \phi_E] = 0^\circ$  longitude (local time 7:30a) at the  $30^\circ$  S latitude band, one notes that the instantaneous zonal wind decreases in the upper cloud at a very high rate of  $35 \text{ m s}^{-1}$  in about 3.5 hours, or  $10 \text{ m s}^{-1} \text{ h}^{-1}$ . At other local longitudes later in the morning (local times 8:10a, 9:05a, 9:50a at west longitudes  $[\phi - \phi_E] = 12^\circ, 24^\circ, 36^\circ$  respectively, the variability is significantly less intense than in early morning, with local variations of the instantaneous zonal wind of the order of  $10 \text{ m s}^{-1}$  during the period, with no trend pattern in the sign of the wind variation. Still at S lat  $30^\circ$ , but at a longitude of  $[\phi - \phi_E] = 50^\circ$  (local time 10:50a), our data are more in agreement with a monotonous decrease of the zonal wind by a total amplitude of  $20 \text{ m s}^{-1}$ , or  $4.5 - 5 \text{ m s}^{-1} \text{ h}^{-1}$  (Fig. 5.27a). On that same day sequences [3], [5] at  $40^\circ$  S latitude, we note a significant local decrease at longitudes  $[\phi - \phi_E] = 0^\circ, 50^\circ$ , each about  $10 \text{ m s}^{-1}$  in a period of about 45 min to 1 hour (Fig. 5.27b). Except for the start and end doublets of sequences [1], [2] / [4], [6] at  $30^\circ$  S, longitude  $0^\circ$ , one should nevertheless remain cautious in interpreting the variations at individual observing points as they remain contained within the statistical error of individual Doppler velocity measurements. Also note that this statistical error reflects our method of defining an upper limit on

the individual Doppler measurement confidence interval by determining the consistency between three repeated short 3-sec exposures at the same position on Venus, over a maximum period of three minutes (see sub-section 5.3.5).

In order to improve the statistical meaningfulness of short-term temporal variations I decided to fit the instantaneous velocities  $v_{z,i}$  at positions  $i$  for each sequence, to a mean zonal wind velocity per latitude band  $v_{z,lat}$ . Note that this instantaneous variable is not averaged over all sequences of the same observing day, as opposed to day-averaged cloud-top zonal velocities  $v_{z,lat}^-$  of Table 5.7. The  $v_{z,lat}$  results for Feb. 19 are presented as Table 5.8. To determine the error on  $v_{z,lat}$  we used a statistical weighted mean on individual measurements so that larger uncertainties reflect larger individual error bars on  $v_{z,i}$  velocities for a given sequence. Sequence's instantaneous velocities data points  $v_{z,i}$  are averaged over the longitudes at local times 7:30a, 8:10a, 9:05a, 9:50a, 10:50a (Table 5.3). Despite values show a trend of temporal variations generally contained within the range of their statistical errors, we can note a similar trend at 30° S and 40° S latitude bands, with a decrease between extreme values of  $v_{z,lat} = (131.8 \pm 17.2) \text{ m s}^{-1}$  for sequence [1] to  $v_{z,lat} = (118.4 \pm 7.8) \text{ m s}^{-1}$  for sequence [6] at S lat. 30° in a time interval of about 3.5 hours, while at 40°  $v_{z,lat}$  varies between  $(117.7 \pm 6.8) \text{ m s}^{-1}$  to  $(109.2 \pm 14.3) \text{ m s}^{-1}$  in a period of about 45 min.

Feb.19, 2011 UT start-end	Sequence [1] 19:05-19:37 $v_{z,lat} \text{ (m s}^{-1}\text{)}$	Sequence [2] 19:38-20:18 $v_{z,lat} \text{ (m s}^{-1}\text{)}$	Sequence [3] 20:19-20:54 $v_{z,lat} \text{ (m s}^{-1}\text{)}$	Sequence [4] 20:55-21:33 $v_{z,lat} \text{ (m s}^{-1}\text{)}$	Sequence [5] 21:24-21:48 $v_{z,lat} \text{ (m s}^{-1}\text{)}$	Sequence [6] 21:49-22:10 $v_{z,lat} \text{ (m s}^{-1}\text{)}$
30°S	131.8±17.2	115.6±5.6	-	122.7±17.2	-	118.4±7.8
40°S	-	-	117.7±6.8	-	109.2 ±14.3	-

Table 5.8: Hour-time scale variation of 1-wind fit to a cloud-top zonal velocity per lat. band  $v_{z,lat}$  on Feb. 19, 2011, sequences [1-6], to the instantaneous velocities  $v_{z,i}$  at positions  $i$  for each sequence on that day. Changes are reported at S lat. 30° and 40°. Longitude range is  $[\phi - \phi_E] = -50^\circ$  to  $0^\circ$  (local time 7:30a - 10:50a). All results are in  $\text{m s}^{-1}$ . Machado et al. (2013).

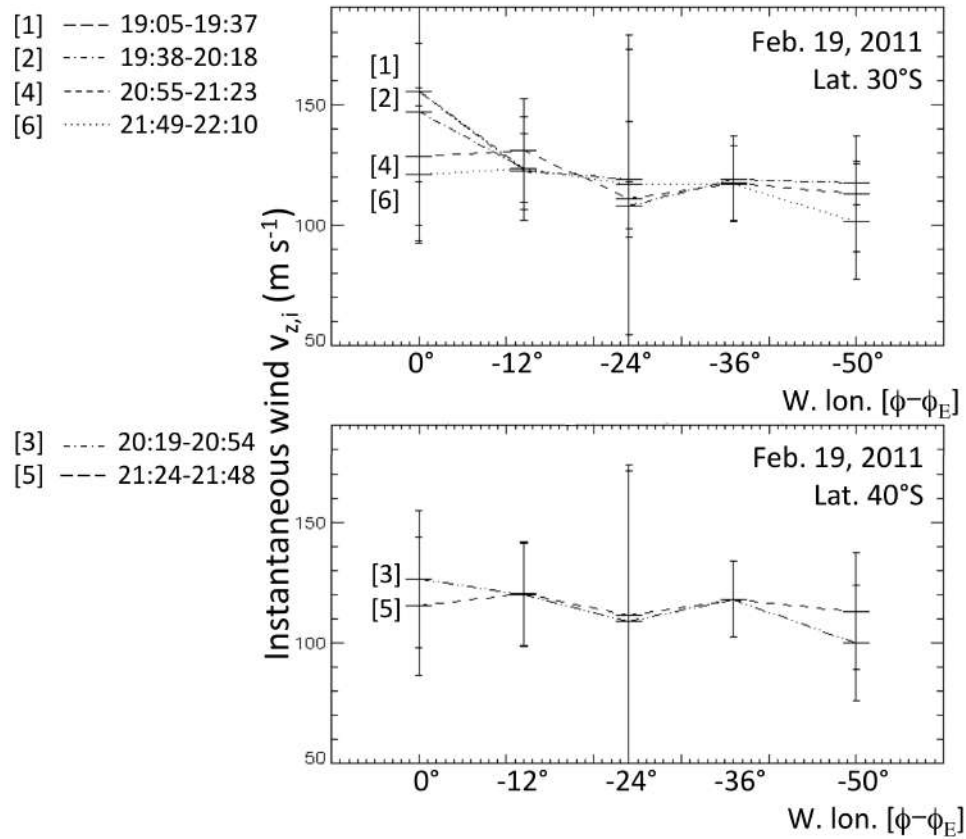


Figure 5.25: Variations of *instantaneous* horizontal wind velocities  $v_{z,i}$  for Feb. 19, 2011, sequences [1-6]. Hourly changes are reported at S lat.  $30^\circ$  (a) and S lat.  $40^\circ$  (b). Longitudinal range of observations extends west (sunward) of sub-terrestrial meridian  $[\phi - \phi_E] = 0^\circ$  to  $-50^\circ$  (local time 7:30a - 10:50a). Sequences of acquisition start-end are [1] 19:05-19:37 UT, [2] 19:38-20:18 UT, [4] 20:55-21:23 UT, [6] 21:43-22:10 UT at lat.  $30^\circ$  S and sequences [3] 20:19-20:54 UT, [5] 21:24-21:48 UT at lat.  $40^\circ$  S. Numbers are reported in the left caption. Data points correspond to the same instantaneous velocity measurements  $v_{z,i}$  as on Fig. 5.17a but plotted vs. longitude instead of vs. time. A fit to a mean zonal wind per lat. band  $v_{z,lat}$  associated with individual sequences is reported in Table 5.8.



*Feb. 20, 2011* - The sequences [7-12] of February 20, 2011 were all acquired on the 30° S latitude band, therefore allowing a sustained monitoring of cloud tops winds in the same region. On Feb. 20 between 19:22-19:44 UT (sequence [7]) and 22:06-22:33 UT (sequence [12]) the instantaneous velocities  $v_{z,i}$  are characterized by a intense variability between time series as we can see at figure 5.26. As on Feb. 19, the longitudinal range of observations extends sunward of sub-terrestrial meridian  $[\phi - \phi_E] = 0^\circ$  to  $-50^\circ$  (local time 7:30a - 10:50a). Variability of the zonal velocity is significant on the hour-scale at all longitudes. Results are shown on Fig. 5.26 and Table 5.9. At  $[\phi - \phi_E] = 0^\circ$  longitude (local time 7:30a) at this same 30° S latitude band, corresponding to point 34 of Table 5.3 and Figure 5.12, we note a large, systematic variation of cloud top winds similar in amplitude to the one we observed on Feb. 19. More interestingly, the variation seems to follow an oscillatory pattern from one sequence to the next within a maximum amplitude of  $\pm 18.5 \text{ m s}^{-1}$  to the mean day-averaged Doppler zonal velocity  $\bar{v}_z = 117.5 \text{ m s}^{-1}$ , over a period limited to 2 hours. Point 34 observed during first sequence [7] gives  $v_{z,i} = (120.6 \pm 10.6) \text{ m s}^{-1}$  at 19:26 UT. At sequence [8] the same point reaches a lower value  $v_{z,i} = (98.6 \pm 12.2) \text{ m s}^{-1}$  at 19:49 UT. It is then measured close to day-averaged  $\bar{v}_z$  at  $v_{z,i} = (116.5 \pm 7.1) \text{ m s}^{-1}$  during sequence [9] at 20:25 UT. In the next half-hour, at 20:57 UT, the instantaneous velocity at  $[\phi - \phi_E] = 0^\circ$  peaks at  $v_{z,i} = (135.4 \pm 17.8) \text{ m s}^{-1}$  while the following velocity measurements at 21:38 UT and 22:09 UT indicate a steady decrease at sequence [11],  $v_{z,i} = (110.7 \pm 19.3) \text{ m s}^{-1}$ , and sequence [12],  $v_{z,i} = (108.9 \pm 11.3) \text{ m s}^{-1}$  respectively. Those data points are plotted separately on Figure 5.28.

Variations at null-Doppler zonal meridian at  $[\phi - \phi_E] = -36^\circ$ , corresponding to point number 31, can be attributed either to a marginal zonal variability component detected over the 1.6 - arcsec aperture size  $v_{z,i} - \bar{v}_z$ , or a meridional velocity component  $\bar{v}_m$ , expected to be strongest at mid-south latitude near 45°S, or more likely a combination of both. At  $[\phi - \phi_E] = -50^\circ$ , I measure a significant, steady decrease between  $v_{z,lat} = (121.0 \pm 8.1) \text{ m s}^{-1}$  and  $v_{z,i} = (119.9 \pm 8.7) \text{ m s}^{-1}$  at sequences [7-8] to  $v_{z,lat} = (96.8 \pm 12.7) \text{ m s}^{-1}$  and  $v_{z,i} = (95.1 \pm 14.4) \text{ m s}^{-1}$  for sequences [10-12] in a time interval of about 2.5 hours.

As on day 1, to improve the statistical meaningfulness of short-term temporal variations I fit the instantaneous velocities  $v_{z,i}$  for each sequence, to a mean zonal wind velocity per latitude band  $v_{z,lat}$ . All data are summarized in Fig. 5.26 and Table 5.9.

*Feb. 21, 2011* - At Figure 5.27 are presented the same variability study then in the two previous cases, but now for Feb 21 at 40° S, (a), and 50° S, (b), latitude bands. As in the case of day 19, the results present higher

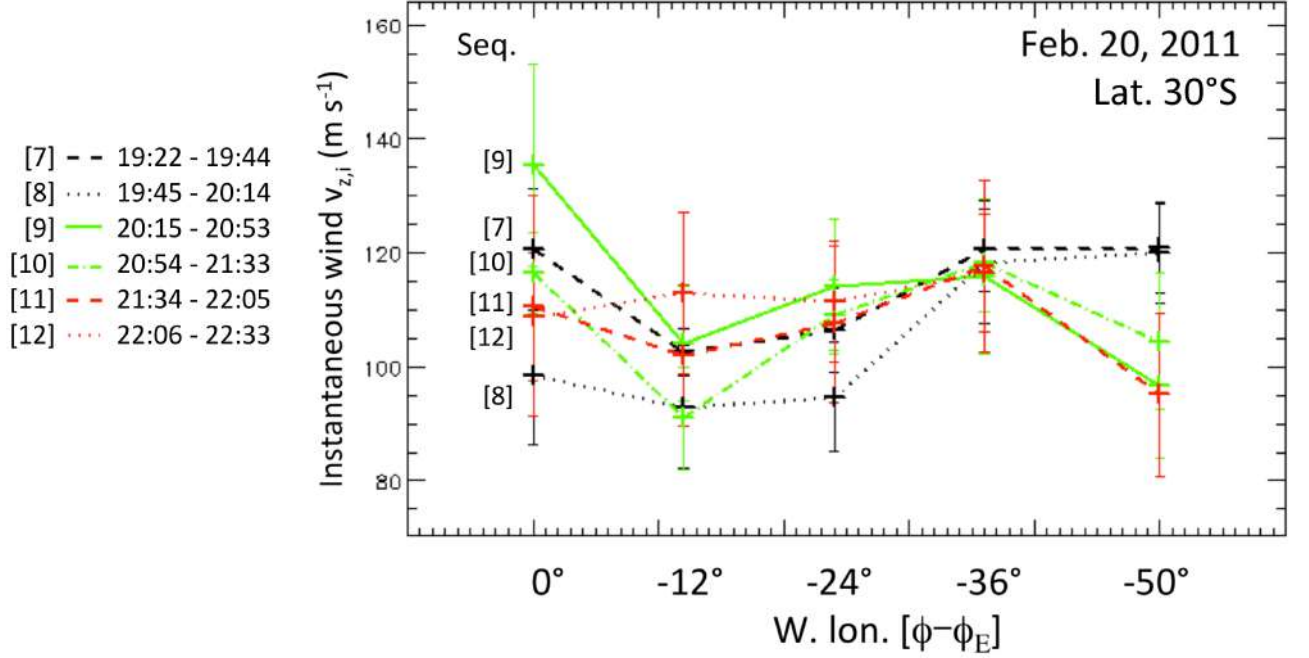


Figure 5.26: Variations of *instantaneous* horizontal wind velocities  $v_{z,i}$  for Feb. 20, 2011, sequences [7-12]. Hourly changes are reported at S lat.  $30^\circ$ , a single latitude band observed on that day. Longitudinal range of observations extends sunward of sub-terrestrial meridian  $[\phi - \phi_E] = 0^\circ$  to  $-50^\circ$  (local time 7:30a - 10:50a). Variability of the zonal velocity is significant on that hour-scale at all longitudes. Variability  $v_{z,i} - \bar{v}_z$  at  $0^\circ$  is reported at the hour time scale with an amplitude of  $\pm 18.5 \text{ m s}^{-1}$  to the mean day-averaged Doppler zonal velocity  $\bar{v}_z = 117.5 \text{ m s}^{-1}$ , over a period of about 2 hours, see also Fig. 5.28. Variability at null-Doppler zonal meridian at  $[\phi - \phi_E] = -36^\circ$  can be attributed either to a marginal zonal variability component detected over the 1.6 - arcsec aperture size  $v_{z,i} - \bar{v}_z$ , or a meridional velocity component  $\bar{v}_m$ , expected to be strongest at mid-south latitude near  $45^\circ\text{S}$ , or more likely a combination of both, see text. Velocities  $v_{z,lat}$  are reported in Table 5.9. All results are presented in  $\text{m s}^{-1}$ .

Feb.20, 2011	Sequence [7]	Sequence [8]	Sequence [9]	Sequence [10]	Sequence [11]	Sequence[12]
UT start-end	19:22-19:44	19:45-20:14	20:15-20:53	20:54-21:33	21:34-22:05	22:06-22:33
	$v_{z,lat}$ (m s <sup>-1</sup> )	$v_{z,lat}$ (m s <sup>-1</sup> )	$v_{z,lat}$ (m s <sup>-1</sup> )	$v_{z,lat}$ (m s <sup>-1</sup> )	$v_{z,lat}$ (m s <sup>-1</sup> )	$v_{z,lat}$ (m s <sup>-1</sup> )
30°S	109.8±2.9	106.1±4.6	109.4±3.6	110.0±5.6	105.7±6.5	112.6±5.7

Table 5.9: Hour-time scale variation of 1-wind fit to a cloud-top zonal velocity per lat. band  $v_{z,lat}$  on Feb. 20, 2011, sequences [7-12], to the instantaneous velocities  $v_{z,i}$  at positions  $i$  for each sequence on that day. Changes are reported at S lat. 30°. Longitude range is  $[\phi - \phi_E] = -50^\circ$  to  $0^\circ$  (local time 7:30a - 10:50a). All results are in m s<sup>-1</sup>. [Machado et al. \(2013\)](#).

variability for the zero degrees longitude position (almost 30 m s<sup>-1</sup>) and 50° (nearly 20 m s<sup>-1</sup>) for the 40° S latitude band. The wind velocities fluctuations between successive time-series for the 50° S latitude band, show the same kind of variability then the previous one, but now without the zero degrees longitude point that was not observed at this latitude band survey because of severe underexposure of its relative observation. Results for instantaneous wind variations  $v_{z,i}$  are shown on Fig. 5.27 while fit to a mean zonal wind per lat. band  $v_{z,lat}$  associated with individual sequences is reported in Table 5.10.

Feb.21, 2011	Sequence [16]	Sequence [17]	Sequence [18]	Sequence [19]
UT start-end	19:27-19:47	19:48-20:07	20:08-20:29	20:30-21:10
	$v_{z,lat}$ (m s <sup>-1</sup> )	$v_{z,lat}$ (m s <sup>-1</sup> )	$v_{z,lat}$ (m s <sup>-1</sup> )	$v_{z,lat}$ (m s <sup>-1</sup> )
40°S	109.9 ± 4.7	-	-	117.3 ± 4.8
50°S	-	112.0 ± 6.0	114.1 ± 4.6	-

Table 5.10: Hour-time scale variation of 1-wind fit to a cloud-top zonal velocity per lat. band  $v_{z,lat}$  on Feb. 21, 2011, sequences [16-19], to the instantaneous velocities  $v_{z,i}$  at positions  $i$  for each sequence on that day. Changes are reported at S lat. 40° and 50°. Longitude range is  $[\phi - \phi_E] = -50^\circ$  to  $0^\circ$  (local time 7:30a - 10:50a). All results are in m s<sup>-1</sup>. [Machado et al. \(2013\)](#).

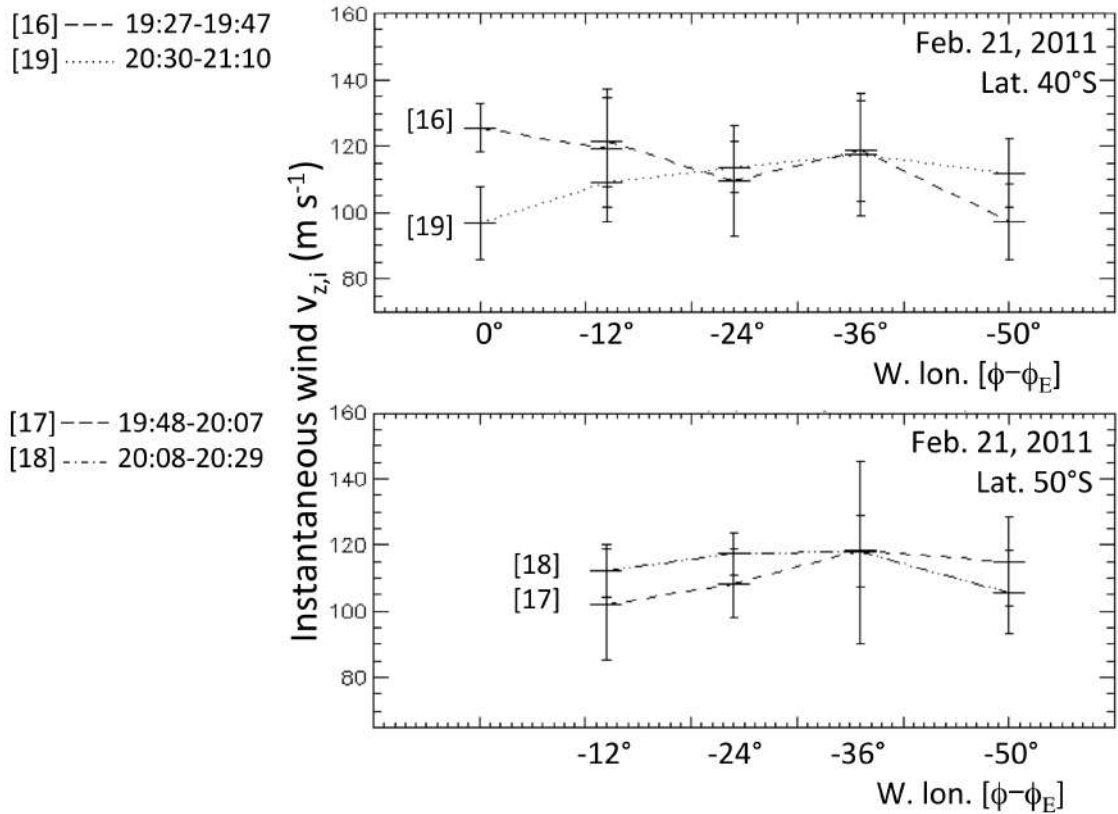


Figure 5.27: Temporal variability of instantaneous zonal wind  $v_{z,i}$  for successive surveys of same latitude bands. (a) Variability for sequences [16], [19] on Feb. 21, 2011 (see Table 2) at lat.  $40^\circ\text{S}$ . (b) Temporal variability for sequences [17-18] at lat  $50^\circ\text{S}$ . These are the same instantaneous velocity measurements  $v_{z,i}$  as on Fig. 7b but plotted vs. longitude instead of vs. time. Variability of mean zonal wind per lat. band  $v_{z,lat}$  are reported in Table 5.8. in Table 5.10. Points at  $[\phi - \phi_E] = 0^\circ$  and high SZA near morning terminator are missing due to low S/N at this position (see Section 5.3.8).

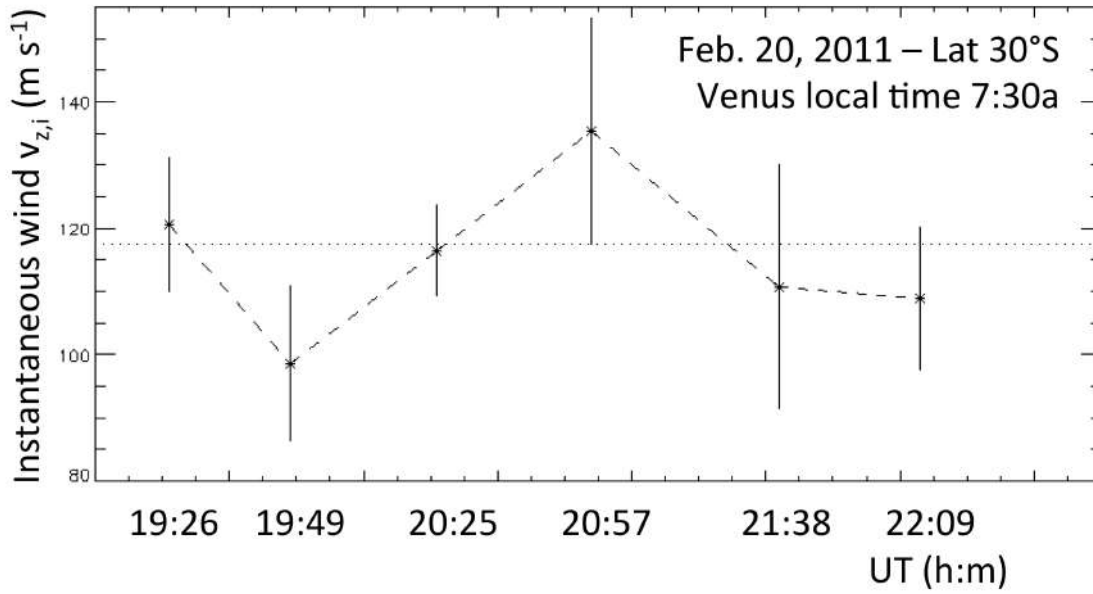


Figure 5.28: Temporal variability of instantaneous zonal wind  $v_{z,i}$  at latitude  $30^\circ$  and W. lon  $[\phi - \phi_E] = 0^\circ$  at 7:30a local time on Venus, observed over repeated acquisitions sequences at south lat. band  $30^\circ\text{S}$  during sequences [7-12] at UT 19:26, 19:49, 20:25, 20:57, 21:38, 22:09 respectively on Feb. 20, 2011 (see Table 2 and Fig.5.26). These are the same instantaneous velocity measurements  $v_{z,i}$  as on Fig. 5.9 at W. lon  $[\phi - \phi_E] = 0^\circ$  in X-axis, plotted vs. time instead of vs. longitude. Variability is reported at the hour time scale with an amplitude of  $\pm 18.5 \text{ m s}^{-1}$  to the mean day-averaged Doppler zonal velocity  $\bar{v}_z = 117.5 \text{ m s}^{-1}$  determined in Table 5.5, and a temporal period of  $v_{z,i} - \bar{v}_z$  of about 2 hours.

## 5.5 Cloud tracking VEx/VIRTIS-M analysis

The cloud tracking analyses, presented in this section, was carried out by Javier Peralta, in the framework of our collaboration that resulted in the publication: Machado et al. (2013). Nevertheless, seen the relevance for the following comparison with the CFHT/ESPaDOnS coordinated observations' results, is shown here.

### 5.5.1 Instrumental description

The Venus-Express Visible and InfraRed Thermal Imaging Spectrometer (VIRTIS-M) is the part of VIRTIS capable of taking spectral images over a range of wavelengths divided into two channels, in the visible range (0.3 to 1  $\mu\text{m}$ ) and the near infrared (1 to 5  $\mu\text{m}$ ) (Drossart et al., 2007). The visible channel of VIRTIS-M instrument can sense in the dayside of the planet the solar scattered light at the cloud tops with ultraviolet wavelengths of about 380 nm, probing UV markings at an altitude of about 66 – 73 km over the Venus surface, while near infrared wavelengths of approximately 1.74  $\mu\text{m}$  allow to sense the scattered photons from the lower cloud on the night side. In our visible observations extending over 0.37-1.05  $\mu\text{m}$  with CFHT/ESPaDOnS, a  $\tau = 1$  level of scattered solar radiation is reached within one scale height of the cloud tops at 70 km of altitude (Widemann et al., 2007; Ignatiev, 2009), see also this work, sub-section 5.3.6. This is also the altitude of the UV cloud markers combined by pairs to provide cloud-tracking wind measurements  $v_{z,CT}$  of UV upper cloud features. The long integration time for getting a complete cube of images, along with the highly elliptical polar orbit of Venus Express (with the pericenter at the north pole) restricts VIRTIS-M observations to the southern hemisphere, and the spatial resolution of the images vary between 15 km per pixel for polar latitudes and about 45 km per pixel for equatorial ones (Figure 5.29).

### 5.5.2 VEx/VIRTIS-M observations

For the campaign of combined observations studied in this work, three Venus Express orbits were selected (VV1766 to VV1768), covering the period from 19 to 21 of February 2011. Unfortunately, the quality of the images is quite variable and only one of this orbit (VV1768) contains images with an acceptable SNR for our purpose of measuring wind speeds manually tracking cloud tracers. Three pairs of images were used, each pair separated by a time interval of 80 minutes, and exhibiting a different region of the southern hemisphere. The first pair at latitude range 23°S-66°S, encompassing the

(1) VEx orbit	(2) Qubes pairs	(3) Date (yyyy/mm/dd)	(4) Time interval (min)	(5) Latitude range	(6) Local time range	(7) Number of points
1766	VV1766_02 VV1766_03	2011/02/19	14	50°S-83°S	07h–13h	40
1768	VV1768_00 VV1768_05	2011/02/21	80	23°S-66°S	08h–12h	26
1768	VV1768_03 VV1768_08	2011/02/21	80	46°S-79°S	07h–16h	34
1768	VV1768_04 VV1768_09	2011/02/21	80	35°S-68°S	07h–10h	24

Table 5.11: ESA Venus Express/VIRTIS-M observations circumstances : (1) orbit number ; (2) VEx-VIRTIS hyper-spectral images or "Qubes" pairs as defined by Cardesín (2010) ; (3) date (UT) ; (4) time interval between selected image pairs at the time of CFHT/ESPaDOnS observations ; (5-6) Latitude and local time he imaging spatial resolution varies between 15 km per pixel for polar latitudes and about 45 km per pixel for equatorial ones ; (7) number of cloud tracers identified in image pairs. Figure 5.29 shows the morphology of the upper cloud observations VV1768\_00 and VV1768\_03 using VIRTIS-M UV-visible channel at 380 nm during VEx orbit 1768 before and after processing and geometrical projection.

dayside morning longitudes simultaneously observed by CFHT/ESPaDOnS (08h–12h). The second pair is at a higher latitude range of 46°S-83°S, with a local time range 07h–16h. The third is at 35°S-68°S also spanning the day-side morning longitudes west of sub-earth meridian at local time 07h–10h (Table 5.11 and see also Table 5.3 for a comparison with CFHT/ESPaDOnS pointing geometry).

The original VIRTIS-M images were navigated and processed to improve the signal-to-noise ratio using the convolution with the directional filter described by Hueso et al. (2010). As the position of the spacecraft changes along this time interval, each couple of images were cylindrically or polar projected depending on whether we are sensing regions closer to the equator or to the south pole respectively. In all the cases, a grid with a spatial resolution of 0.2° employed. Figure 5.29 shows two examples of VIRTIS-M images VV1768\_00 (top) and VV1768\_03 (bottom) in the UV range at 380 nm in the south hemisphere, at the same UT CFHT/ESPaDOnS was acquiring from the ground, over the same latitude and local time range (23°S-66°S

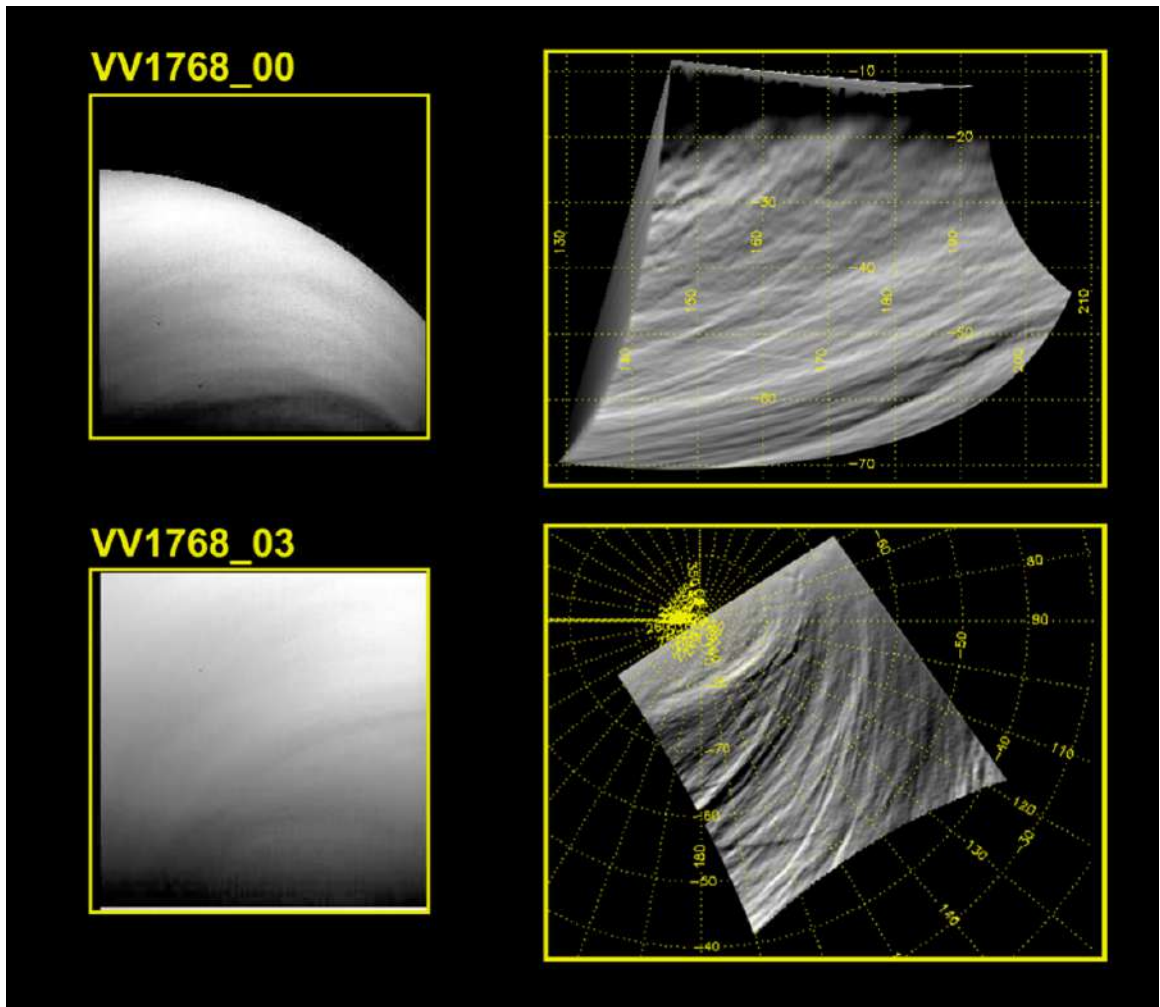


Figure 5.29: Morphology of the upper cloud observations by Venus Express/VIRTIS-M images at 380-nm for simultaneous cloud tracking with CFHT/ESPADONS on 21 February 2011. The apparent motions of UV upper cloud features are measured manually over projected and processed VIRTIS Qubes images (Cardesín, 2010) of the same area. The figure shows VIRTIS-M UV-visible channel images VV1768\_00 (top) and VV1768\_03 (bottom) in the UV range at 380 nm before and after applying the processing and geometrical projection. A total of three pairs of images were used in simultaneous observations, each pair separated by a time interval of 80 minutes, and exhibiting a different region of the southern hemisphere at  $23^{\circ}\text{S}$ - $66^{\circ}\text{S}$  (VV1768\_00),  $46^{\circ}\text{S}$ - $79^{\circ}\text{S}$  (VV1768\_03) and  $35^{\circ}\text{S}$ - $68^{\circ}\text{S}$ . At the hour time-scale such features remain coherent and can be clearly identified in consecutive images (see section 5.5.2 and Table 5.11).



and 08h–12h, for VV1768\_00 on top images ; 46°S–79°S and 07h–16h for bottom images) before and after applying the processing and geometrical projection (Machado et al., 2013).

### 5.5.3 Cloud tracking analysis

The apparent motions of UV upper cloud features are measured manually over projected and processed images of the same area separated by a time interval of 1 to 2 hours, as at the hour time-scale such features remain coherent and can be clearly identified in consecutive images (Hueso et al., 2010, 2012). A total of 84 cloud tracers from three pairs of images separated by a time interval of 80 minutes (see Table 5.11) were identified to carry out the calculation of the wind velocities using the pairs of ultraviolet dayside images of Venus taken by the instrument VIRTIS-M. The following expressions were used for the calculation of the wind components:

$$u = (a + H) \cdot \cos \phi \cdot \frac{\Delta \lambda}{\Delta t} \cdot \frac{\pi}{180} \quad (5.9)$$

$$v = (a + H) \cdot \frac{\Delta \phi}{\Delta t} \cdot \frac{\pi}{180} \quad (5.10)$$

where  $a$  is the Venus radius,  $H$  is the height above the surface,  $\phi$  and  $\lambda$  are the latitude and longitude in degrees, and  $\Delta t$  is the time between the pair of images given in seconds. Considering that the error in time  $\delta t$  is quite small, the absolute errors for both components of the winds will be given by the next expressions following the general expressions given by Bevington et al. (1992), i.e.  $\delta u \approx \delta X / \Delta t$  and  $\delta v \approx \delta Y / \Delta t$ , where  $\delta X$  and  $\delta Y$  are absolute errors for the spatial displacement of the clouds. As the grids used for cloud tracking had a spatial resolution of  $0.2^\circ$ , we have that  $\delta X$  and  $\delta Y$  are about 21 km, thus implying wind speed measurements errors lower than 5 m/s for both components of the wind.

The winds obtained with VIRTIS-M manual cloud tracking are in good agreement with the ones obtained with CFHT/ESPaDOnS Doppler winds in the visible range (0.37–1.05  $\mu\text{m}$ ), as it can be examined in Figures 5.30, 5.31. The general behavior of the wind latitudinal profile is also in general agreement with previous wind studies based on several observing techniques, such as the VMC wind tracking data (Sánchez-Lavega et al., 2008; Moissl et al., 2009) with a uniform zonal wind regime between the equator and mid-latitudes and a steady decrease towards zero poleward of  $55^\circ$  (Hueso et al., 2012; Machado et al., 2012; Kouyama et al., 2013). In both our new datasets

for the meridional component, there is also evidence of poleward winds suggestive of the upper branch of a meridional Hadley-like circulation (Peralta et al., 2007; Hueso et al., 2012), see Fig. 5.31b and the discussion in more details in sub-sections 5.6.1 and 5.6.2.

## 5.6 Comparing Doppler velocimetry and cloud tracking

Fig. 5.30 presents simultaneous wind velocity measurements of VIRTIS-M UV (red arrows) and ESPaDOnS (green arrows). Wind vectors map on 21 Feb. 2011, showing simultaneous wind velocity measurements of VIRTIS-M UV (red arrows) and ESPaDOnS (green arrows). VIRTIS-M arrow length is proportional to wind amplitude  $v_{z,CT}$  in the zonal direction, and to meridional wind amplitude  $v_{m,CT}$  both retrieved in the manual cloud tracking of images pairs of Table 5.11, see text sub-section 5.3. CFHT/ESPaDOnS arrow length is proportional to day-averaged  $\bar{v}_{z,i}$  zonal wind amplitude for 21 Feb. 2011 at latitudes bands from  $10^\circ$  to  $50^\circ$  S lat. by steps of  $10^\circ$ , shown on Fig. 5.23c, and to meridional wind amplitude  $v_{m,\bar{lat}}$  measured on 21 Feb. 2011, also shown on Fig. 5.21.  $v_{z,CT}$  and  $v_{m,CT}$  results integrated over W longitude / local time are also shown on Fig. 5.31. On Figure 5.30, morning terminator is on the right at 6:00 local time, while evening terminator is on the left at 18:00 local time. Noon local time at sub-solar meridian is at center. Figure 5.30 indicates the local time covered by the ESPADONS Doppler winds acquisition on Feb. 21, extending on the morning South hemisphere between 7:30a and 10:50a by steps of  $10^\circ$  in latitude, while VIRTIS-M cloud tracking vectors are more centered at Noon local time with a common region mainly limited between  $30$  and  $50^\circ$ S and 9:05a - 10:50a in local time. The identical wind field vector corresponding to simultaneous measurements using both techniques methods reveals a general agreement both for the cloud top zonal circulation component and the meridional circulation component. The meridional flow is absent in the equatorial region, and a maximum poleward motion at mid latitudes near  $45^\circ$ S with a peak velocity  $v_m^- \simeq 0.1 \times \bar{v}_z$ . We also note an extension of meridional wind detection  $v_{m,CT}$  poleward of  $55^\circ$ S in the VIRTIS-M images.

As discussed in sub-section 5.3.6, a  $\tau = 1$  level is reached within one scale height of the clouds top at 70 km of altitude (Widemann et al., 2007; Ignatiev, 2009), which is also the altitude of the UV cloud markers with both VEx/VIRTIS and VEx/VMC instruments (Sánchez-Lavega et al., 2008; Moissl et al., 2009). This allows a direct comparison of cloud top atmo-

spheric circulation between (i) simultaneous observations by VIRTIS-M and ESPaDOnS on Feb. 21, 2011, and their latitudinal variation ; (ii) comparison with our previous results with Doppler velocimetry in the visible using CFHT/ESPaDOnS (Widemann et al., 2008) and VLT/UVES (Machado et al., 2012), and (iii) comparison with previous VIRTIS-M UV (Sánchez-Lavega et al., 2008; Hueso et al., 2012), VMC (Moissl et al., 2009), and the reanalysis of Galileo fly-by measurements (Peralta et al., 2007), see sub-section 5.6.2 and discussion.

### 5.6.1 Simultaneous velocity measurements with CFHT/ESPaDOnS and VEx/VIRTIS

#### Presentation of coordinated results

One of the objectives of this work has been to provide measurements of the wind and its variability with respect to the background atmosphere, complementary to simultaneous measurements made with the VIRTIS instrument and VMC camera onboard Venus Express. Figure 5.31 shows the comparison between zonal wind velocities  $v_{z,CT}$  obtained by the cloud tracking method with Venus Express/VIRTIS-M cubes pairs, and the instantaneous wind velocities obtained with simultaneous ESPaDOnS/CFHT Doppler observations. Wind variables considered for CFHT/ESPaDOnS results are the instantaneous  $v_{z,i}$  zonal wind velocities on Fig. 5.31a, ordered by latitude bands between 10° and 50°S lat., while day-averaged meridional wind  $v_{z,lat}^-$  per latitude band are plotted on Fig. 5.31b. Note that additional data for the Feb. 21 zonal field also appear as day-averaged  $v_{z,i}^-$  on Fig. 5.23c, and a 1-wind zonal fit is calculated per latitude band  $v_{z,lat}^-$  on Table 5.7 for reference. For all circulation regimes horizontal velocities (x-axis) are plotted vs. latitude (y-axis) in  $\text{m s}^{-1}$  (Machado et al., 2013).

Figure 5.31a shows the comparison for the main retrograde zonal circulation at cloud tops. As the figure is coalesced in longitude, the variability of  $v_{z,i}$  in local time and  $[\phi - \phi_E]$  longitude reflects the scatter of ESPaDOnS zonal velocities at each latitude of reference, as well as the time variability for data points acquired more than once during the day, *i.e.* at 40° and 50°S (see Fig. 5.27a, b in section 4, and the list of sequences of Table 5.2). Our mean zonal latitudinal profile is in general agreement with simultaneous as well as previous CT data, as will be discussed in following subsections 5.6.1 and 5.6.2. In the overlapping region between S lat. 20° and 50° we note an excellent agreement between  $v_{z,i}$  and  $v_{z,CT}$ . Equatorward of 30°S we note a general excess of 10–15  $\text{m s}^{-1}$  of the Doppler velocimetry results with respect to VIRTIS-M. This point will be further discussed in section 5.7. For

reference, day-averaged zonal wind per latitude bands  $v_{z,lat}^-$  appear on Table 5.7, while weighted sequence-averaged zonal wind per latitude band  $v_{z,lat}$ , showing the intra-day variability of the fit, appears in Table 5.10.

Figure 5.31b shows the comparison for the meridional circulation component. Results for cloud-tracking  $v_{m,CT}$  of VIRTIS-M are compared to simultaneous  $v_{m,lat}^-$  in CFHT/ESPaDOnS as they also appear in Figure 5.20 with a 1-wind fit to a pure meridional flow peaking at  $\bar{v}_m = (19.0 \pm 8.3)$  m s<sup>-1</sup> in Feb. 21 data (Table 5.6). We note a good agreement between the two techniques at all latitudes where simultaneous measurements were performed. The meridional circulation found by Sánchez-Lavega et al. (2008); Moissl et al. (2009) displayed positive meridional velocities that increase from 0 m s<sup>-1</sup> at the South pole to about 10 m s<sup>-1</sup> at 55° S and then decrease to 0 m s<sup>-1</sup> at low latitudes (Hueso et al., 2012). We observe a similar latitudinal profile for the pure meridional flow  $\bar{v}_m = (19.0 \pm 8.3)$  m s<sup>-1</sup> in Feb. 21 data (Table 5.6, Figure 5.20). The upper cloud velocimetry in our data is therefore consistent with the poleward branch of a Hadley cell expected in global meridional circulation models. Our model flow  $\bar{v}_m$  is assumed to vary sinusoidally with latitude through its de-projection coefficients ( $c_z$ ), having zero velocity at equator and the poles, and a maximum velocity  $v_m$  (positive for poleward motion) at lat 45° (sub-section 5.4.1).

A comparison between simultaneous velocity measurements with CFHT ESPaDOnS ( $v_{z,i}^-$ ,  $v_{m,lat}^-$ ) and VEx/VIRTIS ( $v_{z,CT}$ ,  $v_{m,CT}$ ) result in an excellent agreement for both the zonal and meridional components of the global circulation, with minor differences equatorward of 30° S and significant temporal variations  $v_{z,i} - \bar{v}_z$  to the mean zonal wind at 30° S, that were detected by Doppler velocimetry near the morning terminator (Fig. 5.28).

### Latitudinal variations of zonal wind velocities $v_{z,i}$ and $v_{z,CT}$

VIRTIS-M UV results for a zonal cloud-tracking wind  $v_{z,CT}$  on February 21 are shown in Fig. 5.31a. Comparison between simultaneous ESPaDOnS zonal velocity measurements in the visible range, 0.37-1.05  $\mu$ m (shown as green triangles) and simultaneous VIRTIS-M zonal velocity measurements in the UV-vis channel at 380 nm (red dots) show a general agreement between the two methods. VIRTIS-M data have an uncertainty on individual motions of the tracked clouds of about 5 m s<sup>-1</sup>, while ESPaDOnS individual measurement uncertainties  $v_{z,i}$ , tributary of additional on-sky calibration and differential techniques have a final value of about 10–12 m s<sup>-1</sup>. The general latitudinal variation of the zonal wind field at cloud tops is properly described by our VIRTIS-M measurements and is in excellent agreement with previously published results of Sánchez-Lavega et al. (2008); Moissl et al.

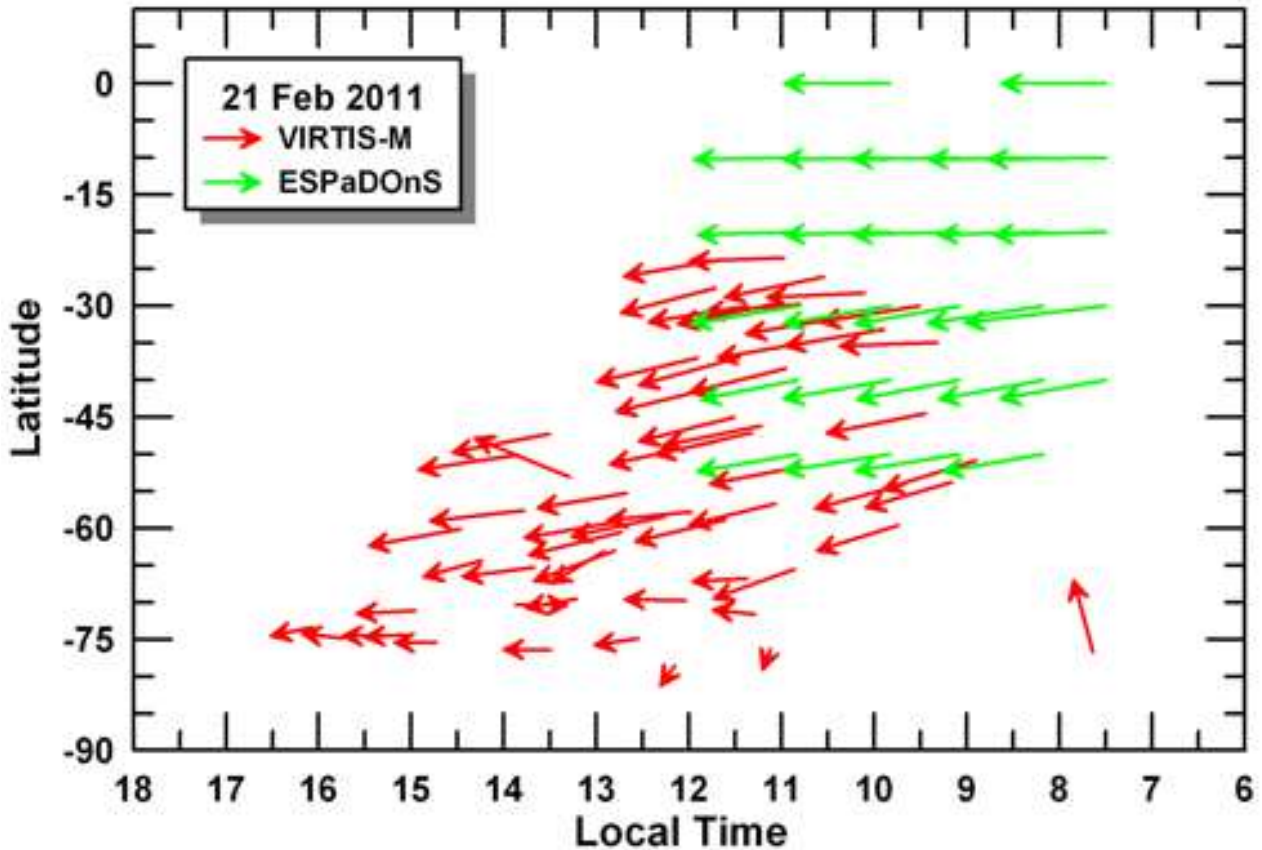


Figure 5.30: Wind vectors map on 21 Feb. 2011, showing simultaneous wind velocity measurements of VIRTIS-M UV (red arrows) and ESPaDOnS (green arrows). VIRTIS-M arrow length is proportional to wind amplitude  $v_{z,CT}$  in the zonal direction, and to meridional wind amplitude  $v_{m,CT}$  both retrieved in the manual cloud tracking of images pairs of Table 5.11, see text subsection 5.3. CFHT/ESPaDOnS arrow length is proportional to day-averaged  $\bar{v}_{z,i}$  zonal wind amplitude for 21 Feb. 2011 at latitudes bands from  $10^\circ$  to  $50^\circ$  S lat. by steps of  $10^\circ$ , shown on Fig.5.23c, and to meridional wind amplitude  $v_{m,lat}$  measured on 21 Feb. 2011, also shown on Fig. 5.21.  $v_{z,CT}$  and  $v_{m,CT}$  results integrated over west longitude / local time on the morning dayside are also shown on Fig. 5.31. Machado et al. (2013).

(2009); Hueso et al. (2012), with zonal wind speed in the upper clouds at nearly constant speed from the equator down to 65°S followed by a steady decrease toward zero velocities at the pole. In the data the meridional shear of the wind between 60° and 80°S is  $-0.03 \text{ m s}^{-1} \text{ km}^{-1}$

The instantaneous wind speed we measure in VIRTIS-M is  $(105.0 \pm 5.0) \text{ m s}^{-1}$ , to be compared with the mean value of  $\bar{v}_z = (117.50 \pm 14.5) \text{ m s}^{-1}$  for our simultaneous Doppler measurements (Table 5.5). The reason can be seen in Fig. 5.31a where ESPaDOnS zonal winds generally lie 10–15  $\text{m s}^{-1}$  over CT winds equatorward of 30°S. In this figure Doppler-wind data are superimposed for all longitudes at 30, 20 and 10°S so this difference appears systematic and not only a result of large temporal amplitude variations at specific points as noted *e.g.* in Fig. 5.28. We interpret this discrepancy closer to the equator as a possible effect of the spatial scale of convective motion in the upper cloud. As noted by Titov et al. (2012), the evolution of the global cloud pattern from dark and patchy low latitudes to bright and longitudinally oriented, streaky features at mid- and high-latitudes imply a strong dependency of turbulence and vertical convective mixing with latitude.

The convective cells of 100–200 km observed by VEx/VMC at low latitude are expected to vertically extend 10–15 km below the cloud tops at low latitudes (Titov et al., 2012), as opposed to convectively stable temperature structure observed close to the polar collar (Tellmann et al., 2009). A possible interpretation of the discrepancy is that signal integrated over ESPaDOnS’s entrance beam of 1.6 arcsec (about 600 km projected at Venus, see Table 5.1, not only would encompass a few turbulence cells, but the scattering of visible sunlight off Venus’ cloud tops  $\tau = 1$  level occurs within one scale height of the clouds and only reflect the projected horizontal motion near the cells top, while motion of CT features may result of a combination of horizontal motion of dark features over 10–15 km or several atmospheric scale heights. As can be noted on Fig. 5.32, discrepancies between ESPaDOnS and VIRTIS occur for low latitudes in the early morning, and for 50°S between 9h-10h, while convective cells are usually found much closer to the subsolar point.

**$[\phi - \phi_E]$  longitudinal (local time) variations of zonal wind velocities  $\bar{v}_{z,i}$  and  $v_{z,CT}$**

Figure 5.32 shows  $[\phi - \phi_E]$  longitudinal (local time) variations of the zonal velocity observed simultaneously from the ground in the visible range (0.37–1.05  $\mu\text{m}$ ) (green triangles) and from space using Venus-Express VIRTIS-M in the UV-vis channel at 0.38  $\mu\text{m}$  (red dots). The zonal winds in the upper cloud change with the local time in a way that can be interpreted in terms of a solar tide. Peralta et al. (2008) explored the variability of cloud top and

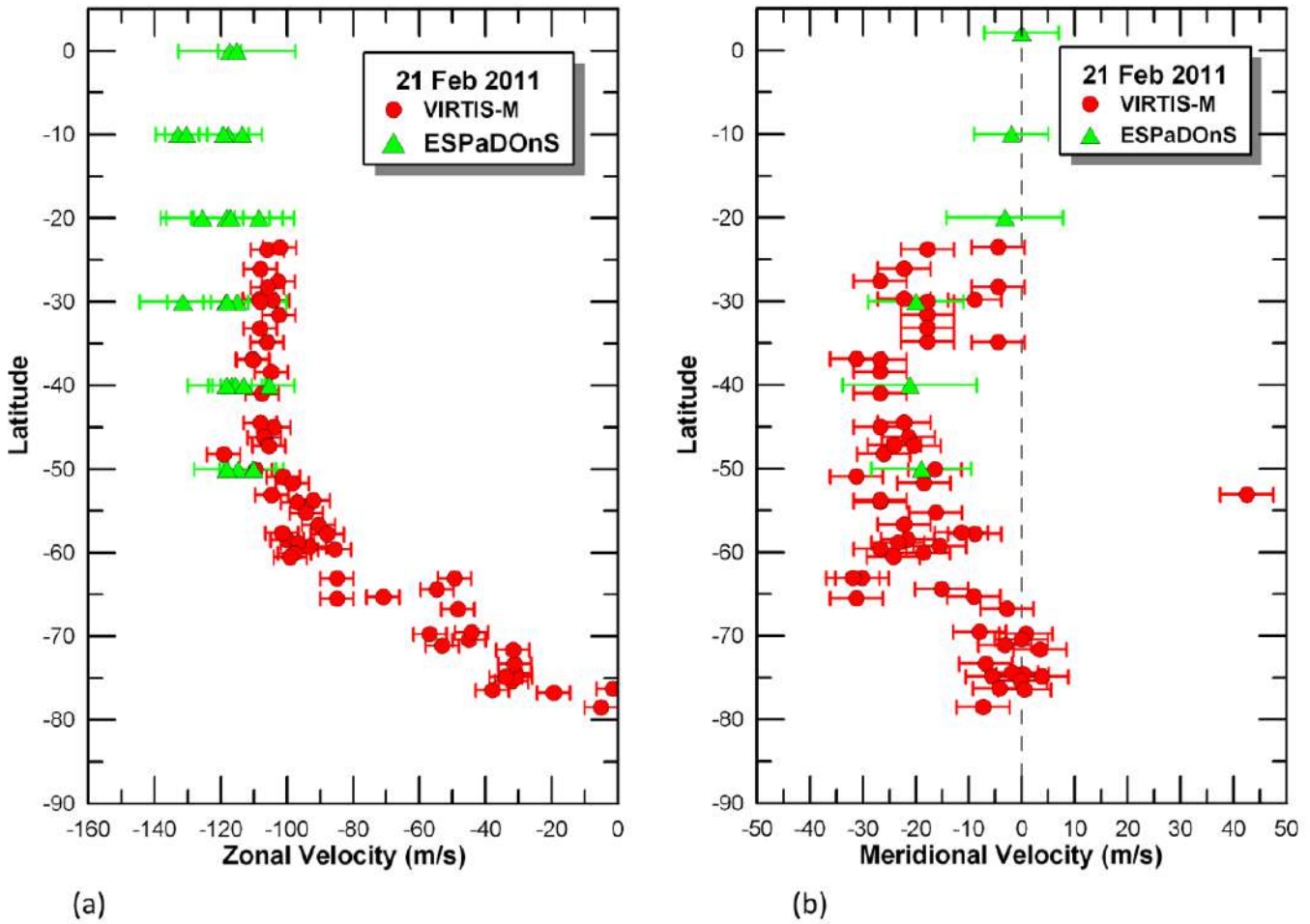


Figure 5.31: Simultaneous cloud-tracking wind velocity measurements of VIRTIS-M UV (dots, red color) and Canada-France-Hawaii Telescope/ESPaDOnS instantaneous Doppler winds (triangles, green color) on February 21, 2011. CFHT/ESPaDOnS  $v_{z,i}$  zonal wind velocities ordered by latitude bands between  $10^\circ$  and  $50^\circ$  S lat. Results for the zonal field also appear as day-averaged  $\bar{v}_{z,i}$  on Fig. 5.23c, and a 1-wind zonal fit is calculated per latitude band  $\bar{v}_{z,lat}$  in Table 5.7. CFHT/ESPaDOnS results for the meridional circulation are the day-averaged  $\bar{v}_{m,lat}$  of Fig. 5.21a. For all results horizontal velocity (x-axis) is plotted vs. latitude (y-axis) in  $\text{m s}^{-1}$ . (a) Results for cloud-tracking  $v_{z,CT}$  compared to instantaneous  $v_{z,i}$  of Feb. 21 at latitude bands  $10^\circ$  to  $50^\circ$  S. (b) Results for cloud-tracking  $v_{m,CT}$  of VIRTIS-M compared to simultaneous  $\bar{v}_{m,lat}$  in CFHT/ESPaDOnS data. Machado et al. (2013).

lower cloud motion to constrain systems of waves with phase speeds  $v_{z,i} - \bar{v}_z$  differing from the background mean velocity. [Sánchez-Lavega et al. \(2008\)](#); [Hueso et al. \(2012\)](#) discuss the local time variations of the mean zonal wind at cloud top. In both initial and completed VIRTIS-M datasets the presence of a thermal solar tide is described in the latitude range  $50^\circ - 75^\circ\text{S}$  with a longitudinal gradient corresponding to a rate of  $2.5 \pm 0.5 \text{ m s}^{-1}$  per local time hour between 9:00a and 3:00p. At other latitudes VIRTIS-M data do not provide evidence for a longitudinal variation. In both our VIRTIS-M and ESPaDONs data plotted on [Fig. 5.32](#), no instantaneous variation in longitude can be inferred, the high value of zonal winds near  $[\phi - \phi_E] = 0^\circ$  at  $30^\circ\text{S}$  being rather the reflect of a highly variable zonal component at 7:30a as already shown in the Feb. 20 data of [Fig. 5.28](#).

The day-to-day variations of *day-averaged*  $\bar{v}_{z,i}$  horizontal wind results  $v_{z,i}$ , shown in [Fig. 5.23](#) allow to better assess the zonal wind change with local time integrated over all sequences on a same day. Among the 3 days of observations, only the repeated sequences [7-12] of Feb. 20 at  $30^\circ\text{S}$  shown on [Fig. 5.23b](#) allow to measure significant variations of the zonal velocity in local time. From  $[\phi - \phi_E] = -12^\circ$  to  $-36^\circ\text{S}$  corresponding to local time 8:10a to 9:50a a monotonous increase of  $10 \pm 3 \text{ m s}^{-1}$  per local time hour can be inferred for the  $30^\circ\text{S}$  latitude band. Points at  $0^\circ$  and  $-50^\circ$ , respectively at 7:30a and 10:50a do not indicate the same tendency, possibly indicating a non monotonous longitudinal variation in our day-averaged  $\bar{v}_{z,i}$  data.

## 5.6.2 Comparison with previous visible Doppler velocimetry measurements

[Figure 5.33](#) compares zonal wind velocities measured with CFHT/ESPaDONs in this work (green diamonds), VEx/VIRTIS simultaneous cloud tracking results in this work (light grey stars) and our previous Doppler velocimetry study with UVES/VLT ([Machado et al., 2012](#)), PL1 (blue), PL2 (red), PL3 (green) curves for measurements with the long slit perpendicular to the equator, and dark gray squares for Doppler measurements parallel to the equator). Both studies points for the existence of an background zonal wind in the order of  $110\text{-}120 \text{ m s}^{-1}$  and relevant spatial and temporal wind variability. Also shown is the latitudinal profile from the reanalysis of Galileo 418 nm violet filter data by ([Peralta et al., 2007](#)).

The latitudinal wind profile obtained with CFHT/ESPaDONs (green triangles on [Fig. 5.33](#)) are consistent with the complete profile previously obtained with UVES at mid-latitudes in measurements perpendicular to the equator. These jet-like structures are moderate, with the southern jet in ex-



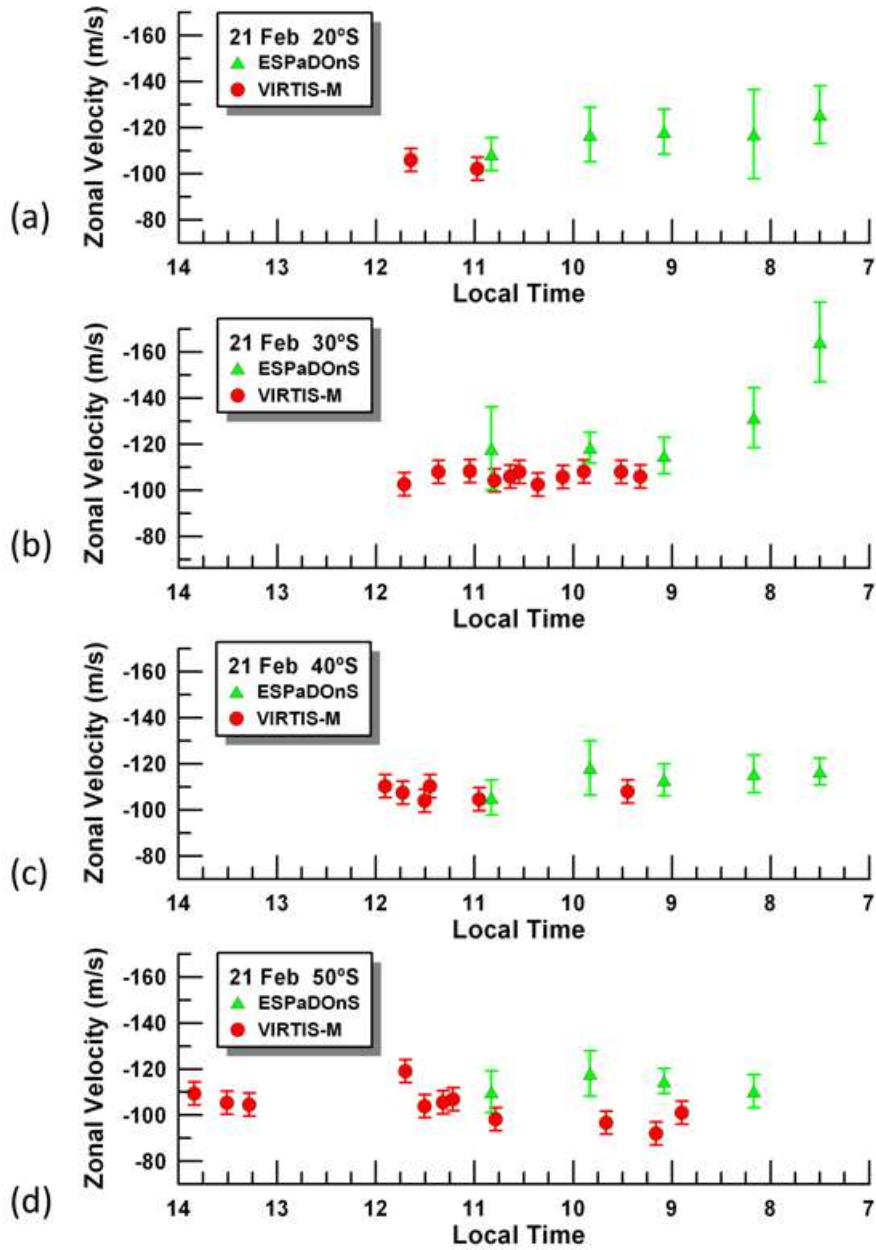


Figure 5.32:  $[\phi - \phi_E]$  longitudinal (local time) variations of the zonal velocity observed simultaneously from the ground in the visible range ( $0.37\text{--}1.05\ \mu\text{m}$ ) (triangles, green color) and from space using Venus-Express VIRTIS-M in the UV-vis channel at  $0.38\ \mu\text{m}$  (dots, red color). Figures are ordered by latitudinal bands. X-axis is local time on Venus' morning hemisphere on February 21, 2011 at the time of the observations. ESPaDOnS data are the *day-averaged*  $v_{z,i}$  horizontal wind results  $v_{z,i}$  at longitudes west of sub-terrestrial meridian  $[\phi - \phi_E] = 0^\circ$  to  $-50^\circ$  also shown on Fig. 5.23c. Figure at (a)  $20^\circ\text{S}$ , with an overlap at 10:50a-11:00a local time ; (b)  $30^\circ\text{S}$ , with an overlap of cloud-tracking and Doppler velocity measurements at W lon  $[\phi - \phi_E] = -24^\circ$  to  $-50^\circ$  (local time 9:05a - 10:50a) ; (c)  $40^\circ\text{S}$ , with an overlap also at  $[\phi - \phi_E] = -24^\circ$  to  $-50^\circ$  (local time 9:05a - 10:50a) ; (d)  $50^\circ\text{S}$ , also with simultaneous measurements at 10:50a-11:00a local time. See text in subsection 5.6.1. Machado et al. (2013).

cess of  $\sim 10$  m/s of its northern counterpart. This jet signature in the 2007 data of Machado et al. (2012), do not appear in the  $v_{z,i}$  CFHT measurements of Feb. 2011, nor do they appear in the simultaneous  $v_{z,CT}$  measurements of Feb. 2011 by VIRTIS. The latitudinal wind shear is not very pronounced in the previous UVES measurements ( $\sim 0.35$  m/s per degree at low latitudes), and stronger shear ( $\sim 3$  m/s per degree) was limited to narrow regions at  $60^\circ\text{S}$ ,  $10^\circ\text{S}$ ,  $30^\circ\text{N}$  and  $40^\circ\text{N}$ . The instantaneous variability of  $v_{z,i}$  measurements of CFHT/ESPaDOnS are also in good agreement with VLT/UVES longitudinal Doppler absolute measurements obtained with the slit parallel to the equator (grey squares).

The observations of temporal variability of instantaneous zonal wind  $v_{z,i}$  at small spatial scale points to small scale wave motions as the most likely processes by which the instability unfolds. Contrary to the lower cloud waves, which are vertically confined in a duct of static stability, these upper cloud waves are not bound vertically. This may result in vertical propagation to levels where they are critically absorbed by the vertically varying mean flow, or dissipated (Schubert and Walterscheid, 1984).

### 5.6.3 Comparison with previous CT measurements

Figure 5.33 also shows the VEx/VIRTIS cloud tracking results in this work (light grey stars) are generally consistent with previous measurements based on cloud tracking (Del Genio and Rossow, 1990; Limaye et al., 2007; Peralta et al., 2007; Sánchez-Lavega et al., 2008; Moissl et al., 2009).

At mid-latitude we obtain the same order of wind velocity magnitudes than Pioneer Venus, Galileo and VEx/VIRTIS measurements. The partial latitudinal wind profile obtained with VEx/VIRTIS (light grey stars) and CFHT/ESPaDOnS are also consistent with the ones from Pioneer Venus and Galileo.

Previous measurements by Pioneer Venus, reanalyzed in Limaye et al. (2007), showed the presence of high latitude zonal jets close to 50 degrees latitude in both hemispheres, with a slight asymmetry between the northern and southern ones. However, long temporal averages of cloud-tracked winds by the Galileo SSI instrument (Peralta et al., 2007), as blue triangles at Figure 5.33, and by the Venus Express VMC and VIRTIS instruments (Sánchez-Lavega et al., 2008; Moissl et al., 2009) do not display any clear evidence for high latitude jets at cloud tops, although shorter time scale averages of VMC measurements in (Moissl et al., 2009) indicate that jets may occur but are short lived.

Rather than being discrepant, different wind measurements provide important insight into the variability inherent to the circulation of Venus. Our

## 5.6. COMPARING DOPPLER VELOCIMETRY AND CLOUD TRACKING 219

direct measurements of instantaneous zonal winds provide additional evidence for the occasional presence of jets and, in general, for variability. The realisation that latitudinal wind profile with jets such as measured by Pioneer Venus is likely to be barotropically unstable ([Limaye et al., 2009](#)), is an argument in favour of variability.

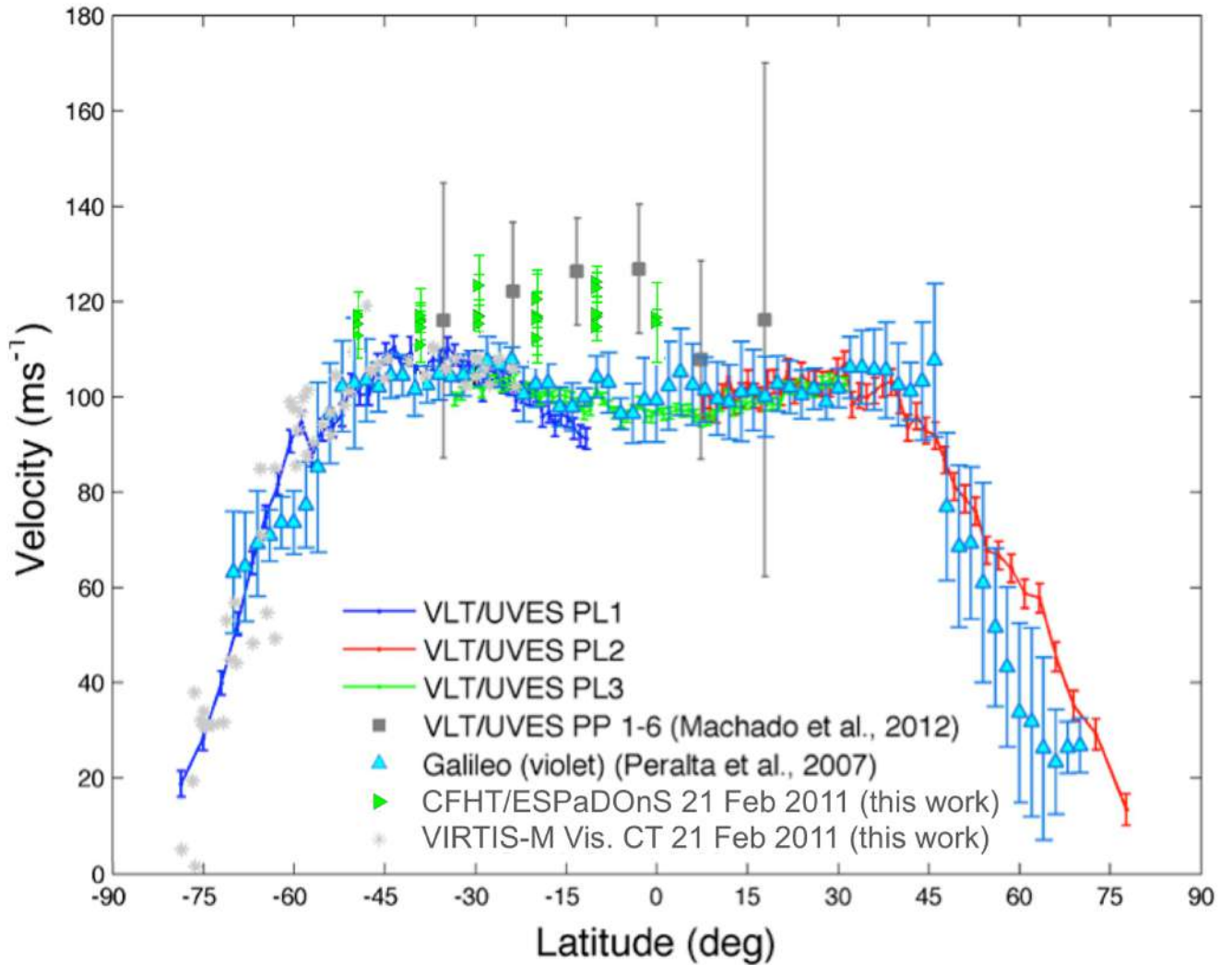


Figure 5.33: Comparison between zonal wind measurements made with CFHT/ESPaDOnS and with VLT/UVES, with the slit perpendicular to the rotation axis (zonal wind velocity, squares) and parallel to the rotation axis (relative zonal wind measurements, PL1-blue, PL2-red, and PL3-green curves) from (Machado et al., 2012). CFHT/ESPaDOnS results are 1-wind fits to  $v_{z,i}$  values to a cloud-top zonal velocity per latitude band ( $v_{z,lat}$ ) on Feb. 21, 2011 (see Table 5.7). VEx/VIRTIS-M cloud tracking measurements on the same day  $v_{z,CT}$  are shown as grey stars, and previous Galileo results as blue triangles. Relative zonal wind curves from VLT/UVES have been offset in order to align them with the Galileo latitudinal profile. Machado et al. (2013).

5.6. *COMPARING DOPPLER VELOCIMETRY AND CLOUD TRACKING*221

## 5.7 Discussion (ESPaDOnS results)

Here it is presented new results based on Doppler wind velocimetry obtained with the 3.60 m Canada-France-Hawaii telescope (CFHT) and the Visible Spectrograph ESPaDOnS, in 2011 (Machado et al., 2013). These observations consisted of high-resolution spectra of Fraunhofer lines in the visible range (0.37-1.05  $\mu\text{m}$ ) to measure the winds at cloud tops using the Doppler shift of solar radiation scattered by cloud top particles in the observer's direction (Widemann et al., 2007, 2008, Machado2013).

The complete optical spectrum was collected over 40 spectral orders, at a resolution of about 80000. We measured the winds using Doppler shifted solar lines and compare with our measurements with VLT/UVES (Machado et al., 2012) and with synchronised coordinated observations by the Visual Monitoring Camera (VMC) and VIRTIS instrument from the orbiter Venus Express. The observations included various points of the dayside hemisphere at a phase angle of  $67^\circ$ , between  $+10^\circ$  and  $-60^\circ$ , in steps of  $10^\circ$ , and from  $+70^\circ$  to  $-12^\circ$  longitude in steps of  $12^\circ$ .

*Mean zonal wind* - Our background zonal wind obtained by Doppler velocimetry presents a magnitude  $\bar{v}_z$  of  $117.4 \pm 18.0 \text{ m s}^{-1}$  on Feb. 19, 2011, and  $117.5 \pm 14.5 \text{ m s}^{-1}$  on Feb. 21, 2011. The previous Doppler velocimetry work (Machado et al., 2012), with UVES/VLT, produced a background zonal wind velocity of nearly  $120 \text{ m s}^{-1}$ , which is also consistent with the present results. They show a good consistency between observational days as well as with simultaneous / complementary VIRTIS-M cloud tracking observations at 380 nm, where the mean zonal wind speed in the upper clouds at nearly constant speed from the equator down to  $60^\circ\text{S}$  followed by a steady decrease toward zero velocities at the pole, with a meridional shear of the wind between  $60$  and  $80^\circ\text{S}$  equal to  $-0.03 \text{ m s}^{-1} \text{ km}^{-1}$ . Results are summarized in Fig. 5.31.

It has been previously discussed whether winds derived from cloud tracking measurements by both VIRTIS-M and VMC (Markiewicz et al., 2007; Peralta et al., 2007; Sánchez-Lavega et al., 2008; Widemann et al., 2007) trace the true atmospheric circulation. Widemann et al. (2008) discussed the possibility of a phase speed of a condensation wave, as in the case of orographic clouds which remain fixed to mountain tops regardless of the wind velocity, while cloud particles are moving at the horizontal wind velocity. We consider that the agreement of cloud motions with the upper cloud velocities retrieved in our new analysis of the simultaneous VIRTIS and CFHT/ESPaDOnS observations of Feb. 2011 at the 70 km altitude level, is in strong support of a sampling of the true atmospheric circulation by the two techniques, for both the zonal and meridional components.

*Detection of meridional wind* - We report the first ground-based detection of a meridional wind velocity at cloud tops, with a mean wind velocity  $\bar{v}_m$  of  $18.8 \pm 11.5 \text{ m s}^{-1}$  on Feb. 19, and  $\bar{v}_m = 19.0 \pm 8.3 \text{ m s}^{-1}$  on Feb. 21. The average meridional wind velocities obtained at different days show remarkable agreement. The wind variability shows magnitude variations of the order of  $20$  to  $30 \text{ m s}^{-1}$ , the planetary positions of these points are quite consistent in day-to-day observations and repeated latitude band surveys.

The simultaneous VIRTIS measurements of a meridional cloud-tracking wind  $v_{m,CT}$  on February, 21 are, also, in good agreement with the meridional wind velocities retrieved by CFHT/ESPaDOnS. On Figure 5.31b results for cloud-tracking  $v_{m,CT}$  of VIRTIS-M are compared to simultaneous  $v_{m,lat}$  in CFHT/ESPaDOnS. We note a good agreement between the two techniques at all latitudes where simultaneous measurements were performed. The upper cloud velocimetry is therefore consistent with the poleward branch of a Hadley cell, and our measurements are homogeneous in terms of local time, is the case of our VIRTIS-M observations (Fig. 5.30). Our model meridional flow  $\bar{v}_m$  is assumed to vary sinusoidally with latitude  $m$  through its de-projection coefficients ( $c_z$ ), and the result is consistent with the meridional circulation found by Sánchez-Lavega et al. (2008), Moissl et al. (2009).

*Longitudinal and temporal variation of zonal wind* - The variation of the zonal wind with local time, by about  $10 \text{ m s}^{-1}$  in the latitude range  $[\phi - \phi_E] = -50^\circ$  to  $0^\circ$  (local time 7:30a - 10:50a), is in general agreement with Venus-Express VIRTIS-M results in the UV (Hueso et al., 2012 and references therein), with the analysis of Pioneer-Venus data (Del Genio and Rossow, 1990) and Galileo fly-by (Toigo et al., 1994). From  $[\phi - \phi_E] = -12^\circ$  to  $-36^\circ\text{S}$  corresponding to local time 8:10a to 9:50a a monotonous increase of  $10 \pm 3 \text{ m s}^{-1}$  per local time hour can be inferred for the  $30^\circ\text{S}$  latitude band on our Feb. 20 observations, with the rest of day-averaged  $v_{z,i}$  results possibly indicating a non monotonous longitudinal variation. Temporal variability of instantaneous zonal wind  $v_{z,i}$  is detected at latitude  $30^\circ$  and W. lon  $[\phi - \phi_E] = 0^\circ$  at 7:30a local time on Venus, observed over repeated acquisitions sequences at south lat. band  $30^\circ\text{S}$  (see Table 5.2 and Fig.5.26).

The variation seems to follow an oscillatory pattern from one sequence to the next within a maximum amplitude of  $\pm 18.5 \text{ m s}^{-1}$  to the mean day-averaged Doppler zonal velocity  $\bar{v}_z = 117.5 \text{ m s}^{-1}$ , over a period of approximately 2 hours (see Fig. 5.27). This is suggestive of wave activity at  $30^\circ\text{S}$  near morning terminator and may be used for future searches of wave phenomena. Moreover, high amplitude, local instantaneous variations also occur up to  $160 \text{ m s}^{-1}$  at  $30^\circ\text{S}$  near morning terminator (see Fig. 5.24), which may be suggestive of gravity wave breaking. Line-of-sight winds in excess of  $180 \text{ m s}^{-1}$  have been detected by Sornig et al. (2013) at 110 km at the

evening terminator and this may be partly caused by gravity wave breaking and subsequent momentum deposition in the lower thermosphere (Nakagawa et al., 2013).

The comparison between instantaneous wind velocity measurements, from ground-based CFHT/ESPaDOnS and VLT/UVES Doppler velocimetry, and cloud tracking from Venus Express/VIRTIS-M coordinated observations clearly shows that both techniques are equally valid and mutually cross-validate each other. The variability inherent to atmospheric motions over different time scales, and the temporal and spatial sampling of the data, however, must be taken into account when interpreting velocity measurements.

We finally note that CFHT/ESPaDOnS spectra contains a number of  $CO_2$  visible bands at 705.6, 710.7, 716.3, 782.0, 788.3, 868.9 and 1036.2 nm, which are simultaneously observed, in particular the  $2\nu_1+5\nu_3$  triad. A spectroscopic analysis of this band will be useful to derive wind measurements in  $CO_2$  bands and constrain the instantaneous wind gradients in the two scale heights above cloud tops and coupling mechanisms between lower and upper Venusian mesosphere.



# Chapter 6

## Observing missions

This section outlines the most relevant participations in observational campaigns in the framework of my thesis. I had the extraordinary chance to integrate the “Venus Twilight Experiment” international campaign, a ground-based programme outlined with the aim of exploiting the 5-6 June 2012 Venus’ transit to study the mesosphere with simultaneous Venus Express observations; I also had the opportunity to perform Venus nightside observations (IR) at the Telescopio Nazionale Galileo (TNG) at the Canary Islands on July 2013.

With the objective of preparing myself to the ground-based observation of astronomical time critical events, and also seen the similarities between the specific transit’s observation and stellar occultation techniques, I participated in an observing mission for the stellar occultation of the trans-neptunian object (TNO) Quaoar, in April 2012. The site of this observation was in the Cape Verde archipelago.

### 6.1 The 2012 Venus transit

Planetary transits are a powerful method for discovering and characterizing exoplanets, but no transits can be seen in more detail than those involving our own Solar System celestial bodies, such as the transits of Venus and Mercury in front of the Sun. I had the rare opportunity to become part of the team who organized the coordination of ground-based measurements of the Venus atmosphere at the time of the 2012 transit, in coordination with ESA’s Venus Express project.

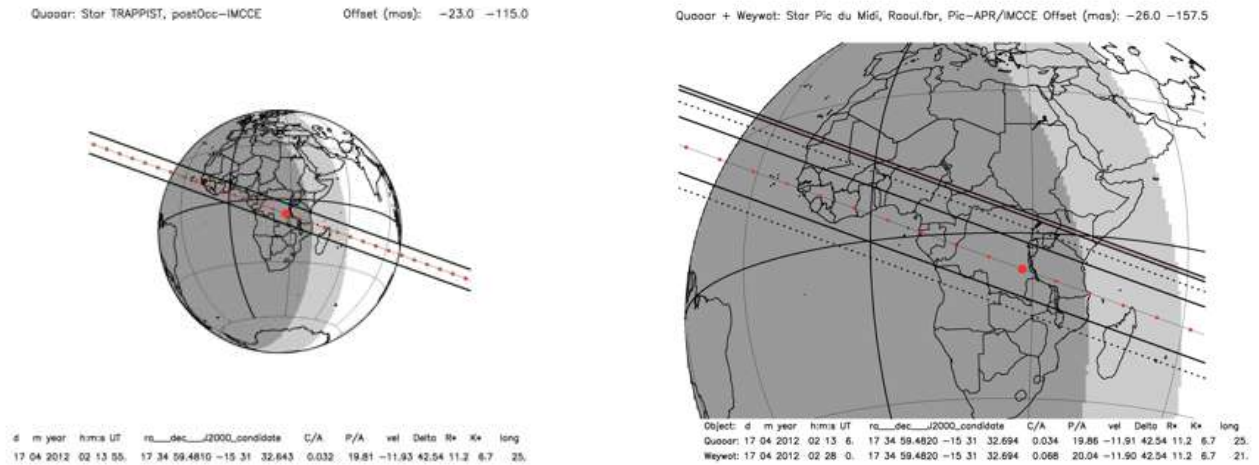


Figure 6.1: Left: Predicted Quaoar’s shadow passing along the Earth. Right: Zoom view of the previous case, showing Cape Verde’s islands within predicted shadow trajectory.

## 6.1.1 Preparation

### Quaoar occultation

Trans-Neptunian Objects (TNOs) are exceptionally difficult to observe icy bodies that orbit the Sun at large distances and are thought to be leftovers of the era of planetary formation.

According to IMCCE’s ephemeris predictions, a stellar occultation by Quaoar was to occur on 17 April, 2012, between 02:23UT and 02:38UT (and also its satellite Weywot from 02:23UT to 02:38UT). The occulting star had coordinates: RA 17h 34’ 59.4809” and  $\delta$  15° 31’ 32.654” (J2000), and has a magnitude of 12 (R). The overall occultation time was about 90 s (and 7 s for the satellite). A multisite observational campaign was prepared with observation sites in Cape Verde, Canary islands, Morocco, La Réunion and several continental European sites, along the predicted shadow cone’s passing.

Previously to the mission, I received practical training in manipulating the CCD camera and GPS connection, as absolute time accuracy is essential for data analysis. I also learned the basics about the production and interpretation of light curves (photometry measurements as a function of time). At the observing site, myself and Felipe Braga Ribas, we started an intense practical training of operating the small portable telescope (C10) the CCD camera and finding, in advance, the star field containing the occulting star, we fine-tuned the exposure time and gain, in order to prevent saturation and

optimize the recorded image sequences.

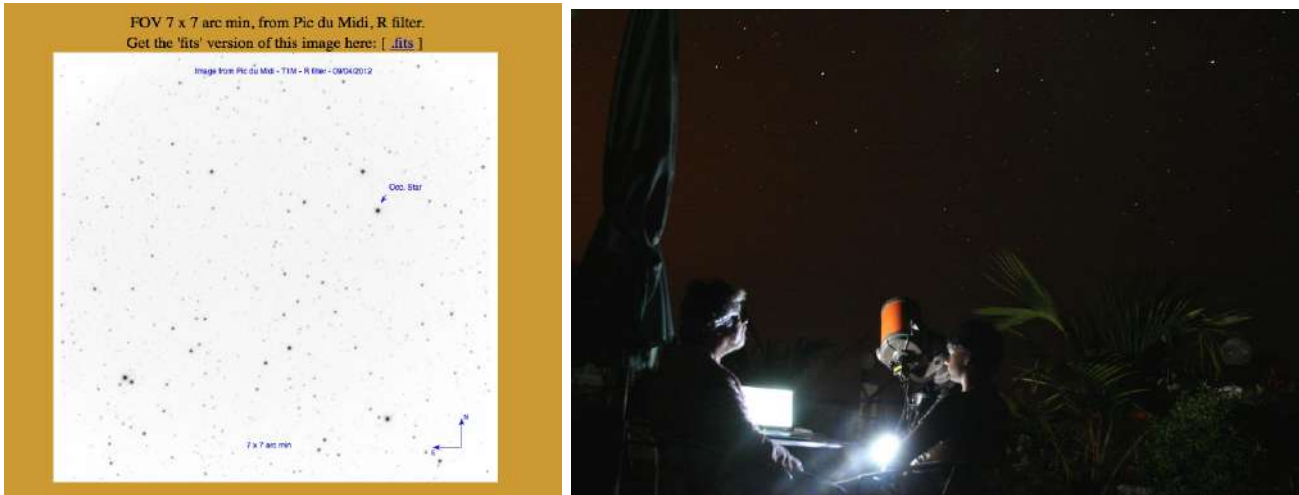


Figure 6.2: Left: Field of stars with the star that was occulted by the TNO Quaoar at 17 April, 2012. Right: At the observation site (Santiago island, Cape Verde archipelago) a few minutes before the time critical event. It can be seen the 25 cm diameter (C10) telescope used in the observations.

With the stellar occultation technique it is possible to derive several of the body's main physical properties. The integration of the recorded occultation chords from all sites (from the exact coordinated time of the star's ingress and egress), allows to retrieve the size and shape projected in the plane of the sky. The construction and analysis of the light curve associated with the stellar occultation, enables to detect the presence of a TNO's atmosphere (as was the case for Pluto) or search for the upper limit for an atmosphere (case of Makemake - at least as a global Pluto-like one, see [Ortiz et al. \(2012\)](#)).

### Training with the Venus Transit Experiment

The VTE coronagraphs were assembled and tested at the Nice Observatory, where I could conduct the first observational tests in presence of the international team (fig. 6.4). The main issues that stood out were the fine tuning of the desired perfect match between the solar disk and the occulting cone, the way of adjusting the circular polariser in order not to saturate the CCD camera, and the way of predicting the right position of ingress and egress in the field of view over the solar disk (to prepare in advance the correct position of the occulting cone in the coronagraph field of view).

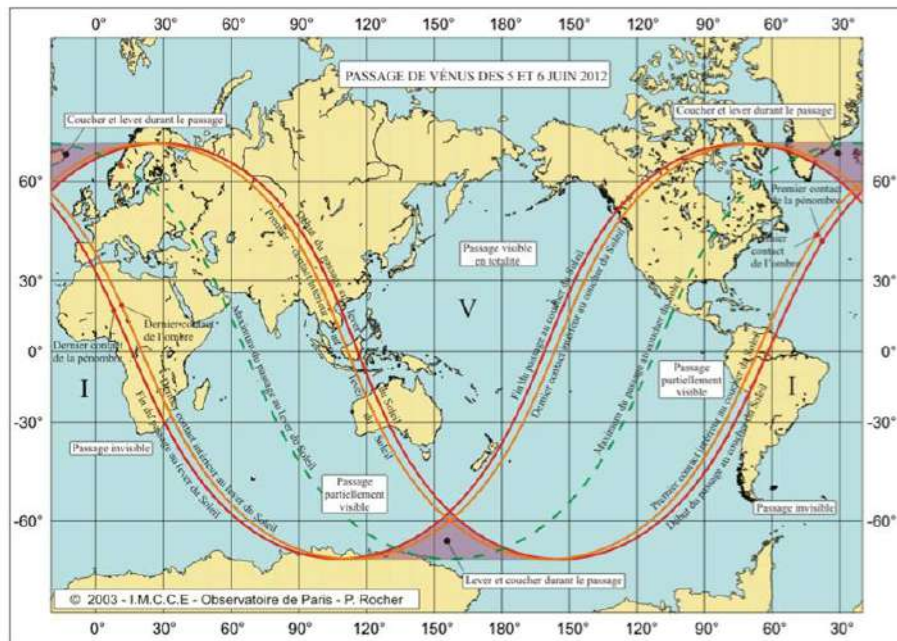


Figure 6.3: Venus’ transit at 5-6 June, 2012, world visibility map.

### 6.1.2 Transit event

During Venus transits, rare phenomena occur that can be related to the physical and chemical properties of the upper atmosphere, around 130-150 km. During a solar transit, close to the ingress and egress phases, the fraction of Venus disk projected outside the solar photosphere appears outlined by an irregular thin arc of light called the “aureole”. It has been shown that the deviation due to refraction and the aureole intensity are related to the local density scale height and the altitude of the refraction layer above the opaque upper haze layers (Tanga et al., 2012). Further away from the Sun, the aureole, due to direct sunlight refraction, disappears. This phenomenon has been described since Lomonosov’s observations of the 1761 Venus transit, in Siberia.

An international collaboration was established (*Venus Twilight Experiment*) in order to deploy dedicated and specialized instruments (adapted coronagraphs called “cytherographs”) in nine geographically distinct observational stations, in the visibility area of the transit. My contribution consisted in setting up the transit observations from Udaipur, India. The “cytherographs” were all equipped with different filters in order to provide multi-wavelength data. The collected data can be interpreted using a dedicated

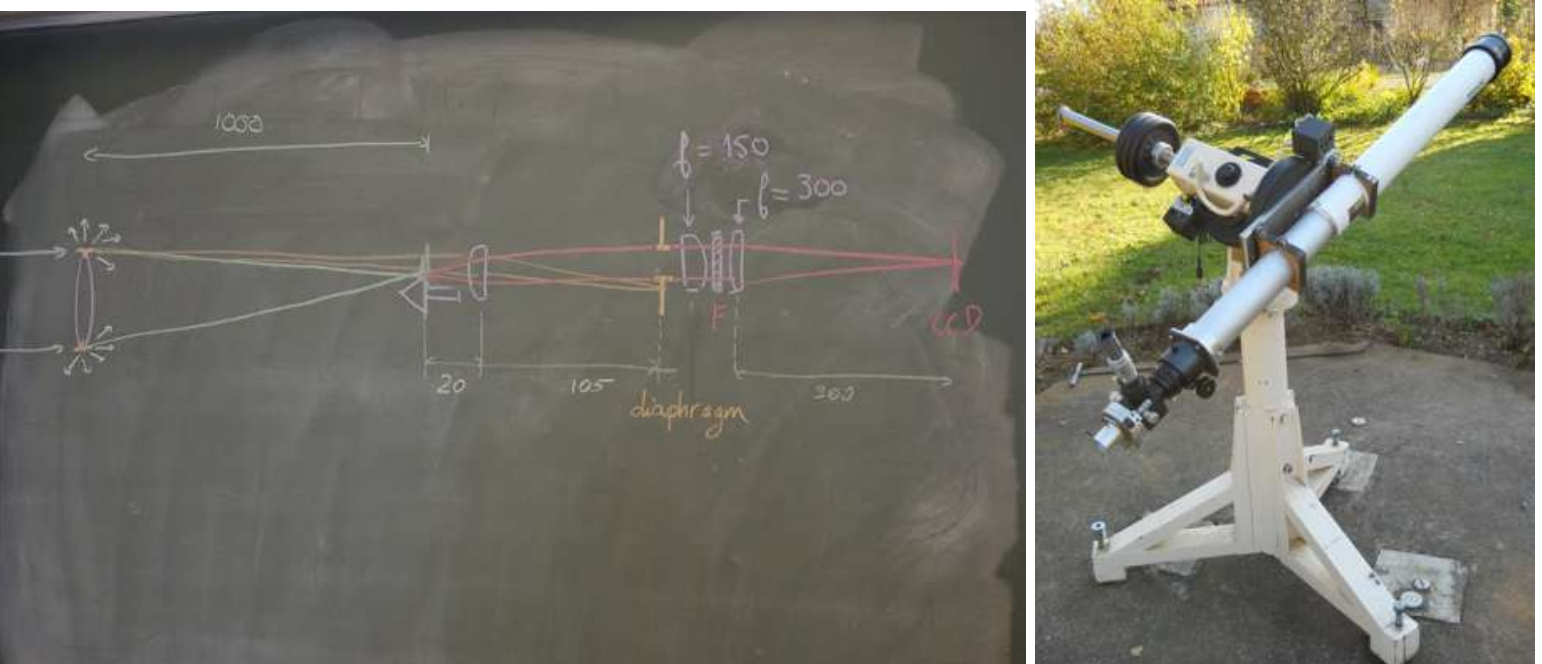


Figure 6.4: Left: Scheme of the coronagraph's optical design. Main lens' diameter: 102 mm, focal length: 1000 mm. A field lens and an achromatic lens, an interferential filter with a bandwidth smaller than 10nm and a diaphragm are aligned in the same concept as a solar coronagraph. In the Cytherograph the occulting cone is offset from the optical axis so the final image of the solar limb at transit contacts I-II, III-IV is at the field center, near optical axis. The pixel scale, for my camera, was 0.416 arcsec/pixel. Right: Mounting with one of the cytherographs assembled in the Observatory of Paris - Meudon, in May 2012.

differential refraction model (see [Tanga et al. \(2012\)](#)), that can be applied to a numerical model in order to reproduce the observations (see next subsection). One of the main goals of this campaign was to take this unique opportunity of characterizing the unknown upper layers of Venus atmosphere above the clouds, with different spectral domains: B (450 nm), V (535 nm), R (607 nm) and I (760 nm).

Besides offering the chance of investigating the mesosphere of the planet, this unique opportunity also provided an analog of exoplanet transits. Several studies using the transmission spectroscopy technique have provided significant insights into the atmospheric composition, structure, and dynamics of transiting exoplanets (for instance the ECHO - Exoplanet Characterization Observatory, a M3-class candidate mission in the framework of ESA's Cosmic Vision program). In this context, Venus is our closest model of a telluric exoplanet with a dense terrestrial atmosphere transiting its star. Obtaining its transmission spectrum during the transit across the Sun serve, both as a comparison basis for transiting Earth-mass exoplanets now being discovered, and as a proof of feasibility that such observations can effectively probe the atmospheres of exoplanets in this mass range. In addition, transit observations of Venus can bring precious information (such is the case of the retrieval of an atmospheric temperature altitude profile) about how the atmosphere of a non-habitable world, observed as an exoplanet, differ from that of a habitable planet, the Earth.

Close to ingress and egress transit's phases, the fraction of Venus' disk seen outside the solar photosphere is trimmed with a glowing thin arc of light (*the aureole*). This transmitted light through Venus' mesosphere carries the signature of several important mesosphere parameters, such as density, composition and temperature, as a function of altitude, since the aureole intensity is related to altitude.

The observers' main task was to measure the brightness of the aureole. The different filters that equipped the different instruments provided multi-band observations.

Previous observations with SPICAV/SOIR, VIRTIS-M and SPICAV/UV (stellar occultations) contributed decisively to better constrain some of the key parameters of the atmosphere ([Mahieux et al., 2012](#)). It has been shown that the deviation due to refraction and the luminosity of the aureole are related to the local density scale height and the altitude of the refractive layer.

Since the aureole brightness is the quantity that can be measured during the transit, an appropriate model allows us to determine the scale height  $H$  and the half-occultation radius relative to slanted opacity  $\tau \sim 1$  best reproducing the observations ([Tanga et al., 2012](#)). In general, different portions of

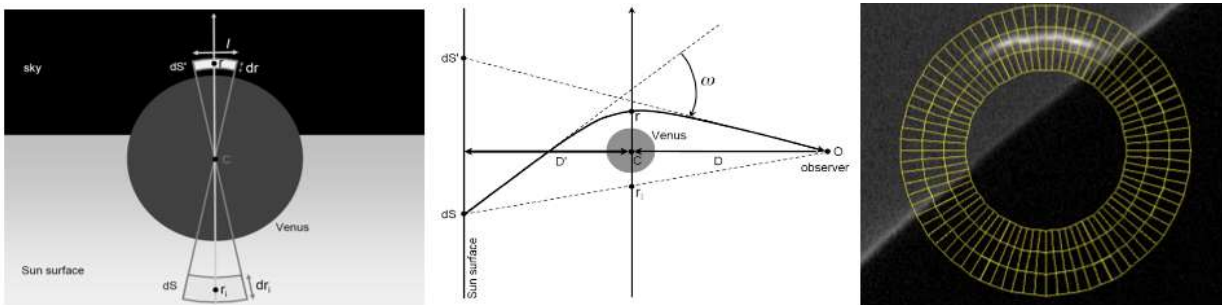


Figure 6.5: Left: Venus (dark grey disk) observed from Earth, partly against the solar disk and partly against the sky (black background). Each solar surface element  $dS$  surrounding  $r_i$  has a refracted image  $dS_0$  of length  $l$  and width  $dr_0$ , caused by Venus atmospheric refraction. The image  $dS_0$  has the same surface brightness as  $dS$  if the atmosphere is transparent. Center : Geometry of the refraction of solar rays by Venus' atmosphere, where  $D'$  (resp.  $D$ ) is the distance of Venus to the Sun (resp. Earth). A ray emitted from the solar surface at  $dS$ , is deviated by an angle  $\omega$  (here negative) before reaching the observer  $O$ , who observes the images  $dS_0$  just above Venus' limb (the aureole). The observer sees  $dS$  projected at algebraic position  $r_i$  in the plane going through Venus and perpendicular to the line of sight. The origin of  $r_i$  is at Venus' center  $C$  and  $r_i$  increases upward. All sizes and angles have been greatly increased for better viewing. Right : Photometry extraction of ingress aureole brightness latitudinal dependency at Lowell Observatory, data obtained June 5, 2012 using one of the Cytherographs in a 10-nm band-pass filter centered at 535nm. The frame shows a clear brightening of the polar region eventually related to temperature and opaque aerosol layers in the  $H_2SO_4$  upper haze.

the arc can yield different values of these parameters, thus providing a useful insight of the physical properties variations of the Venus atmosphere as a function of latitude. The results obtained on 8 June 2004 and June 5-6, 2012 thus depend strongly upon transmittance and extinction profiles obtained by Venus Express' SOIR instrument. The SOIR instrument (Solar Occultation in the InfraRed) is one of the three channels of the SPICAV/SOIR instrument onboard VEx. It is an infrared spectrometer covering the 2200 to 4400  $\text{cm}^{-1}$  region. Observations were made both during the ingress (latitude  $50^\circ$  N, denoted as 2238.1 in the figures below) and at egress (latitude  $30^\circ$  N, denoted below as 2238.2), at 3:30 - 4:00 UTC, SOIR recorded transmission spectra on the whole altitude range, from which temperature profiles) and aerosol vertical distribution has been investigated (Wilson et al., 2012).

A new refraction model assumes that a surface element  $dS$  on the Sun will reach the observer after being refracted by an angle  $\omega$  in Venus's atmosphere, at a closest tangent altitude  $r$  from the planet center. The model retrieves both scale height  $H$  and  $\Delta r$ , altitude above  $H_2SO_4$  upper haze slanted geometry opacity  $\tau = 1$ . The refractive deviation of light is related to the physical structure of the planet atmosphere (see figure 6.5). The formalism of this deviation, for the cases of stellar occultations by planets, has been developed by Baum and Code (1953). Their approach assumes that (i) the local density scale height  $H$  of the atmosphere is constant and much smaller than the planet radius  $R_v$ , (ii) the atmosphere is transparent, (iii) and has spherical symmetry (Tanga et al., 2012).

Deviation  $\omega$  and attenuation of flux  $\phi$  are related to scale height  $H$  and thickness of the refracting layer, upward of the opaque tangential aerosol opacity (for details about the equations below, see Tanga et al. (2012)),

$$\omega = -\nu\sqrt{2\pi r/H} \quad (6.1)$$

$$\frac{1}{k}\left(\frac{1}{\phi} - 1\right) + \log\left(\frac{1}{\phi} - 1\right) = \frac{r_{1/2} - r_i}{H} \quad (6.2)$$

where, for a given geometry the aureole brightness depends upon:  $r_{1/2}$  that represents the closest approach distance, corresponding to  $\phi = 0.5$ ,  $k$  is the geometric parameter,  $\Delta r = r_0 - r_{1/2}$ , with  $\tau = 1$  at  $r_0$  and  $H$  is the atmosphere scale height at  $\Delta r = r_0 - r_{1/2}$ .



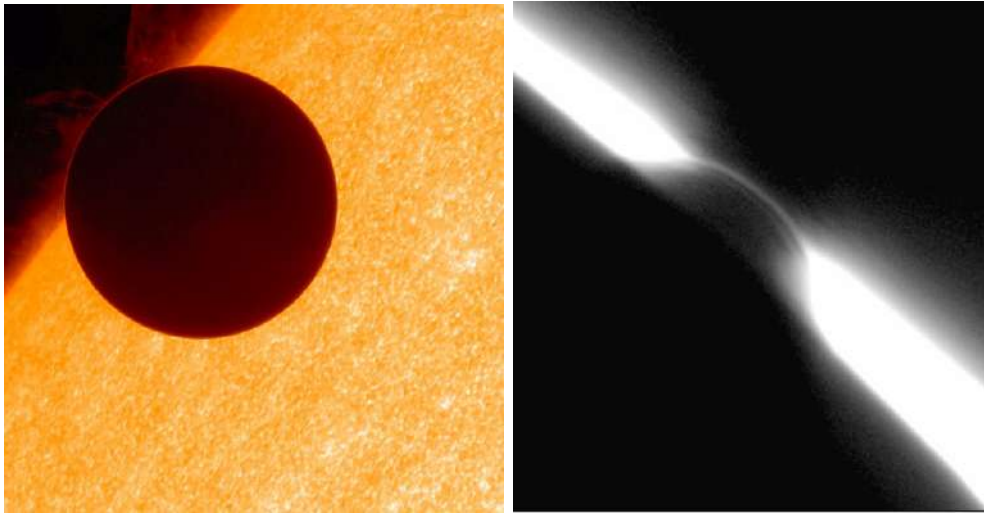


Figure 6.6: Left: Hinode's solar satellite image. Some instants before Venus' transit second contact. Right: Image from our site. Venus' transit short after third contact. It can be seen the almost perfect match between the sun disk and the occulting cone profile. A narrow solar photosphere's rim is visible, as intended, the reappearing Venus is surrounded by its glowing "aureole".

### Udaipur Solar Observatory - Brief observational report

Venus Twilight Experiment - Udaipur Team - India: Pedro Machado, João Retrê. Latitude: 24.4 °N, Longitude: 20 °E, Altitude: 498 m. It was used the coronagraph # 9, with the filter at 610 nm (red filter), in a equatorial mount (Optical Guidance System - BISQUE) from the Udaipur Solar Observatory (USO), India. It was used a circular polarizer in order to control and avoid saturation from the camera's CCD detector. To help navigation it was used a solar camera attached in the same mount and aligned with the coronagraph. Has been used, as well, the real-time Sun images from the solar project GONG produced by the Udaipur Solar observatory. We also used the shareware program Measure in order to measure angles and determine egress exact position upon the solar image in our camera. For navigation upon the solar disk image were used the relative position of sunspots. We used a camera: DNK with a matrix of 1024x768 pixels, pixelscale of 4.65  $\mu\text{m}$ . Focal length of the coronagraph: 1000 mm. CCD size: 4.76x3.57 mm. FOV of 16'x12' = 192'. FOV per pixel: 0.96"/pixel. Control program: Fire Capture. FPS rate at 30. Egress coordinates: R.A.: 4h57.69',  $\delta$ : 22° 47.122'. Venus apparent size: 58 arcsec, Sun apparent size: 30'. Weather and observational conditions: Temperature: 42° Celsius, clear skies with passing clouds (<

5%), notorious atmospheric turbulence with an estimated seeing of about 4. Sunrise at Udaipur USO: 6h:45m. First contact: 6h:45m (local time), third contact at 10:06 and fourth contact at 10:24.

## 6.2 Observing Venus with TNG/NICS

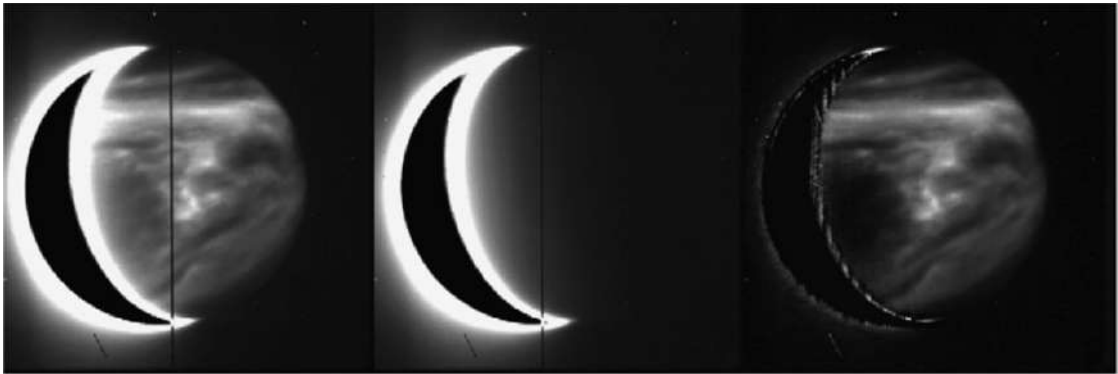


Figure 6.7: From left to right, a Continuum-K image, a Bracket-gamma, and the result of subtracting a scaled Bracket-gamma image from the one taken in Continuum-K. The black line seen in the first two images is from the IRTF SpeX slit. On these images the dark regions are clouds, the bright regions are optically thinner areas between the clouds that allow thermal emission from the lower atmosphere to escape, and the outlined crescent is the saturated day side of the planet. Figure: (Tavener et al., 2008).

I participated in the measurement of zonal winds at the lower cloud level of Venus' atmosphere, based on Venus' nightside observations carried out at the *Telescopio Nazionale Galileo*, a 3.58m optical/infrared telescope located in the Island of San Miguel de La Palma, Canary Islands, with the Near Infrared Camera Spectrometer (NICS).

The purpose was to measure the horizontal wind field at the lower cloud level of Venus' atmosphere, at 48 km altitude, in order to characterize the latitudinal zonal wind profile, study variability, constrain the effect of large scale planetary waves in the maintenance of superrotation, and to map the cloud distribution. This work has made part of the network of ground-based observations of Venus coordinated with ESA's Venus Express orbiter for the 2012 Venus transit campaign.

Our main objective has been to provide direct absolute wind measurements, by tracking cloud features in a series of images of the night side at 2.28  $\mu\text{m}$ , and to map the cloud distribution at the lower cloud level in the

Venus troposphere, in order to complement Venus Express (VEX) and other ground-based observations of the cloud layer wind regime.

The lower Venusian atmosphere is a strong source of thermal radiation, with the gaseous CO<sub>2</sub> component allowing radiation to escape in windows at 1.74 and 2.28  $\mu\text{m}$ . At these wavelengths radiation originates below 35 km, and unit opacity is reached at the lower cloud level, close to 48 km. Therefore, in these windows it is possible to observe the horizontal cloud structure, with thicker clouds seen silhouetted against the bright thermal background of the low atmosphere.



Figure 6.8: Left: Galileo telescope (TNG) at La Palma. Right: A preliminary image of the 48 km altitude Venus' cloud layer.

The obtained data is, at this moment, in a preliminary phase of data reduction. By monitoring of the horizontal cloud structure at 2.28  $\mu\text{m}$  (NICS Kcont filter), it is possible to determine winds using the technique of cloud tracking (Young et al., 2008). These measurements will provide a complementary view of the winds at the lower cloud, allowing the construction of the latitudinal profile of zonal wind at that level and the search for variability relative to past measurements. The field camera used has a 0.13 arcsec pixel scale that allows to resolve  $\sim 3$ -pixel displacements. The absolute spatial resolution on the disk was  $\sim 100$  km/pixel, and the (0.8-1 arc sec) seeing-limited resolution was  $\sim 400$  km/pixel.



# Chapter 7

## Conclusions and outlook

### 7.1 Conclusions

In this section I will try to put into perspective the results presented along this dissertation. It has been investigated the dynamics of Venus mesosphere at cloud top level, using two datasets of ground-based observations, one obtained with VLT/UVES and the other one with CFHT/ESPaDOnS, with a simultaneous comparison with VEx orbiter investigations.

Doppler velocimetry based on long slit spectroscopy with VLT/UVES, has enabled the first ground-based, direct measurement of the instantaneous latitudinal profile of zonal wind in the atmosphere of Venus. The technique allowed (1) the simultaneous determination of the zonal wind across a wide range of latitudes and local times and (2) to determine the presence of local, small scale variations relative to the background mean zonal wind. The method achieved a spatial resolution of about 110 km/pixel at disk center and the results were consistent with previous wind field retrievals based on cloud tracking. The spatial profiles (lat-local-time) of the zonal wind at Venus's cloud tops have been measured in the VLT/UVES datasets. These were the first direct instantaneous measurements of latitudinal wind profiles in the visible. Several scales in the wind spatial structure have been determined unambiguously (Machado et al., 2012).

The ground-based Doppler velocimetry using CFHT/ESPaDOnS and comparison with simultaneous cloud tracking measurements using VEx/ VIRTIS allowed two kinds of relevant results : (1) to characterize the latitudinal zonal wind profile and its variability in local time, (2) to retrieve instantaneous winds and detect from the ground the presence, and evolution, of wavelike phenomena. The presence of wave may have an impact in the global circulation at cloud level and above. Rapidly variable winds and temperature

profiles have been monitored in the upper mesosphere using sub-millimeter line measurements of  $^{12}\text{CO}$  and  $^{13}\text{CO}$  (Clancy et al., 2008, 2011). Sornig et al. (2013) have detected line-of-sight winds in excess of  $180 \text{ m s}^{-1}$  near 110 km at the evening terminator and this may be partly caused by gravity wave breaking. Characteristics and propagation remains to be fully characterized in future coordinated observation programs.

Zonal wind field variations were observed with CFHT/ESPaDOnS within mean background velocities of  $\bar{v}_z = 117.35 \pm 18.0 \text{ ms}^{-1}$  on Feb. 19, and  $117.5 \pm 14.5 \text{ ms}^{-1}$  on Feb. 21, 2011. A temporal, local variation at the hour-scale of  $\pm 18.5 \text{ ms}^{-1}$  was detected as evidence of a wave-like activity near morning terminator at low latitude ( $30^\circ \text{ S}$ ). It has been possible, as well, to obtain the first unambiguous detection from the ground of a poleward meridional wind flow on the morning dayside hemisphere, of  $18.8 \pm 11.5 \text{ ms}^{-1}$  on Feb. 19, and  $19.0 \pm 8.3 \text{ ms}^{-1}$  on Feb. 21. These values are in general agreement with previous observations and with the expected presence of a Hadley cell spanning from the equatorial region to about  $45^\circ$  southern latitude (Machado et al., 2013).

In this thesis has been demonstrated the near instantaneous capability of the Doppler velocimetry techniques to better constrain Venus' atmospheric dynamics. Furthermore, spatial and temporal atmospheric surveys, at spatial and temporal resolution of the same order or with a better accuracy compared to orbiter-based cloud tracking, can be made from the ground.

Two different techniques using ground-based (CFHT/ESPaDOnS) Doppler velocimetry in the visible range, and coordinated/simultaneous space-based (Vex/VIRTIS) tracking of cloud features at Venus' cloud-top ( $\sim 70 \text{ km}$ ), based on image pairs acquired in orbit from the Venus Express spacecraft, were inter-compared for the first time. This work evidenced the complementarity of both techniques, regarding their temporal span, and their latitudinal and local time coverage. The good consistency between the two approaches to obtain averaged wind velocities contributed to a cross-validation of both methods. As can be evidenced from the comparison between the Doppler velocimetry results from this work and cloud tracking results, the complementary character of these two methods of observations and in both spatial coverage, temporal resolution and for internal cross-validation, is noteworthy. Combined results from both techniques offer interesting synergies for constraining different aspects of the cloud top dynamics.

This thesis has capitalized on recent works on Venus atmospheric dynamics including mesospheric measurements from space-based cloud tracking by Markiewicz et al. (2007); Limaye et al. (2007); Sánchez-Lavega et al. (2008); Moissl et al. (2009); Luz et al. (2011); Hueso et al. (2012); Peralta et al. (2012); Garate-Lopez et al. (2013). Cloud tops region was studied as well by

Doppler velocimetry techniques by Gabsi et al. (2008); Gaulme et al. (2008); Widemann et al. (2007, 2008); Machado et al. (2012, 2013), upper mesospheric winds velocity retrievals from (Lellouch et al., 2008; Clancy et al., 2008, 2012; Rengel et al., 2008; Sornig et al., 2008, 2011, 2012) using heterodyne and millimetre lines Doppler velocimetry techniques. The altitude of about 95 km, about 5-6 scale heights above cloud tops, was studied using the nightside oxygen airglow (Gerard et al., 2009), other upper mesosphere altitude studies include Crisp et al. (1996); Ohtsuki et al. (2008); Bailey et al. (2008) offering interesting indirect access to sub-solar to anti-solar circulation. The lower atmosphere layers have been studied by Counselman et al. (1980); Kerzhanovich and Limaye (1985); Preston et al. (1986); Kerzhanovich and Limaye (1985) from the analyzes of entry probes and balloons. The retrieval of thermal winds in recent studies (Zasova et al., 2007; Piccialli et al., 2008, 2012) also made an important contribution for constraining atmospheric dynamics, since some altitude ranges are not accessible to direct wind measurements techniques.

Also relevant in the context of this work are the studies of dynamical tracers, such as SO<sub>2</sub>, CO, OCS, carried out by Sandor and Clancy (2012); Clancy et al. (2012); Cottini et al. (2012); Encrenaz et al. (2012); Matsui et al. (2012); Marcq et al. (2005, 2006), which can reflect small scale spatial and temporal activity relevant to this characterization.

To summarize, Doppler velocimetry in the visible range can contribute for constraining the atmospheric global circulation, regarding retrograde zonal super-rotation and the meridional circulation at several spatial and times scales of the order of one hour to several days, since instantaneous winds are retrieved. It can be helpful in the process of constructing a three dimensional picture of the wind velocity field by integrating different altitude and techniques results in complement to other ground-based observing techniques. I also want to underline the contribution of this work to cross validate the Doppler velocimetry technique, used here, and the cloud tracking technique, when the datasets overlapped. This work clearly established the complementary characteristics of these methods and highlights the utility of joint user of both techniques in coordinated observing campaigns. It remains essential to pursue coordinated wind measurements at different altitudes, and from different techniques from the ground as well as from space, in order to better understand how the dynamics of Venus' atmosphere works.

## 7.2 Future work

After having developed the Doppler velocimetry techniques based on long-slit and single-beam spectroscopy, it seems logic to make the most out of what these methods can bring to the atmospheric dynamics community. So, on a short term basis, I intend to apply the programs I developed to an unpublished data retrieved with CFHT/ESPaDOnS, in 2009. I also intend to prepare new observing campaigns, both with VLT/UVES and CFHT/ESPaDOnS in the first and second semesters of 2014.

Research I am interested in include using long slit spectroscopy to study the meridional circulation and its hypothetical symmetry; extending the research programme in order to cover all the dayside hemisphere with repeated exposures at the same latitudinal bands, since observations with this particular geometry proved extremely successful, and unfortunately were made under sky conditions that were far from optimal, which was reflected in a low S/N and subsequent loss of the best possible Doppler velocimetry analyses. It would be interesting in complement to cloud top wind velocimetry, to perform wind velocity retrievals using the dayside CO<sub>2</sub> lines near 870 nm, in particular the  $2\nu_1 + 5\nu_3$  triad (Widemann et al., 2007). A spectroscopic analysis of this band will be useful to derive wind measurements in CO<sub>2</sub> bands and constrain the vertical wind shear above clouds top, as well as new constraints on altitude retrieval using bands rotational temperature.

Regarding my work based on CFHT/ESPaDOnS, these observations, were constrained by optimal overlap with VEx's coordinated observations, and as a consequence the southern hemisphere was privileged. In a future observing campaign I intend to cover both hemispheres and in particular the half phase angle meridian, which revealed to be so fruitful in the present work.

Understanding the vertical, horizontal and temporal distributions of minor species in the troposphere of Venus is also pertinent for constraining the atmospheric dynamics, radiative processes and chemical interactions. To study the abundance and distribution of greenhouse gases, such as water vapour, is critical to understand their influence on planetary evolution. In the lower troposphere below 40 km, the absence of clouds precludes the direct measurement of the winds, and indirect methods such as tracer distributions must be used to infer the flow in the lower branch of the Hadley circulation. Sulfur dioxide and water vapor, two key species of Venus photochemistry, are known to exhibit significant spatial and temporal variations above the cloud top (Encrenaz et al., 2012, 2013). Thermal imaging spectroscopy at high spectral resolution has shown evidence for strong SO<sub>2</sub> variations on timescales shorter than a day, which obviously come in support of local dy-



namical properties which remain to be fully characterized.

I am very interested in participating in coordinated campaigns for probing different heights, such as the upper mesosphere heterodyne measurements and within the clouds probing at lower mesosphere. I would be very glad to integrate, in a near future, coordinated campaigns combining different velocimetry techniques and retrieval of minor species abundances that might be correlated with dynamics. In a broader approach, I am very interested in the study of atmospheric and surface evolution, which signature is, to some extent, written in its rare gas and isotopic abundances.

The stability of Venus' climate and its coupling with the effectiveness of atmospheric CO<sub>2</sub> reactions with surface minerals, is a very interesting topic as well. A comparative climatology approach between Venus and Earth, regarding their similarities and differences in the greenhouse effect, consists in a research programme that I would be glad to contribute.

### 7.3 Final remarks

The state of the art of our knowledge about super-rotation is still incomplete and it urges to understand how the atmosphere is accelerated to the observed high velocities on a slowly-rotating planet, as is the case of Venus, and to decipher the still puzzling mechanisms that support and maintain super-rotation itself and the high vertical wind shear. At this point, the information we have is clearly not sufficient to constrain current models of the zonal super-rotation.

I partly developed and optimized, tools to retrieve winds at cloud top region using Doppler velocimetry that is available to the planetary community. These tools can be used for other planetary targets with scattering clouds or hazes such as Titan, Jupiter and Saturn. On the other hand, with the advent of new instruments in a near future, which is the case of ESO's ELT, perhaps it will be possible to apply these techniques to study exoplanets' atmospheres.

With the end approaching for the successful Venus Express mission at a time when so many new questions remain open, we feel the urge to prepare a new space mission towards Venus. Extended temporal surveys and good spatial resolution are two key issues in order to reveal the fascinating secrets of our permanently veiled twin sister planet. Ground-based observations must carry on with coordinated observing campaigns and projects, such as the case of the brand new EuroVenus project, that I am honoured to be part

of.

# Bibliography

- Achterberg, R., Conrath, B., Gierasch, P., Flasar, F. and Nixon, C., Titan's middle-atmospheric temperatures and dynamics observed by the Cassini Composite Infrared Spectrometer. *Icarus*, 194:263-277, 2008.
- Allen, D., Crawford, J., Cloud structure on the dark side of Venus, *Nature*, vol. 307, p. 222-224, 1984.
- Ahrens, D., *Meteorology Today*, Brooks/Cole-Thomson Learning, 2003.
- Andrews, D., *An introduction to atmospheric physics*. Cambridge University Press, 2010.
- Avduevsky, V., Marov, M., Noykina, A., Polezhaev, V., Zavelevich, F., Heat Transfer in the Venus Atmosphere, *Journal of Atmospheric Sciences*, vol. 27, pp.569-579, 1970.
- Baker, D., Leovy, C., Zonal winds near Venus' cloud top level - A model study of the interaction between the zonal mean circulation and the semidiurnal tide, *Icarus*, vol. 69, Feb. 1987, p. 202-220, 1987.
- Baker, D. and Schubert, G., Cellular convection in the atmosphere of Venus, *Nature*, volume 355, p. 710-712, 1992.
- Ballester, P.; Rosa, M. R., Modeling echelle spectrographs, *A&A Supplement series*, Vol. 126, 563-571, 1997.
- Baker et al, High Rayleigh number compressible convection in Venus atmosphere: Penetration, entrainment, and turbulence, *Journal of Geophysical Research*, Volume 104, p. 3815-3832, 02/1999.
- Ballester, P., Boitquin, O., Modigliani, A., Wolf, S., in *UVES Pipeline User Manual*. Issue 5 (V2.0.0), 2003.
- Balme, M. and Greeley, R., Dust devils on Earth and Mars. *Reviews of Geophysics*, 44: 3003, 2006.

- Baranne, A. et al., A spectrograph for accurate radial velocity measurements. *Astronomy and Astrophysics Suppl. Ser.*, volume 119, p. 373-390, 1996.
- Basilevsky, A.T., and J.W. Head, Global stratigraphy of Venus: Analysis of a random sample of thirty-six test areas, *Earth, Moon and Planets*, 66, 285-336, 1995.
- Bailey, J., Chamberlain, S., Crisp, D., Meadows, V., Near infrared imaging spectroscopy of Venus with the Anglo-Australian telescope. *Planet Space Sci.* 56, 1385-1390, 2008.
- J. Kelly Beatty, Carolyn Collins Petersen, Andrew Chaikin: *The New Solar System*, 4th Edition, Cambridge University Press, 1999.
- Belton, M., Smith, G., Elliott, D., Klaasen, K., Danielson, G., Space-time relationships in the UV markings on Venus, 1996.
- Belton, M.J.S. et al., Images from Galileo of the Venus cloud deck. *Science*, volume 253, p. 1531-1536, 1991.
- Bengtsson, L., and Grinspoon, D., Towards understanding the climate of Venus, (Vol. 11). Springer, 2013.
- Bertaux, J.-L., Widemann, T., Hauchecorne, A., Moroz, V., and Ekonomov, A., Vega-1 and Vega-2 entry probes: An investigation of UV absorption (220-400 nm) in the atmosphere of Venus, *J. Geophys. Res.*, 101, 12, 709-12, 745, 1996.
- Bézard, B., de Bergh, C., Crisp, D. and Maillard, J., The deep atmosphere of Venus revealed by high-resolution nightside spectra, *Nature*, 345, 508 - 511, 1990.
- Bézard, B., de Bergh, C., Fegley, B., Maillard, J., Crisp, D., Owen, T., Pollack, J. and Grinspoon, D., The abundance of sulfur dioxide below the clouds of Venus, *Geophys. Res. Lett.*, 20, 1587-1590, 1993.
- Bézard, B., de Bergh, C., Composition of the atmosphere of Venus below the clouds, *Journal of Geophysical Research*, Volume 112, 2007.
- Bézard, B., Tsang, C., Carlson, R., Piccioni, G., Marcq, E., Drossart, P., Water vapor abundance near the surface of Venus from Venus Express/VIRTIS observations, *Journal of Geophysical Research*, Volume 114, 2009.

- Bézar, B., Fedorova, A., Bertaux, J-L., Rodin, A., Korablev, O., The 1.10 and 1.18  $\mu\text{m}$  nightside windows of Venus observed by SPICAV-IR aboard Venus Express, *Icarus*, Volume 216, p. 173-183, 2011.
- Belyaev, D., Korablev, O., Fedorova, A., Bertaux, J.-L., Vandaele, A.-C., Montmessin, F., Mahieux, A., Wilquet, V., Drummond, R., First observations of  $\text{SO}_2$  above Venus' clouds by means of Solar Occultation in the Infrared, *Journal of Geophysical Research*, Volume 113, CiteID E00B25, 2008.
- Belyaev, D., Montmessin, F., Bertaux, J-L., Mahieux, A., Fedorova, A., Korablev, O., Marcq, E., Yung, Y., Zhang, X., Vertical profiling of  $\text{SO}_2$  and SO above Venus' clouds by SPICAV/SOIR solar occultations, *Icarus*, Volume 217, p. 740-751, 2012.
- Bevington P.R. and Robinson D.K., 1992: Data reduction and error analysis for the physical sciences. New York: McGraw-Hill, 2nd edition, 1992.
- Blamont, J., Planetary balloons. *Exp. Astron.* 22, 1-39, 2008.
- Bougher, S., Hunten, D. and Philips, R., Upper Atmosphere Dynamics, Global Circulation and Gravity Waves, Venus II: Geology, Geophysics, Atmosphere, and Solar Wind Environment, University of Arizona Press, Tucson, AZ, Bougher S.W, Hunten D.M. and Phillips R.J., Eds., p. 259-291, 1997.
- Bougher, S., Rafkin, S., Drossart, P., Dynamics of the Venus upper atmosphere: Outstanding problems and new constraints expected from Venus Express, *Planetary Space Science*, 54, 1371-1380, 2006.
- Boyer, Ch. and Carmichel, H., Observations photographiques de la planète Vénus, *Annales d'Astrophysique*, volume 24, p. 531, 1961.
- Boyer, Ch. and Camichel, H., Observations photographiques de la planète Vénus, *Annales d'Astrophysique*, volume 24, p. 531, 1961.
- Brecht, A. S. et al., Atomic oxygen distributions in the Venus thermosphere: Comparisons between Venus Express observations and global simulations, *Icarus*, volume 217, p. 759-766, 2011.
- Bullock, A., M.A., D.H. Grinspoon, and J.W. Head, Venus resurfacing rates: Constraints provided by 3-D Monte Carlo simulations, *Geophys. Res. Lett.*, 20, 2147-2150, 1993.

- Bullock, M.A., and Grinspoon, D. H., The stability of climate on Venus, *J. Geophys. Res.*, 101, 7521-7529, 1996.
- Bullock, A., The stability of climate on Venus, Doctoral thesis, 1997.
- Bullock, A., Grinspoon, D.H., The recent evolution of climate on Venus. *Icarus* 150, 19-37, 2001.
- Calvillo, J., Ventos, Turbulência y Ondas en las Nubes de Venus (Doctoral thesis), Universidad de País Vasco, Noviembre de 2008.
- Cardesín, Study and Implementation of the End-to-End data pipeline for the VIRTIS imaging spectrometer on board Venus Express : From Science operation Planning to Data Archiving and Higher Level Processing", PhD thesis, Centro Interdipartimentale di Studi e Attività Spaziali (CISAS), Università degli Studi di Padova, 2010.
- Peter Cattermole: *Venus - The geological Story*, University College London (UCL) Press, 1994.
- Chassefière, E., Wieler, R., Marty, B., and Leblanc, F., The evolution of Venus : Present state of knowledge and future exploration, *Planetary and Space Science* 63-64, 15-23, 2012.
- Carlson, R.W., Kamp, L., Baines, K., Pollack, J., Grinspoon, D., Encrenaz, T., Drossart, P., Lellouch, E., and Bezaud, B., Variations in Venus cloud particle properties: A new view of Venus's cloud morphology as observed by the Galileo near-infrared mapping spectrometer, *Planet Space Sci.*, 41, 477-486, 1993.
- Civeit, T. et al., On measuring planetary winds using high-resolution spectroscopy in visible wavelengths, *Astronomy and Astrophysics*, volume 431, p. 1157-1166, 2005.
- Clancy, R.T., Sandor, B.J. and Moriarty-Schieven, G. H., Venus upper atmospheric CO, temperature, and winds across the afternoon/evening terminator from June 2007 JCMT sub-millimeter line observations, *Planet. Space Sci.*, volume 56, p. 1344-1354, 2008.
- Clancy, R.T., Sandor, B.J. and Moriarty-Schieven, G. H., Circulation of the Venus upper mesosphere/lower thermosphere: Doppler wind measurements from inferior conjunction, sub-millimeter CO absorption line observations, *Icarus*, 2011.

- Clancy, R., Sandor, B., Moriarty-Schieven, G., Thermal structure and CO distribution for the Venus mesosphere/lower thermosphere: 2001-2009 inferior conjunction sub-millimeter CO absorption line observations, *Icarus*, Volume 217, Issue 2, p. 779-793, 2012
- Clancy, R.T., Sandor, B.J. and Moriarty-Schieven, G. H., Circulation of the Venus upper mesosphere/lower thermosphere: Doppler wind measurements from 2001-2009 inferior conjunction, sub-millimeter CO absorption line observations, *Icarus*, Volume 217, p. 794-812, 2012b.
- Colin, L., Hunten, D., Pioneer Venus experiment descriptions. *Space Sci. Rev.* 20, 451-525, 1977.
- Connes, P., Absolute astronomical accelerometry, *Astrophysics and Space Science* (ISSN 0004-640X), volume 110, no. 2, p.211-255, 1985.
- Cottini, V., Ignatiev, N., Piccioni, G., Drossart, P., Grassi, D., Markiewicz, W., Water vapour near the cloud tops of Venus from Venus Express/VIRTIS dayside data, *Icarus*, Volume 217, Issue 2, p. 561-569, 2012.
- Counselman, C., Gourevitch, S., King, R., Lorient, G., and Ginsberg, E., Zonal and meridional circulation of the lower atmosphere of Venus determined by radio interferometry. *Journal of Geophysical Research*, 85:8026-8030, 1980.
- Crisp, D., Ingersoll, A., Hildebrand, C., Preston, R., VEGA balloon meteorological measurements, *Advances in Space Research*, vol. 10, no. 5, p. 109-124, 1990.
- Crisp, D., McMuldroch, S., Stephens, S., Sinton, W., Ragent, B., Hodapp, K., Probst, R., Doyle, L., Allen, D., Elias, J., Ground-based near-infrared imaging observations of Venus during the Galileo encounter. *Science* 253, 1538-1541, 1991.
- Crisp, D., Meadows, V., Bezaud, B., deBergh, C., Maillard, J., Mills, F., Ground-based near-infrared observations of the Venus nightside:  $1.27\text{-}\mu\text{m}$   $\text{O}_2(\text{a}^1\Delta(\text{g}))$  airglow from the upper atmosphere. *J. Geophys. Res.-Planets* 101, 4577-4593, 1996.
- de Bergh, C., Bezaud, B., Owen, T., Crisp, D., Maillard, J.-P., Lutz, B., Deuterium on Venus - Observations from earth, *Science*, vol. 251, p. 547-549, 1991.

- de Bergh, Bezaud, B., Crisp, D., Maillard, J., Owen, T., Pollack, J. and Grinspoon, D., Water in the deep atmosphere of Venus from high-resolution spectra of the night Side, *Adv. Space Res.*, 15, (4)79-(4)88, 1995.
- de Bergh, C., Moroz, V., Taylor, F., Crisp, D., Bezaud, B., Zasova, L., The composition of the atmosphere of Venus below 100 km altitude: An overview. *Planet Space Sci.* 54, 1389-1397, 2006.
- Del Genio A.D. and Rossow W.B., Planetary-scale waves and the cyclic nature of cloud top dynamics on Venus, *Journal of the Atmospheric Sciences*, volume 47, p. 293-318, 1990.
- Del Genio A., Zhou, W. and Eichler, T., Equatorial superrotation in a slowly rotating GCM - Implications for Titan and Venus, *Icarus*, 101, 1-17, 1993.
- Del Genio A., and Zhou, W., Simulations of Superrotation on Slowly Rotating Planets: Sensitivity to Rotation and Initial Condition, *Icarus*, 120, 332-343, 1996.
- Dekker, H.; D'Odorico, S; Status report on the ESO VLT echelle spectrograph UVES, *International Symposium on the Scientific and Engineering Frontiers for 8 - 10 m Telescopes*, p. 217 - 224, 1995.
- Dekker, Hans; D'Odorico, Sandro; Kaufer, Andreas; Delabre, Bernard; Kotzlowski, Heinz; Design, construction, and performance of UVES, the echelle spectrograph for the UT2 Kueyen Telescope at the ESO Paranal Observatory, *Proc. SPIE Vol. 4008*, p. 534-545, *Optical and IR Telescope Instrumentation and Detectors*, Masanori Iye; Alan F. Moorwood; Eds, 08/2000.
- Dollfus, A. et al., Photometry of Venus. I - Observations of the brightness distribution over the disk, *Icarus*, vol.26, p. 53-72, 1975.
- Dollfus, A., Venus - evolution of upper atmospheric clouds. *J. Atmos. Sci.* 32, 1060-1070, 1975b.
- Dollfus, A. et al., Photometry of Venus. I - Observations of the brightness distribution over the disk, *Icarus*, vol.26, p. 53-72, 1975.
- Donati, J. F., Semel, M., Carter, B. D., Rees, D. E., Cameron, A. C. Spectropolarimetric observations of active stars. *Monthly Notices of the Royal Astronomical Society*, 291(4), 658-682, 1997.



- Donahue, T.M., Hoffman, J.H., Hodges, R., Watson, A., Venus was wet - a measurement of the ratio of deuterium to hydrogen. *Science* 216, 630-633, 1982.
- Donahue, T., Hodges, R., Past and present water budget of Venus, *Journal of Geophysical Research* (ISSN 0148-0227), vol. 97, no. E4, p. 6083-6091, 1992.
- Donahue, T., Grinspoon, D., Hartle, R., Hodges R. Jr, in *Ion/neutral Escape of Hydrogen and Deuterium: Evolution of Water* ed. by S.W. Bougher, D.M. Hunten, R.J. Phillips. *Venus II Geology, Geophysics, Atmosphere and Solar Wind Environment* (University of Arizona Press), Tucson, 1997.
- Dorn, Reinhold J.; Beletic, James W.; Cavadore, Cyril; Lizon, Jean-Louis; Optical detector systems of UVES: the echelle spectrograph for the UT2 Kueyen Telescope at the ESO Paranal Observatory, *Proc. SPIE Vol. 4008*, p. 344-355, *Optical and IR Telescope Instrumentation and Detectors*, Masanori Iye; Alan F. Moorwood; Eds, 08/2000.
- Drossart, P., Bezaud, B., Encrenaz, T., Lellouch, E., Roos, M., Taylor, F., Collard, F., Calcutt, S., Pollack, J., Grinspoon, D., Carlson, R., Baines, K., Kamp, L., Search for spatial variations of the H<sub>2</sub>O abundance in the lower atmosphere of Venus From Nims-Galileo. *Planet Space Sci.* 41, 495-504, 1993.
- Drossart, P., Piccioni, G., Gerard, et al., A dynamic upper atmosphere of Venus as revealed by VIRTIS on Venus Express. *Nature* 450, 641-645, 2007.
- Drossart, P., Piccioni, G., Gerard, J.C., et al. A dynamic upper atmosphere of Venus as revealed by VIRTIS on Venus Express. *Nature*, vol. 450, no 7170, p. 64-645, 2007.
- Drossart, P., Piccioni, G., Adriani, A., Angrilli, F., Arnold, G., Baines, K., Bellucci, G., Benkhoff, J., Bzard, B., Bibring, J., Blanco, A., Blecka, M., Carlson, R., Coradini, A., di Lellis, A., Encrenaz, T., Erard, S., Fonti, S., Formisano, V., Fouchet, T., Garcia, R., Haus, R., Helbert, J., Ignatiev, N., Irwin, P., Langevin, Y., Lebonnois, S., Lopez-Valverde, M., Luz, D., Marinangeli, L., Orofino, V., Rodin, A., Roos-Serote, M., Saggin, B., Sanchez-Lavega, A., Stam, D., Taylor, F., Titov, D., Visconti, G., Zambelli, M., Hueso, R., Tsang, C., Wilson, C., and Afanasenko T. Scientific goals for the observation of Venus by VIRTIS on ESA/Venus express mission. *Planetary and Space Science*, 55:1653-1672, 2007

- Encrenaz, T., Greathouse, T. K., Roe, H., et al. HDO and SO<sub>2</sub> thermal mapping on Venus: evidence for strong SO<sub>2</sub> variability. *Astronomy and Astrophysics*, vol. 543, 2012.
- Encrenaz, T. K. Greathouse, M. J. Richter, J. Lacy, T. Widemann, B. Bezard, T. Fouchet, C. deWitt, and S. K. Atreya 2013, HDO and SO<sub>2</sub> thermal mapping on Venus. II. The SO<sub>2</sub> spatial distribution above and within the clouds, *Astron. Astrophys.* accepted.
- Esposito, L. W., Knollenberg, R., Marov, M., Toon, O. and Turco, R., The clouds and hazes of Venus, in *Venus*, edited by D.M. Hunten, L. Colin, T.M. Donahue, and V.I. Moroz, pp. 484-564, University of Arizona Press, Tucson, 1983.
- Esposito, L., Sulfur dioxide: Episodic injection shows evidence for active Venus volcanism, *Science*, 223, 1072-1074, 1984.
- Esposito, L. W., Bertaux, J. L., Krasnopolsky, V., Moroz, V. I., Zasova, L. V. (1997). Chemistry of lower atmosphere and clouds. *Venus II*, 415-458, 1997.
- Fedorova, A., Korablev, O., Vandaele, A.-C., Bertaux, J.-L., Belyaev, D., Mahieux, A., Neefs, E., Wilquet, W. V., Drummond, R., Montmessin, F., Villard, E, HDO and H<sub>2</sub>O vertical distributions and isotopic ratio in the Venus mesosphere by Solar Occultation at Infrared spectrometer on board Venus Express, *Journal of Geophysical Research*, Volume 113, 2008.
- Fegley, B., and A.H. Treiman, Chemistry of atmosphere-surface interactions on Venus and Mars, in *Venus and Mars: Atmospheres, Ionospheres and Solar Wind Interactions*, edited by J.G. Luhmann, M. Tatrallyay, and R.O. Pepin, pp. 7-71, American Geophysical Union, Washington, DC, 1992.
- Fegley, B., Klingelhofer, G., Lodders, K., Widemann, T., Geochemistry of Surface-Atmosphere Interactions on Venus, *Venus II*, S.W. Bougher, D.M. Hunten, & R.J. Phillips Eds., University of Arizona Press, Tucson, pp. 591-636, 1997.
- Gabsi, Y. et al., Measuring Venus winds using the Absolute Astronomical Accelerometer: Solid super-rotation model of Venus clouds. *Planetary and Space Science*, volume 56, p. 1454-1466, 2008.
- Garate-Lopez, I., Hueso, R., Sanchez-Lavega, A., Peralta, J., Piccioni, G., Drossart, P., A chaotic long-lived vortex at the southern pole of Venus, *Nature Geoscience* 6, 254-25, 2013.

- Gaulme, P., Schmider, F.-X., Grec, C., Ariste, A. L., Widemann, T., and Gelly, B., Venus wind map at cloud top level with the MTR/Themis visible spectrometer, Instrumental performance and first results, *Planetary and Space Science*, Special issue on Ground-based measurements in support of Venus Express, volume 56, p. 1335-1343, 2008.
- Gerard, J.-C., Cox, C., Soret, L., Saglam, A., Piccioni, G., Bertaux, J.-L., and Drossart, P., Concurrent observations of the ultraviolet nitric oxide and infrared O<sub>2</sub> nightglow emissions with Venus Express, *Journ. Geophys. Res.*, volume 114, E00B44, 2009.
- Gierasch, P., Meridional circulation and Venus atmospheric rotation, *Journal of the Atmospheric Sciences*, volume 32, p. 1038-1044, 1975.
- Gierasch, P. et al., The general circulation of the Venus atmosphere: an assessment, *Venus II: Geology, Geophysics, Atmosphere, and Solar Wind Environment*, University of Arizona Press, Tucson, AZ, Bougher S.W, Hunten D.M. and Phillips R.J., Eds., p. 459-500, 1997.
- Goldstein, J. et al., Absolute wind velocities in the lower thermosphere of Venus using infrared heterodyne spectroscopy, *Icarus*, volume 94, p. 45-63, 1991.
- Goody, R.; Walker, J. *Atmosferas Planetárias*, Editora Edgard, 1975.
- Grinspoon, D.H., *Venus Revealed: A New Look Below the Clouds of Our Mysterious Twin Planet* (Helix Books, Perseus Publishing, Cambridge, Massachusetts, 1997.
- Grinspoon, D.H., Bullock, M., in *Astrobiology and Venus Exploration*, ed. by L.W. Esposito, E.R. Stofan, T.E. Cravens. *Exploring Venus as a Terrestrial Planet* (American Geophysical Union, Washington DC, 2007.
- Husler, B. et al. Radio science investigations by VeRa onboard the Venus Express spacecraft. *Planetary and Space Science*, 54:1315-1335, 2006.
- Hide, R., Dynamics of the Atmospheres of the Major Planets with an Appendix on the Viscous Boundary Layer at the Rigid Bounding Surface of an Electrically-Conducting Rotating Fluid in the Presence of a Magnetic Field. *Journal of Atmospheric Sciences*, volume 26, p. 841-853, 1969.
- Hansen, J.E., Hovenier, J.W., 1974. Interpretation of the polarization of Venus. *J. Atmos. Sci.* 31, 1137-1160.

- Hide, R., Dynamics of the Atmospheres of the Major Planets with an Appendix on the Viscous Boundary Layer at the Rigid Bounding Surface of an Electrically-Conducting Rotating Fluid in the Presence of a Magnetic Field. *Journal of Atmospheric Sciences*, volume 26, p. 841-853, 1969.
- Holland, H.D., *The Chemistry of the Atmospheres and Oceans*, Wiley, New York, 1978.
- Holton, J., *An introduction to dynamic meteorology*, (Academic Press), 2004.
- Hueso R., Legarreta J., Rojas J.F., Peralta J., Pérez-Hoyos S., Del Río-Gaztelurrutia T. and Sánchez-Lavega A.: The Planetary Laboratory for Image Analysis (PLIA). *Advances in Space Research*, 46, 1120-1138, 2010.
- Hueso, R., Peralta, J., Sánchez-Lavega, A., Assessing the long-term variability of Venus winds at cloud level from VIRTIS-Venus Express, *Icarus*, volume 217, p. 585-598, 2012.
- Ignatiev, N., Moroz, V., Moshkin, B., Ekonomov, A., Gnedykh, V., Grigoriev, A., Khatuntsev, I., Water vapour in the lower atmosphere of Venus: A new analysis of optical spectra measured by entry probes. *Planet Space Sci.* 45, 427-438, 1997.
- Ignatiev, N.I. et al., Altimetry of the Venus cloud tops from the Venus Express observations, *Journal of Geophysical Research*, vol. 114, E00B43, 2009.
- Ingersoll, A., The Runaway Greenhouse: A History of Water on Venus, *Journal of Atmospheric Sciences*, vol. 26, Issue 6, pp.1191-1198, 1969.
- Ip, W.-H., and J.A. Fernandez, Exchange of condensed matter among the outer and terrestrial proto-planets and the effect on surface impact and atmospheric accretion, *Icarus*, 74, 47-61, 1988.
- Irwin, P., de Kok, R., Negrão, A., Tsang, C., Wilson, C., Drossart, P., Piccioni, G., Grassi, D., Taylor, F., Spatial variability of carbon monoxide in Venus' mesosphere from Venus Express/Visible and Infrared Thermal Imaging Spectrometer measurements, *Journal of Geophysical Research*, Volume 113, CiteID E00B01, 2008.
- Kargel, J.S., R.L. Kirk, B. Fegley, and A.H. Treiman, Carbonate-sulfate volcanism on Venus?, *Icarus*, 112, 219-252, 1994.
- Kasting, J.F., Runaway and moist greenhouse atmospheres and the evolution of Earth and Venus, *Icarus*, 74, 472-494, 1988.

- Kawabata, K., Coffeen, D.L., Hansen, J.E., Lane, W.A., Sato, M., Travis, L.D., Cloud and haze properties from pioneer Venus polarimetry. *J. Geophys. Res.* 85, 8129-8140, 1980.
- Keating, G., Bertaux, J.-L., Bougher, S., Dickinson, R., Cravens, T., and Hedin, A., Short-term cyclic variations and diurnal variations of the Venus upper atmosphere. *Science*, vol. 205, p. 62-64, 1979.
- Kerzhanovich, V. and Limaye, S., Circulation of the atmosphere from the surface to 100 km. *Advances in Space Research*, 5:59-83, 1985.
- Khatuntsev, I., Patsaeva, M., Titov, D., Ignatiev, N., Turin, A., Limaye, S., Markiewicz, W., Almeida, M., Roatsch, Th., Moissl, R., Cloud level winds from the Venus Express Monitoring Camera imaging, *Icarus*, Volume 226, p. 140-158, 2013.
- Kliore, A., Moroz, V. and Keating, G., The Venus International Reference Atmosphere, in *COSPAR*, Pergamon Press, Oxford, 1986.
- Knollenberg, R. G.; Hunten, D. M., The microphysics of the clouds of Venus - Results of the Pioneer Venus particle size spectrometer experiment, *Journal of Geophysical Research*, vol. 85, p. 8039-8058, 12/1980.
- Kouyama T., Imamura T., Nakamura M., Satoh T. and Futaana Y.: Long-term variation in the cloud-tracked zonal velocities at the cloud top of Venus deduced from Venus Express VMC images. *Journal of Geophysical Research: Planets*, 118, 37-46, 2013.
- Korablev, O. et al., SPICAV IR acousto-optic spectrometer experiment on Venus Express, *Planetary and Space Science*, 65:38-57, 2012.
- Kostiuk, T. et al., Direct measurement of winds on Titan. *Geophysical Research Letters*, volume 28, p. 2361-2364, 2001.
- Kostiuk, T. et al., Titan's stratospheric zonal wind, temperature, and ethane abundance a year prior to Huyghens insertion, *Geophysical Research Letters*, volume 32, p. 4, 2005.
- Krasnopolsky, V., and Parshev, V., Photochemistry of the Venus atmosphere, in *Venus*, edited by D.M. Hunten, L. Colin, T.M. Donahue, and V.I. Moroz, pp. 431-458, University of Arizona Press, Tucson, 1983.
- Krasnopolsky, V., Spatially-resolved high-resolution spectroscopy of Venus 2. Variations of HDO, OCS, and SO<sub>2</sub> at the cloud tops, *Icarus*, Volume 209, p. 314-22, 2010.

- Krasnopolsky, V., High-resolution spectroscopy of Venus: Detection of OCS, upper limit to H<sub>2</sub>S, and latitudinal variations of CO and HF in the upper cloud layer, *Icarus*, Volume 197, p. 377-385, 2008.
- Kurucz, R.L., 1993. Stellar atmospheres database, currently available at Space Telescope Science Institute Calibration Database System (CDBS) at <http://www.stsci.edu/hst/observatory/cdb/k93models.html>.
- Lane, W.A., and Opstbaum, R. High Altitude Venus Haze from Pioneer Venus Limb Scans, *Icarus*, volume 54, 48-58, 1983.
- Lebonnois, S., Hourdin, F., Eymet, V., Cressin, A., Fournier, R., and Forget, F., Superrotation of Venus' atmosphere analyzed with a full general circulation model, *Journal of Geophysical Research (Planets)*, 115 , 2010.
- Lee, C., and Richardson, M., A general circulation model ensemble study of the atmospheric circulation of Venus, *Journal of Geophysical Research (Planets)*, 115, E04,002, 2010.
- Lellouch, E. et al., Global circulation, thermal structure, and carbon monoxide distribution in Venus' mesosphere in 1991, *Icarus*, volume 110, no. 2, p. 315-339, 1994.
- Lellouch, E. et al., Monitoring of mesospheric structure and dynamics, in: Bougher, S.W., Hunten, D.M., Phillips, R.J.(Eds.), *Venus II. The University of Arizona Press, Tucson, AZ, Bougher S.W, Hunten D.M. and Phillips R.J., Eds., p. 295-324, 1997.*
- Lellouch, E. et al., Monitoring Venus' mesospheric winds in support of Venus Express: IRAM 30-m and APEX observations, *Planetary and Space Science*, volume 56, p. 1355-1367, 2008.
- Lellouch, E. and Witasse, O., A coordinated campaign of Venus ground-based observations and Venus Express measurements, *Planetary and Space Science*, volume 56, p. 1317-1319, 2008.
- Leovy, C., Rotation of the upper atmosphere of Venus, *Journal of Atmospheric Science*, Vol. 30, p. 1218-1220, 1973.
- Lewis, J. *Physics and Chemistry of the Solar System*, Elsevier Academic Press, 2004.
- Limaye, S. S.; Suomi, V. E., 1981. Cloud motions on Venus - global structure and organization. *Journal of Atmospheric Sciences*, volume 38, p. 1220-1235, 1981.

- Limaye, S., Grund, C., Burre, S., Zonal mean circulation at the cloud level on Venus - Spring and fall 1979 OCPP observations, *Icarus*, vol. 51, p. 416-439, 1982.
- Limaye, S., Venus atmospheric circulation: Observations and implications of the thermal structure. *Adv. Space Res.* 5, 51-62, 1985.
- Limaye, S., Venus: Cloud level circulation during 1982 as determined from Pioneer cloud photopolarimeter images. II - Solar longitude dependent circulation, *Icarus*, 73, 212-226, 1988.
- Limaye, S.S. et al., Venus Atmospheric Circulation: Known and unknown, volume 112, E04S09, 2007.
- Limaye, S.S. et al., Vortex circulation on Venus: Dynamical similarities with terrestrial hurricanes, *Geophysical Research Letters*, volume 36, L04204, doi:10.1029/2008GL036093, 2009.
- Luz, D. and Hourdin, F., Latitudinal transport by barotropic waves in Titan's stratosphere. I. General properties from a horizontal shallow-water model, *Icarus*, volume 166, p. 328-342, 2003.
- Luz, D. et al. Characterization of zonal winds in the stratosphere of Titan with UVES, *Icarus*, volume 179, p. 497-510, 2005a.
- Luz, D. et al. Characterization of zonal winds in the stratosphere of Titan with UVES: 2. Observations coordinated with the Huygens Probe entry, *Journal of Geophysical Research*, volume 111, CiteID E08S90, 2006.
- Luz, D. et al. Venus's Southern Polar Vortex Reveals Precessing Circulation, *Science*, volume 332, p. 577-580, 2011.
- Luz, D., Lellouch, E., Widemann, T., Witasse, O., Bertaux, J., Scientific Proposal - ESO, 2006.
- Machado, P., Luz, D. Widemann, T., Lellouch, E., Witasse, O, Characterizing the atmospheric dynamics of Venus from ground-based Doppler velocimetry, *Icarus*, Volume 221, p. 248-261, 2012.
- Machado, P., Widemann, T., Luz, D., Peralta, J., Wind circulation regimes at Venus' cloud tops : Ground-based Doppler velocimetry using CFHT/ESPaDOnS and comparison with simultaneous cloud tracking measurements using VEx/VIRTIS in February 2011, *Icarus*, 2013. Submitted.

- Mahieux, A., et al., J. Geophys. Res. Vol. 117, E07001, doi:10.1029/2012JE004058, 2012.
- Marcq, E., Bézard, B., Encrenaz, T., Birlan, M., Latitudinal variations of CO and OCS in the lower atmosphere of Venus from near-infrared nightside spectro-imaging, *Icarus*, Volume 179, p. 375-386, 2005.
- Marcq, E., Encrenaz, T., Bézard, B., Birlan, M., Remote sensing of Venus' lower atmosphere from ground-based IR spectroscopy: Latitudinal and vertical distribution of minor species, *Planetary and Space Science*, Volume 54, p. 1360-1370, 2006.
- Marcq, E., Bézard, B., Drossart, P., Piccioni, G., Reess, J. M., Henry, F., A latitudinal survey of CO, OCS, H<sub>2</sub>O, and SO<sub>2</sub> in the lower atmosphere of Venus: Spectroscopic studies using VIRTIS-H. *Journal of Geophysical Research: Planets*, 113(E5), 2008.
- Marcq, E., Belyaev, D., Montmessin, F., Fedorova, A., Bertaux, J-L., Vandaele, A-C., Neefs, E., An investigation of the SO<sub>2</sub> content of the venusian mesosphere using SPICAV-UV in nadir mode, *Icarus*, Volume 211, p. 58-69, 2011.
- Marcq, E., Bertaux, J-L., Montmessin, F., Belyaev, D., Variations of sulphur dioxide at the cloud top of Venus's dynamic, atmosphere, *Nature Geoscience*, Volume 6, pp. 25-28, 2013.
- Markiewicz, W. et al., Morphology and dynamics of the upper cloud layer of Venus, *Nature*, volume 450, p. 633-636, 2007.
- Markiewicz, W. et al., Venus Monitoring Camera for Venus Express, *Planetary and Space Science*, volume 55, p. 1701-1711, 2007.
- Marov, M., Avduevsk, V., Borodin, N., Ekonomov, A., Kerzhano, V., Lysov, V., Moshkin, B., Rozhdest, M., Raybov, O., Preliminary results on Venus atmosphere from Venera-8 Descent Module. *Icarus* 20, 407-421, 1973.
- Marov, M., Grinspoon, D., *The Planet Venus*, Yale University Press New Haven and London, Yale Planetary Exploration Series, 1998.
- Martic, M. et al., 1999. Evidence for global pressure oscillations on Procyon. *Astron. Astrophys.*, volume 351, p. 993, 1999.
- Martic, M.; Lebrun, J.-C.; Schmitt, J.; Lebreton, J.-P.; Appourchaux, T., Feasibility demonstration of Titan wind measurement technique at OHP



- using absolute accelerometry method. Technical report, Observatoire de Haute Provence, 2001.
- Matsui, H., Iwagami, N., Hosouchi, M., Ohtsuki, S., Hashimoto, G., Latitudinal distribution of HDO abundance above Venus' clouds by ground-based 2.3  $\mu\text{m}$  spectroscopy, *Icarus*, Volume 217, Issue 2, p. 610-614, 2012.
- McGouldrick, K., Momary, T.W., Baines, K.H., and Grinspoon, D., Quantification of middle and lower cloud variability and mesoscale dynamics from Venus Express/VIRTIS observations at 1.74 $\mu\text{m}$ , *Icarus*, 2011.
- Moissl, R. et al., Morphology and dynamics of the upper cloud layer of Venus, *Nature* Vol. 450, p. 633-636, 2007.
- Moissl, R. et al., Venus cloud top winds from tracking UV features in Venus Monitoring Camera, *Journal of Geophysical Research*, volume 114, E00B31, 2009.
- Montmessin, F., Bertaux, J.-L., Lefevre, F., Marcq, E., Belyaev, D., Gérard, J.-C., Korablev, O., Fedorova, A., Sarago, V., Vandaele, A. C., A layer of ozone detected in the nightside upper atmosphere of Venus, *Icarus*, Volume 216, p. 82-85, 2011.
- Mueller-Wodarg I.C.F., Forbes J.M., and Keating G.M., The thermosphere of Venus and its exploration by a Venus Express Accelerometer Experiment, *Planet. Space Sci.*, volume 54, p. 1415-1424, 2006.
- Mueller, N.T., Helbert, J., Erard, S., Piccioni, G., and Drossart, P., Rotation period of Venus estimated from Venus Express VIRTIS images and Magellan altimetry, *Icarus*, volume 217, p. 474-483, 2011.
- Nakagawa, H., Hoshino, N., Sornig, M., Kasaba, Y., Sonnabend, G., Stupar, D., Aoki, S., Murata, I., Comparison of general circulation model atmospheric wave simulations with wind observations of venusian mesosphere, *Icarus*, Volume 225, p. 840-849, 2013.
- Nakamura, M. et al., Planet-C: Venus Climate Orbiter mission of Japan, *Planetary and Space Science*, Volume 55, p. 1831-1842, 2007.
- Nakamura, M., Iwagami, N., Satoh, T., Taguchi, M., Watanabe, S., Takahashi, Y., Imamura, T., Suzuki, M., Ueno, M., Yamazaki, A., Fukuhara, T., Yamada, M., Ishii, N., Ogohara, K., Return to Venus of AKATSUKI, the Japanese Venus Orbiter, American Geophysical Union, Fall Meeting 2011, abstract ‡ P13A-1646, 2011.

- Newman, M., and Leovy, C., Maintenance of strong rotational winds in Venus' middle atmosphere by thermal tides, *Science*, 257, 647-650, 1992.
- D'Odorico, Sandro; Cristiani, Stefano; Dekker, Hans; Hill, Vanessa; Kaufer, Andreas; Kim, Taesun; Primas, Francesca: Performance of UVES, the echelle spectrograph for the ESO VLT and highlights of the first observations of stars and quasars, *Proc. SPIE Vol. 4005*, p. 121-130, Discoveries and Research Prospects from 8- to 10-Meter-Class Telescopes, Jacqueline Bergeron; Ed,(2000).
- Ohtsuki, S., Iwagami, N, Sagawa, H., Ueno, M., Kasaba, Y., Imamura, T., Yanagisawa, K., and Nishihara, E. 2008, Distributions of the Venus 1.27- $\mu\text{m}$  O<sub>2</sub> airglow and rotational temperature, *Plan. Space Sc.*, volume 56, p. 1391-1398, 2008.
- Ortiz, J., et al., Albedo and atmospheric constraints of dwarf planet Make-make from a stellar occultation, *Nature*, Volume 491, pp. 566-569, 2012.
- Oyama, V.I., Carle, G., Woeller, F., Pollack, J., Reynolds, R., and Craig, R., Pioneer Venus gas chromatography of the lower atmosphere of Venus, *J. Geophys. Res.*, 85, 7891-7902, 1980.
- Pater, I.; Lissauer, J., *Planetary Sciences*, Cambridge University Press, 2001.
- Ptzold, M., Husler, B., Bird, M., Tellmann, S., Mattei, R., Asmar, S., Dehant, V., Eidel, W., Imamura, T., Simpson, R., and Tyler, G. The structure of Venus' middle atmosphere and ionosphere. *Nature*, 450:657-660, doi: 10.1038/nature06239, 2007
- Pasachoff, J.M., Schneider, G., Widemann, T., High-resolution satellite imaging of the 2004 transit of Venus and asymmetries in the Cytherean atmosphere, *Astron. J.* 141, 112, 2011.
- Peralta, J.; Hueso, R.; Sánchez-Lavega, A., A reanalysis of Venus winds at two cloud levels from Galileo SSI images, *Icarus*, volume 190, p. 469-477, 2007.
- Peralta, J.; Hueso, R.; Sánchez-Lavega, A., Characterization of mesoscale gravity waves in the upper and lower clouds of Venus from VEx-VIRTIS images, *Journal of Geophysical Research*, volume 113, E00B18, 2008.
- Peralta, J. et al., Solar Migrating Atmospheric Tides in the Winds of the Polar Region of Venus, *Icarus*, *in press*, 2012.

- Pérez-Hoyos, S.; Sánchez-Lavega, A.; French, R., Short-term changes in the beltzone structure of Saturn's Southern Hemisphere, *Astronomy & Astrophysics*, vol. 460, 641-645, 2006.
- Phillips, R.J., and M.C. Malin, The interior of Venus and tectonic implications, in *Venus*, edited by D.M. Hunten, L. Colin, T.M. Donahue, and V.I. Moroz, pp. 159-214, University of Arizona Press, Tucson, 1983.
- Piccialli, A., et al., Cyclostrophic winds from the Visible and Infrared Thermal Imaging Spectrometer temperature sounding: A preliminary analysis, *Journal of Geophysical Research*, volume 113, E00B11, 2008.
- Piccialli, A., Cyclostrophic wind in the mesosphere of Venus from Venus Express observations, PhD thesis, 2010.
- Piccialli, A., et al., Dynamical properties of the Venus mesosphere from the radio-occultation experiment VeRa onboard Venus Express, *Icarus*, volume 217, p. 669-681, 2012.
- Piccioni G. et al., South-polar features on Venus similar to those near the north pole, *Nature*, volume 450, p. 637-640, 2007.
- Piskunov, N. E.; Valenti, J. A., New algorithms for reducing cross-dispersed echelle spectra, *Astronomy and Astrophysics*, v.385, p.1095-1106, 2002.
- Pollack, J., Toon, O. and Boese, R., Greenhouse models of Venus' high surface temperature, as constrained by Pioneer Venus measurements, *J. Geophys. Res.*, 85, 8223-8231, 1980.
- Pollack, J., Dalton, J., Grinspoon, D., Wattson, R., Freedman, R., Crisp, D., Allen, D., Bezar, B., de Bergh, C., Giver, L., Ma, Q. and Tipping, R., Near infrared light from Venus' nightside: A spectroscopic analysis, *Icarus*, 103, 1-42, 1993.
- Preston, R., et al., Determination of Venus winds by ground-based radio tracking of the VEGA balloons, *Science* (ISSN 0036-8075), vol. 231, p. 1414-1416., 1986.
- Read, P., Super-rotation and diffusion of axial angular momentum: II. A review of quasiaxisymmetric models of planetary atmospheres. *Quarter. J. R. Met. Soc.* 112, 253-272, 1986.
- Rengel, M., Hartogh, P., and Jarchow, C., Mesospheric vertical thermal structure and winds on Venus from HHSMT CO spectral-line observations, *Plan. Space Sc.*, volume 56, p. 1368-1384, 2008.

- Roos-Serote, M., Drossart, P., Encrenaz, Th., Lellouch, E., Carlson, R., Baines, K., Taylor, F., Calcutt, S., The thermal structure and dynamics of the atmosphere of Venus between 70 and 90 KM from the Galileo-NIMS spectra, *Icarus* (ISSN 0019-1035), vol. 114, no. 2, p. 300-309, 1995.
- Rossow, W., Williams, G., Large-scale motion in the Venus stratosphere, *Journal of the Atmospheric Sciences*, volume 36, p. 377-389, 1979.
- Rossow, W., del Genio, A., Limaye, S., Travis, L., Cloud morphology and motions from Pioneer Venus images, *Journal of Geophysical Research*, vol. 85, p. 8107-8128, 1980.
- Rossow, W.; Del Genio, A.; Limaye, S.; Travis, L.; Stone, P., Cloud morphology and motions from pioneer Venus images. *Journal of Geophysics Research*, volume 85, p. 8107-8128, 1981.
- Rossow, W.; Del Genio, A. and Eichler, T. Cloud tracked winds from Pioneer Venus OCPP images. *Journal of Atmospheric Sciences*, volume 47, p. 2053-2084, 1990.
- Russell, C., Zhang, T., Delva, M., Magnes, W., Strangeway, R., Wei. Y., Lightning on Venus inferred from whistler-mode waves in the ionosphere, *Nature* 450, 661-662, 2007.
- Rybicki, G. and Lightman, A, *Radiative processes in Astrophysics*, Wiley-VCH Verlag GmbH, 2004.
- Sánchez-Lavega, A., Comparison of the averaged thermal profile and condensable species, 2004.
- Sánchez-Lavega, A., Hueso, R., Piccioni, G., Drossart, P., Peralta. J., Pérez-Hoyos, J., Wilson, C., Taylor, F., Baines, K., Luz, D., Erard, S., Lebonnois, S.: Variable winds on Venus mapped in three dimensions, *Geophysical Research Letters*, vol. 35, 2008.
- Sánchez-Lavega, A., *An introduction to planetary atmospheres*. Taylor and Francis, 2011.
- Sagan, C., The Surface Temperature of Venus, *Astronomical Journal*, Vol. 65, p. 352-353, 1960.
- Sagan, C., and G. Mullen, Earth and Mars: Evolution of atmospheres and surface temperatures, *Science*, 177, 52-56, 1972.

- Sandor, B., Clancy, R., chemistry of vibrationally excited O<sub>3</sub> from diurnal microwave measurements of O<sub>3</sub>( $\nu$ 1), O<sub>3</sub>( $\nu$ 2), O<sub>3</sub>( $\nu$ 3), and O<sub>3</sub>(ground state), *Journal of Geophysical Research: Atmospheres*, Volume 115, 2010.
- Sandor, B., Clancy, R., Observations of HCl altitude dependence and temporal variation in the 70-100 km mesosphere of Venus, *Icarus*, Volume 220, p. 618-626, 2012.
- Saunders, R.S., A.J. Spear, P.C. Allin, R.S. Austin, A.L. Berman, R.C. Chandler, J. Clark, A.V. Decharon, E.M. DeJong, D.G. Griffith, J.M. Gunn, S. Hensley, W.T.K. Johnson, C.E. Kirby, K.S. Leung, D.T. Lyons, G.A. Michaels, J. Miller, R.B. Morris, R.G. Pierson, J.F. Scott, S.J. Schaffer, J.P. Slonski, E.R. Stofan, R.W. Thompson, and S.D. Wall, Magellan mission summary, *J. Geophys. Res.*, 97, 13067-13090, 1992.
- Schaber, G.G., R.G. Strom, H.J. Moore, L.A. Soderblom, R.L. Kirk, D.J. Chadwick, D.D. Dawson, L.R. Gaddis, J.M. Boyce, and J. Russel, Geology and distribution of impact craters on Venus: What are they telling us?, *J. Geophys. Res.*, 97, 13257-13302, 1992.
- Schubert, G., Covey, C., del Genio, A., Elson, L. S., Keating, G., Seiff, A., Young, R., Counselman, C., Kliore, A., Limaye, S., Revercomb, H., Sromovsky, L., Suomi, V., Taylor, F., Woo, R., von Zahn, U, Structure and circulation of the Venus atmosphere, *Journal of Geophysical Research*, vol. 85, p. 8007-8025, 1980.
- Schubert, G., General circulation and the dynamical state of the Venus atmosphere, *Venus (A83-37401 17-91)*. Tucson, AZ, University of Arizona Press, 1983, p. 681-765, 1983.
- Schubert, G., Walterscheid, R., Propagation of small-scale acoustic-gravity waves in the Venus atmosphere, *Journal of the Atmospheric Sciences*, vol. 41, p. 1202-1213, 1984.
- Schubert, G., and D.T. Sandwell, A Global Survey of Possible Subduction Sites on Venus, *Icarus*, 117, 173 - 196, 1995.
- Schubert, G., Bougher, S., Covey, C., Del Genio, A., Grossman, A., Hollingsworth, J., Limaye, S., Young, R., Venus atmosphere dynamics: A continuing enigma, in *Exploring Venus as a Terrestrial Planet*, ed. by L.W. Esposito, E.R. Stofan, T.E. Cravens (American Geophysical Union, Washington, DC), pp. 101-120, 2007.

- Seiff, S., Thermal structure of the atmosphere of Venus, Venus (A83-37401 17-91). Tucson, AZ, University of Arizona Press, p. 215-279, 1983.
- Seiff, Schofield, J., Kliore, A., Taylor, F., Limaye, S., Models of the structure of the atmosphere of Venus from the surface to 100 kilometers altitude, *Advances in Space Research*, vol. 5, no. 11, 1985, p. 3-58, 1985.
- Shapiro, I., Rotation of Venus, *Science*, 159, 1124, doi: 10.1126/science.159.3819.1124, 1968.
- Slanger, T.; Cosby, P.; Huestis, D.; Bida, T., Discovery of the Atomic Oxygen Green Line in the Venus Night Airglow, *Science*, volume 291, p. 463-465, 2001.
- Smith, A., Rotation of Venus: Continuing Contradictions, *Science*, Volume 158, Issue 3797, pp. 114-116,
- Smith, M. D., Gierasch, P. J., Global-Scale Winds at the Venus Cloud-Top Inferred from Cloud Streak Orientations, *Icarus*, 123, 313-323, 1996.
- Smrekar, S., Stofan, E., Mueller, N., Treiman, A., Elkins-Tanton, L., Helbert, J., Piccioni, G., Drossart, P., Recent hotspot volcanism on Venus from VIRTIS emissivity data. *Science* 328, 605-608, 2010.
- Sonett, C., A summary review of the scientific findings of the Mariner Venus mission. *Space Sci. Rev.* 2, 751-777, 1963.
- Sonnabend, G.; Sornig, M.; Krötz, P. J.; Schieder, R. T.; Fast, K. E., High spatial resolution mapping of Mars mesospheric zonal winds by infrared heterodyne spectroscopy of  $CO_2$ , *Geophysical Research Letters*, volume 33, CiteID L18201, 2006.
- Sonnabend, G.; Sornig, M.; Scheider, R.; Kostiuk, T.; Delgado, J., Temperatures in Venus upper atmosphere from mid-infrared heterodyne spectroscopy of  $CO_2$  around 10  $\mu m$  wavelength, *Planetary and Space Science*, Special issue on Ground-based measurements in support of Venus Express, volume 56, p. 1407-1413, 2008.
- Sonnabend, G.; Kroetz, P.; Sornig, M.; Stupar, D., Direct observations of Venus upper mesospheric temperatures from ground based spectroscopy of  $CO_2$ , *Geophysical Research Letters*, volume 37, CiteID L11102, 2010.
- Soret, L. et al., Venus OH nightglow distribution based on VIRTIS limb observations from Venus Express, *Geophys. Res. Let.*, volume 37, L06805, 2010.

- Soret, L. et al., Atomic oxygen on the Venus nightside: global distribution deduced from airglow mapping, *Icarus*, doi:10.1016/j.icarus.2011.03.034, 2011.
- Sornig, M., et al., Venus upper atmosphere winds from ground-based heterodyne spectroscopy of  $CO_2$  at 10  $\mu m$  wavelength, *Planetary and Space Science*, volume 56, p. 1399-1406, 2008.
- Sornig, M. et al., Direct Wind Measurements from November 2007 in Venus' Upper Atmosphere Using Ground-Based Heterodyne Spectroscopy of  $CO_2$  at 10  $\mu m$  Wavelength, *Icarus*, doi:10.1016/j.icarus.2011.03.019, 2011.
- Sornig, M., Livengood, T., Sonnabend, G., Stupar, D., Kroetz, P., Direct wind measurements from November 2007 in Venus' upper atmosphere using ground-based heterodyne spectroscopy of  $CO_2$  at 10  $\mu m$  wavelength, *Icarus* Volume 217, Issue 2, p. 863-874, 2012.
- Sornig, M., Sonnabend, G.; Stupar, D.; Kroetz, P.; Nakagawa, H.; Mueller-Wodarg, I., Venus' upper atmospheric dynamical structure from ground-based observations shortly before and after Venus' inferior conjunction 2009, *Icarus*, Volume 225, Issue 1, p. 828-839, 2013.
- Suomi, V. Cloud Motions on Venus, *The Atmosphere of Venus*. Proceedings of a conference held at Goddard Institute for Space Studies, New York, 15-17, Edited by James E. Hansen. NASA SP-382. Washington, DC: National Aeronautics and Space Administration, 1975., p.42, 1975.
- Suomi, V.; Limaye, S., Venus - Further evidence of vortex circulation, *Science*, volume 201, p. 1009-1011, 1978.
- Stiepen, A., Gérard, J.-C., Dumont, M., Cox, C., Bertaux, J.-L., Venus nitric oxide nightglow mapping from SPICAV nadir observations, *Icarus*, Volume 226, Issue 1, p. 428-436, 2013.
- Smrekar, E., Stofan, E., Mueller, N., Treiman, A., Elkins-Tanton, L., Helbert, J., Piccioni, G., Drossart, P., Recent hotspot volcanism on Venus from VIRTIS emissivity data. *Science* 328, 605-608, 2010.
- Svedhem, H.; Titov, D.; Taylor, F.; Witasse O., Venus as a more Earth-like planet, *Nature*, volume 450, p. 629-632, 2007.
- Tanga, P., Widemann, T., Sicardy, B., Pasachoff, J., Arnaud, J., Comolli, L., Rondi, A., Rondi, S., Suetterlin, P. 2011, Sunlight refraction in the mesosphere of Venus during the transit on June 8th, 2004, *Icarus* 218, 207-219, 2012.

- Takagi, M., Matsuda, Y., Effects of thermal tides on the Venus atmospheric superrotation. *J. Geophys. Res.-Atmos.* 112, 9112, 2007.
- Tavener, T. et al., *Planetary Sp. Sciences*, 56, pp. 1435, 2008.
- Taylor, F., McCleese, D., Elson, L., Martonchik, J., Diner, D., Houghton, J., Delderfield, J., Schofield, J., Bradley, S., Infrared remote sensing of the atmosphere of Venus from the Pioneer 12 Orbiter, *Space research. Volume 20 - Proceedings of the Open Meetings of the Working Groups on Physical Sciences, Bangalore, India, May 29-June 9, 1979.* Oxford and Elmsford, N.Y., Pergamon Press, p. 227-230, 1980.
- Taylor, F., Hunten, D. and Ksanfomaliti, L., The thermal balance of the middle and upper atmosphere of Venus, pages 650-680. 1983.
- Taylor, F., Climate Variability on Venus and Titan. *Space Science Reviews*, 125:445-455, 2006.
- Taylor, F., Grinspoon, D., Climate evolution of Venus, *Journal of Geophysical Research*, Volume 114, 2009.
- Tellmann, S., Pätzold, M., Häusler, B., Bird, M., Tyler, L., Structure of the Venus neutral atmosphere as observed by the Radio Science experiment VeRa on Venus Express, *Journal of Geophysical Research*, volume114, 2009.
- Tellmann, S., Häusler, B., Hinson, D., Tyler, G., Andert, T., Bird, M., Imamura, T., Pätzold, M., Remus, S., Small-scale temperature fluctuations seen by the VeRa Radio Science Experiment on Venus Express, *Icarus*, Volume 221, p. 471-480, 2012.
- Thompson, R., Venus's General Circulation is a Merry-Go-Round., *Journal of Atmospheric Sciences*, 27, 1107-1116, 1970.
- Titov, D., Svedhem, H., Taylor, F., In *The Atmosphere of Venus: Current Knowledge and Future Investigations*, ed. by P. Blondel, J.W. Mason. *Solar System Update (Springer-Praxis, Berlin)*, 2006.
- Titov, D.; Bullock, M.; Crisp, D.; Renno, N.; Taylor, F. and Zasova, L., Radiation in the Atmosphere of Venus, *Geophysical Monograph Series 176.* 10.1029/176GM08, 2007.



- Titov, D.; M. Titov, F.W. Taylor, H. Svedhem, N.I. Ignatiev, W.J. Markiewicz, G. Piccioni and P. Drossart, Atmospheric structure and dynamics as the cause of ultraviolet markings in the clouds of Venus, 456, 620-623, doi:10.1038/nature07466, 2008.
- Tellmann, S., Paetzold, M., Hausler, B., Bird, M. K., and Tyler, G.L., Structure of Venus neutral atmosphere as observed by the Radio Science experiment VeRa on Venus Express, *J. Geophys. Res. (Planets)*, volume 114, E00B36, 2009.
- Titov, D., Markiewicz, W., Ignatiev, N., Li, S., Limaye, S., Sanchez-Lavega, A., Hesemann, J., Almeida, M., Roatsch T., Matz T., Scholten, F., Crisp, D., Esposito, L., Hviid, S., Jaumann R., Keller, H., Moissl, R., Morphology of the cloud tops as observed by the venus express monitoring camera. *Icarus*, 217, 2, 682-701, doi:10.1016/j.icarus.2011.06.020, 2012.
- Toigo, A.; Gierasch, P.; Smith, M., High-resolution cloud feature tracking on Venus by Galileo. *Icarus*, volume 109 (2), p. 318-336, 1994.
- Tomasko, M., Smith, P., Suomi, V., Sromovsky, L., Revercomb, H., Taylor, F., Martonchik, D., Seiff, A., Boese, R., Pollack, J., Ingersoll, A., Schubert, G., Covey, C., The thermal balance of Venus in light of the Pioneer Venus mission. *J. Geophys. Res.-Atmospheres*, 85, 8187-8199, doi:10.1029/JA085iA13p08187, 1980.
- Traub, W.; Carleton, N., Retrograde winds on Venus - Possible periodic variation, *Astrophysical Journal*, Part 1, volume 227, p. 329-333, 1979.
- Tsang, C., Irwin, P., Wilson, C., Taylor, F., Lee, C., Kok, R., Drossart, P., Piccioni, G., Bezaud, B., and Calcutt, S., Tropospheric carbon monoxide concentrations and variability on Venus from Venus Express/VIRTIS-M observations. *Journal of Geophysical Research (Planets)*, 113, doi: 10.1029/2008JE003089, 2008.
- Turcotte, D.L., How did Venus lose heat?, *J. Geophys. Res.*, 100, 16,931 - 16,940, 1995.
- Widemann, T.; Lellouch, E., Wind Field in Venus' Lower Mesosphere, Recent Progress in Planetary Exploration, 25th meeting of the IAU, Special Session 1, 2003.
- Widemann, T. et al., New wind measurements in Venus lower mesosphere from visible spectroscopy, *Planetary and Space Science*, volume 55, p. 1741-1756, 2007.

- Widemann et al., Venus Doppler winds at cloud tops observed with ES-PaDONs at CFHT, Planetary and Space Science, Volume 56, p. 1320-1334, 2008.
- Wilquet, V., Drummond, R., Mahieux, A., Robert, S., Vandaele, A-C., Bertaux, J-L, Optical extinction due to aerosols in the upper haze of Venus: Four years of SOIR/VEX observations from 2006 to 2010, Icarus, Volume 217, p. 875-881, 2012.
- Wilson, C.F., Perez-Ayucar, M., Vandaele, A.C., Wilquet, V., Mahieux, A., Markiewicz, W.J., Bertaux, J.L., Piccioni, G., Venus Express Observations during the 2012 Venus Transit, EPSC, Madrid, 2012.
- Yamamoto, M., and Takahashi, M., Superrotation maintained by meridional circulation and waves in a Venus-like AGCM. *J. Atmos. Sci.* 63, 296-314, 2006.
- Yamamoto, M., and Takahashi, M., Simulations of superrotation using a GCM for Venus' middle atmosphere, *Earth, Planets, and Space*, 59, 971-979, 2007.
- Yamamoto, M., and Takahashi, M., Influences of Venus' topography on fully developed superrotation and near-surface flow, *Earth, Planets, and Space*, 61, 2009a.
- Yamamoto, M., and Takahashi, M., Dynamical effects of solar heating below the cloud layer in a Venus-like atmosphere, *Journal of Geophysical Research (Planets)*, 114, 2009b.
- Young A., Is the Four-Day "Rotation" of Venus Illusory?, *Icarus*, volume 24, p. 1-10, 1975.
- Young, L.D.G. and Kattawar, G.W., Scattering in the Atmosphere of Venus III. Line Profiles and Phase Curves for Rayleigh Scattering, *Icarus*, volume 30, 360-366, 1977.
- Young, R. and Pollack, J., A three-dimensional model of dynamical processes in the Venus atmosphere, *Journal of Atmospheric Sciences*, 34, 1315-1351, 1977.
- Young, A.; Schorn, R.; Young, L.; Crisp, D., Spectroscopic observations of winds on Venus, I-technique and data reduction. *Icarus*, volume 38, p. 435-450, 1979.

- Young, E., et al., *Bulletin American Astronomical Society*, 40, pp. 513, 2008.
- Young, E.; Bullock, M.; Limaye, S.; Bailey, J.; Tsang, C., Evidence For And Against 8-day Planetary Waves In Ground-based Cloud-tracking Observations Of Venus' Nightside, *Bulletin of the American Astronomical Society*, volume 42, p. 975, 2010.
- Yung, Y., and DeMore, W., Photochemistry of the stratosphere of Venus: Implications for atmospheric evolution, *Icarus*, 51, 199-248, 1982.
- Zahnle, K.J., Planetary noble gases, in *Protostars and Planets III*, edited by E.H. Levy, and J.I. Lunine, pp. 1305-1338, University of Arizona Press, Tucson, 1993.
- Zhang, X.; Liang, M-C., Montmessin, F., Bertaux, J-L., Parkinson, C., Yung, Y., Photolysis of sulphuric acid as the source of sulphur oxides in the mesosphere of Venus, *Nature Geoscience*, Volume 3, Issue 12, pp. 834-837, 2010.
- Zasova, L., Khatountsev, I., Moroz, V. and Ignatiev, N., Structure of the Venus middle atmosphere: Venera 15 fourier spectrometry data revisited, *Advances in Space Research*, 23:1559-1568, 1999.
- Zasova, L., Ignatiev, N., Khatuntsev, I., Linkin, V., Structure of the Venus atmosphere. *Planet Space Sci.* 55, 1712-1728, 2007.



# Publications

## Refereed contributions

Characterizing the atmospheric dynamics of Venus from ground-based Doppler velocimetry.

**Machado, P.**, Luz, D. Widemann, T., Lellouch, E. and Witasse, O.  
Icarus, Volume 221, p. 248-261, 2012.

Wind circulation regimes at Venus' cloud tops : Ground-based Doppler velocimetry using CFHT/ESPaDOnS and comparison with simultaneous cloud tracking measurements using VEx/VIRTIS in February 2011.

**Machado, P.**, Widemann, T., Luz, D. and Peralta, J.  
Icarus, 2013. (Submitted).

## Communications

- D. Luz, P. Machado, E. Lellouch, T. Widemann, O. Witasse, J.-L. Bertaux, Characterization of Venus' atmosphere with ground based observations by Doppler velocimetry. Presentation at the European Congress of Planetary Sciences, EPSC, Potsdam, September 2009.
- P. Machado, D.Luz, T. Widemann, Characterizing the Venus atmospheric dynamics from ground-based Doppler velocimetry. International Venus Conference. Aussois, 2010.

- P. Machado, D. Luz, T. Widemann, Characterization of Venus' atmospheric dynamics with ground-based Doppler velocimetry. EGU - European Geosciences Union, Vienna, 2010.
- P. Machado, D. Luz, T. Widemann, Caracterização da Atmosfera de Vénus por Velocimetria Doppler. Física Ilda. Faculdade de Ciências da Universidade de Lisboa, Lisbon, May 2011.
- P. Machado, D. Luz, T. Widemann, Characterization of Venus' atmospheric Dynamics with ground-based Doppler Velocimetry, II Encuentros de Exploración del Sistema Solar. Bilbao, June 2011.
- P. Machado, D. Luz, T. Widemann, Current results from UVES/VLT. Lisbon Venus Team Meeting, Lisbon, Portugal, May 2011.
- P. Machado, D. Luz, T. Widemann, Characterization of Venus' cloud top dynamics using ground-based Doppler velocimetry. Joint EPSC-DPS Meeting, Nantes, France, October 2011.
- P. Machado, D. Luz, T. Widemann, Characterization of Venus' atmospheric dynamics with ground-based Doppler velocimetry. Atmospheric Waves Workshop - ESA/ESTEC, Netherlands, November 2011.
- P. Machado, D. Luz, T. Widemann, Characterization of Venus' atmospheric dynamics with ground-based Doppler velocimetry, Coordinated Ground-Based Measurements with VCO/Akatsuki and Venus Express. 3rd Sakura meeting - JAXA/ISAS, Tokyo, Japan - November 2011.
- P. Machado, T. Widemann, D. Luz, Characterization of cloud top dynamics of Venus with ground-based Doppler velocimetry. 3rd Europlanet workshop - 4th PHC/Sakura meeting: Venus as a transiting exoplanet. March 5 - 7 2012, Paris, France.

- P. Machado, D.Luz, T. Widemann, Venus winds with ground-based Doppler velocimetry. EGU - European Geosciences Union General Assembly, Vienna, April 2012.
- Machado P., Widemann T., Luz D., Peralta J., Chamberlain S., Observation of Dynamical Tracers in the Venus Atmosphere. Comparative Climatology of Terrestrial Planets. Boulder, Colorado - U.S.A., June 2012.
- P. Machado, T. Widemann, D. Luz, J. Peralta and L. Rossi, New measurements of Venus dayside winds with CFHT/ESPaDOnS, European Planetary Science Congress (EPSC) - Madrid, September 2012.
- iTOUR - Investigative Tour of Uranus, I. Gerth, P. Machado, F. Duschel, M. Hässig, K. Hayes, K. Konstantinidis, P. Lewkowicz, J. MacArthur, C. Nabert, J.Ruffio, J. Stude, C. Terhes, N. Themessl, J. Vicent, M. Wu. European Planetary Science Congress (EPSC), Madrid, September 2012.
- Venus Twilight Experiment: Observation and analysis of the aureole during the 2012 transit. T. Widemann, P. Tanga, B. Sicardy, P. Machado, F. Braga-Ribas, C. Veillet, J. Pasachoff, F. Colas, F. Vachier, S. Bouley, L. Maquet, J. Berthier, T. Fukuhara, D. Luz. European Planetary Science Congress (EPSC), Madrid, September 2012.
- The Venus Twilight Experiment: Probing the Mesosphere in 2004 and 2012. P. Tanga, T. Widemann, A. Ambastha, B. A. Babcock, J. Berthier, S. Bouley, F. Braga-Ribas, K. Brasch, W. Burke, F. Colas, T. Fukuhara, L. Fulham, M. Imai, M. Lu, P. Machado, L. Maquet, J. M. Pasachoff, J. Roberts, G. Schneider, W. Sheehan, C. Sigismondi, N. Thouvenin, F. Vachier, C. Veillet, X. Wang. Division for Planetary Sciences of the American Astronomical Society (DPS). Reno, Nevada, U.S.A., October 2012.

- P. Machado, T. Widemann, D. Luz, J. Peralta, Venus winds with ground-based Doppler velocimetry and comparison with coordinated cloud tracking method winds. Lunar and Planetary Science Congress (LPSC), Woodlands - Houston, Texas, U.S.A., March, 2013.
- P. Machado, T. Widemann, D. Luz, J. Peralta, Venus cloud tops winds with ground-based Doppler velocimetry and comparison with cloud tracking method. International Venus Workshop, Catania, Italy, June, 2013.

## Prizes and grants

- First Prize in Scientific Communications, workshop Física Ilimitada, Faculdade de Ciências da Universidade de Lisboa, Lisbon, May 2011.
- First Prize - Scientific Case, Summer School Alpbach 2012 - ESA. Austria, August 2012 .
- First Prize - Best Presentation, Summer School Alpbach 2012 - ESA. Austria, August 2012 .
- Prize - Best Scientific Communication, Encontro Nacional de Astronomia e Astrofísica. Lisbon, July 2013.
- Conference Travel Grant, Fundação Luso-Americana para o Desenvolvimento (FLAD, Portugal). April 2013
- PhD Grant, Fundação para a Ciência e a Tecnologia (FCT, Portugal), reference: SFRH/BD/66473/2009.



## Observing missions

- Quaoar Occultation - (TNO). Santiago Islands, Cape Verde. March 2012.
- Observing Tests - with the Venus transit's dedicated Coronagraph (Cytherograph). Nice, France, April 2012.
- 2012 Venus Transit - International coordinated observing campaign - "Twilight Venus Experiment", Udaipur, India, May-June 2012.
- Measurement of zonal winds at the lower cloud level of the atmosphere of Venus - Telescopio Nazionale Galileo/NICS. La Palma, Canary Islands, Spain, July 2012.

## Workshops and Advanced Formation

Atmospheric Waves Workshop - ESA/ESTEC, Netherlands, November 2011.

Giant Planets of the Solar System - Summer School Alpbach - ESA. Alpbach, Austria, August 2012.



To finish with a smile



Figure 7.1: There is the equatorial mount, the azimuthal mount and... the “Elephantorial” mount... After the successful observation of the 5-6 June, 2012, Venus’ transit, at Udaipur, Rajasthan, India.